Medical Imaging Methods

Recent Trends

Ashutosh Kumar Shukla
Editor

Springer

Medical Imaging Methods

Ashutosh Kumar Shukla
Editor

Medical Imaging Methods

Recent Trends

Springer

Editor
Ashutosh Kumar Shukla
Department of Physics
Ewing Christian College
Prayagraj
Uttar Pradesh
India

ISBN 978-981-13-9120-0 ISBN 978-981-13-9121-7 (eBook)
https://doi.org/10.1007/978-981-13-9121-7

This Springer imprint is published by the registered company Springer Nature Singapore Pte Ltd.
The registered company address is: 152 Beach Road, #21-01/04 Gateway East, Singapore 189721, Singapore

Dedicated to my parents

Preface

Medical imaging techniques have a crucial role to play in clinical diagnostics. This volume covers the different imaging tools as applied in the diagnosis of brain tumors, oral diseases, kidney cysts, and skin cancer. This volume includes three chapters on spectroscopic imaging techniques based on magnetic resonance with a greater emphasis on EPR imaging. Chapters introduce the particular technique in the beginning followed by detailed description including examples and comparison with other imaging method such as MRI. Application of nanomaterials to enhance the imaging modalities has been included in a separate chapter.

I am thankful to the expert contributors for making this collection a unique addition to the existing knowledge base. My special thanks to Prof. Przemysław M. Płonka and Prof. Martyna Elas, Department of Biophysics, Faculty of Biochemistry, Biophysics, and Biotechnology, Jagiellonian University, Krakow, Poland, who kindly reviewed manuscripts for this volume. I am also thankful to Prof. K. Nakagawa, Division of Regional Innovation, Graduate School of Health Sciences, Hirosaki University, Japan, for his contribution as a reviewer.

I sincerely thank Dr. Naren Aggarwal, Executive Editor, Clinical Medicine, Springer (India) Private Limited, for giving me the opportunity to present this book to the readers. I also thank Teena Bedi, Associate Editor (Clinical Medicine), and Saanthi Shankhararaman for their support during the publication process.

While going through the individual chapters, I learnt a lot and hope that it will be a good experience for the readers too.

Prayagraj, India
May 2019

Ashutosh Kumar Shukla

Contents

About the Editor

Ashutosh Kumar Shukla is currently an Associate Professor of Physics at Ewing Christian College, Prayagraj, which is a constituent college of the University of Allahabad, India. Dr. Shukla has successfully completed research projects funded by the University Grants Commission, New Delhi, and has presented his research at various international events. He is a member of the review panel for several international journals and is a member of the International EPR Society (IES) and of the International Society of Magnetic Resonance (ISMAR). In addition to journal publications, he has also edited numerous volumes on major topics, such as medicine, food science, and crude oil in collaboration with leading global experts.

Electron Paramagnetic Resonance Imaging-Solo and Orchestra

1

Martyna Elas, Martyna Krzykawska-Serda, Michał Gonet, Anna Kozińska, and Przemysław M. Płonka

Magnetism is a common property of the matter and magnetic interactions inseparably bound to the interactions with the mediation of the electric fields are one of the principal types of physical interactions (recently unified with the weak interaction to electroweak interactions). The nature of magnetic interactions is a deliverable of the phenomenon of spin defined as early as in 1920s [1–3]. On the atomic level, these properties are a result of the possession of a resultant nonzero spin, which can be attributed both to the nucleus and to the electrons. The magnetic nuclei interacting with the external magnetic fields give the base for the phenomenon of the nuclear magnetic resonance and the nonzero resultant electron spin—to the phenomenon of the electron spin (ESR, also called paramagnetic, EPR) resonance. From the physical point of view, the nature of both phenomena are similar and can be described with similar mathematic formulas. The only difference, resulting from the differences between the gyromagnetic ratios for proton and electron, and actually, from the respective differences in their mass, affects the working spectrum of radiation used to observe the phenomenon—for NMR it is the radio waves, and for the EPR—microwaves. But from the point of view of chemistry and biology, the quality of information delivered by these techniques is totally different. While the NMR techniques convey messages on the elemental composition and the types of molecules constituted by the NMR-active elements, in the case of EPR almost the whole information concerns unpaired electrons (with the uncompensated spins) which here are either components of transient metal ions, or free radicals and similar molecules [4].

M. Elas (✉) · M. Krzykawska-Serda · A. Kozińska · P. M. Płonka
Department of Biophysics, Faculty of Biochemistry, Biophysics and Biotechnology, Jagiellonian University, Kraków, Poland
e-mail: martyna.elas@uj.edu.pl

M. Gonet
Department of Biophysics, Faculty of Biochemistry, Biophysics and Biotechnology, Jagiellonian University, Kraków, Poland
Novilet, Poznań, Poland

A. K. Shukla (ed.), *Medical Imaging Methods*,
https://doi.org/10.1007/978-981-13-9121-7_1

The information may, therefore, concern the occurrence of free radicals due to radiation or redox reactions. Exogenous EPR-active substances may also deliver information on their magnetic microenvironment (including fine and hyperfine interactions with other unpaired electrons, and magnetic nuclei, and relaxation phenomena, concluding on the local redox properties of the environment, e.g., oxygenation), and from the anisotropy of these interactions one can conclude about local movements, affecting such important "microphysiological" phenomena as local fluidity, viscosity, molecular dynamics and transport.

In both cases, the information conveyed by the phenomenon of the magnetic/paramagnetic resonance may additionally inform of the spatial distribution of NMR- or EPR-active species. This is possible if the external stable magnetic field becomes inhomogeneous, e.g., changing regularly along a given space variable (forming the so-called field gradient). Such techniques are called techniques of magnetic/paramagnetic resonance imaging (NMRI/EPRI). And again, while based on the same physics, the nature of this information is totally different for NMRI than for EPRI, therefore often delivering complementary, medically important information (e.g., on spatial distribution of tissue polarity and hydration in NMRI, and distribution of a spin label and its magnetic interaction with oxygen in EPRI).

This chapter concerns the uniqueness of EPRI, but also the possibilities to use it as a complementary method with other ways to biological and biomedical imaging. EPRI has become an important method in the research of the distribution of redox properties, oxygenation, melanization, blood flow, penetration of epidermis, and other medically important phenomena, for which the spatial distribution of the phenomenon or the process is crucial. In particular, it shall focus on three experimental approaches related to the primary techniques of EPR spectroscopy, namely continuous wave (CW) EPR, pulse EPR imaging, and the rapid scan (RS) methods. A separate dose of attention will be paid to the application of EPRI in multi-technique approach.

1.1 Methodology of EPR

1.1.1 Introduction to the EPR Technique

EPR is oriented on studying unpaired electrons, basically magnetically induced splitting of electronic spin states [5–11]. One of the characteristic features of electron is presence of the spin (S = 1/2), which leads to magnetic moment. The presence of external magnetic field significantly influences the spin orientation, which takes parallel or anti-parallel orientation to the applied direction of magnetic field. One can define arbitrary axis of the electron position based on the external magnetic field, which leads to projections of magnetic momentum of the unpaired electron equal $m_s = \pm 1/2$. Possessing unpaired electrons in the sample is important, because the two distinct energy levels of the spin are created and the EPR technique is focused on measuring the energy difference between them. What is more, how big is the separation of the energy levels will strongly depend on magnetic field strength. Next, the question occurs—how one can measure the energy difference between

these two levels? In the EPR technique, the sample is placed in the homogenous magnetic field and excited with a specific frequency of electromagnetic radiation, next, one can sweep the magnetic field, and when the frequency tunes to the energy difference between upper and lower electron stages the microwave frequency is absorbed. The point is that when measuring the energy of microwave in the system, one is able to see the absorption as a specific peak (it will be visible as a decrease of the microwave energy in the system). This physical phenomenon, when the system can absorb very specific energy and change its energy state, is called the resonance. The resonance will occur when the energy difference ($\Delta E = h\nu$, where h is Planck constant and ν is the wave frequency) will be equal to the product of electron g-factor, Bohr magneton (μ_B), and the induction of the external magnetic field (B_0) [Eq. 1.1].

$$h\nu = g_e \mu_B B_0 \tag{1.1}$$

The position of a selected signal in the spectrum measured from a sample placed in EPR cavity will inform about the energy differences between the spin states. To be more precise, it is a Gaussian/Lorentzian distribution of energy absorption for the sample, whose shape depends on the relaxation time of the exited electron and the localization of density of unpaired electron in the molecule [12]. According to the principle of uncertainty, the longer the relaxation time, the smaller the signal width is observed. What information can be obtained from the EPR spectrum of a sample? Main characterization of the signal includes: signal intensity, hyperfine splitting, *g*-factor, spin relaxation times, and signal line shape (Fig. 1.1a). It is important to remember that all of those characteristic signals could be influenced by several environmental factors, e.g., temperature. Because of that, a careful designing condition for reliable calibration curves for the spin probes is necessary.

The signal linewidth can be a crucial parameter which carries information about the change in paramagnetic center environment. For example, a very popular spin probe for oximetry studies—lithium phthalocyanine (LiPc)—has a strong dependency of signal linewidth in relation to oxygen partial pressure in surrounding area. In general, signal width can be measured, either using first derivative of the absorbance spectrum as peak-to-peak, or as full width at half maximum of the absorbance line and is expressed in magnetic induction units (Gs). Which method of calculation is better depends strictly on other signal's properties.

Next signal feature, related to the signal intensity, is amplitude. Amplitude is calculated based on pick-to-pick distance in *y*-axis of spectrum.

The *g*-factor can be measured which can be understood as a molecule fingerprint. According to Eq. 1.1, Bohr magneton is constant and external magnetic field is known during the measurement, so the energy between two spin levels is determined by g-factor. Measuring of g-factor can be easy in low-viscosity solution, but when paramagnetic molecules have fixed orientation in the sample the deviation of g-factor can be observed. This effect is related to spin–orbit coupling—when the orbitals are oriented in the molecule in the fixed position, and the sample become anisotropic (sensitive to the position in the spectrometer). In axis system, the g-factor anisotropy can be studied and g_x, g_y, g_z can be calculated.

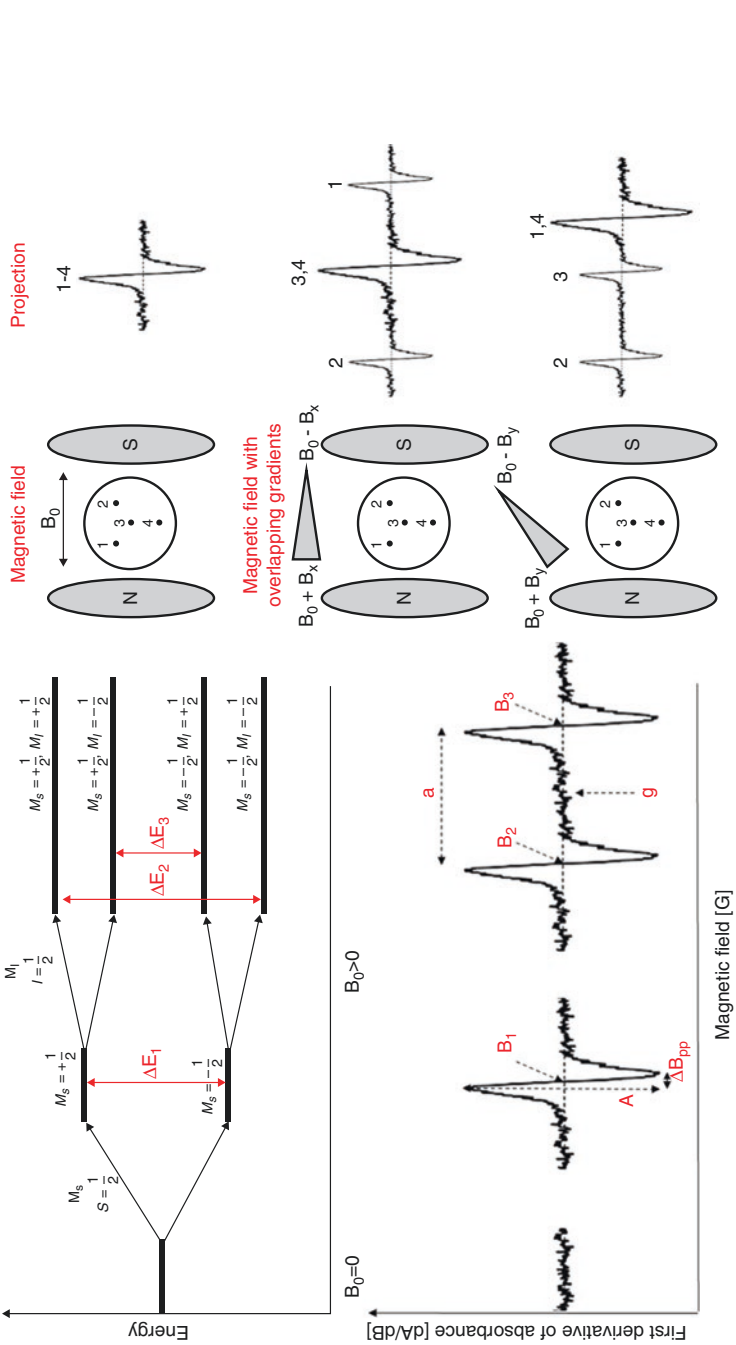

Fig. 1.1 (**a**) Upper panel shows Zeeman splitting of the energy levels in the presence of magnetic field. Lower panel presents the first derivative of energy absorbed by the sample. B1, B2, and B3 show different position of the signal in the magnetic field; A—signal amplitude, ΔBpp—signal linewidth peak-to-peak. (**b**) EPR spectroscopy provides a signal averaged over sample volume. Adding additional magnetic field gradients in three Cartesian dimensions allow spatial encoding of the signal position within the sample volume

Unpaired electron is sensitive to local environment. It is worthy to mention that a lot of atoms relevant for biology (e.g., H, C, N, O, P, S, Cl, Fe, Mn) have isotopes with a nonzero nuclear spin. The single electron can interact with a magnetic nucleus (magnetic field generated from nucleus magnetic moment is "strong enough" to affect the electron); this effect is observed in EPR signal as hyperfine splitting. The signal parameter which is responsible for this interaction is termed hyperfine coupling constant (A).

When electron excitation of a paramagnetic compound is leading to generation of dipole with magnetic momentum, the T_2 and T_1 relaxation times describe the behavior of the spin. Relaxation times are reflected in how EPR signal changes in time, due to spins going back to the initial value (magnetization dipole loses the orientation adopted in the magnetic field). T_2 relaxation time is related to transverse magnetization (M_{xy}) after microwave absorption and spin–spin interactions. On the other hand, T_1 relaxation time is related to energy exchange between spin and external environment and affects longitudinal component of the spin and that is why is called spin–lattice relaxation time. T_2 relaxation time parameter is characterized by exponential decay character and is shorter or equal to T_1. Relaxation times can be studied with different types of EPR techniques, but pulse EPR technique is the first method of choice.

1.1.2 When EPR Meets Biology

For EPR only paramagnetic compounds are visible. Therefore, for studying biological objects, the presence of paramagnetic compounds (e.g., radical-containing unpaired electrons) is necessary to register the EPR signal. The EPR signal may come from endogenous or exogenous paramagnetics. Naturally occurring in living systems endogenous paramagnetics are some metal ions, melanins, paramagnetic gases (oxygen, nitric oxide, nitric dioxide), and free radicals. Usually the compounds with at least one unpaired electron and present at very low concentration and with very short lifetime, require more stable spin traps to allow EPR measurement. That is why study of physiological process driven by paramagnetic compounds such as nitric oxide, superoxide, or hydroxyl radicals is difficult. On the other hand, one of the most relevant molecules for the living organisms—oxygen—in the stable form is in the triplet state with paramagnetic and diradical properties [13, 14]. Unfortunately, according to very broad signal from triplet oxygen, direct measurement of this compound especially in biological samples is hardly possible. This is due to extremely short relaxation time of molecular oxygen in dissolved state. One of the substances naturally occurring in biological samples is melanin, the dark pigment responsible for example for hair and skin color. Melanin gives very strong EPR signal due to presence of more than one paramagnetic center [15]. Next group of paramagnetic compounds naturally present in living organisms are some metal ions. Metalloenzymes can be successfully studied by EPR, for example the oxygen evolving complex in photosystem II (PSII), the FeMo cofactor of nitrogenase (enzyme involved in N_2 reduction to NH_3). Interestingly, extremely important metal

ions for enzymes like Mg or Zn can be substituted with paramagnetic analogues (Zn^{+2} with Co^{+2} and Mg^{2+} with Mn^{2+}) allowing for EPR measurements. The last group of naturally occurring paramagnetic compounds are free radicals such as reactive oxygen and nitrogen species, which are extremally important in physiological processes involved in oxidative stress and redox signaling [16]. From definition free radicals are molecules with one or more unpaired electrons, so they are also paramagnetic compounds (but not each paramagnetic compound is a free radical). EPR provides unique possibilities to study free radicals interaction in long time scales (for compounds like ascorbyl radical or tocopheroxyl radical) and very short living forms like hydroxyl radical or superoxide radical anion [17–19].

Fortunately, the wide variety of spin probes and spin traps provide the possibility to measure oxygenation, some free radical concentration, redox state, acidosis, cell viability, viscosity, tissue perfusion, and molecular motion in biological systems [20, 21]. Generally, in experiments which involve synthetic spin probes, the changes of EPR signals of the spin probe are observed in dependence of selected environmental factors. For example: to measure oxygen concentration in the tissue, the EPR signal depends on oxygen concentration in probe (e.g., LiPc) localization; measurement of tissue redox state can be related to spin probe decay rate, which is associated to the intracellular glutathione concentration. It should be highlighted that these procedures require proper calibration curves in controlled conditions to measure physical values (units), not only the changes in the system. In summary, spin probe is a compound which provides paramagnetic properties to the investigated biological process; on the other hand, usually diamagnetic spin traps are making possible the EPR measurement of unpaired electrons from compounds already present in the system (chemical interaction between trap and spin is required). It should be mentioned that the special type of spin probes are spin labels, usually from nitroxyl family, and they are useful for, e.g., membrane fluidity measurements.

It is very important to select a proper spin probe to the specific research problem, according to the known spin probe biodistribution and biokinetics, toxicity, signal intensity, time of measurements, and total observation time. For example, to study tissue oxygenation for several weeks in specific, well-defined place, the OxyChip (encapsulated lithium octa-n-butoxynaphthalocyanine: LiNc-BuO implants) is the properly chosen probe [22]. In contrast, the water-soluble trityl radicals could be used to image oxygenation in high volume tissues with high resolution, due to a very good biopharmacokinetics profile [23]. The main disadvantage of the first choice is the single point measurement; on the other hand, the pO_2 selectivity is very high and this leads to very high signal-to-noise ratios (no real need for sophisticated EPR equipment—CW spectroscopy can be done at S and L bands). The water-soluble spin probes such as nitroxides or trityl radicals are sensitive not only to pO_2, which can be used as an advantage because, e.g., tissue pH can be measured in the same set of measurements. Unfortunately, such procedure will require very good calibration curves to calculate selected parameters and this can introduce additional errors [24–28]. Water-soluble spin probes have limited toxicity which can be almost irrelevant for, e.g., mice organism homeostasis during experiment, but the total dose

of the spine probe injected over imaging time needs to be always considered during data analysis. Unfortunately, water-soluble spin probes are expensive, one way to deal with this problem is purification of compounds obtained from, e.g., urine sample after imaging [29].

For the measurement of partial pressure of oxygen (pO_2) in the tissue the spin probe is required, despite the fact that oxygen molecule has two unpaired electrons in triplet state. The observed changes in spin probe signal, i.e., changes in the relaxation time, are caused by interaction of molecular oxygen and the probe. It needs to be highlighted that such interaction does not change the oxygen concentration in the tissue, in contrast to more invasive oximetry techniques (e.g., polarimetry). This is why very often EPR oximetry is treated like a direct method of oxygen measurement in the tissue, despite the fact that spin probes are involved. Generally, two EPR approaches are used in EPR oximetry: (1) methods related to T_2 relaxation time (spin–spin) or (2) T_1 relaxation time (spin–lattice). In the first case, the oxygen concentration can be calculated for example based on changes in signal linewidth or superhyperfine structure. Second types of approaches are related to, e.g., saturation recovery in pulse technique or continuous saturation with microwave power.

Generally, the glutathione (GSH) concentration and presence of thiol (-SH) functional groups is a crucial factor for determination of redox balance and pH values in biological systems. It should be highlighted that pH and redox states are crucial parameters for tissue inflammation, ischemia, tumor microenvironment, drug pharmacokinetics and effectiveness. Consequently, there is an urgent need for development of non-invasive, direct measurements of GSH in the tissue. EPR is a very promising tool to accomplish these goals. To study redox balance in the tissue the thiol-sensitive spin probes are used, such as paramagnetic disulfides sensitive to thiol-disulfide exchange [20].

The pH levels can be measured by EPR technique only when the molar concentration of hydrogen ions which are surrounded of the spin probe is influenced by the change in spectrum (change of g-factor and hyperfine splitting constant). Commonly, the stable nitroxides radicals are used as spin probes (based on imidazoline and imidazolidine scaffolds). Nowadays, for in vivo pH measurement NMR is the most common approach, but due to low resolution and dependency of metabolism in the tissue the novel approaches, like EPRI, are highly needed. The types and mechanism of action of spin probes used for pH and redox balance EPR measurements were described elsewhere by [20, 30].

As described above, for resonance at the energy of electronic stage to occur, a corresponding magnetic field strength and microwave frequency is required. Furthermore, the resonator for specific microwave wavelength needs to be used, i.e., the 9.5 GHz microwave has around 3 cm wavelength and resonator cavity needs to be similar in size. In this context, it is obvious why the experimental setup is so important and why different types of measurements require different EPR conditions. Various ranges of microwave frequency have been assigned letters. The most important of them for biological studies are: L-band for frequency range 1–2 GHz, S for 2–4 GHz, X for 8–12 GHz, and Q for 30–50 GHz (the letters are random and are legacy of WW2). The X and Q spectrometers are quite popular due to relatively

low cost of magnets (weak magnetic field is needed), but used microwave energy is not able to penetrate deeply into the tissues. Q-band, with high-power microwave amplifiers and the application of shaped pulse in PW EPR techniques, is often used to study objects at a small scale with high sensitivity. This last feature can be extremely useful when some critical in concentration paramagnetic substances need to be detected, i.e., metals or/and neuromelanin in brain tissue [31]. The L-band and lower frequencies are successfully used for animal imaging studies, especially due to better microwaves penetration into the tissue [32]. Low frequency of microwaves guarantees cavity of the resonator big enough to image mice, rabbits, pigs, and parts of much bigger organisms like humans with good resolution [32]. It should be mentioned that magnetic field homogeneity becomes a big issue for big objects imaging. To sum up, it should be clarified that the higher the microwave frequency is used, the higher the resonator sensitivity and noise will be. At the same time, microwave penetration will decrease, and this is why imagers very often operate at 250–750 MHz frequency [33–35].

1.1.3 EPR Imaging

The aim of imaging procedures is oriented towards acquiring spatial information of paramagnetic species distribution. The challenge is the process of transition from Spectral EPR to EPR Imaging (EPRI) [36, 37]. To obtain 2D or 3D images, the series of spectra needs to be collected. Each of them needs to have a precise address of its location described with coordinates XYZ. This leads to set of pixels (for 2D image) or voxels (for 3D image)—the smallest elements of the image, and each of these elements contains spectral information. It is noticeable that a better quality image will contain more pixels/voxels than the poorer one. This will define image resolution, but a large number of elements do not necessarily determine better image. How many elements will be forming the sample representation in EPRI and providing good image quality? It will depend on such parameters as image acquisition technique, spectral shape of the sample that can be related to blurring, noise, data processing artifacts, and microwave frequency [8]. It is worth mentioning that image deconvolution (image processing technique) can increase EPRI resolution without collecting additional spectra from sample. Additional problem for imaging of biological samples is the microwave penetration—the size of the sample is limited by absorption of microwave energy by water, described below (Sect. 1.5). It should be highlighted that to study in vivo systems, the submillimeter image resolution is the needed minimum.

How the information about EPR spectrum XYZ orientation in sample can be acquired? How can one collect a set of separate spectra from the sample instead of one average signal? This is possible due to the additional magnetic field oriented in X, Y, and Z positions. These additional coils are able to create magnetic field gradient. As a result, the position of the signal in the spectrum, when the field gradient overlaps with the external magnetic field, which is swept between particular values, will depend not only on the position of the resonance, but also on the spatial

position of the paramagnetic probe in the sensitive volume of the resonant cavity (Fig. 1.1b). The collection of all signals position in the axis of the magnetic field gradient is called the projections. The crucial problem in 2D/3D image generation is related to number and position of projections [38, 39]. If too few projections are acquired, the image will not be represented properly. Additionally, not enough projections will create the image very sensitive to errors related to the misidentification of a signal frequency. It should be clear now why highly defined magnetic field is so important in EPRI—each magnetic field distortion will affect the signal projection and will perturbate the image (for that reason each metal object too close to the magnet can introduce imaging artifact). On the other hand, too high number of projections will extend imaging time and the biologically significant information can be lost (e.g., during oximetry study the short-time increase of tissue oxygenation will be undetectable during long-time scans). To solve the problem with accurate projection number, a few different solutions are proposed, e.g., sampling the spatial polar, spatial azimuthal and spectral projection angles, limitations of field of view, obtaining less projections in low gradient field and more in high gradient projections (due to much better signal-to-noise ratio in low gradient projections), and number of scans for each projection also can vary.

The single spectrum parameter measurement, e.g., amplitude measured in two or three spatial dimensions, delivers only the more or less precise information on the position of the paramagnetic species in the cavity. Such an imaging is often not enough to obtain biologically relevant information. To get a meaningful image of, e.g., oxygen distribution in the tissue, it is necessary to include a spectral dimension along with two or three spatial dimensions. Such a technique is termed spectral-spatial EPRI (described further below). Spectral-spatial EPRI is useful to study, e.g., diffusion of the spin probes in the system because it can provide the information about spin concentration. In the Cartesian coordinate system, it can be presented as one spatial axis (intrinsic frequency coordinate, which carries information about EPR spectrum related to, e.g., spin concentration) while on the other axis the relation about the spectrum position is carried. The situation can become more sophisticated when the time axis is introduced into spectral-spatial measurement—each spatial pixel (for 2D) or voxel (for 3D) will then contain information not only about the whole spectrum shape, but also about its evolution over time. Such an imaging can allow one to calculate, e.g., probe diffusion coefficient into the tissue. The spectral-spatial data are collected for all projections, and then the image can be reconstructed with one of the tomographic methods.

1.1.4 EPRI versus MRI

There is a lot of similarities between magnetic resonance imaging (MRI) and EPRI, but the most important difference (which determines other alterations) is the presence of electrons in the center of the EPR method, instead of protons (especially water protons for MRI). This leads to around 1000 times lower magnetic field and different range of applied frequency radiation (GHz for EPR vs MHz for MRI). For

example, when the applied frequency is 250 MHz the MRI magnetic field is 5.9 T and EPR is 9 mT. During the pulse imaging the radiofrequency width for MRI is in the range of μs to ms, when for EPR it will be 10–100 ns. When we consider the endogenous source of signal, water protons will be the ones for MRI, while for EPR we can investigate HbNO (nitrosylhemoglobin) or melanin. The MRI image based on water protons will provide detailed anatomical information about the tissue, whereas EPRI without additional spin probes will be far behind. This is why to provide useful EPRI imaging exogenous spin probes need to be added, e.g., nitroxides or trityls. It is worthy to mention that MRI also provides the option of contrast imaging (with exogenous compound) like gadolinium-based molecules. Interesting fact is that spin probe concentration needed for a high quality image for EPR is more than 1000 times smaller than for MRI (<1 mM concentration for EPR, >60 M for MRI). Based on the whole range of available signal source for MRI, the signal can be classified as a stable one, while the EPR signals can be categorized as non-stable ones in the range of minutes (the exception is melanin and solid state spin probe like LiPc which can provide week-long signal stability). The linewidth of the signal for MRI is in the range of Hz to kHz, while for EPR it is 100 kHz to MHz [40–42]. Imaging requires additional gradients of magnetic field, and the wider the EPR signal is, the more powerful gradients are needed [43].

1.1.5 Problems and Limitations

One of the main problems of EPRI technique is the fact that water molecules absorb microwaves. The higher the energy of microwaves, the greatest the water absorption. This leads to limited application of microwave frequency applied to biological systems, the L (0.8–1.2 GHz) and S (3.4–3.8 GHz) microwave frequency bands are the most useful for this purpose. In detail, the 250 MHz wave frequency will penetrate easily the mouse, rat, or rabbit (>10 cm), although 1–2 GHz will provide the information only about a part of the mouse body. Additional issue related with microwave absorption by water is sample heating, due to non-resonant effects [44]. This can not only affect the size of the imaged object but also affect the biological sample with thermal effects (and, consequently, e.g., blood perfusion in the tissue).

One of the most relevant problems during spectroscopy and imaging techniques is signal-to-noise ratio (STN). Gradient dependence of noise can be observed during imaging, which is associated with the problem of obtaining high quality image with high gradients for short time and low scan number (the highest the gradients, the highest number of scans are needed).

One more problem during EPR imaging is related to the resonator type. Volume resonators are extremely useful for 2D and 3D imaging and they provide a good sensitivity. On the other hand, the tuning is difficult especially for big tissue volume due to high water concentration and non-resonant microwave absorption. Nowadays, the volume resonators can be successfully used for whole body mice imaging in pulse wave and rapid scan techniques (described further below). The popular alternative to the volume resonator is the surface coil. The main advantage of it is easy way

to place it on the whole body (the internal organ measurement is possible but invasive that way), the sensitivity strongly depends on signal source distance from the coil (~$1/r^2$)—the best STN ratio will be coming from object placed very close (generally <2 mm) or inside the coil. Such a sensitivity dependence provides limited information about 2D/3D imaged area. Many new resonators from specific applications are being developed such as surface resonators [45] or implantable resonators [46].

1.2 EPRI Modalities

Nowadays for biological application three EPRI modalities are in use: Pulse Wave EPR (PW), Continuous Wave (CW) EPRI and its enhancement called Rapid Scan (RS) EPRI (Fig. 1.2). The main problems to achieve during imaging are good signal-to-noise ratio and creation of the image with good resolution in short time scale. It can be crucial for biological experiments to obtain such an image quickly because many of important processes (e.g., change of redox balance in the tissue) are fast. Furthermore, the possibility of imaging live system without anesthesia or/and analgesia allows one to observe biological activity with minimal intervention. Generally, CW imaging needs time and image requires large number of projection. Due to possibility of more projection acquisition over time in contrast to classical CW imaging, RS-EPRI is a great achievement and promising tool for EPR research in vivo.

On the other hand, the PW EPRI modalities provide very good image quality with decent resolution. Unfortunately, to obtain such an image of object in scale of cm^3 in PW mode the power of hundreds to thousands of watts needs to be delivered by radiofrequency amplifier [47]. It should be also mentioned that for PW EPR the spin probes with longer relaxation times are preferred—so selection of non-optimal spin probe for PW modality can decline the advantage of this technique [48].

Like all in vivo imaging techniques, EPR imaging also sets up hardware and software development [37]. Many aspects not unessential in spectroscopy supposed to be immensely complex in imaging applications. For preclinical application, possibility of imaging small animals is the crucial part. It requires equipment such as magnets, resonators, and electronics capable to generate homogenous magnetic field in larger regions with good sensitiveness for electron spin probe distributed in animals. In recent years, immense effort was put to reduce EPR imaging time plausible for animal anesthesia. Continuous wave (CW) and time-domain (pulse) EPR spectrometers were transformed into imagers significantly different from each other, both having strengths and weaknesses [49]. Development of rapid scan (RS)

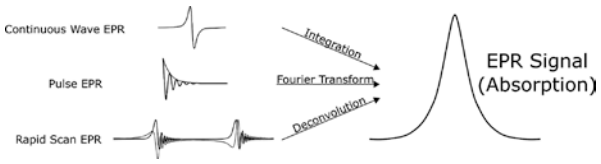

Fig. 1.2 Different EPR modalities—CW, pulse, and RS all provide information on the amount of energy absorbed by the sample

technique is a unique achievement [50]. Rapid scan EPRI allows to improve signal-to-noise ratio and significantly shorten imaging time and therefore has a great potential to become a leading EPR imaging method especially suited for nitroxide imaging [51, 52]. A great description with many details of EPRI hardware was provided by Eatons and Ohno [36]. Below we will describe hardware challenges, as well as IT approaches in EPR imaging playing a crucial role for EPRI to become a popular technique for biomedical applications, explain how images are reconstructed from the acquired data and present the perspective for future of EPRI technology in biomedical applications.

1.2.1 Continuous Wave EPRI

After placing sample or animal in the center of static magnetic field and when resonance condition is satisfied in conventional continuous wave EPR, the main magnetic field is slowly swept through resonance. Slowly changing magnetic field is modulated at frequency range from 10 to 100 kHz. At particular modulation frequency phase-sensitive detection acquires signal in the same phase as field modulation. If amplitude of the field modulation is small in relation to the linewidth of EPR spectrum [53] (the rule of thumb: it is less than 1/3 of EPR signal linewidth), the detected EPR signal is linear with the slope of absorption spectrum. Conventional CW-EPR detection is very effective in noise elimination, but by increasing modulation amplitude (larger then 1/3 of EPR linewidth) EPR signal becomes distorted and is not useful in applications where linewidth has an important role.

CW-EPRI system should contain a few essentials parts: (a) radiation source at frequency at and below 1GHz, (b) microwave bridge with circulator to isolate transmission from detector arm, (c) magnets generating homogenous magnetic field with possibility to sweep, (d) resonator or coil for cumulating energy according to the position of the imaged object, (e) modulation unit, (f) three pairs of orthogonal gradient coils required for imaging, and (g) computer for controlling the imager and data acquisition [54].

During imaging, the object (e.g., an animal) is positioned in the center of the resonator (the maximum of homogenous magnetic field). Resonator is tuned and matched to the radiation source until there is the minimum reflection of microwave power from the cavity. To assess quality of tuning and matching, a ratio between stored and dissipated energy per cycle of radiation is measured. This ratio is called Q (quality)-value or Q-factor of resonator cavities. For CW-EPRI the higher Q-value the better. For low frequency EPRI, the loop-gap resonator [55], re-entrant cavity resonator [56], and parallel-coil resonators [57] are usually used. Animal motions during EPRI experiment such as heart beating, peristalsis, urination, or breathing are major causes of resonator detuning. Therefore, well-designed automatic frequency control (AFC) and/or automatic coupling/matching controls (AMC/ACC) are necessary during the in vivo imaging to correct magnetic field shifts and to keep matching and tuning conditions during animal anesthesia. Great review and practicum describing EPRI resonators for in vivo imaging is provided by Rinard and co-workers [58].

For imaging, the necessary magnetic field homogeneity is determined by spin probe used to imaging. In brief, magnetic field inhomogeneity should be much less than the linewidth of the spin probe. It is due to the spatial resolution. Spatial resolution is defined as a distance D [cm] between two spatially resolved points. In practice, resolution is determined by linewidth and gradient magnitude G [Gs/cm]. Therefore, homogeneity should be much better than $G\,x\,D$. For example, for nitroxides concentration of ~200 ppm is more than enough, but for a narrower spin probe such us trityls better homogeneity over the imaging volume would be required [59].

The magnetic field is modulated sinusoidally at frequency up to 100 kHz. This brings about an improvement of the amplitude of signal reflected from resonator at this particular frequency as the amplitude is proportional to the slope of the absorption signal. Additionally, all signals with phases and frequencies differing from the applied modulation frequency are removed. Advantage of CW-EPRI is no limitation regarding the used spin probe. Paramagnetic probes with narrow as well as large linewidth are possible to image. However, because magnetic fields have to be swept for each projection, the imaging times are usually long (from minutes to hours depending on the image dimensionality).

Finally, the extra three sets of coils are required to convert static magnetic field into gradient magnetic field. Maximum gradient magnitude is determined by line shape of spin probe and size of imaged object, and it directly affects the obtained spatial resolution. Methodology of encoding gradient steps can be different and allows for shortening of imaging time and improving quality of reconstructed images [60].

1.2.2 Rapid Scan EPRI

Large amplitude modulation relative to EPR linewidth in combination with direct detection of EPR signal gave the beginning for the new type of EPR modality called rapid scan EPR [50]. In RS-EPR, magnetic field is swept through resonance in a time that is short relative to electron spin relaxation times. By proper deconvolution, EPR absorption spectra are obtained from rapid scan signal [61]. RS-EPR absorption spectrum is nothing other than integrated conventional CW-EPR spectrum. In comparison to CW, rapid scan is characterized by significant signal-to-noise (STN) improvement firmly decreases time required for imaging or using the same acquisition time as in CW, and greatly improves image quality [52]. Moreover, in rapid scan experiment higher power is required to saturate signal so more power can be used without saturation effect. To achieve similar STN for an image of phantom CW-EPRI acquisition is about 10 times longer than RS-EPRI [48].

1.2.3 Pulse EPRI

Pulse EPRI also called time-domain mode EPRI is analogous to magnetic resonance imaging (MRI). In both cases, spins (of magnetic nuclei in MRI and of

unpaired electrons in EPRI) are placed in the magnetic field and perturbed by a pulse of radiation at the resonance frequency. Technical progress of MRI apparatus has reached much farther than it did for pulsed EPRI [62, 63]. This fact is due to the extremely reduced relaxation times of the paramagnetic spin probes. As already mentioned above, EPR linewidths are much wider than a typical NMR linewidth. Moreover, larger linewidths are also responsible for a substantial worsening of spatial resolution and the inability to use some of the acquisition or reconstruction techniques currently used in MRI [40]. For NMR pulse width is typically in the range of microseconds and NMR spectra are spread over a very narrow range of frequencies (10–100 kHz). The impulse response of the nuclei (free induction decay, FID) is in the range of milliseconds to seconds and can be recovered after a typical spectrometer recovery time (dead time) of several microseconds. For pulse EPR, the time resolution in the experiment requires nanosecond scale. Because EPR spectra are spread over a broader range (several MHz), the excitation pulse width has to be less than 100 ns, requiring the ability to deposit narrow intense pulse to disturb the spin system. Time-domain responses (which are comparable to the spectrometer recovery time) have to be acquired with a fast digitizer at rates dictated by the frequency bandwidth of the resulting spectrum [64]. Recent studies have demonstrated applications of field-programmable gate array (FPGA) technology in pulse equipment design. It provides a low-cost and high-performance solution to the synchronization and control of logic pulses required for time-domain EPR experiments [65]. Currently several groups developed CW as well as pulsed EPR imagers for academic purposes and a few companies such as Bruker, Novilet, and O_2M provide commercial devices.

While there is not much differences between CW and time-domain EPRI in case of magnet and gradient coils requirements, resonators for pulse EPRI should have slightly different features from those used in CW-EPRI. Well-known resonators characterized by relatively large Q-factor such as solenoidal, saddle surface coil or birdcage were not found to be suitable for pulsed EPRI because of diminutive spin–spin relaxation of paramagnetic spin probes. On the other hand, higher Q-value determines better sensitivity. Therefore, as a compromise for short recovery times and the need to cover a reasonable bandwidth of excitation (10–20 MHz) and maintain the sensitivity, resonators with relatively low Q-value are dedicated for time-domain EPR imaging of small animals [64]. In recent studies, the group from Chicago developed resonator where Q-value is changing and controlled during experiment and achieved 30% better signal-to-noise ratio compared to traditional resonators [24].

An important factor in pulse in vivo experiment is pulse power (pulse height) which is related to the resonator volume and the filling factor (η) [Eq. 1.2]:

$$\eta = \frac{\int_{sample} B_1^2 dV}{\int_{cavity} B_1^2 dV} \tag{1.2}$$

i.e., the ratio of B_1 squared integrated over the sample volume to B_1 squared integrated over the resonator volume [66].

The right combination of power and pulse width allows to conduct in vivo experiment with appropriate standards regarding specific absorption rate (SAR) which protects animals/samples against delivery of too much energy into the imaged object.

1.2.4 Other Approaches

1.2.4.1 Overmodulation and Multiharmonic Analysis

In conventional CW-EPRI, the first derivative of the absorption spectrum is acquired by phase-sensitive detection at the modulation frequency usually at 100 kHz. To avoid spectrum distortion, modulation amplitude is kept much below of the paramagnetic probe linewidth. Combining information from multiple harmonics of the field modulation frequency has been shown to give the first-derivative spectrum with minimal distortion to modulation amplitudes that are several times the linewidths [67]. Main advantage of using higher amplitude modulation and multiharmonics analysis is significant improvement of S/N without increasing scan time and possibility to apply this method to imaging without distortion on reconstructed image [68].

1.2.4.2 Rotating Gradients

Traditional CW-EPR imaging is done by setting proper gradient magnetic field and performing a CW-EPR scan. Distribution of unpaired spin probe is done by collecting multiple, separate projections at different angles through the sample. Each projection takes typically a few seconds to acquire and full data collections for 2D to 4D images, can range from several minutes to hours. For higher dimensionalities (3D or 4D), this approach is beyond in vivo experiments. An alternative for constant gradients which significantly minimize imaging time is combination of rapid scan EPR and rotating gradients. Instead of many independent projections, a continuously rotating magnetic field gradient is applied. The first, straightforward application of rotating gradient by using fast scanning of magnetic field was performed by Koscielniak et al. [69]. Special hardware for control magnet current allowed to obtain 50 Gs field sweep in 4 s without any distortion on spectral EPR and demonstrate 2D and 3D imaging in, respectively, 2 and 9 min. The minimum time to measure single projections was determined to about 50 ms. However, presence of rotating gradient significantly decreased STN, and in vivo imaging required signal accumulation and extended imaging time to minutes. Other reports demonstrate that by decreasing the setup time of gradients and sweeping time, the acquisition of a single projection may take from 4.1 to 7.4 ms for 2D and up to 4 s for 3D image acquisition [70–72]. Recent methods involving rapid scan EPR allow for extra shortening of imaging time. The approaches based on the rapid scan strategy employ the fast triangular or sinusoidal modulation of the main magnetic field at frequency of 1–10 kHz to observe resonances [73]. Some new approaches which combine high-frequency sinusoidal modulation with simultaneously applied magnetic field gradient whose orientation is changed at low frequency are capable to decrease acquisition time for 2D imaging even to 10 ms [74].

1.2.5 Software

1.2.5.1 Image Reconstruction

A set of spectra treated with magnetic field gradient (the so-called projection) is obtained as the result of EPR imaging. Mathematical process leading to the transformation of projections into the image is called image reconstruction [38, 75, 76]. Most common and well-established method is the filtered back projection technique. It is based on inverse Radon transform and it is mostly used in X-ray CT (computer tomography) [77]. In EPRI experiment, there are two types of imaging: spatial-spatial and spatial-spectral. Spatial-spatial EPR imaging contains information on spin probe distribution where projections are a convolution between the spatial spin distribution along the gradient direction and the undistorted shape of the resonance line and have to be deconvolved before image reconstruction (*see Deconvolution section*), while in spatial-spectral EPR imaging, apart from spatial distribution of spin probe, other spectral characteristics such as line shape, linewidth, hyperfine split, etc. could be obtained (Fig. 1.3). In time-domain EPR, projections are collected as FIDs in the presence of stationary gradients as free induction decay responses. These are subjected to a fast Fourier transform (FFT) which provides the projections that are, generally, identical to those obtained in CW-EPRI. By appropriate changes in magnitude and orientation of stationary gradient, it is possible to obtain two- or three-dimensional projections of the imaged object. So in the EPR sense, a two-dimensional image is the complete set of projections on a selected plane. Main disadvantage of EPRI and image reconstruction is that there is no easy way to "slice-selection" as it is in MRI [71], therefore, information from the whole volume of spins in the object inside the resonator will contribute to the image data and reconstructed 2D image will reflect projection of the image on the selected

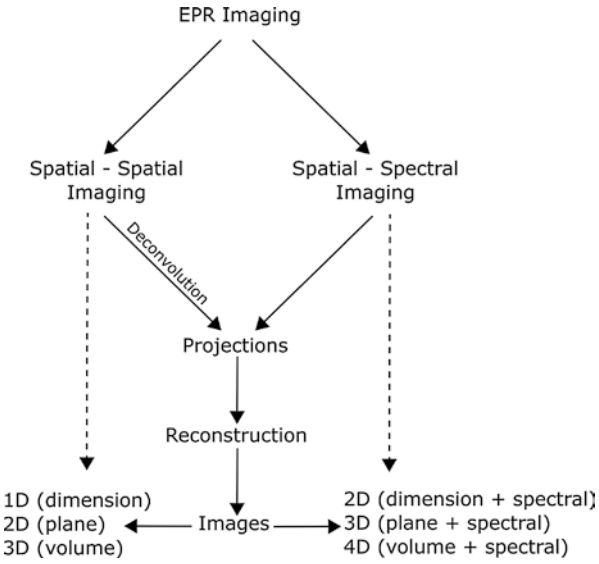

Fig. 1.3 Data processing in EPR spatial-spatial and spatial-spectral imaging

plane. To obtain 2D cross-section slice, it is necessary to perform 3D imaging and re-slice volume image to obtain an interested slice.

1.2.5.2 Spatial-Spatial Images

When planning spatial-spatial EPRI imaging, beside spectroscopic parameters, before acquisition two extra parameters are: gradient magnitude (commensurate with linewidth of the paramagnetic probe and the required resolution) and number of projections (in theory infinite number of projections will provide reconstructed image identical with imaged object). For 2D imaging, a vector gradient of appropriate magnitude is applied radially at N equal intervals in steps of $\vartheta = 180^o/N$ and N projections are collected—this is mathematically equivalent to rotation of projection direction in Radon transformation. For 3D imaging, all the three orthogonal gradients x, y and z are used. Number of projections is a product of amount of azimuthal and polar angles. Pathway of the gradient vector is more complex and could be defined on different ways to cover a surface of hemisphere.

To reconstruct the image using back projection boils down to the performance of inverse Radon transform on acquired projections. After back projection, the obtained image is not similar to the original but rather is a blurred version of it. To eliminate the blurring, filtering is implemented by multiplying the Fourier transform of the individual projections with an appropriate filter and then the product is inverse Fourier-transformed. After filtering, projections are back-projected to produce the image. This image reconstruction algorithm is very common and is referred to as the Filtered Back Projection (FBP) algorithm. 2D images are reconstructed in one step using FBP, while 3D images involve a two-stage reconstruction scheme [83]. Using suitable 3D visualization software the resulting images can be surface-rendered, or a cross section can be displayed.

1.2.5.3 Spatial-Spectral Imaging

Spatial-spectral imaging is more complex and allows to obtain not only signal amplitude but also a signal shape which may be more sensitive to spin probe environment, and spectral features such as line shape or linewidth can be mapped. From the biological point of view, changes in EPR line shapes provide more functional information, e.g., on oxygen partial pressure or redox state. Therefore, in a 2D spatial-spectral image a *pseudo* vector object is introduced [Eq. 1.3].

$$\tan(\alpha) = \frac{\text{spatial window}}{\text{spectral window}} \times \text{gradient magnitude} \tag{1.3}$$

Changes of the gradient amplitude in spatial-spectral image are mathematically equivalent to the rotation of the projection direction in spatial-spatial image. In practice, gradient is gradually incremented without changing its direction. Once the suitable widths for the spectral and spatial windows are selected, the gradient magnitude required can be calculated. Combination of 3D spatial and spectral acquisition gives a 4D spatial-spectral image in which EPR line shape is measured in every spatial location. In practice, EPR spectrum in every point of the sample is imaged. Contrary to spatial-spatial methodology, gradient magnitude is varied during imaging to fill not only the surface but volume of the sphere or hemisphere. 2D

spatial-spectral imaging experiment will take equal time duration corresponding to 3D spatial-spatial imaging, and a 4D (3D spatial and 1D spectral) image will be much more time consuming. Also there are several ways in which the projections data can be gathered, such as uniform distribution of solid angles over the surface of a sphere, etc. [49]. EPR images are usually reconstructed using FBP method, because of its speed and simplicity. But, when number of projections is limited or when projections are noisy FBP algorithm fails. Moreover, it also suffers due to star artifact. Iterative algorithms such as additive algebraic reconstruction technique (AART) or multiplicative algebraic reconstruction technique (MART) represent another class of tomographic reconstruction methods. These methods provide artifact-free imaging with minimal number of projections but its application is much more complex and time consuming [84]. Beside FBP and iterative algorithms, total variation methods (TV) are developing and used in image reconstruction [75, 85].

1.2.5.4 Deconvolution

In EPR imaging, spatial resolution is obtained by superimposing a magnetic field gradient to the main field. Because of this each projection represents the convolution between the spatial spin distribution along the gradient direction and the undistorted shape of the resonance line [86, 87]. In EPRI where linewidths are much wider than in NMR particularly in biomedical applications where nitroxides are used (linewidth up to 1.6 Gs and hyperfine triplet), simplification in the form of direct reconstruction from obtained projections cannot be adopted. To obtain projections which contained only spatial distribution of paramagnetic probe deconvolution procedure must be involved before reconstruction. Deconvolution is usually performed in the Fourier space with low-pass filtering. The choice of filter cutoff frequency is crucial and must be a compromise between two opposite needs: suppression the high-frequency noise and maintaining the high-frequency signal components [88]. Moreover, for higher imaging dimensionalities the number of projections to be deconvoluted may be very large so there is the need for an automatic selection of filter bandwidth criteria [89]. In RS-EPRI transitions through resonance occur in a time that is short relative to electron spin relaxation times, which causes oscillation in the recorded signal. Because of this nonlinearity conventional deconvolution such as in slow linear scan cannot be used. Deconvolution for sinusoidal rapid scan is much more complex and requires more sophisticated methods [61, 73].

1.2.5.5 Post-Processing Software

The EPRI experiment provides set of projections which require reconstruction procedure to generate images. Beside home-build image reconstruction programs, there are a few toolboxes and software available online to deal with EPRI data. Dr. Boris Epel from University of Chicago has created *SpecMan4EPR* (www.specman4epr.com)—high performance software capable to control virtually any EPR spectrometer or imager, and provides online support for SpecMan4EPR users. Additionally, he has also developed *Matlab EPR-IT toolbox* collection for EPRI image reconstruction and co-registration EPRI data with other imaging modalities (http://epr-it.specman4epr.com/) and together with Dr. Alexey Silakov from

Pennsylvania State University they have created *Kazan Viewer*—graphical user interface (GUI) for visualization and post-processing of EPR and NMR data (https://sites.google.com/site/silakovalexey/kazan-viewer). Another, powerful matlab toolbox dedicated for simulating and fitting a wide range of EPR spectra is *EasySpin* (https://www.easyspin.org/) maintained by Dr. Stefan Stoll. All abovementioned software are constantly developing and authors provide great documentation with application examples so that even a user without advanced programming skills can easily take advantage of post-processing software.

1.3 What Can Be Seen with EPRI?

1.3.1 First Attempts: Establishing the Methodology

First EPR images were obtained by Hoch and Day using diamonds. Their goal was to visualize the nitrogen impurities present in the crystal structure. As the EPR line was narrow (0.3 Gs), a very nice resolution could be achieved in these X-band 2-dimensional spatial images [90]. First EPR image of the biological object was a cross section of a celery slice saturated with a nitroxide and 2D image was taken at L-band [91, 92]. A number of laboratories continued to develop the technology towards the animal imaging, despite some skepticism in the field of the feasibility of EPR imaging of live animals. A lot of work was necessary first to understand the characteristics of nitroxyl spin probes and spin traps and their pharmacokinetics in vivo. This was performed using EPR spectroscopy in cells [93–100] and using organs, such as isolated beating heart [101, 102] or liver and lung [103] ex vivo. In 1986, Subczynski et al. reported the first in vivo EPR oximetry measurement which was conducted in mice using an L-band EPR spectrometer [104].

In the late 1980s, first phantom 1D CW images were shown [105]. First in vivo images in the living animals followed soon after, such as 2D nitroxide distribution in the skin [106], or 2D nitroxide in the lung [107], or 1D image of whole body rat [108, 109]. Nitroxides were also used for 2D imaging of a mouse brain [110, 111], as well as the whole body of a mouse [112]. Images of higher dimensions were first performed using isolated organs—3DSS image of an isolated heart [113] and 4D spectral-spatial image of isolated heart [114]. The same group carried out tumor 2D redox imaging and oximetry spectroscopy in a living animal [115].

Introducing spin probes other than nitroxide has been a breakthrough. Trityl family of stable free radicals advanced the field dramatically, providing spin probe that is non-toxic, soluble, highly sensitive to oxygen and of very short relaxation times [116–118]. Trityl spin probes together with imaging hardware and software developments enabled EPRI to achieve the excellent experimental results we appreciate today. Both CW and pulse EPR approaches were developed in parallel, with rapid scan joining in later. Spin probes other than trityls, like nitroxides specifically targeted for the brain [119–121] and different cellular compartments [122] were introduced. The design of nitroxides for pH, thiol, and phosphate [123, 124] opens up new possibilities as well. Spectroscopic oximetric measurements (not imaging) have been developed towards the clinical applications [125–127].

1.3.2 Going Faster and Seeing More

Recent years have seen significant advances in the development of EPRI hardware, spin probes, and experimental approaches enabling acquisition of EPRI data in oximetry, redox state, and other parameters with an excellent spatial and time resolution. Below are presented the recent results in biomedical EPRI.

1.3.2.1 Oximetry and Oxygen-Guided Radiotherapy of Murine Tumors

EPRI imaging was employed for oxygen-guided radiotherapy in murine tumors [78, 128]. Hypoxic subvolumes of tumors were given an extra radiation boost, resulting in higher survival of the animals. This was the first demonstration that dose-painting postulated for many years is indeed feasible.

A strong correlation between HIF-1α, VEGF, and CA9 and EPRI-identified hypoxic fractions (pO_2<10 torr) was found in spatially co-registered biopsies from murine tumors [78]. EPRI oxygen maps were based on the inversion recovery electron spin echo (IRESE) determination of T1 of the trityl oximetric probe.

The different methods for obtaining spin–lattice relaxation times in EPRI were compared and it was shown that the best accuracy and precision for small animal size objects is the inversion recovery sequence combined with the filtered back projection reconstruction. In contrast, for large animals, in which large radio frequency energy deposition might be critical, free induction decay and three pulse stimulated echo sequences might find better practical usage [14, 129].

The upper limit of the imaged tumor size was ca. 4 cm. Both CW and electron spin echo EPR oxygen images of a VX-2 tumor located on the leg of a New Zealand white rabbit were acquired [130].

EPR pO_2 imaging indicated that areas of transient hypoxia exist at the periphery of tumors [131–133]. Images can trace sub-minute variations of oxygen in the tumor. Difference in pO_2 variations is clear in different parts of the tumor, allowing differentiation of the chronically hypoxic core of the tumor from the tumor periphery with higher vascular access (Figs. 1.4 and 1.5) [79].

A new field for oximetry imaging is tissue engineering in regenerative medicine. Successful implantation of stem cells alone, as well as stem cell-grafted scaffolds to repair damaged tissue, e.g., in the heart, or in arthritis-damaged cartilage depends on oxygenation level. First steps in utilizing EPRI O_2 mapping have been taken for assessing scaffold porosity and local oxygen dynamics in engineered tissues [26, 134].

Nitroxides may be used as oximetric probes, for example isolated and beating heart was 2D spatial-spectral imaged using N^{15} DCP at L-band [135]. However, their lower pO_2 sensitivity and relatively short half-life make imaging more challenging. A very important discovery was confirmation of existence of cycling hypoxia in tumors, its extent and time dependence in living animals in non-perturbed tumors [133, 136, 137]. Using nitroxides localizing either extracellularly or intracellularly, it was shown that in tumors in vivo the extracellular pO_2 is similar to that of normal muscle, whereas intracellular pO_2 was much lower [136, 138, 139].

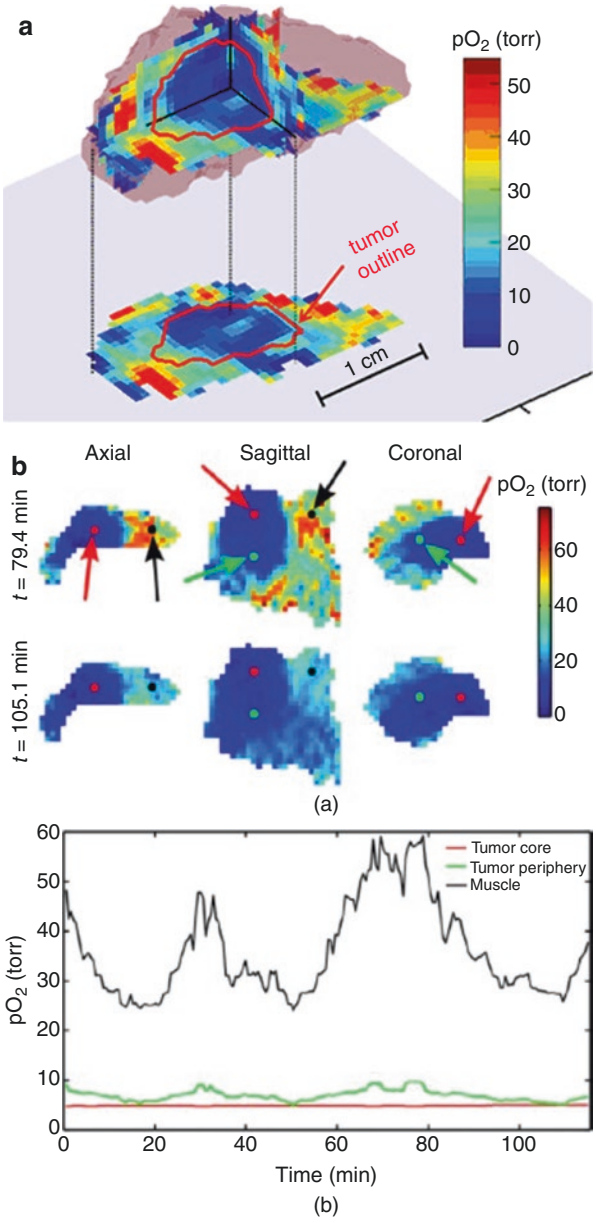

Fig. 1.4 (**a**) Three-dimensional oxygen map of fibrosarcoma tumor and bearing leg. Tumor outline, from a registered MRI image is shown in red. Reprinted with permission from Epel et al. [78]. (**b**) (a) pO_2 maps at two time points and (b) variation over time at voxels of different tissue types (indicated by the colored arrows). Difference in pO_2 variations is clear in different parts of the tumor, allowing differentiation of the chronically hypoxic core of the tumor from the tumor periphery with higher vascular access. Reprinted with permission from [79]

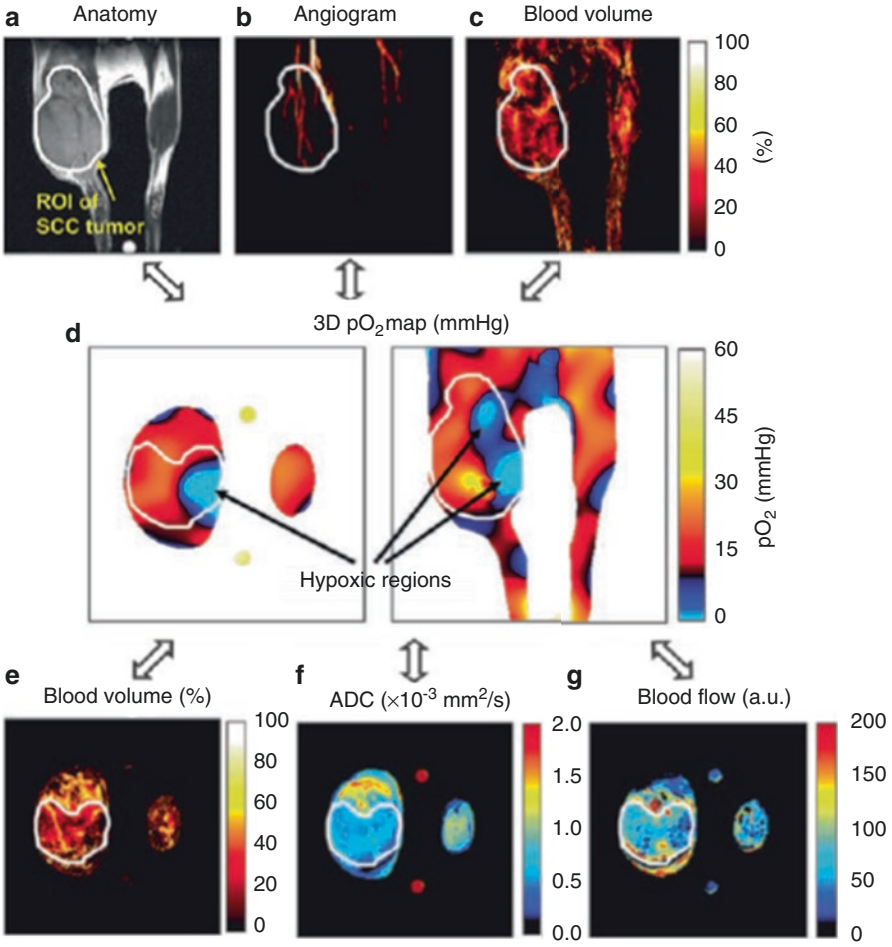

Fig. 1.5 Fusion of pO_2 image derived from EPRI and other flow-related image data from MRI. (**a**) MRI T2-weighted anatomical image showing the selected ROI of the SCC tumor. (**b**) MRI angiogram with an outline of the tumor region derived from MRI T2-weighted anatomical image. (**c**) MRI coronal blood volume image. (**d**) Axial and coronal pO_2 maps by EPRI. (**e**) MRI axial blood volume image. (**f**) MRI ADC image (axial). (**g**) MRI blood flow image obtained using arterial spin labeling technique. Reprinted with permission from [80]

One of the highest achievements of the recent years has been introducing the EPR oximetry into the clinic [140]. It is not imaging as yet, but first EPR spectroscopic pO_2 measurements were carried out in volunteers [141], in human skin [142]. After these first attempts, longitudinal pO_2 measurements were carried out in diabetic patients [126, 127], and also in cancer patients [143]. New oximetric spin probe preparations in lipid nanocapsules for better tissue distribution [144] or films for transcutaneous measurements [145] were developed, with clinical applications in mind.

1.3.2.2 Tumor Microenvironment

A comprehensive approach to image various features of the tumor environment is being developed by the Khramtsov group [124, 146, 147]. Based on the development of nitroxide, di-nitroxides, and trityl-based spin probes, they propose to measure oxygen, pH, thiol level, redox state as well as phosphates and glucose, either using several spin probes consecutively, or using a single, multifunctional spin probe. A possibility to acquire even a few of the above parameters noninvasively in the same animal and then possibly following these parameters longitudinally would provide a wealth of information on the tissue microenvironment, e.g., during tumor growth and response to treatment. The most suited technology for these measurements seems to be rapid scan, enabling fast acquisition of nitroxide spectra [51, 52].

pH is an important tissue microenvironment parameter, especially for tumors (Fig. 1.6). Designing spin probes based on di-nitroxides [135, 148], as well as trityls [149, 150] might allow using both pulse and rapid scan. Tissue pH may also be measured using Overhauser-enhanced MRI (OMRI) [151–153] or CW [154].

Thiol levels play an important role in tissue redox state, or its response to oxidative stress [155, 156]. EPR spectra of ^{1}H, ^{14}N- and ^{2}H, ^{15}N-disulfide di-nitroxides and the corresponding monoradicals resulting from cleavage by glutathione have been characterized at 250 MHz, 1.04 GHz, and 9 GHz and phantom was imaged by rapid scan EPR at 250 MHz [149, 150].

Rapid scan EPR was applied to obtain in vivo images of thiol redox status, i.e., the intracellular thiol concentration in vivo. This technology enabled remarkably fast (30 s) 3D images, thus resolving the kinetic processes occurring on the 100-second time scale. Using PxSSPx spin probe thiol content in mouse tumors was imaged on the physiologically relevant time scales [24–27].

Multifunctional spin probes include extracellular spectroscopic measurement of pH and redox state [157–159], intracellular thiol and redox state [160, 161] or extracellular pO_2, pH and phosphate ions [123, 146, 162]. Rapid development of EPR technology provides hope that spatial mapping of these parameters in vivo will be possible in the nearest future.

1.3.2.3 Tumor Metabolic State

Combining pO_2 maps with other tissue microenvironment parameters such as blood flow, blood volume, tissue diffusion/perfusion, and lactate level provides a powerful tool for studying cancer metabolism. This approach was developed by combining pulsed EPRI and co-registered MRI and NMR spectroscopy (MRS) [80, 163] and was used to show the mechanism of action of pyruvate-enhanced hypoxia-activated antitumor drugs [164, 165], or mechanism of rapamycin-induced vascular renormalization and resultant transient increase in tumor oxygenation in squamous cell carcinoma (SCC) tumors [166, 167]. Characterization of tumor metabolic state is important for predicting radio-, chemo-, and immunotherapy sensitivity and results [168]. Studies on tumor metabolic state using pulsed EPRI were summarized by Kishimoto et al. [169].

Multimodality imaging providing complementary data from various advanced imaging techniques seems to be the common trend, making EPR one of the

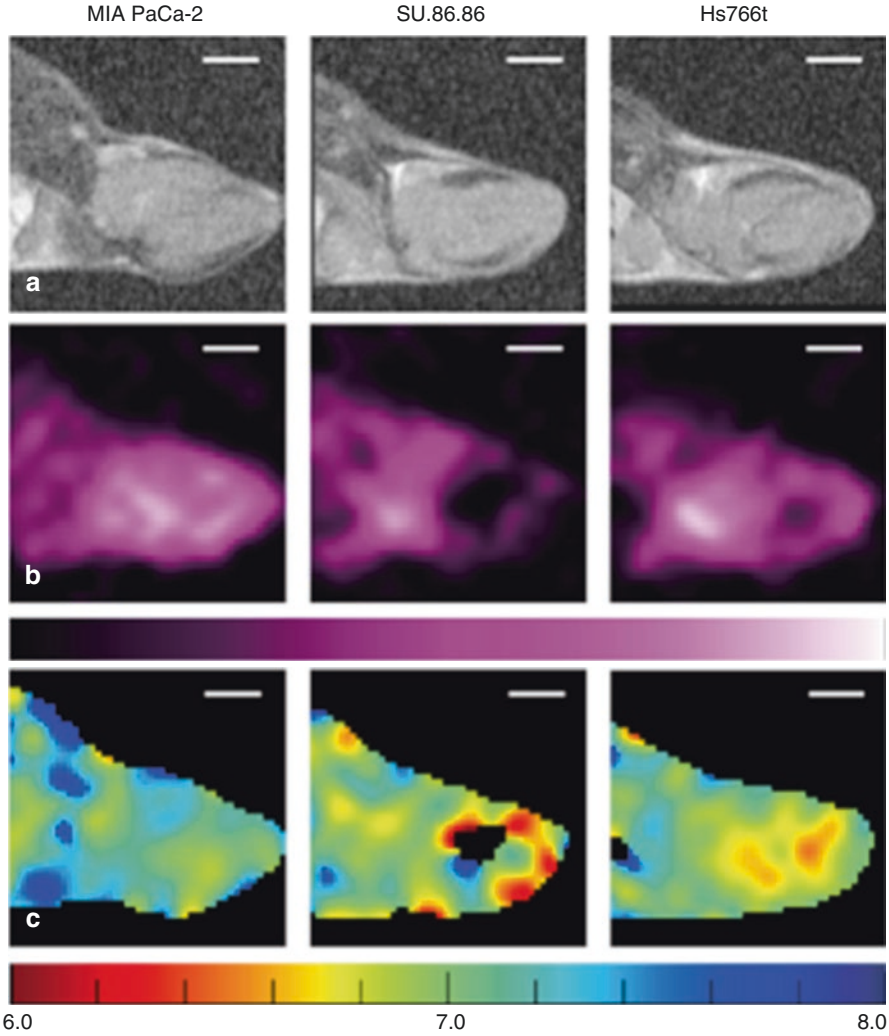

Fig. 1.6 Visualization of pHe in mouse legs bearing the human-derived pancreatic ductal adenocarcinoma xenografts MIA PaCa-2,SU.86.86, and Hs766t. (**a**) Representative T2-weighted MR anatomical images of tumor-bearing mouse legs in the sagittal plane, (**b**) corresponding slices of EPR signal intensity, and (**c**) maps of pHe. The matrix size of the EPR images was 48 × 48 × 48 with a field-of-view of 25.0 mm × 25.0 mm × 25.0 mm. MR images were scaled and cropped to match the corresponding EPR images. The white scale bar on the images corresponds to 5 mm in all cases. Reprinted with permission from [81]

orchestra players. For example, positron emission tomography (PET), EPRI, and ^{13}C-hyperpolarizated MRS were used to characterize the metabolic phenotype of tumors in vivo [170]. Combining EPRI with ^{13}C-hyperpolarized MRS might be especially useful in studying the possibilities to manipulate the tumor metabolic state [171] and may detect an early response to radiotherapy [172].

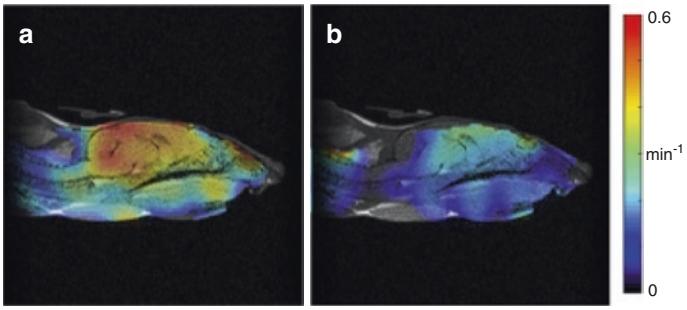

Fig. 1.7 Redox map of MCP in DEM-treated and control mouse heads. The redox maps from control (**a**) and DEM-treated (**b**) mouse heads were co-registered to the anatomical images of the same mice obtained with MRI before MCP injection. Reprinted with permission from [82]

1.3.2.4 Tissue Redox State

The redox state of tissue plays a role in both normal and pathological conditions and is an important feature of the tissue microenvironment. EPR allows measurement of several parameters connected to redox processes, such as reducing capability of the tissue or level of free radicals and thiols [100]. There are extensive reviews describing the mechanisms of reducing capability [147] as well as numerable applications of redox state spectroscopic measurements and imaging in animal models [173–175] (Fig. 1.7).

A few recent examples include intracellular and extracellular redox state detected by OMRI [176, 177], as well as estimating redox state in the whole body of the mouse [178] or in SCC tumors and comparison of EPR spectroscopy, EPRI and MRI [179]. EPRI oxygen mapping was correlated with redox mapping of tumors using nitroxides and co-registered MRI, showing that redox status and pO_2 change in parallel with tumor growth [180]. Classical tumor tissue redox state was imaged by EPRI and correlated with a single-point pO_2 measurement [181]. 3D tumor redox images were acquired using CW single-point technique [182]. Alternatively, imaging thiol status in living animals provides information on the most important component of the reducing capability and thiol level imaging has been demonstrated [27, 149].

Many redox state studies have been focused on the brain and neuropathologies. Application of blood–brain barrier permeable nitroxides is crucial for obtaining good images, both using EPRI and MRI [136, 139, 183–186].

1.3.2.5 Melanin

Melanin belongs to the most important and characteristic paramagnetic constituents of the living organism, revealing strong and unusually stable paramagnetism [187]. Free radicals are short-living and transient species, so that it is difficult to register their EPR signal, let alone to perform an EPRI experiment basing solely on their presence, which results in the necessity of spin trapping or using spin probes. The persistence of EPR melanin signal covers the time scale counted in millions of years [188]. No wonder that melanin enjoys the leading position in paramagnetomics [18]. Its EPR signal was registered as one of the first EPR signals detected in

biological materials, as early as in 1954 [189]. To make matters even more intriguing, melanin is the most characteristic feature of a notorious skin tumor—melanoma. The temptation to use melanin as a spin probe and a contrast agent in EPR imaging appeared quite early [190]. Initially, the melanoma tumors used for one of the first in vivo EPRI measurements were amelanotic, and the contrast agent was an exogenous spin label—CTPO [191].

The work on application of melanin to EPRI progressed slowly. Melanin turned out to reveal too wide EPR spectrum to obtain a satisfactory resolution, and the actual concentration of this anyway strong paramagnetic compound, as compared to the obtainable concentrations of spin labels, was often too low. Another obstacle was heterogenous pigmentation of melanoma tumors. The first successful attempt to measure the spatial melanin distribution dates back to 1990 [192], the experiment was performed under rapid scan regime using a pin-hole TE102 cavity at X-band, so the desiccated fragments of a pigmented tumor of murine B16 melanoma were imaged, however, of a poor resolution.

The most substantial series of experiments showing the applicability of EPRI to melanoma research using endogenous melanin comes from the Bernard Gallez group, who started the systematic study over 10 years ago. They showed in the proof-of-concept study that it is possible to use L-band EPRI to map pigmentation of in situ growing B16 melanoma under in vivo conditions, which was accompanied with an X-band in vitro study of human melanoma and its metastases to the lungs (in paraffin blocks) [193]. This was soon supplemented with the analysis of pigmented metastases distribution in lungs (ex vivo, X-band) where the actual presence of pigmented metastases was confirmed by bioluminescence imaging of luciferase expressed in the inoculated cells of transgenic B16 melanoma [194]. EPR turned out in this study as a valuable method complementary to other traditional methods of melanoma diagnosis. This study was soon followed by a more systematic analysis of the progression of human melanoma using EPRI-related parameters of its growth and metastasizing, again, in the ex vivo system using an X-band instrumentation [195]. In a paper from 2013, EPR imaging was used to identify the melanotic or amelanotic character of tumors of human melanoma in several paraffin blocks [196]. The usefulness of EPRI was additionally confirmed with the experiment in which the degree of pigmentation of melanoma (measured with EPR) was attempted to be correlated with NMR relaxation times T_1, T_2, and T_2*. The studies revealed that melanin itself does not affect the NMR relaxation times, so that EPRI but not MRI can be used to detect melanoma tumors and metastases based on tumor pigmentation [197]. The possibility to employ melanin as a contrast agent for MRI in melanoma is rather due to the ability of the pigment to adsorb strongly paramagnetic agents like metal ions [40].

These investigations have now been progressing in two directions—(1) towards elaborating new melanin-based contrast agents to explore the unique physicochemical properties of melanin. Melanin nanoparticles (<10 nm) can be used in multifunctional nanoplatforms exploring their multifunctional modalities in molecular imaging in such techniques, besides EPRI, as photoacoustic imaging, PET or MRI [198]; (2) towards improving selectivity and sensitivity of EPRI of natural

pigmented materials from, e.g., malignant melanoma and *nevus pigmentosus*. While some new reports in this field are based on ex vivo CW X-band EPRI performed on paraffin blocks [199], there are attempts to use more advanced techniques, e.g., DNP-MRI (dynamic nuclear polarization-MRI; [200]) being an implementation of OMRI [201]. An interesting suggestion seems to explore S-band EPR spectroscopy for in vivo melanoma EPRI, as the method sensitive enough to detect signals of melanin [202] and other paramagnetic substances in native tissues [4] or even in the in vivo growing melanoma [203].

1.3.2.6 Other Biological Applications of EPRI

An interesting approach to spin trapping is the immune-spin trapping combined with MRI detection of the antibodies against DMPO. The immune DMPO adducts were detected in vivo in several disease models, including multi-tissue assessment in diabetic mice with further assessment of cardiomyopathy, amyotrophic lateral sclerosis (ALS)-like mice, glioma-bearing mice, and mice with septic encephalopathy [204].

Various biological objects have been imaged with high resolution. Mouse knee joint was imaged in vivo using trityl probe and CW at L-band with spatial resolution under 200 μm [205]. EPR imaging at X-band was applied to image free radicals naturally occurring in pepper [206] and apple seeds [207]. Spatial resolution of less than 2 mm was achieved. EPRI at submillimeter scale is being developed [208]. For example, pO_2 maps of live cancer cell spheroids were acquired with 20 μm spatial resolution EPR microscopy of spheroids [209]. Higher level of ROS was shown in artheriosclerotic plaques ex vivo using CW X-band 2D imaging [210].

1.3.3 OMRI

Many orchestral approaches have been developed to include EPRI and some other imaging modality, e.g., MRI [211], ultrasound [212], and PET [213]. The main advantage of Overhauser methods (similarly to EPRI/MRI hybrid methods) over EPR-alone imaging is a spatially registered proton MR image providing anatomy. Moreover, the spatial resolution is independent on the linewidth of the free radical. Both trityl and nitroxide derivatives can be used to induce Overhauser effect. OMRI in living animals has been used to study redox state [201, 214, 215], pH [151–153], and/or tissue oxygen concentration [216]. Multiparametric imaging, e.g., tumor pO_2 and redox state, is also possible [217]. Tissue redox state imaging might be useful to study different pathologies, i.e., gastric ulcers [177] or neurodegenerative diseases [218]. An additional mechanism of leakage of spin polarization due to an interaction of a spin system with oxygen was shown recently. This approach may improve the accuracy of OMRI oximetry. The authors demonstrated 2D and 3D concentration and oxygen maps of phantoms and tumors [219]. An interesting application of DNP-MRI was imaging of melanin in a B16 melanoma tumor growing in a mouse leg [200]. First attempts towards imaging of enzymatic activity in living animals were undertaken [220].

1.3.4 Spin Probe Development

Rapid progress in development of spin probes enables broadening the range of applications of EPR studies in the biomedical field. All three major classes of spin probes: nitroxides, trityl family derivatives, and solid state spin probes were being developed and some of the new functionalities are discussed below.

Recently, several groups intensified the efforts towards synthesis of new trityl derivatives, soluble and sensitive oximetric probes. For imaging, trityl derivatives family is particularly attractive due to very short relaxation times, resulting in increased spatial resolution. Beside the most commonly used OX063 [63], the deuterated form, OX071 provides better resolution for oximetric imaging [14, 116]. There were several attempts to improve synthesis and develop non-toxic derivatives [221–226].

To improve in vivo retention in the circulation, adding dendrimers was proposed [227], or dendrimers and PEG dendritic PEGylated trityl radicals [228]. To make trityls enter the cells different approaches were used, e.g., adding acetoxymethyl esters [229] or polyarginine [230]. Beside oximetry, adding other functionalities, for example for concurrent pO_2 and pH measurement phosphonated trityl probe was proposed [123]. Trityl probe with higher sensitivity towards superoxide [231] and nitro-conjugated trityl radical for superoxide detection was developed [232]. Trityl bisulfide conjugates are used for thiol measurement [233]. Improved administration was suggested by applying trityl probes in perfluorocarbon emulsions [234, 235], lipophilic gel implants [236], or in lipid nanocapsules [144].

EPR spectroscopic oximetry using solid state spin probes, like LiPc, LiBu, and charcoals is characterized by high sensitivity and long-term stability of the implanted probes, allowing longitudinal measurements of pO_2 from the same spot over time. Recent developments in this field are remarkable, introducing implantable Oxychip [125, 237] and percutaneous Oxyspot [145], with applications in the clinic. Also charcoals are being developed into films and capsules for clinical use [238].

Nitroxide family of spin probes and spin traps provides a very wide range of functionalities. Their application to imaging was limited, due to short stability in vivo and long relaxation times. Introducing rapid scan, however, opens up the possibility of fast imaging of many physiologically relevant parameters, as nitroxides are easily modified and have been used since 1960s in EPR spectroscopic studies [239]. In the near future, it may be perhaps feasible to image free radical spin trapping [51]. Nitroxides may be developed to be sensitive to different parameters of their milieu and also to localize in different cellular compartments. Beside classic redox capabilities measurements, pH, and thiol, there are inorganic phosphate sensitive probes [158] or multiple functionalities probes, such as nitroxide-trityl dual probes for simultaneous redox and pO_2 measurements [240, 241].

Nitroxide probes may be used in the "orchestral" applications, where EPRI is used together with other imaging modalities, for example in MRI as contrast agents [173, 178, 242], or in OMRI [151].

1.4 Final Conclusions

EPR spectroscopy enjoys stable and dynamic development since the beginning of its history. The same may be said about its favorite child—EPR imaging. Being originally an exotic implementation invented as a method created for the inventor's sake, it has gained on an experimental and clinical applicability, mainly because of the importance of paramagnetic species in living systems [18]. The recent progress in EPRI is mainly supported by the powerful development of information technologies, which enable deconvolution of more projections in shorter time, reaching not only a better resolution of the image, but also possibility to perform dynamic real time registration of qualitative and quantitative changes in the distribution of paramagnetic centers in the sample. It more and more boldly penetrates to the territory of clinical application, being not only an important basic tool of research, but a mode of diagnosis. The clinical applications, initially limited to the distribution of a paramagnetic contrast agent in a solid tumor growing on the mouse tail, have "metastasized" to other organs present in various places of the body, on its surface or inside, down to such deeply hidden organs, as the brain or the heart, and providing such crucial information as tissue oxygenation and its dynamics, vascularization, predominance of donors or acceptors of electrons and other physiological parameters.

EPRI acting solo becomes consequently a sensitive tool for diagnosis and prognosis as such physiologic parameters may determine vulnerability of a tissue to therapeutic agents. But its value as a member of orchestra is comparable—it not only supports the sensitivity and applicability of other methods (e.g., NMR in DNP-MRI or OMRI), but delivers complementary information on its own specific character, e.g., on heterogenous melanization of a solid tumor, which is a factor influencing radiosensitivity of melanoma, but not measureable with standard NMR relaxometry techniques, while MRI, on the other hand, delivering structural information is important for tumor radiosensitivity. Nevertheless, invention of new, in particular multimodal spin probes and spin labels of better EPRI-related parameters will probably dominate the future of this technology. The applicability of the standard CW techniques is still high, while the RS and pulse technologies themselves become standard. Moreover, there are numerous paramagnetic (e.g., nitric oxide and its metabolites [203]) and even diamagnetic (e.g., phosphate anion [158]) species in the organism awaiting their spin traps and modes of measurement with the help of EPRI solo, and orchestra, the clinical importance of whose is underestimated or even not known yet.

Acknowledgements We acknowledge the support of grants from the National Science Centre OPUS No. 2015/17/B/NZ7/03005 to ME and 2018/29/B/NZ5/02954 to MKS. ME is partially supported by Horizon2020 grant no 668776. Faculty of Biochemistry, Biophysics, and Biotechnology of Jagiellonian University was a partner of the Leading National Research Center (KNOW) supported by the Ministry of Science and Higher Education., grant KNOW 35p/10/2015 to PMP.

References

1. Gerlach W, Stern O. Das Magnetische Moment Des Silberatoms. Z Phys. 1922;9(1):353–5.
2. Pauli W. Über Den Zusammenhang Des Abschlusses Der Elektronengruppen Im Atom Mit Der Komplexstruktur Der Spektren. Z Phys. 1925;31(1):765–83.
3. Uhlenbeck GE, Goudsmit S. Spinning electrons and the structure of spectra. Nature. 1926;117(2938):264–5.
4. Plonka PM. Electron paramagnetic resonance as a unique tool for skin and hair research. Exp Dermatol. 2009;18(5):472–84.
5. Eaton GR. Quantitative EPR. Berlin: Springer; 2014.
6. Geschwind S. Electron paramagnetic resonance. Berlin: Springer; 1972.
7. Gilbert BC, Davies MJ, Murphy DM, Becker D. Electron paramagnetic resonance volume 19: a review of the recent literature: Royal Soc Chem; 2004.
8. Goldfarb D, Stoll S. EPR spectroscopy: fundamentals and methods. New York: Wiley; 2018.
9. Schweiger A, Jeschke G. Principles of pulse electron paramagnetic resonance. New York: Oxford University Press; 2001.
10. Weil JA, Bolton JR. Electron paramagnetic resonance: elementary theory and practical applications. New York: Wiley-Interscience; 2007.
11. Wertz JE, Bolton JR. Electron spin resonance: elementary theory and practical applications. London: Chapman and Hall; 1986.
12. Sahu ID, McCarrick RM, Lorigan GA. Use of electron paramagnetic resonance to solve biochemical problems. Biochemistry. 2013;52(35):5967–84.
13. Ahmad R, Kuppusamy P. Theory, instrumentation, and applications of electron paramagnetic resonance Oximetry. Chem Rev. 2010;110(5):3212–36.
14. Epel B, Halpern HJ. In vivo pO_2 imaging of tumors: Oxymetry with very low-frequency electron paramagnetic resonance. Methods Enzymol. 2015b;564:501–27.
15. Sarna T, Plonka PM. Biophysical studies of melanin. In: Eaton SS, Eaton GR, Berliner LJ, editors. Biomedical EPR, part a: free radicals, metals, medicine, and physiology. New York: Springer; 2005. p. 125–46.
16. Gustafsson H, Hallbeck M, Lindgren M, Kolbun N, Jonson M, Engström M, de Muinck E, Zachrisson H. Visualization of oxidative stress in ex vivo biopsies using electron paramagnetic resonance imaging. Magn Reson Med. 2015;73(4):1682–91.
17. Pavelescu LA. On reactive oxygen species measurement in living systems. J Med Life. 2015;8:38–42.
18. Płonka PM. Paramagnetomics. In: Shukla AK, editor. Electron spin resonance spectroscopy in medicine. Singapore: Springer Singapore; 2019. p. 189–221.
19. Zweier JL, Kuppusamy P. Electron paramagnetic resonance measurements of free radicals in the intact beating heart: a technique for detection and characterization of free radicals in whole biological tissues. Proc Natl Acad Sci U S A. 1988;85(15):5703–7.
20. Khramtsov VV, Grigor'ev IA, Foster MA, Lurie DJ. In vitro and in vivo measurement of pH and Thiols by EPR-based techniques. Antioxid Redox Signal. 2004;6(3):667–76.
21. Rosen GM. Free radicals: biology and detection by spin trapping. Oxford: Oxford University Press; 1999.
22. Blank A, Halevy R, Shklyar M, Shtirberg L, Kuppusamy P. ESR micro-imaging of LiNc-BuO crystals in PDMS: spatial and spectral grain distribution. J Magn Reson. 2010;203(1):150–5.
23. Bobko AA, Dhimitruka I, Eubank TD, Marsh CB, Zweier JL, Khramtsov VV. Trityl-based EPR probe with enhanced sensitivity to oxygen. Free Radic Biol Med. 2009;47(5):654–8.
24. Epel B, Sundramoorthy SV, Halpern HJ. 250 MHz passive Q-modulator for reflection resonators. Concepts Magn Reson Part B: Magn Reson Eng. 2017a;47B(2):e21356.
25. Epel B, Sundramoorthy SV, Krzykawska-Serda M, Magio MC, Tseytlin M, Eaton GR, Eaton SS, Rosen GM, Kao JY, Halpern HJ. Imaging Thiol redox status in murine tumors in vivo with rapid-scan electron paramagnetic resonance. J Magn Reson. 2017b;276:31–6.
26. Epel B, Kotecha M, Halpern HJ. In vivo preclinical cancer and tissue engineering applications of absolute oxygen imaging using pulse EPR. J Magn Reson. 2017c;280:149–57.

27. Epel B, Krzykawska-Serda M, Tormyshev V, Maggio MC, Barth ED, Pelizzari CA, Halpern HJ. Spin lattice relaxation EPR pO_2 images may direct the location of radiation tumor boosts to enhance tumor cure. Cell Biochem Biophys. 2017d;75(3–4):295–8.
28. Krzykawska-Serda M, Dąbrowski JM, Arnaut LG, Szczygieł M, Urbańska K, Stochel G, Elas M. The role of strong hypoxia in tumors after treatment in the outcome of Bacteriochlorin-based photodynamic therapy (PDT). Free Radic Biol Med. 2014;73:239–51.
29. Serda M, Wu Y-K, Barth ED, Halpern HJ, Rawal VH. EPR imaging spin probe Trityl radical OX063: a method for its isolation from animal effluent, redox chemistry of its Quinone Methide oxidation product, and in vivo application in a mouse. Chem Res Toxicol. 2016;29(12):2153–6.
30. Sotgiu A, Mäder K, Placidi G, Colacicchi S, Ursini CL, Alecci M. pH-sensitive imaging by low-frequency EPR: a model study for biological applications. Phys Med Biol. 1998;43(7):1921–30.
31. Lopiano L, Chiesa M, Digilio G, Giraudo S, Bergamasco B, Torre E, Fasano M. Q-band EPR investigations of Neuromelanin in control and Parkinson's disease patients. Biochim Biophys Acta. 2000;1500(3):306–12.
32. Colacicchi S, Alecci M, Gualtieri G, Quaresima V, Ursini CL, Ferrari M, Sotgiu A. New experimental procedures for in vivo L-band and radio frequency EPR spectroscopy/imaging. J Chem Soc Perkin Trans. 1993;20(11):2077.
33. Epel B, Sundramoorthy SV, Mailer C, Halpern H. A versatile high speed 250-MHz pulse imager for biomedical applications. Con Magn Reson Part B Magn Reson Eng. 2008;33B(3):163–76.
34. Epel B, Redler G, Halpern HJ. How in vivo EPR measures and images oxygen. Adv Exp Med Biol. 2014;812
35. Krishna MC, Devasahayam N, Cook JA, Subramanian S, Kuppusamy P, Mitchell JB. Electron paramagnetic resonance for small animal imaging applications. ILAR J Nat Res Council Inst Lab Anim Resour. 2001;42(3):209–18.
36. Eaton GR, Eaton SS, Ohno K. EPR Imaging and in Vivo EPR. 1st ed. Hoboken: CRC; 1991.
37. Williams BB, Halpern HJ. In vivo EPR imaging. Biomedical EPR, part A: free radicals, metals, medicine, and physiology. New York: Springer; 2005. p. 283–319.
38. Qiao Z, Zheng Z, Pan X, Epel B, Redler G, Xia D, Halpern H. Optimization-based image reconstruction from sparsely sampled data in electron paramagnetic resonance imaging. J Magn Reson. 2018;294:24–34.
39. Redler G, Epel B, Halpern HJ. Maximally spaced projection sequencing in electron paramagnetic resonance imaging. Concepts Magn Reson Part B: Magn Reson Eng. 2015;45(1):33–45.
40. Danhier P, Gallez B. Electron paramagnetic resonance: a powerful tool to support magnetic resonance imaging research. Contr Media Mol Imag. 2015;10(4):266–81.
41. Subramanian S, Devasahayam N, McMillan A, Matsumoto S, Munasinghe JP, Saito K, Mitchell JB, Chandramouli GVR, Krishna MC. Reporting of quantitative oxygen mapping in EPR imaging. J Magn Reson. 2012a;214(1):244–51.
42. Subramanian S, Mitchell JB, Krishna MC. Time-domain radio frequency EPR imaging. In: Berliner LJ, editor. In vivo EPR (ESR): theory and application. Berlin: Springer Science & Business Media; 2012b. p. 153–97.
43. Berliner LJ, editor. In Vivo EPR (ESR), vol. 18. Springer: Boston, MA; 2003.
44. Dawkins AW, Nightingale NR, South GP, Sheppard RJ, Grant EH. The role of water in microwave absorption by biological material with particular reference to microwave hazards. Phys Med Biol. 1979;24(6):1168–76.
45. Dayan N, Ishay Y, Artzi Y, Cristea D, Reijerse E, Kuppusamy P, Blank A. Advanced surface resonators for electron spin resonance of single microcrystals. Rev Sci Instrum. 2018;89(12):124707.
46. Hou H, Krishnamurthy Nemani V. Monitoring oxygen levels in Orthotopic human Glioma Xenograft following Carbogen inhalation and chemotherapy by implantable resonator based Oximetry. Int J Cancer. 2014;136(7):1–27.
47. Pursley R, Enomoto A, Wu H, Brender JR, Pohida T, Subramanian S, Krishna MC, Devasahayam N. Towards reduction of SAR in scaling up in vivo pulsed EPR imaging to larger objects. J Magn Reson. 2019;299:42–8.

48. Biller JR, Tseitlin M, Quine RW, Rinard GA, Weismiller HA, Elajaili H, Rosen GM, Kao JPY, Eaton SS, Eaton GR. Imaging of Nitroxides at 250 MHz using rapid-scan electron paramagnetic resonance. J Magn Reson. 2014;242:162–8.
49. Subramanian S, Krishna MC. Dancing with the electrons: time-domain and CW in vivo EPR imaging. Magn Reson Insights. 2008;2:43–74.
50. Eaton SS, Shi Y, Woodcock L, Buchanan LA, McPeak J, Quine R, Rinard GA, Epel B, Haleprn HJ, Eaton GR. Rapid-Scan EPR imaging. J Magn Reson. 2017;280:140–8.
51. Biller JR, Mitchell DG, Tseytlin M, Elajaili H, Rinard GA, Quine RW, Eaton SS, Eaton GR. Rapid scan electron paramagnetic resonance opens new avenues for imaging physiologically important parameters in vivo. J Vis Exp. 2016;115:e54068.
52. Möser J, Lips K, Tseytlin M, Eaton GR, Eaton SS, Schnegg A. Using rapid-scan EPR to improve the detection limit of quantitative EPR by more than one order of magnitude. J Magn Reson. 2017;281:17–25.
53. Czoch R, Francik A. Instrumental effects in homodyne electron paramagnetic resonance spectrometers. Warszawa, Chichester: PWN Polish Scientific Publishers and Ellis Horwood Ltd Publishers; 1989.
54. Subramanian S, Krishna MC. Electron paramagnetic resonance imaging. Resonance. 2016;21(8):717–40.
55. Froncisz W, Hyde S, Hyde JS. The loop-gap resonator: a new microwave lumped circuit ESR sample structure. J Magn Reson. 1982;521:515–21.
56. Chzhan M, Kuppusamy P, Samouilov A, He G, Zweier JL. A tunable reentrant resonator with transverse orientation of electric field Forin Vivo EPR spectroscopy. J Magn Reson. 1999;137(2):373–8.
57. Devasahayam N, Subramanian S, Murugesan R, Cook JA, Afeworki M, Tschudin RG, Mitchell JB, Krishna MC. Parallel coil resonators for time-domain radiofrequency electron paramagnetic resonance imaging of biological objects. J Magn Reson. 2000;142(1):168–76.
58. Rinard GA, Quine RW, Buchanan LA, Eaton SS, Eaton GR, Epel B, Sundramoorthy SV, Halpern HJ. Resonators for in vivo imaging: practical experience. Appl Magn Reson. 2017;48:11–2; 1227–1247
59. Matsumoto K-i I, Chandrika B, Lohman JABB, Mitchell JB, Krishna MC, Subramanian S. Application of continuous-wave EPR spectral-spatial image reconstruction techniques for in vivo Oxymetry: comparison of projection reconstruction and constant-time modalities. Magn Reson Med. 2003;50(4):865–74.
60. Ahmad R, Clymer B, Deng Y, He G, Vikram D, Kuppusamy P, Zweier JL. Optimization of data acquisition for EPR imaging. J Magn Reson. 2006;179(2):263–72.
61. Tseytlin M. Full cycle rapid scan EPR Deconvolution algorithm. J Magn Reson. 2017;281:272–8.
62. Subramanian S, Krishna MC. Time-domain radio frequency EPR imaging. Biomedical EPR, part a: free radicals, metals, medicine, and physiology. New York: Springer; 2005. p. 321–82.
63. Krishna MC, Matsumoto S, Yasui H, Saito K, Devasahayam N, Subramanian S, Mitchell JB. Electron paramagnetic resonance imaging of tumor pO_2. Radiat Res. 2012;177(4):376–86.
64. Subramanian S, Matsumoto K-I, Mitchell JB, Krishna MC. Radio frequency continuous-wave and time-domain EPR imaging and Overhauser-enhanced magnetic resonance imaging of small animals: instrumental developments and comparison of relative merits for functional imaging. NMR Biomed. 2004;17(5):263–94.
65. Sun L, Savory JJ, Warncke K. Design and implementation of an FPGA-based timing pulse programmer for pulsed-electron paramagnetic resonance applications. Concepts Magn Reson Part B: Magn Reson Eng. 2013;43(3):100–9.
66. Eaton GR, Eaton SS, Barr DP, Weber RT. Quantitative EPR: a practitioners guide. Wien: Springer; 2010.
67. Tseitlin MP, Iyudin VS, Tseitlin OA. Advantages of digital phase-sensitive detection for upgrading an obsolete CW EPR spectrometer. Appl Magn Reson. 2009;35(4):569–80.
68. Tadyszak K, Boś-Liedke A, Jurga J, Baranowski M, Mrówczyński R, Chlewicki W, Jurga S, Czechowski T. Overmodulation of projections as signal-to-noise enhancement method in EPR imaging. Magn Reson Chem. 2016;54(2):136–42.

69. Koscielniak J, Devasahayam N, Moni MS, Kuppusamy P, Yamada K, Mitchell JB, Krishna MC, Subramanian S. 300 MHz continuous wave electron paramagnetic resonance spectrometer for small animal in vivo imaging. Rev Sci Instrum. 2000;71(11):4273–81.
70. Sato-Akaba H, Abe H, Fujii H, Hirata H. Slice-selective images of free radicals in mice with modulated field gradient electron paramagnetic resonance (EPR) imaging. Magn Reson Med. 2008a;59(4):885–90.
71. Sato-Akaba H, Fujii H, Hirata H. Development and testing of a CW-EPR apparatus for imaging of short-lifetime Nitroxyl radicals in mouse head. J Magn Reson. 2008b;193:191–8.
72. Sato-Akaba H, Kuwahara Y, Fujii H, Hirata H. Half-life mapping of Nitroxyl radicals with three-dimensional electron paramagnetic resonance imaging at an interval of 3.6 seconds. Anal Chem. 2009;81(17):7501–6.
73. Tseitlin M, Rinard GA, Quine RW, Eaton SS, Eaton GR. Rapid frequency scan EPR. J Magn Reson. 2011;211(2):156–61.
74. Czechowski T, Chlewicki W, Baranowski M, Jurga K, Szczepanik P, Szulc P, Kedzia P, Szostak M, Malinowski P, Wosinski S, Prukala W, Jurga J. Two-dimensional spectral–spatial EPR imaging with the rapid scan and modulated magnetic field gradient. J Magn Reson. 2014;243:1–7.
75. Durand S, Frapart Y-M, Kerebel M. Electron paramagnetic resonance image reconstruction with Total variation and Curvelets regularization. Inv Probl. 2017;33:114002.
76. Giuseppe S, Di G, Placidi J, Brivati A, Alecci M, Sotgiu A. Pulsed EPR imaging: image reconstruction using selective acquisition sequences. Phys Med Biol. 1999;44(6):N137–44.
77. Williams BB, Pan X, Halpern HJ. EPR imaging: the relationship between CW spectra acquired from an extended sample subjected to fixed stepped gradients and the radon transform of the resonance density. J Magn Reson. 2005;174(1):88–96.
78. Marr RB, Chen C-N, Lauterbur PC. On two approaches to 3D reconstruction in NMR zeugmatography. In: Herman GT, Natterer F, editors. Mathematical aspects of computerized tomography, Lecture notes in medical informatics, vol. 8. Berlin: Springer; 1981. p. 225–40.
79. Sivakumar S, Aart A, Krishna MC. Evaluation of algebraic iterative algorithms for reconstruction of electron magnetic resonance images. Iccvgip. 2004;2014:353–8.
80. Qiao Z, Redler G, Epel B, Qian Y, Halpern H. 3D pulse EPR imaging from sparse-view projections via constrained, Total variation minimization. J Magn Reson. 2015;258:49–57.
81. Ohno K. Application of ESR imaging to a continuous flow method for study on kinetics of short-lived radicals. J Magn Reson. 1982;49(1):56–63.
82. Sotgiu A, Gazzillo D, Momo F. ESR imaging: spatial Deconvolution in the presence of an asymmetric hyperfine structure. J Phys C Solid State Phys. 1987;20(36):6297–304.
83. Momo F, Colacicchi S, Sotgiu A. Limits of Deconvolution in enhancing the resolution in EPR imaging experiments. Meas Sci Technol. 1993;4(1):60–4.
84. He G, Deng Y, Li H, Kuppusamy P, Zweier JL. EPR/NMR co-imaging for anatomic registration of free-radical images. Magn Reson Med. 2002;47(3):571–8.
85. MJR H, Day AR. Imaging of paramagnetic Centres in Diamond. Solid State Commun. 1979;30(4):211–3.
86. Berliner LJ, Fujii H. Magnetic resonance imaging of biological specimens by electron paramagnetic resonance of Nitroxide spin labels. Science. 1985;227(4686):517–9.
87. Fujii H, Berliner LJ. One- and two-dimensional EPR imaging studies on phantoms and plant specimens. Magn Reson Med. 1985;2(3):275–82.
88. Bacic G, Nilges MJ, Magin RL, Walczak T, Swartz HM. In vivo localized ESR spectroscopy reflecting metabolism. Magn Reson Med. 1989;10(2):266–72.
89. Chen K, Glockner JF, Morse PD, Swartz HM. Effects of oxygen on the metabolism of Nitroxide spin labels in cells. Biochemistry. 1989;28(6):2496–501.
90. Chen K, Morse PD, Swartz HM. Kinetics of enzyme-mediated reduction of lipid soluble nitroxide spin labels by living cells. BBA-Biomembranes. 1988;943(3):477–84.
91. Dobrucki JW, Sutherland RM, Swartz HM. Nonperturbing test for cytotoxicity in isolated cells and spheroids, using electron paramagnetic resonance. Magn Reson Med. 1991;19(1):42–55.

92. Halpern HJ, Jaffe DR, Nguyen TD, Haraf DJ, Spencer DP, Bowman MK, Weichselbaum RR, Diamond AM. Measurement of bioreduction rates of cells with distinct responses to ionizing radiation and Cisplatin. BBA Mol Cell Res. 1991;1093(2-3):121–4.
93. Mitchell JB, Samuni A, Krishna MC, DeGraff WG, Ahn MS, Samuni U, Russo A. Biologically active metal-independent superoxide dismutase mimics. Biochemistry. 1990;29(11):2802–7.
94. Suzuki-Nishimura T, Swartz HM. Characterization of redox activity in resting and activated mast cells by reduction and Reoxidation of lipophilic Nitroxides. Gen Pharmacol. 1998;31(4):617–23.
95. Swartz HM, Khan N, Khramtsov VV. Use of electron paramagnetic resonance spectroscopy to evaluate the redox state in vivo. Antioxid Redox Signal. 2009;9(10):1757–71.
96. Kuppusamy P, Li H, Ilangovan G, Cardounel AJ, Zweier JL, Yamada K, Krishna MC, Mitchell JB. Noninvasive imaging of tumor redox status and its modification by tissue glutathione levels. Cancer Res. 2002;62(1):307–12.
97. Kuppusamy P, Wang P, Jay L, Zweier JL, Krishna MC, Mitchell JB, Ma L, Trimble CE, Hsia CJC. Electron paramagnetic resonance imaging of rat heart with Nitroxide and Polynitroxylalbumin. Biochemistry. 1996;2960(22):7051–7.
98. Plonka PM, Wisniewska M, Stefan C, Elas M, Rosen GM. X-band and S-band EPR detection of nitric oxide in murine Endotoxaemia using spin trapping by Ferro-Di(N-(Dithiocarboxy) Sarcosine). Acta Biochim Pol. 2003;50(3):799–806.
99. Subczynski WK, Lukiewicz S, Hyde JS. Murine in vivo L-band ESR spin-label Oximetry with a loop-gap resonator. Magn Reson Med. 1986;3(5):747–54.
100. Halpern HJ, Spencer DP, Van Polen J, Bowman MK, Nelson AC, Dowey EM, Teicher BA. Imaging radio frequency electron-spin-resonance spectrometer with high resolution and sensitivity for in vivo measurements. Rev Sci Instrum. 1989;60(6):1040–50.
101. Fuchs J, Freisleben HJ, Groth N, Herrling T, Zimmer G, Milbradt R, Packer L. One- and two-dimensional electron paramagnetic resonance imaging in skin. Free Radic Res Comms. 1991;15(5):245–53.
102. Takeshita K, Utsumi H, Hamada A. ESR measurement of radical clearance in lung of whole mouse. Biochem Biophys Res Commun. 1991;177(2):874–80.
103. Alecci M, Ferrai M, Quaresima V, Sotgiu A, Ursini CL, Quaresimna V. Simultaneous 280 MHz EPR imaging of rat organs during Nitroxide free radical clearance. Biophys J. 1994;67(1):1274–9.
104. Quaresima V, Alecci M, Ferrari M, Sotgiu A. Whole rat paramagnetic resonance imaging of a Nitroxide free radical by a radio frequency (280 MHz) spectrometer. Biochem Biophys Res Commun. 1992;183(2):829–35.
105. Oikawa K, Ogata T, Togashi H, Yokoyama H, Ohya-Nishiguchi H, Kamada H. A 3D- and 4D-ESR imaging system for small animals. Appl Radiat Isot. 1996;47(11–12):1605–9.
106. Yokoyama H, Itoh O, Ogata T, Obara H, Ohya-Nishiguchi H, Kamada H. Temporal brain imaging by a rapid scan ESR-CT system in rats receiving intraperitoneal injection of a methyl ester nitroxide radical. Magn Reson Imaging. 1997;15(9):1079–84.
107. Halpern HJ, Peric M, Yu C, Barth ED, Chandramouli GVR, Makinen MW, Rosen GM. In vivo spin-label murine pharmacodynamics using low-frequency. Biophys J. 1996;71(July):403–9.
108. Kuppusamy P, Chzhan M, Vij K, Shteynbuk M, Lefer DJ, Giannella E, Zweier JL. Three-dimensional spectral-spatial EPR imaging of free radicals in the heart: a technique for imaging tissue metabolism and oxygenation. Proc Natl Acad Sci U S A. 1994;91(8):3388–92.
109. Kuppusamy P, Chzhan M, Samouilov A, Wang PH, Zweier JL. Mapping the spin-density and Lineshape distribution of free radicals using 4D spectral-spatial EPR imaging. J Magn Reson B. 1995;107(2):116–25.
110. Kuppusamy P, Afeworki M, Shankar RA, Coffin D, Krishna MC, Hahn SM, Mitchell JB, Zweier JL. In vivo electron paramagnetic resonance imaging of tumor heterogeneity and oxygenation in a murine model. Cancer Res. 1998;58(7):1562–8.
111. Ardenkjaer-Larsen JH, Laursen I, Leunbach I. EPR and DNP properties of certain novel single electron contrast agents intended for Oximetric imaging. J Magn Reson. 1998;12: 1–12.

112. Kuppusamy P, Wang P, Chzhan M, Zweier JL. High resolution electron paramagnetic resonance imaging of biological samples with a single line paramagnetic label. Magn Reson Med. 1997;37(4):479–83.
113. Petersson JS, Järvi A, Vahasalo S, Golman K, Ardenkjær-Larsen JH, Ehnholm G, Wistrand LG, Petersson JS, Järvi A, Vahasalo S. Overhauser-enhanced MR imaging (OMRI). Acta Radiol. 1998;39(1):10–7.
114. Hyodo F, Chuang K-H, Goloshevsky AG, Sulima A, Griffiths GL, Mitchell JB, Koretsky AP, Krishna MC. Brain redox imaging using blood-brain barrier-permeable Nitroxide MRI contrast agent. J Cereb Blood Flow Metab. 2008a;28(6):1165–74.
115. Sano H, Naruse M, Matsumoto KI, Oi T, Hideo U, Tetsuo OI, Utsumi H. A new Nitroxyl-probe with high retention in the brain and its application for brain imaging. Free Radic Biol Med. 2000;28(6):959–69.
116. Utsumi H, Sano H, Naruse M, Matsumoto KI, Ichikawa K, Oi T. Nitroxyl probes for brain research and their application to brain imaging. Methods Enzymol. 2002;352:494–506.
117. Hu H, Sosnovsky G, Li SW, Rao NUM, Morse PD, Swartz HM. Development of Nitroxides for selective localization inside cells. BBA Mol Cell Res. 1989;1014(3):211–8.
118. Dhimitruka I, Bobko AA, Eubank TD, Komarov DA, Khramtsov VV. Phosphonated Trityl probes for concurrent in vivo tissue oxygen and PH monitoring using electron paramagnetic resonance-based techniques. J Am Chem Soc. 2013;135(15):5904–10.
119. Khramtsov VV, Bobko AA, Tseytlin M, Driesschaert B. Exchange phenomena in the electron paramagnetic resonance spectra of the Nitroxyl and Trityl radicals: multifunctional spectroscopy and imaging of local chemical microenvironment. Anal Chem. 2017;89(9):4758–71.
120. Khan N, Hou H, Swartz HM, Kuppusamy P. Direct and repeated measurement of heart and brain oxygenation using in vivo EPR Oximetry. 1st ed. New York: Elsevier Inc.; 2015.
121. Swartz HM. The clinical aspects of oxygen and methods related to its measurement. Adv Exp Med Biol. 2014;812:vii–viii.
122. Williams BB, Khan N, Zaki B, Hartford A, Ernstoff MS, Swartz HM. Clinical electron paramagnetic resonance (EPR) Oximetry using India ink. Adv Exp Med Biol. 2010;662:149–56.
123. Krzykawska-Serda M, Miller RC, Elas M, Epel B, Barth ED, Maggio M, Halpern HJ. Correlation between hypoxia proteins and EPR-detected hypoxia in tumors. Adv Exp Med Biol. 2017;977:319–25.
124. Epel B, Maggio MC, Barth ED, Miller RC, Pelizzari CA, Krzykawska-Serda M, Sundramoorthy SV, Aydogan B, Weichselbaum RR, Tormyshev VM, Halpern HJ. Oxygen-guided radiation therapy. Int J Radiat Oncol Biol Phys. 2018;14:1–8.
125. Epel B, Halpern HJ. Comparison of pulse sequences for R1–based electron paramagnetic resonance oxygen imaging. J Magn Reson. 2015;254:56–61.
126. Epel B, Haney CR, Hleihel D, Wardrip C, Barth ED, Halpern HJ. Electron paramagnetic resonance oxygen imaging of a rabbit tumor using localized spin probe delivery. Med Phys. 2010;37(6):2553.
127. Redler G, Barth ED, Bauer KS, Kao JPY, Rosen GM, Halpern HJ. In of differential tumor targeting using Cis-3,4-Di(Acetoxymethoxycarbonyl)-2,2,5,5-Tetramethyl-1-Pyrrolidinyloxyl. Magn Reson Med. 2014a;71(4):1650–6.
128. Redler G, Epel B, Halpern HJ. Principal component analysis enhances SNR for dynamic electron paramagnetic resonance oxygen imaging of cycling hypoxia in vivo. Magn Reson Med. 2014b;71(1):440–50.
129. Yasui H, Matsumoto S, Devasahayam N, Munasinghe JP, Choudhuri R, Saito K, Subramanian S, Mitchell JB, Krishna MC. Low-field magnetic resonance imaging to visualize chronic and cycling hypoxia in tumor-bearing mice. Cancer Res. 2010;70(16):6427–36.
130. Christodoulou AG, Redler G, Clifford B, Liang ZP, Halpern HJ, Epel B. Fast dynamic electron paramagnetic resonance (EPR) oxygen imaging using low-rank tensors. J Magn Reson. 2016;270:176–82.
131. Matsumoto S, Hyodo F, Subramanian S, Devasahayam N, Munasinghe J, Hyodo E, Gadisetti C, Cook JA, Mitchell JB, Krishna MC. Low-field paramagnetic resonance imaging of tumor oxygenation and glycolytic activity in mice. J Clin Investig. 2008;118(5):1965–73.

132. Kotecha M, Epel B, Ravindran S, Dorcemus D, Nukavarapu S, Halpern H. Noninvasive absolute EPR oxygen imaging for the assessment of tissue graft oxygenation. Tissue Eng Part C Methods. 2018;24(1):14–9.
133. Gorodetsky AA, Kirilyuk IA, Khramtsov VV, Komarov DA. Functional electron paramagnetic resonance imaging of ischemic rat heart: monitoring of tissue oxygenation and pH. Magn Reson Med. 2015;76(1):350–8.
134. Matsumoto A, Matsumoto K-i, Matsumoto S, Hyodo F, Sowers AL, Koscielniak JW, Devasahayam N, Subramanian S, Mitchell JB, Krishna MC. Intracellular hypoxia of tumor tissue estimated by noninvasive electron paramagnetic resonance Oximetry technique using paramagnetic probes. Biol Pharm Bull. 2011a;34(1):142–5.
135. Matsumoto S, Yasui H, Mitchell JB, Krishna MC. Imaging Cycling Tumor Hypoxia. Cancer Res. 2010;70(24):10019–23.
136. Matsumoto K-i, Hyodo F, Anzai K, Mitchell JB, Krishna MC. Brain Redox Imaging. In: Modo M, Bulte JWM, editors. Magnetic Resonance Neuroimaging, vol. 711. Totowa, NJ, USA: Humana Press; 2011. p. 397–411.
137. Matsumoto S, Batra S, Saito K, Yasui H, Choudhuri R, Gadisetti C, Subramanian S, Devasahayam N, Munasinghe JP, Mitchell JB, Krishna MC. Antiangiogenic agent sunitinib transiently increases tumor oxygenation and suppresses cycling hypoxia. Cancer Res. 2011;71(20):6350–9.
138. Flood AB, Wood VA, Schreiber W, Williams BB, Swartz HM. Guidance for academics to transfer 'bench-ready' medical technology into usual clinical practice: case study: sensors and spectrometer used in EPR Oximetry. Adv Exp Med Biol. 2018;1072:233–9.
139. Swartz HM, Khan N, Buckey J, Comi R, Gould L, Grinberg O, Hartford A, Hopf H, Hou H, Hug E, Iwasaki A, Lesniewski P, Salikhov I, Walczak T. Clinical applications of EPR: overview and perspectives. NMR Biomed. 2004;17(5):335–51.
140. He G, Samouilov A, Kuppusamy P, Zweier JL. In vivo EPR imaging of the distribution and metabolism of Nitroxide radicals in human skin. J Magn Reson. 2001;148(1):155–64.
141. Swartz HM, Williams BB, Hou H, Khan N, Jarvis LA, Chen EY, Schaner PE, Ali A, Gallez B, Kuppusamy P, Flood AB. Direct and repeated clinical measurements of pO_2 for enhancing cancer therapy and other applications. Adv Exp Med Biol. 2016;923:95–104.
142. Nel J, Desmet CM, Driesschaert B, Saulnier P, Lemaire L, Gallez B. Preparation and evaluation of Trityl-loaded lipid Nanocapsules as oxygen sensors for electron paramagnetic resonance Oximetry. Int J Pharm. 2019;554:87–92.
143. Kmiec MM, Hou H, Kuppusamy LM, Drews TM, Prabhat AM, Petryakov SV, Demidenko E, Schaner PE, Buckey JC, Blank A, Kuppusamy P. Transcutaneous oxygen measurement in humans using a paramagnetic skin adhesive film. Magn Reson Med. 2018;81(2):781–94.
144. Bobko AA, Eubank TD, Driesschaert B, Khramtsov VV. In vivo EPR assessment of PH, pO_2, redox status, and concentrations of phosphate and glutathione in the tumor microenvironment. J Vis Exp. 2018;133:2–11.
145. Khramtsov VV, Gillies RJ. Janus-faced tumor microenvironment and redox. Antioxid Redox Signal. 2014;21(5):723–9.
146. Komarov DA, Ichikawa Y, Yamamoto K, Stewart NJ, Matsumoto S, Yasui H, Kirilyuk IA, Khramtsov VV, Inanami O, Hirata H. In vivo extracellular pH mapping of tumors using electron paramagnetic resonance. Anal Chem. 2018;90(23):13938–45.
147. Khramtsov VV, Caia GL, Shet K, Kesselring E, Petryakov S, Zweier JL, Samouilov A. Variable field proton-electron double-resonance imaging: application to PH mapping of aqueous samples. J Magn Reson. 2010;202(2):267–73.
148. Elajaili H, Biller JR, Rosen GR, Kao J, Tseytlin M, Buchanan L, Rinard G, Quine R, McPeak J, Shi Y, Eaton SS, Eaton GR. Imaging disulfide Dinitroxides at 250 MHz to monitor Thiol redox status. J Magn Reson. 2015a;260:77–82.
149. Elajaili HB, Biller JR, Tseytlin M, Dhimitruka I, Khramtsov V, Eaton SS, Eaton GR. Electron spin relaxation times and rapid scan EPR imaging of PH-sensitive amino substituted Trityl radicals. Magn Reson Chem. 2015b;53(4):280–4.

150. Efimova OV, Sun Z, Petryakov S, Kesselring E, Caia GL, Johnson D, Zweier JL, Khramtsov VV, Samouilov A. Variable radio frequency proton-electron double-resonance imaging: application to PH mapping of aqueous samples. J Magn Reson. 2011;209(2):227–32.
151. Potapenko DI, Foster MA, Lurie DJ, Kirilyuk IA, Hutchison JMS, Grigor'ev I a, Bagryanskaya EG, Khramtsov VV. Real-time monitoring of drug-induced changes in the stomach acidity of living rats using improved PH-sensitive Nitroxides and low-field EPR techniques. J Magn Reson. 2006;182(1):1–11.
152. Samouilov A, Efimova OV, Bobko AA, Sun Z, Petryalov S, Eubank TD, Trifomov DG, Kirilyuk IA, Takahasji W, Zweier JL, Khramtsov VV. In vivo proton–electron double-resonance imaging of extracellular tumor PH using an advanced Nitroxide probe. Anal Chem. 2014;86(2):1045–52.
153. Goodwin J, Yachi K, Nagane M, Yasui H, Miyake Y, Inanami O, Bobko A, Khramtsov VV, Hirata H. In vivo tumour extracellular PH monitoring using electron paramagnetic resonance: the effect of X-ray irradiation. NMR Biomed. 2014;27(4):453–8.
154. Khramtsov VV, Yelinova VI, Weiner LM, Berezina TA, Martin VV, Volodarsky LB. Quantitative determination of SH groups in low- and high-molecular-weight compounds by an electron spin resonance method. Anal Biochem. 1989;182(1):58–63.
155. Khramtsov VV. Functional EPR spectroscopy and imaging of nitroxides. In: Pifat-Mrzljak G. (eds) Supramolecular structure and function 9. Springer, Dordrecht. 2007, 181-208
156. Bobko AA, Evans J, Denko NC, Khramtsov VV. Concurrent longitudinal EPR monitoring of tissue oxygenation, acidosis and reducing capacity in a mouse Xenograft tumor models. Cell Biochem Biophys. 2017a;75(2):247–53.
157. Bobko AA, Eubank TD, Driesschaert B, Dhimitruka I, Evans J, Mohammad R, Tchekneva EE, Dikov MM, Khramtsov VV. Interstitial inorganic phosphate as a tumor microenvironment marker for tumor progression. Sci Rep. 2017b;7:1–12.
158. Bobko AA, Eubank TD, Voorhees JL, Efimova OV, Igor A, Petryakov S, Trofimiov DG, Marsh CB, Zweier JL, Samouilov A, Khramtsov VV. In vivo monitoring of pH, redox status, and glutathione using L-band EPR for assessment of therapeutic effectiveness in solid tumors. Magn Reson Med. 2012;67(6):1827–36.
159. Roshchupkina GI, Bobko AA, Bratasz A, Reznikov VA, Kuppusamy P, Khramtsov VV. In vivo EPR measurement of glutathione in tumor-bearing mice using improved disulfide Biradical probe. Free Radic Biol Med. 2008;45(3):312–20.
160. Khramtsov VV. In vivo molecular electron paramagnetic resonance-based spectroscopy and imaging of tumor microenvironment and redox using functional paramagnetic probes. Antioxid Redox Signal. 2017;28(15):2017–7329.
161. Bobko AA, Dhimitruka I, Zweier J, Khramtsov VV. Fourier transform EPR spectroscopy of Trityl radicals for multifunctional assessment of chemical microenvironment. Angew Chem Int Ed Engl. 2014;53(10):2735–8.
162. Krishna MC, Matsumoto S, Saito K, Matsuo M, Mitchell JB, Ardenkjaer-Larsen JH. Magnetic resonance imaging of tumor oxygenation and metabolic profile. Acta Oncologica. 2013;52(7):1248–56.
163. Takakusagi Y, Matsumoto S, Saito K, Matsuo M, Kishimoto S, Wojtkowiak JW, DeGraff W, Kesarwala AH, Choudhuri R, Devasahayam N, Subramanian S, Munasinghe JP, Gillies RJ, Mitchell JB, Hart CP, Murali C. Krishna. Pyruvate induces transient tumor hypoxia by enhancing mitochondrial oxygen consumption and potentiates the anti-tumor effect of a hypoxia-activated Prodrug TH-302. PLoS One. 2014;9(9):e107995.
164. Wojtkowiak JW, Cornnell HC, Matsumoto S, Saito K, Takakusagi Y, Dutta P, Kim M, Zhang X, Leos R, Bailey KM, Martinez G, Lloyd MC, Weber C, Mitchell JB, Lynch RM, Baker AF, Gatenby RA, Rejniak KA, Hart C, Krishna MC, Gillies RJ. Pyruvate sensitizes pancreatic tumors to hypoxia-activated Prodrug TH-302. Cancer Metab. 2015;3:1–13.
165. Matsumoto S, Saito K, Takakusagi Y, Matsuo M, Munasinghe JP, Morris HD, Lizak MJ, Merkle H, Yasukawa K, Devasahayam N, Suburamanian S, Mitchell JB, Krishna MC. In vivo imaging of tumor physiological, metabolic, and redox changes in response to the anti-Angio-

genic agent Sunitinib: longitudinal assessment to identify transient vascular renormalization. Antioxid Redox Signal. 2014;21(8):1145–55.
166. Saito K, Matsumoto S, Yasui H, Devasahayam N, Subramanian S, Munasinghe JP, Vyomesh P, Silvio Gutkind J, Mitchell JB, Krishna MC. Longitudinal imaging studies of tumor microenvironment in mice treated with the MTOR inhibitor Rapamycin. PLoS One. 2012;7(11):e49456.
167. Naz S, Kishimoto S, Mitchell JB, Krishna MC. Imaging metabolic processes to predict radiation responses. Semin Radiat Oncol. 2019;29(1):81–9.
168. Kishimoto S, Matsumoto K-I, Saito K, Enomoto A, Matsumoto S, Mitchell J, Devasahayam N, Krishna MC. Pulsed EPR imaging: applications in the studies of tumor physiology. Antioxid Redox Signal. 2018;28(15):1378–93.
169. Neveu MA, De Preter G, Marchand V, Bol A, Brender JR, Saito K, Kishimoto S, Porporato PE, Sonveaux P, Grégoire V, Feron O, Jordan BF, Krishna MC, Gallez B. Multimodality imaging identifies distinct metabolic profiles in vitro and in vivo. Neoplasia. 2016;18(12):742–52.
170. Matsumoto S, Saito K, Hironobu Y, Douglas Morris H, Munasinghe JP, Lizak M, Merkle H, Ardenkjaer-Larsen JH, Choudhuri R, Devasahayam N, Subramanian S, Koretsky AP, Mitchell JB, Krishna MC. EPR oxygen imaging and hyperpolarized 13C MRI of pyruvate metabolism as noninvasive biomarkers of tumor treatment response to a glycolysis inhibitor 3-Bromopyruvate. Magn Reson Med. 2013;69(5):1443–50.
171. Saito K, Matsumoto S, Takakusagi Y, Matsuo M, Morris HD, Lizak MJ, Munasinghe JP, Devasahayam N, Subramanian S, Mitchell JB, Krishna MC. 13C-MR spectroscopic imaging with hyperpolarized [1-13C]pyruvate detects early response to radiotherapy in SCC tumors and HT-29 tumors. Clin Cancer Res. 2015;21(22):5073–81.
172. Hyodo F, Soule BP, Matsumoto K-i, Matusmoto S, John A, Hyodo E, Sowers AL, Krishna MC, Mitchell JB, John A. Assessment of tissue redox status using metabolic responsive contrast agents and magnetic resonance imaging. J Pharm Pharmacol. 2008c;60(8):1049–60.
173. Utsumi H, Muto E, Masuda S, Hamada A. In vivo ESR measurement of free radicals in whole mice. Biochem Biophys Res Commun. 1990;172(3):1342.
174. Utsumi H, Yamada K-i I. In vivo electron spin resonance-computed tomography/Nitroxyl probe technique for non-invasive analysis of oxidative injuries. Arch Biochem Biophys. 2003;416(1):1–8.
175. Emoto MC, Matsuoka Y, Yamada K, Sato-Akaba H, Fujii HG. Non-invasive imaging of the levels and effects of glutathione on the redox status of mouse brain using electron paramagnetic resonance imaging. Biochem Biophys Res Commun. 2017;485(4):802–6.
176. Hyodo F, Matsumoto K-I, Matsumoto A, Mitchell JB, Krishna MC. Probing the intracellular redox status of tumors with magnetic resonance imaging and redox-sensitive contrast agents. Cancer Res. 2006;66(20):9921–8.
177. Tun X, Ichikawa K, Yamada K-I, Mutsumoto Y, Utsumi H, Yasukawa K, Oda F, Kanbe T, Shigemi R. In vivo imaging of the intra- and extracellular redox status in rat stomach with indomethacin-induced gastric ulcers using Overhauser-enhanced magnetic resonance imaging. Antioxid Redox Signal. 2018;8:1–44.
178. Davis RM, Matsumoto S, Bernardo M, Sowers A, Matsumoto K-I, Krishna MC, Mitchell JB. Magnetic resonance imaging of organic contrast agents in mice: capturing the whole-body redox landscape. Free Radic Biol Med. 2011a;50(3):459–68.
179. Matsumoto K-i, Mitchell JB, Krishna MC. Comparative studies with EPR and MRI on the in vivo tissue redox status estimation using redox-sensitive Nitroxyl probes: influence of the choice of the region of interest. Free Radic Res. 2018;5762:1–8.
180. Hyodo F, Davis RM, Hyodo E, Matsumoto S, Krishna MC, Mitchell JB. The relationship between tissue oxygenation and redox status using magnetic resonance imaging. Int J Oncol. 2012;41(6):2103–8.
181. Takeshita K, Kawaguchi K, Fujii-Aikawa K, Ueno M, Okazaki S, Ono M, Krishna MC, Kuppusamy P, Ozawa T, Ikota N. Heterogeneity of regional redox status and relation of the redox status to oxygenation in a tumor model, evaluated using electron paramagnetic resonance imaging. Cancer Res. 2010;70(10):4133–40.

182. Kubota H, Komarov DA, Yasui H, Matsumoto S, Inanami O, Kirilyuk IA, Khramtsov VV, Hirata H. Feasibility of in vivo three-dimensional mapping using Dicarboxy-PROXYL and CW-EPR-based single-point imaging. MAGMA. 2017;30(3):291–8.
183. Davis RM, Sowers AL, Degraff W, Bernardo M, Krishna MC, Mitchell JB. A novel Nitroxide is an effective brain redox imaging contrast agent and in vivo Radioprotector. Free Radic Biol. 2011b;51(3):780–90.
184. Emoto MC, Sato-Akaba H, Hirata H, Fujii HG. Dynamic changes in the distribution and time course of blood–brain barrier-Permeative Nitroxides in the mouse head with EPR imaging: visualization of blood flow in a mouse model of ischemia. Free Radic Biol Med. 2014;74:222–8.
185. Fujii H, Sato-Akaba H, Kawanishi K, Hirata H. Mapping of redox status in a brain-disease mouse model by three-dimensional EPR imaging. Magn Reson Med. 2011;65(1):295–303.
186. Yordanov AT, Yamada K-i, Krishna MC, Russo A, Yoo J, English S, Mitchell JB, Brechbiel MW. Acyl-protected Hydroxylamines as spin label generators for EPR brain imaging. J Med Chem. 2002;45(11):2283–8.
187. Meredith P, Sarna T. The physical and chemical properties of Eumelanin. Pigment Cell Res. 2006;19(6):572–94.
188. Glass K, Ito S, Wilby PR, Sota T, Atsushi N, Russell Bowers C, Vinther J, Dutta S, Summons R, Briggs DEG, Wakamatsu K, Simon JD. Direct chemical evidence for Eumelanin pigment from the Jurassic period. Proc Natl Acad Sci U S A. 2012;109(26):10218–23.
189. Commoner B, Townsend J, Pake GW. Free radicals in biological materials. Nature. 1954;174:689–91.
190. Lukiewicz S, Pilas B. A new method of measuring oxygenation in pigmented tumors growing in situ. P. 65 in III European workshop on melanin pigmentation. Prague, Czech: Charles University; 1981.
191. Berliner LJ, Fujii H, Wan X, Lukiewicz SJ. Feasibility study of imaging a living murine tumor by electron paramagnetic resonance. Magn Reson Med. 1987;4(4):380–4.
192. Katsuda H, Kobayashi T, Saito H, Matsunaga T, Ikeya M. Electron spin resonance imaging of mouse B16 melanoma. Chem Pharm Bull. 1990;38(10):2838–40.
193. Vanea E, Charlier N, Dewever J, Dinguizli M, Feron O, Baurain J-F, Gallez B. Molecular electron paramagnetic resonance imaging of melanin in melanomas: a proof-of-concept. NMR Biomed. 2008;21(3):296–300.
194. Godechal Q, Gallez B. The contribution of electron paramagnetic resonance to melanoma research. J Skin Cancer. 2011;2011:273280.
195. Godechal Q, Leveque P, Marot L, Baurain JF, Gallez B. Optimization of EPR imaging for visualization of human skin melanoma in various stages of invasion. Exp Dermatol. 2012;21(5):341–6.
196. Godechal Q, Ghanem GE, Cook MG, Bernard G, Ghanem E, Cook G, Gallez B. Electron paramagnetic resonance spectrometry and imaging in melanomas: comparison between pigmented and nonpigmented human malignant melanomas. Mol Imaging. 2013;12(4): 218–23.
197. Godechal Q, Mignion L, Karroum O, Magat J, Danhier P, Morandini R, Ghanem GE, Leveque P, Gallez B. Influence of paramagnetic melanin on the MRI contrast in melanoma: a combined high-field (11.7 T) MRI and EPR study. Contr Media Mol Imag. 2014;9(2):154–60.
198. Fan Q, Cheng K, Hu X, Ma X, Zhang R, Yang M, Lu X, Xing L, Huang W, Gambhir SS, Cheng Z. Transferring biomarker into molecular probe: melanin nanoparticle as a naturally active platform for multimodality imaging. J Am Chem Soc. 2014;136(43):15185–94.
199. Nakagawa K, Minakawa S, Sawamura D, Hara H. Characterization of melanin radicals in paraffin-embedded malignant melanoma and nevus Pigmentosus using X-band EPR and EPR imaging. Anal Sci. 2017;33(12):1357–61.
200. Hyodo F, Naganuma T, Eto H, Murata M, Utsumi H, Matsuo M. In vivo melanoma imaging based on dynamic nuclear polarization enhancement in melanin pigment of living mice using in vivo dynamic nuclear polarization magnetic resonance imaging. Free Radic Biol Med. 2019;134:99–105.

201. Utsumi H, Hyodo F. Free radical imaging using in vivo dynamic nuclear polarization-MRI, vol. 564. 1st ed. New York: Elsevier Inc.; 2015.
202. Al Khatib M, Harir M, Costa J, Baratto MC, Schiavo I, Trabalzini L, Pollini S, Rossolini GM, Basosi R, Pogni R. Spectroscopic characterization of natural melanin from a Streptomyces Cyaneofuscatus strain and comparison with melanin enzymatically synthesized by Tyrosinase and Laccase. Molecules. 2018;23(8):E1916.
203. Pustelny K, Bielanska J, Plonka PM, Rosen GM, Elas M. In vivo spin trapping of nitric oxide from animal tumors. Nitric Oxide. 2007;16(2):202–8.
204. Towner R, Smith N. Vivo and in situ detection of macromolecular free radicals using Immuno-spin trapping and molecular MRI. Antioxid Redox Signal. 2017;28(15):187.
205. Bézière N, Decroos C, Mkhitaryan K, Kish E, Richard F, Bigot-Marchand S, Durand S, Cloppet F, Chauvet C, Corvol M-T, Rannou F, Xu-Li Y, Mansuy D, Peyrot F, Frapart Y-M. First combined in vivo X-ray tomography and high-resolution molecular electron paramagnetic resonance (EPR) imaging of the mouse knee joint taking into account the disappearance kinetics of the EPR probe. Mol Imaging. 2012;11(3):220–8.
206. Nakagawa K, Epel B. Location of radical species in a black pepper seed investigated by CW EPR and 9 GHz EPR-imaging. Spectrochim Acta A Mol Biomol Spectrosc. 2014;131:342–6.
207. Nakagawa K, Epel B. Investigation of the distribution of stable paramagnetic species in an apple seed using X-band EPR and EPR imaging. J Oleo Sci. 2017;66(3):315–9.
208. Shin CS, Dunnam CR, Borbat PP, Dzikovski B, Barth ED, Halpern HJ, Freed JH. ESR microscopy for biological and biomedical applications. Nanosci Nanotech Lett. 2011;3(4):561–7.
209. Hashem M, Weiler-Sagie M, Kuppusamy P, Neufeld G, Neeman M, Blank A. Electron spin resonance microscopic imaging of oxygen concentration in cancer spheroids. J Magn Reson. 2015;256:77–85.
210. Lilledahl MB, Gustafsson H, Ellingsen PG, Zachrisson H, Hallbeck M, Hagen VS, Kildemo M, Lindgren M. Combined imaging of oxidative stress and microscopic structure reveals new features in human atherosclerotic plaques. J Biomed Opt. 2015;20(2):020503.
211. Matsumoto K-i, Subramanian S, Murugesan R, Mitchell JB, Krishna MC. Spatially resolved biologic information from in vivo EPRI, OMRI, and MRI. Antioxid Redox Signal. 2007;9(8):1125–41.
212. Gonet M, Epel B, Elas M. Data processing of 3D and 4D in-vivo electron paramagnetic resonance imaging co-registered with ultrasound. 3D printing as a registration tool. Comput Electr Eng. 2019;74:130–7.
213. Tseytlin M, Stolin A, Guggilapu P, Bobko A, Khramtsov V, Tseytlin O, Raylman R. A combined positron emission tomography (PET)- electron paramagnetic resonance imaging (EPRI) system: initial evaluation of a prototype scanner. Phys Med Biol. 2018;63(10):1–18.
214. Eto H, Hyodo F, Kosem N, Kobayashi R, Yasukawa K, Nakao M, Kiniwa M, Utsumi H. Redox imaging of skeletal muscle using in vivo DNP-MRI and its application to an animal model of local inflammation. Free Radic Biol Med. 2015;89:1097–104.
215. Hyodo F, Murugesan R, Matsumoto K-i, Hyodo E, Subramanian S, Mitchell JB, Krishna MC. Monitoring redox-sensitive paramagnetic contrast agent by EPRI, OMRI and MRI. J Magn Reson. 2008b;190(1):105–12.
216. Matsumoto S, Yasui H, Batra S, Kinoshita Y, Bernardo M, Munasinghe JP, Utsumi H, Choudhuri R, Devasahayam N, Subramanian S, Mitchell JB, Krishna MC. Simultaneous imaging of tumor oxygenation and microvascular permeability using Overhauser enhanced MRI. Proc Natl Acad Sci U S A. 2009;106(42):17898–903.
217. Ahn K-H, Scott G, Stang P, Conolly S, Hristov D. Multiparametric imaging of tumor oxygenation, redox status, and anatomical structure using Overhauser-enhanced MRI-Prepolarized MRI system. Magn Reson Med. 2011;65(5):1416–22.
218. Ichikawa K, Yasukawa K. Imaging in vivo redox status in high spatial resolution with OMRI. Free Radic Res. 2012;46(8):1004–10.
219. Gorodetskii AA, Eubank TD, Driesschaert B, Poncelet M, Ellis E, Khramtsov VV, Bobko AA. Oxygen-induced leakage of spin polarization in Overhauser-enhanced magnetic resonance imaging: application for Oximetry in tumors. J Magn Reson. 2018;297:42–50.

220. Niidome T, Chijiiwa N, Yamasaki T, Yamada K-i, Utsumi H, Mori T, Ichikawa K, Naganuma T, Niidome T, Katayama Y, Chijiiwa N. Change in Overhauser effect-enhanced MRI signal in response to UPA highly expressing in tumor. Chem Lett. 2014;43(7):999–1001.
221. Decroos C, Li Y, Bertho G, Frapart Y, Mansuy D, Boucher J-L. Oxidation of Tris-(p-Carboxyltetrathiaaryl)methyl radical EPR probes: evidence for their oxidative decarboxylation and molecular origin of their specific ability to react with $O2^{\bullet-}$. Chem Commun (Camb). 2009;(11):1416–8.
222. Dhimitruka I, Grigorieva O, Zweier JL, Khramtsov VV. Synthesis, structure, and EPR characterization of Deuterated derivatives of Finland Trityl radical. Bioorg Med Chem Lett. 2010;20(13):3946–9.
223. Dhimitruka I, Velayutham M, Bobko AA, Khramtsov VV, Villamena FA, Hadad CM, Zweier JL. Large-scale synthesis of a persistent Trityl radical for use in biomedical EPR applications and imaging. Bioorg Med Chem Lett. 2007;17(24):6801–5.
224. Rogozhnikova OY, Vasiliev VG, Troitskaya TI, Trukhin DV, Mikhalina TV, Halpern HJ, Tormyshev VM. Generation of Trityl radicals by Nucleophilic quenching of Tris(2,3,5,6-Tetrathiaaryl)methyl Cations and practical and convenient large-scale synthesis of persistent Tris(4-Carboxy-2,3,5,6-Tetrathiaaryl)methyl radical. Eur J Org Chem. 2013;(16):3347–55.
225. Tormyshev VM, Rogozhnikova OY, Bowman MK, Trukhin DV, Troitskaya TI, Vasiliev VG, Shundrin LA, Halpern HJ. Preparation of diversely substituted Triarylmethyl radicals by the quenching of Tris(2,3,5,6-Tetrathiaaryl)methyl Cations with C-, N-, P-, and S-nucleophiles. Eur J Org Chem. 2014;2014(2):371–80.
226. Trukhin DV, Rogozhnikova OY, Troitskaya T, Vasiliev VG, Bowman MK, Tormyshev VM, Troitskayaa TI, Vasiliev VG, Bowman MK, Tormyshev VM. Facile and high-yielding synthesis of TAM Biradicals and Monofunctional TAM radicals. Synlett. 2015;27(6):893–9.
227. Liu Y, Villamena FA, Zweier JL. Highly stable dendritic Trityl radicals as oxygen and pH probe. Chem Commun. 2008;1(36):4336–8.
228. Liu W, Nie J, Tan X, Liu H, Yu N, Han G, Zhu Y, Villamena FA, Song Y, Zweier JL, Liu Y. Synthesis and characterization of PEGylated Trityl radicals: effect of PEGylation on physicochemical properties. J Org Chem. 2017;82(1):588–96.
229. Liu Y, Villamena FA, Sun J, Wang T. Esterified Trityl radicals as intracellular oxygen probes. Free Radic Biol Med. 2009;46(7):876–83.
230. Driesschaert B, Bobko AA, Eubank TD, Samouilov A, Khramtsov VV, Zweier JL. Polyarginine conjugated Triarylmethyl radical as intracellular spin label. Bioorg Med Chem Lett. 2016;26(7):1742–74.
231. Tan X, Tao S, Liu W, Rockenbauer A, Villamena FA, Zweier JL, Song Y, Liu Y. Synthesis and characterization of the Perthiatriarylmethyl radical and its dendritic derivatives with high sensitivity and selectivity to superoxide radical. Chem Eur J. 2018;24(27):6865.
232. Driesschaert B, Bobko AA, Khramtsov V, Zweier JL. Nitro-Triarylmethyl radical as dual oxygen and superoxide probe. Cell Biochem Biophys. 2017;75(2):241–6.
233. Liu Y, Song Y, Rockenbauer A, Sun J, Hemann C, Villamena FA, Zweier JL. Synthesis of Trityl radical-conjugated disulfide Biradicals for measurement of Thiol concentration. J Org Chem. 2011;76(10):3853–60.
234. Charlier N, Driesschaert B, Wauthoz N, Beghein N, Préat V, Amighi K, Marchand-Brynaert J, Gallez B. Nano-emulsions of fluorinated Trityl radicals as sensors for EPR Oximetry. J Magn Reson. 2009;197(2):176–80.
235. Dhimitruka I, Alzarie YA, Hemann C, Samouilov A, Zweier JL. Trityl radicals in Perfluorocarbon emulsions as stable, sensitive, and biocompatible Oximetry probes. Bioorg Med Chem Lett. 2016;26(23):5685–8.
236. Lampp L, Rogozhnikova OY, Trukhin DV, Tormyshev VM, Bowman MK, Devasahayam N, Krishna MC, Mäder K, Imming P. A radical containing injectable in-situ-Oleogel and Emulgel for prolonged in-vivo oxygen measurements with CW EPR. Free Radic Biol Med. 2019;130:120–7.
237. Meenakshisundaram G, Eteshola E, Pandian RP, Bratasz A, Lee SC, Kuppusamy P. Fabrication and physical evaluation of a polymer- encapsulated paramagnetic probe for biomedical Oximetry. Biomed Microdevices. 2009;11:773–82.

238. Desmet CM, Tran LBA, Danhier P, Gallez B. Characterization of a clinically used charcoal suspension for in vivo EPR Oximetry. MAGMA. 2018;32(2):205–12.
239. Kocherginsky N, Swartz HM. Nitroxide spin labels: reactions in biology and chemistry. Boca Raton: CRC Press; 1995.
240. Liu Y, Villamena FA, Rockenbauer A, Zweier JL. Trityl-Nitroxide Biradicals as unique molecular probes for the simultaneous measurement of redox status and oxygenation. Chem Commun (Camb). 2010a;46(4):628–30.
241. Liu Y, Villamena FA, Song Y, Sun J, Rockenbauer A, Zweier JL. Synthesis of (14)N- and (15) N-labeled Trityl-Nitroxide Biradicals with strong spin-spin interaction and improved sensitivity to redox status and oxygen. J Org Chem. 2010;75(22):7796–802.
242. Matsumoto K-I, Hyodo F, Matsumoto A, Koretsky AP, Sowers AL, Mitchell JB, Krishna MC. High-resolution mapping of tumor redox status by magnetic resonance imaging using Nitroxides as redox-sensitive contrast agents. Clin Cancer Res. 2006;12(8):2455–62.

Magnetic Resonance Spectroscopic Analysis in Brain Tumors

2

Ghazaleh Jamalipour Soufi, Nastaran Fallahpour, Kaveh Jamalipour Soufi, and Siavash Iravani

2.1 Introduction

Brain tumors are one of the most health problems in the world, and tumor grading is critical for the determination of appropriate treatment approaches [1]. Indeed, patients with some types of brain tumors (e.g., glioblastoma) have poor prognosis, and the time to progression and median survival can be mediated for selected subpopulations of patients by applying aggressive therapy [2, 3]. In fact, decide on the treatment which has highest suitable effects on a patient, and leading that therapy to the region of active tumor is very crucial for achievement of the appropriate results. Some critical considerations for analyzing prognosis are tumors type, grade, and volume [4, 5]. Considering the brilliant soft tissue contrast obtained by magnetic resonance imaging (MRI), the sensitivity and specificity with which this modality defines tumor type and grade is restricted. This is partially attributable to the presence of gadolinium (Gd)-enhanced necrosis which might be incorrect for tumor and partially to the inconvenience in differentiating between tumor, edema, and non-specific treatment consequences in the section of hypointensity on T2-weighted images [6, 7]. Overcoming these important challenges needs the development of new imaging modalities which highlight functional or metabolic characteristics of tumors. Though some researches about positron emission tomography and single photon emission tomography for such evaluation have been

G. J. Soufi
Radiology Department, Isfahan University of Medical Sciences, Isfahan, Iran

N. Fallahpour · K. J. Soufi
School of Medicine, Isfahan University of Medical Sciences, Isfahan, Iran

S. Iravani (✉)
Faculty of Pharmacy and Pharmaceutical Sciences, Isfahan University of Medical Sciences, Isfahan, Iran

A. K. Shukla (ed.), *Medical Imaging Methods*,
https://doi.org/10.1007/978-981-13-9121-7_2

stated, there would be an important saving in cost and patient suffering, if above-mentioned challenging information could be described by using magnetic resonance methodologies [8–10]. For instance, two methods of imaging investigated for this application are perfusion-weighted and diffusion-weighted MRI. These make applying echo planar pulse sequences to study the architecture of tissues and microvasculature in the lesion and surrounding brain parenchyma. They offer information of physiological characteristics of tumors linked to cellularity, structural integrity, and angiogenesis; however, they are applied irregularly for clinical management of patients [11, 12].

In this chapter, MRS technique in diagnosis, follow-up and characterization of brain tumors, and grading of primary brain tumors has been discussed with latest developments; the efficiency of MRS in evaluation of treatment response of brain tumors is highlighted.

2.2 Important Brain Metabolites Detected by MRS

Magnetic resonance spectroscopy (MRS) technique can be applied for detecting metabolites, including N-acetyl aspartate (NAA), choline (Cho)-containing compounds, creatine (Cr)/phosphocreatine, and lactate (Lac) (Fig. 2.1) [13]. Presently, many studies in this field applied echo times of 144 or 270 ms, that offer spectra dominated by five various metabolite peaks: Cho; Cr; NAA; Lac; and lipid. The Cho peaks consist of different Cho-containing compounds, and demonstrate membrane synthesis and turnover. Cr is important in cellular energetics, and NAA is a neuronal marker. Lac indicates anaerobic metabolism, and LP can be detected in regions of cellular breakdown produced by necrosis [13]. Brandão and Castillo comprehensively reviewed the clinical applications of MRS in adult brain tumors [14]. Important MRS applications and crucial concerns in initial analysis of brain tumors

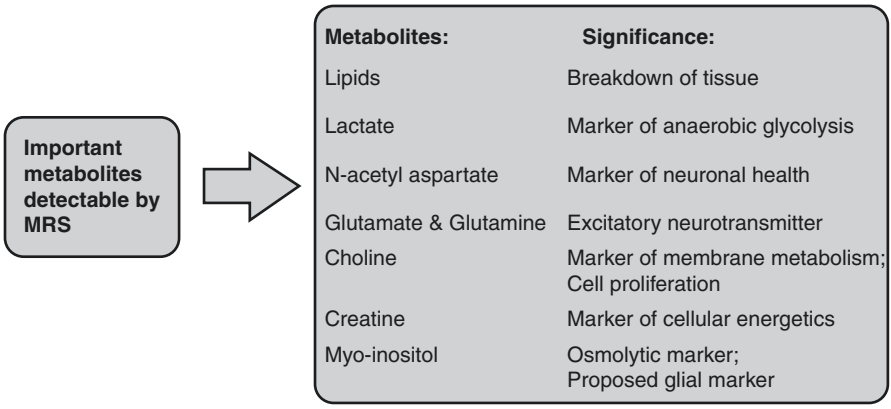

Fig. 2.1 Important metabolites detected by MRS

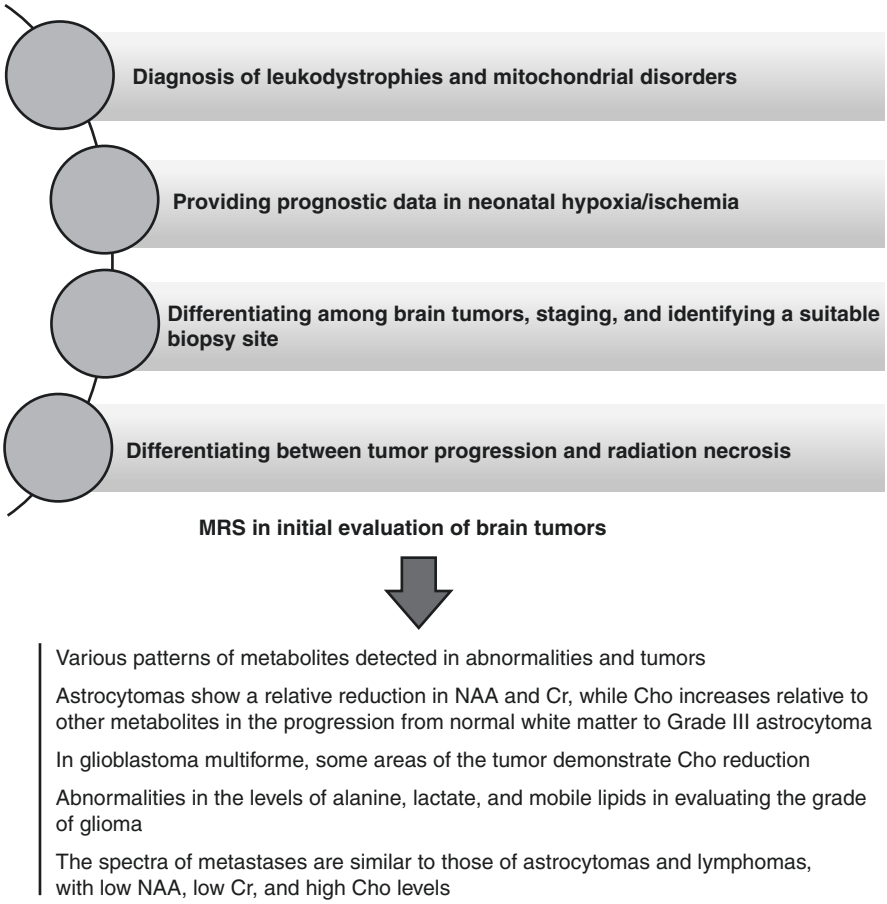

Fig. 2.2 Some important examples of clinical applications of MRS; important issues in initial evaluation of brain tumors are highlighted

are highlighted in Fig. 2.2 [1–12]. MRS can supply exclusive information for the researchers about the neurobiological substrates of brain functions in health and disease [15, 16]. Indeed, two categories of spatial localization techniques are existed for MRS; single-voxel (SV) techniques, frequently applied approaches include PRESS and STEAM, that record spectra from single region of the brain at a time, or multi-voxel techniques (magnetic resonance spectroscopic imaging (MRSI)), also recognized as chemical shift imaging (CSI) that concurrently record spectra from multiple regions and thus can be applied for mapping the spatial metabolite distribution inside the brain [17–19]. MRSI is typically performed in 2- or 3-dimensions, but does not regularly have full brain coverage. It should be noticed that important concern for brain tumors is their metabolic inhomogeneity [19]. For instance, the MRSI spectrum from the necrotic core of a high-grade brain tumor is entirely dissimilar from a spectrum of the actively growing rim, although peri-tumoral edema

is different from tumor invasion into surrounding brain tissue; thus, high-resolution MRSI is often preferred for analyzing brain tumor metabolism [20]. It was shown that proton MRSI may have a promising role in differentiating pediatric brain lesions, and crucial diagnostic value, especially for inoperable or inaccessible lesions [20]. Studying all potential metabolite ratios combinations, the best discriminant function for differentiating between non-brain tumors and neoplastic lesions was found to include only the ratio of Cho/Cr. The best discriminant function for differentiating between high- and low-grade tumors involved the ratios of NAA/Cr and Cho $_{norm}$. Cr levels in low-grade tumors were considerably lower than or comparable to control regions and ranged from 53 to 165% of the control values in high-grade tumors [20].

It was established that approximately all kinds of brain tumors show reduced NAA signals, frequently show accelerated Cho levels, and make an accelerated Cho/NAA ratios. The reduction of NAA is widely elucidated as the dysfunction, loss, or displacement of normal neuronal tissue, because NAA is identified to be mainly of neuronal and axonal origin [21]. Indeed, the Cho signal contains involvements from various Cho-containing compounds, which are contributed in membrane synthesis and degradation; it is increased in brain tumors by reason of accelerated membrane turnover. In vitro study showed that the increased Cho signal in brain tumors is because of accelerated phosphor choline levels. Additionally, it was suggested that MRSI can be applied for mapping Cho levels, and therefore been offered as a defining technique for tumor boundaries in the process of treatment [19].

Other usual metabolic alterations in human brain tumors consist of increased signals in the Lac and lipid region of the spectrum, and accelerated myo-inositol (mI) levels in short echo time (TE) spectra. The acceleration in Lac is almost certainly the consequence of anaerobic glycolysis. Furthermore, it can be due to inadequate blood flow that makes the ischemia or because of the necrosis. The detection of increased lipid levels is supposed to be related with necrosis and membrane breakdown. Accelerated levels of mI can be due to the elevated numbers of glial cells containing high levels of mI, and especially have been reported to be high in grade II gliomas. Additionally, patients with gliomatosis cerebri may show accelerated inositol levels, even in the absence of elevated Cho [19, 22]. MRS efficacy in diagnosis and assessment of treatment response of brain tumors has been widely reported, but this technique has not been typically established as a routine clinical tool. Robust and automated techniques are required to collect the information, evaluate the spectra, and show the consequences, comprehensively. Standardization across sites and various vendors of acquisition and evaluation technique is very critical. Additionally, carefully created, multicenter trials complying with criteria of evidence-based medicine have not been completed until now, and consequently, MRS is only comparatively infrequently applied for evaluating tumor by researchers in the field [19].

H-MRS can be applied in tumor histology and grading and may better describe tumor extension and the appropriate site for biopsy compared with conventional MRI. Combination of H-MRS with other developed imaging techniques, including

diffusion-weighted imaging, perfusion-weighted imaging, and permeability maps enhances the diagnostic accuracy for intra-axial brain tumors. Short echo time allows for detecting higher amounts of metabolites compared with long echo time, which is crucial for differential analysis of brain masses and grading tumors. Additionally, higher Cho levels and lower mI/Cr ratio are detected in more malignant tumors compared with lower-grade tumors. Lac is precisely related with brain tumor grading. Though, Lac is found in basically all pediatric brain tumors regardless of histologic grade. Gliomas are often invasive and show enhanced Cho levels in surrounding tissues, and thus, this can be applied for differentiating these lesions from metastases. It appears that lymphoma should be stated, when LP and Lac are found in a solid lesion. A prominent lipid peak is detected in lymphomatosis cerebri, while a considerable acceleration in mI is characteristic of gliomatosis cerebri. High acceleration in the Cho peak and the existence of LP and Lac are normally detected in pilocytic astrocytoma, a grade I tumor. Characteristically, higher levels of Cho happen in grade III gliomas; while, in glioblastoma multiforme, the Cho levels may be much lower because of the necrosis. If the Cho/NAA ratio is accelerated outside the area of enhancement, tumor infiltration can be detected. An enhancement in Cho-containing compounds after radiation therapy may be observed in radiation necrosis misclassified as tumors. H-MRS in exclusive cases enhances the accuracy and level of confidence in differentiating neoplastic from non-neoplastic masses [14].

2.3 Applications of MRS Metabolite Analysis in Brain Tumors

MRS offers significant and valuable clinical data permitting more precise diagnosis including differentiating the brain tumors from abscesses, defining the tumoral characteristic of the investigated lesion and better evaluation of brain tumors, and determining an extended local evaluation of morphological abnormalities detected in conventional MRI [23]. It can be applied for the therapeutic follow-up of evaluating the most active area in lesion, guiding and optimizing the biopsy, and differentiating the recurrent tumor. Additionally, MRS is suitable in radiosurgery as a criterion for representing the acceleration or reduction of the irradiation during tumor radiotherapy [13, 24]. In earlier differentiation between tumor and radionecrosis, MRS offers significant consequences. Accordingly, the lesion persistence or evolvement is recognized by an enhanced Cho, while a radionecrosis is stated by spectra where all metabolisms disappeared except free lipids (LP) [25].

The diagnostic variations between MRS and the conventional MRI analogue image, i.e., the accuracy and sensitivity of MRS, MRI, and CT relative to histological section, were reported. Consequently, brain tumors signify an incidence of 54% in Sudan during 2014–2017 with an increasing factor of 7.2/year. MRS demonstrated outstanding diagnostic achievement relative to standard (histology) with accuracy, sensitivity, and specificity as 93%, 90%, and 85%, respectively, and the diagnosis of analogue MRI by radiologists revealed 91%, 83%, and 76% for

accuracy, sensitivity, and specificity, correspondingly, while CT revealed 80%, 75%, and 15% for accuracy, sensitivity, and specificity, correspondingly. MRS typically surpasses MRI compared with the standard (histology) and the T-test showed a substantial point of 0.5, depending on the level of Cho, NAA, Cr/phosphocreatine, and Lac [26]. In another study, MRS was applied for differential analysis of brain tumors and inflammatory brain lesions. The examinations of 81 individuals by brain MRS evaluation have been performed. The patients with ages between 10 and 80 years old were separated into two groups. Group A consisted of 42 individuals with diagnoses of cerebral toxoplasmosis and Group B was formed of 39 individuals with diagnosis of glial neoplasms. On analyzing the ROC curve, the discriminatory boundary for the Cho/Cr ratio between inflammatory lesions and tumors was 1.97, and for the NAA/Cr ratio it was 1.12. MRS can be applied in the distinction of inflammatory brain lesions and high-degree tumors when the Cho/Cr ratio is higher than 1.97 and the NAA/Cr ratio is less than 1.12 [27]. Additionally, in two patients with heterogeneous intracranial tumors, in vivo 1H MRS and in vitro biochemical evaluations have been performed. Histology established the tumor heterogeneity. Cho was raised in the cellular portion of both tumors, but reduced in the necrotic or cystic portions. Cr was diffusely reduced while Lac was accelerated in all regions of both tumors. Furthermore, the acceleration in the choline peak on 1H MRS appeared to be due to upsurges in water-soluble Cho compounds [28].

2.4 Combining MRS and MRI-Based Diagnosis of Brain Tumors

Indeed, for metastatic lesions, the volume of Gd acceleration on T1-weighted spin echo or gradient echo images is reported to encompass the entire active tumor. In many cases, there are also central regions of hypointensity within the enhancing lesion which correspond to necrosis. The region of hypointensity on the T1-weighted image and corresponding hyperintensity on T2-weighted images that characteristically surrounds the enhancing volume is reported to correspond to edema or generic treatment consequences rather than to infiltrative tumor. Diagnosis of small lesions and enhanced visualization of larger enhancing lesions is possible using double or triple doses of Gd [29]. The number and size of metastatic lesions within the brain affects the decision as to whether the most appropriate treatment is surgery, radiosurgery, or whole brain radiation therapy. Other important issues are the status of the primary lesion and metastases in other organs. Definition of grade is based upon histological analysis of tissue samples obtained by biopsy or during surgical resection. Because it is typical for there to be regions of different tumor grade within the same lesion, directing the surgeon to the region that is possibly to be of highest grade is crucial to achieve typical experiments for histological evaluation. While tumor cells are recognized to be outside the MRI-defined lesion as well, the enhancing lesion is extensively applied as the target for surgery resection or for planning radiation therapy [7].

Generally, it is challenging to make a correct diagnosis of ring-like enhanced lesions on Gd-enhanced MR brain images. For differentiating these lesions using proton 1H MRS, the correlation between the 1H-MR spectra and histopathological results was evaluated, retrospectively. Additionally, proton MR spectra obtained from the lesions in 45 patients, including metastasis ($n = 19$), glioblastoma ($n = 10$), radiation necrosis ($n = 7$), brain abscess ($n = 5$), and cerebral infarction ($n = 4$) were evaluated. Consequently, the misdiagnosis rate was lowest at the threshold level of 2.48 for the (Cho-containing compounds)/ (Cho/Cr) detected from the whole lesions, which consist of the enhanced rim and the non-enhanced inner region. The positive predictive values of a Cho/Cr greater than 2.48 for detecting metastasis or glioblastoma was 88.9% and 60.0%, respectively, and the positive predictive value of a Cho/Cr less than 2.48 for detecting radiation necrosis or cerebral infarction was 71.4% and 100%, respectively. For additional differentiation between metastasis and glioblastoma, information about the existence and absence of an NAA peak and lipid- or Lac-dominant peak was helpful. In 73.7% of metastasis cases, a lipid-dominant peak was reported in the whole lesion without an NAA peak in the inner region, while the same pattern was detected in only 10% of the glioblastoma cases. The correlation with the histopathological consequences showed that a high Cho signal is suggestive of neoplasm. Lipid signal in the non-enhanced central region was correlated to necrosis. Lac signals were often found in glioblastoma, abscess, and sometimes metastasis, presumably reflecting the anaerobic glycolysis by the living cells in the ring-like enhanced rim. It was suggested that single-voxel proton MRS can be applied as a valuable technique for providing suitable data of differentiating ring-like enhanced lesions which cannot be detected properly by only applying improved magnetic resonance images [25].

The combination of MRS and perfusion-weighted imaging might develop assessment and evaluation of brain lesions [30]. The efficiency of perfusion and MRS in analysis and characterization of brain tumors was reported. Distribution of tumor territory in the brain site has significant relation with age. Astrocytomas were reported in 58 (45.3%) cases; gliomatosis cerebri, glioblastoma multiforme (GBM), and oligodendroglioma were in 44 (34.4%) cases; and the lymphoma and meningioma were detected in 2 (1.6%) and 8 (6.3%) cases, respectively, where the metastases constitute 3 (2.3%). Significant results have been reported between the perfusion findings and the MRS values regarding Cho/NAA and Cho/Cr. Astrocytomas demonstrated a relative decrease in NAA and Cr, and Cho comparing with the lymphoma. The spectra of metastases are similar to those of meningioma, gliomatosis cerebri, and ependymal tumors, with low NAA, low Cr, and high Cho levels. The difference was reported meaningful in the NAA values at various brain lesions with no significant reduction or increasing in Cho and Cr. Cho/Cr had major impact in differentiation of lymphoma from other lesions at p value = 0.004, where the other factors including Cho/NAA, NAA/Cr, Lac, and lipid showed no major relations. By combining both MRS and perfusion-MRI, the diagnosis of lesions was improved with value of 0.94 ± 0.89 for NAA and 1.83 ± 1.22 for Cho/NAA. Perfusion-MRI and MRS are beneficial for providing the differential diagnosis between brain metastases and brain tumors. Both have significant role in differentiation and diagnosis of brain tumors [30].

2.5 Gliomas and MRS

Gliomas are the most common shape of central nervous system neoplasm which come from glial cells, and are regular in all primary brain tumors [1]. The efficacy of 1H MRS in preoperative quantitative assessment of intracranial gliomas was evaluated [1, 31–33]. MRS has been suggested as an alternative modality for grading of brain tumors [34]. For a dependable MRS technique, spectroscopic localization approaches and data acquisition should be appropriately controlled [35]. Another critical parameter which can largely influence the spectrum is the TE. At short TE, it is possible to detect more metabolites. However, there are several disadvantages, including the distortion of the spectra baseline under the effects of eddy current, water contamination, and the overlapped LP and Lac peaks, resulting in higher shimming demands. On the contrary, intermediate TE MRS may be selected to distinguish the metabolites of longer relaxation times with little or no contamination of residual water, LP, or fat tissue and thus without baseline distortions. Limited investigations are focused on the influences of both short and intermediate TE MRS for tumor grading [36–38]. In order to evaluate the efficacy of MRS in grading of primary brain tumors, MRS was performed in 22 patients with primary brain tumors. Metabolite ratios of Cho/NAA, Cho/Cr, Cho + Cr/NAA, LP and Lac/Cr were evaluated and analyzed at short and intermediate echo times. Additionally, ratio of mI/Cr was analyzed at short echo time. On the basis of histopathology, tumors were subdivided into low grades and high grade. Receiver operating characteristic evaluation of metabolite ratios was achieved to find cutoff values between high- and low-grade tumors. The resulting sensitivity, specificity, and accuracy were assessed. Consequently, at intermediate echo time, Cho/NAA, Cho + Cr/NAA, and Cho/Cr were considerably higher in high-grade tumors than in low-grade tumor. At short echo time, Cho/Cr and Lac/Cr ratios were meaningfully higher in high-grade tumors than in low-grade tumor. The diagnostic accuracy of metabolite ratios at intermediate echo time was 86% while at short echo time the diagnostic accuracy was 75%. The combination of both echo times showed a diagnostic accuracy of 88%. Cho/NAA, Cho + Cr/NAA, and Cho/Cr are dependable in evaluating the grade of tumors. Lac/Cr is significantly associated with high-grade tumors. The combination of both short and intermediate echo times offers better accuracy, in grading of brain neoplasm, compared to that when applying each echo time alone [39].

Two-dimensional 1-H MRSI was applied for determining an outstanding classification of patients via a multivariate pattern recognition assessment of peaks corresponding to Cho, Cr, NAA, Lac, lipid, and alanine [40]. From looking at the metabolite levels in each class, it was well-defined that meningiomas were exclusively differentiated as they were the only lesions which had alanine. Grade 2 gliomas tended to have low Lac and lipid, some NAA, and some Cr. Grade 3 gliomas tended to have low Lac and lipid, less NAA and Cr, with higher Cho. Grade 4 gliomas tended toward high Lac and lipid, with very low NAA. Another possible important clinical role for 1-H MRSI is the capability of making an early assessment of whether a lesion has responded to treatment. If this were achievable, it can permit

tailoring therapy to each individual patient and moderating an unsuccessful treatment approach before the lesion shows a large increase in volume. It can also be possible to avoid giving unnecessary treatment in the case which acceleration in enhancing volume is attributable to generation of treatment-induced necrosis as opposed to recurrent or residual tumor. For 1-H MRSI to be involved in the clinical managing of the patient in this manner, it is crucial to map out both the temporal and spatial distribution of metabolite alterations in response to the therapy of interest. This involves the application of three-dimensional 1-H MRSI, and is most simply obtained for the case of focal treatments such as surgery or radiation [41]. Registration of the MR images and 1-H MRSI findings are critical for correlating data from such sequential analyses [42].

2.6 Single-Voxel and Multi-voxel MRS

Single-voxel proton MRS was applied for analyzing the metabolic signatures of brain tumors [32, 43, 44]. There is robust indication for a decrease in NAA and acceleration in Cho-containing compounds in tumor compared with normal brain parenchyma [28, 45]. Additionally, typically for some metastatic lesions and for high-grade gliomas, there are resonances corresponding to Lac or LP [44, 46]. Early investigations regarding the potential for single-voxel MRS in tumor grading offered different consequences with a large variability in information quality between institutions [47]. With the presentation of automated packages for performing single-voxel proton MRI on clinical scanners, the quality and reproducibility of the information were developed. Multivariate statistical evaluation procedures were applied for detecting patterns which explain exact tumor types and grades [48, 49]. Additionally, researches have showed the acquisition of spectra with both short and long echo times, and consequently levels of mI, glutamine, and glutamate can be involved in the assessment and provide the potential for better discrimination between various types of lesions [40, 50]. While single-voxel proton MRS is a relatively fast approach for obtaining information and indications about the metabolism in a 4–8-cm^3 region within the lesion, it does not address spatial heterogeneity and is not able to contribute in defining the spatial extent of the lesion. These factors are mainly crucial for planning focal treatments such as radiation and surgical resection and for following reaction to treatment. For representing these subjects, it is vital to consider multi-voxel proton MRSI (1-H) [32].

One of the best analytical approaches for generalizing single-voxel MRS is to select a larger volume of interest and then apply phase encoding to gain localization to a one-, two-, or three-dimensional array of voxels [51]. Multi-voxel MRS offers high spatial coverage and may be more valuable than single-voxel approaches for gaining a metabolic map of a large size of tumors [32]. PRESS and stimulated echo acquisition mode (STEAM) are the two most usual techniques applied for volume selection, with PRESS being preferred when the TE allows due to its intrinsically higher signal to noise ratio [52, 53]. Two-dimensional or three-dimensional array of spectra demonstrated some benefits, such as observation of heterogeneity within the

lesion and examination of surrounding tissue that may appear normal on MRI. This offers a reference for comparing metabolite levels in the tumor and permits to distinguish regions of abnormal metabolism outside the morphological lesion [51, 52]. For treatment planning and long-term follow-up, it is crucial to analyze tumor progression, and it is very critical to obtain three-dimensional coverage of a large volume of interest [54]. The normal brain has NAA which is about twice the intensity of Cho and Cr. Because of the nominal voxel size for a volume head coil at 1.5 T is 1 cm^3, individual voxels may consist of a mixture of tumor, necrosis, and normal brain tissue [51].

While it is possible to gain three-dimensional 1-H MRSI information with chemical shift selective water suppression and conventional volume selection radiofrequency pulses, there are numerous conditions where the water and lipid suppression are insufficient and compromise the quality of the data achieved. This is particularly true for patients who have had surgical resection and can be a severe problem for patients treated by brachytherapy using permanent radioactive seeds. For improving the quality of water suppression, it is possible to implement alternative radiofrequency pulses which are capable of offering improved spatial and frequency selection [55]. Another important technique for gaining full coverage of the lesion and for sharpening the edges of the selected volume has been the implementation of very spatially selective saturation bands. These have a very sharp transition band and can be applied parallel to the edges of the selective volume to make it more cubic in shape or at an oblique orientation to conform the volume to the anatomy [56].

Other approaches for gaining volumetric coverage of the lesion are to apply multislice and multiple TE approaches for offering spatial localization in a time effective fashion [57]. In this case, lipid suppression has characteristically been offered by spatial and frequency selective pulses, inversion recovery, and spatial saturation pulses. These methods have the advantage of gaining complete in-plane coverage but may be restricted close to the sinuses or surgery cavities due to susceptibility artifacts. For multislice acquisitions, it is essential to have a slice gap to avoid crosstalk, and two acquisitions are needed to offer complete coverage of the lesion. Another approach for gaining volumetric coverage of the brain with a rational acquisition time is to apply echo planar spectroscopic imaging with either oscillating gradients in one spatial dimension or spiral sampling within a given plane [58]. This has been shown to offer good data quality for normal volunteers and patients with neurodegenerative diseases but may be restricted for patients with brain tumors once they have undergone surgical resection. Additional researches are focused on the application of a hybrid PRESS-echo planar spectroscopic imaging technique with spatially selective saturation bands which allow greater k-space coverage but completely remove signals from regions that are likely to cause susceptibility artifacts.

The reconstruction of 1-H MRSI information and assessment of the resulting arrays of spectra combines Fourier transforms and apodization (an optimal filtering technique) with automated techniques of spectral processing to offer information that can be elucidated by visual inspection or quantified to produce maps of the

spatial distribution of various metabolites. The first step is applying an apodization function to the k-space-free induction decays and making a Fourier transform to produce k-space spectra [59]. The next step is to reconstruct the spatial dependence of the information. For spiral or irregular k-space sampling, the technique is to first re-grid the k-space data onto a rectangular array. For conventional phase encoding, this step is not essential. To center the information at the most suitable spatial location, it is achievable to phase-weight the k-space array with the proper voxel shift. This is followed by applying any needed spatial apodization and then performing the spatial Fourier transformations. The resulting array of spectra will characteristically have spatially dependent frequency and phase errors that need to be adjusted, in addition to the baseline variations because of residual water [60].

Various techniques for assessing frequency, phase, and baseline corrections for spectral information were reported. Characteristics of the 1-H MRSI information which guide the choice of methodology are the larger number of spectra that are essential to be considered, and the need for whatever technique is chosen to be robust to differences in signal to noise and peak configurations corresponding to various tissue types. One approach is to acquire a separate dataset with no water suppression. This is time consuming, but the high signal to noise of the water resonance permits for an accurate assessment of frequency and phase factors. Provided that the data acquisition window is timed correctly, there should be no necessity for frequency-dependent phase correction, and the phase of the water in each voxel may be the same as for the other metabolites [61]. A substitute for obtaining a separate water reference dataset is to deliberately limit the water suppression to leave behind a relatively large water peak in the spectrum. The accuracy of this technique depends upon the quality of the volume selection and out of voxel suppression due to incomplete suppression of water outside the excited volume may cause spurious peaks with various frequency and phase to be folded into the selected volume. Another method is applying prior information of possible peak locations, obtaining estimates of corrections from metabolite peaks in voxels that have sufficient signal to noise, and then applying spatial interpolation to fill in corrections for voxels with low signal to noise [59, 61].

More quantitative assessment of the information needs the valuation of peak locations, heights, and areas. Earlier data of relative peak locations are beneficial for accomplishing this evaluation, and offer the basis for a robust technique which recognizes statistically major peaks, analyzes peak heights, and calculates peak areas by integration inside a defined range of frequencies for each metabolite. Additionally, more sophisticated fitting algorithms can be applied to spectra which have adequate signals to noise for the optimization routines to be reliable. The yield of the assessment is a number of spatial maps of metabolite parameters applied to distinguish regions of abnormal and normal metabolisms. Further corrections for spatial variations in intensity produced by the information acquisition processes may also be needed if comparing relative intensities of metabolites such as Cho, Cr, NAA, Lac, and lipid [59]. It was reported that the relative acceleration in Cho and decrease in NAA are crucial for identifying the spatial extent of the metabolic abnormality corresponding to active tumor [62].

One of the critical issues in 1-H MRSI for evaluating brain tumors is whether the spatial extent of the metabolic lesion is diverse from the Gd-enhancing region and hyperintensity on T2-weighted images [63]. If there is no distinction between these lesions, there might be no extra value for the 1-H MRSI information over and above conventional MR images. For metastases, the focus is on distinguishing between regions of tumor and enhancing necrosis. In practice, it is hard to get definitive evidence, because it is infrequent for such lesions to be biopsied. Assessment of a lesion corresponding to active tumor is characteristically based on whether it consequently gets larger on Gd-enhanced MRI. Another complication was described that the lesion gets larger, it generates central necrosis and, with a voxel size of 1–2 cm^3, it is complicated for obtaining spectra free from partial volume of tumor and necrosis. In a study of eighteen patients with brain metastases treated with gamma knife radiosurgery, it was described that all but two of the lesions had reduced NAA, in addition to a peak corresponding to Lac or lipid. Of the lesions followed after treatment, all lesions which demonstrated reductions in the volume of the enhancing lesion also exhibited decrease in Lac, lipid, and Cho peaks. There were also three lesions which demonstrated decreased metabolism but had stable or slightly increasing volume. Lesions that demonstrated accelerated enhancement on long-term follow-up also had a corresponding enhancement in Cho and Lac or lipid peaks [63]. The situation is more complex for patients with gliomas as there is the need to separate tumor from necrosis and to distinguish non-enhancing tumor from edema and treatment consequences. For evaluating the viability of applying 1-H MRSI in this way, the alterations in anatomical and metabolic lesions in patients with recently detected gliomas scanned before surgical resection should be concerned [64].

2.7 Conclusion

In conclusion, MRS is a diagnostic technique which provides a noninvasive vision into the biochemical profiles of the brain tumors, and it can provide extra diagnostic information for improvement of managing and treating patients with brain tumors. But it has low sensitivity and can only detect selected nuclei. This technique is a challenging method and can be used when spectral data will provide clinical data which is not gained by other imaging approaches. The technique is very sensitive to inhomogeneities in the magnetic field, requires careful manual regulation to ensure field uniformity, and is also very sensitive to motion. Due to the smaller voxel size and restrictions in the length of time of image acquisition, MRSI information is noisier than single-voxel MRS. In order to overcome the aforementioned limitations of MRS, clinical researchers have moved their investigations to higher field strengths to gain signal-to-noise ratio and to detect additional metabolites more reliably. Furthermore, they focused on faster MRSI sequences to overcome low spatial resolution and lengthy data acquisitions, and applied motion corrected MRS acquisitions. 1-H MRSI as a suitable technique for anatomical imaging in analysis of tumor types and grading, and in evaluation of the treatment outcomes. Though, the prognostic value of this method is yet under investigations, but it can offer useful

information regarding the selection of the appropriate treatment strategies for patients and for recognizing the mechanistic aspects of treatments (successful or unsuccessful therapies). This is especially crucial for evaluating treatments based upon the biological characteristics of tumors, where it is very important to distinguish whether the insufficiency of response was due to the agent being unable to approach the tumor or to the lesion being insensitive to that particular method. Potentials for refining the sensitivity and specificity of the 1-H MRSI data contain the application of shorter echo times and radiofrequency coils with better-qualified signal to noise and of magnets with advanced field strength.

References

1. Inoue T, Ogasawara K, Beppu T, Ogawa A, Kabasawa H. Diffusion tensor imaging for preoperative evaluation of tumor grade in gliomas. Clin Neurol Neurosurg. 2005;107:174–80.
2. Moriarty TM, Loeffler JS, Black PM, Shrieve DC, Wen PY, Fine HA, et al. Long term follow-up of patients treated with stereotactic radiosurgery for single or multiple brain metastases. In: Kondziolka D, editor. Radiosurgery, vol. 1. Basel, Switzerland: Karger; 1995. p. 83–91.
3. Leibel SA, Scott C, Loeffler J-S. Contemporary approaches to the treatment of malignant gliomas with radiation therapy. Semin Oncol. 1994;21:198–219.
4. Russell DS, Rubenstein LJ. Pathology of tumors of the nervous system. 5th ed. London: Lippincott, Williams and Wilkins; 1989.
5. Kleihues P, Burger PC, Scheithauer B-W. Histological typing of tumors of the central nervous system. 2nd ed. Berlin: Springer; 1993.
6. Dean BL, Drayer BP, Bird CR, Flom RA, Hodak JA, Coons SW, et al. Gliomas: classification with MR imaging. Radiology. 1990;174:411–5.
7. Earnest F, Kelly P, Scheithauer BW, Kall BA, Cascino TL, Ehman RL, et al. cerebral astrocytomas: histopathologic correlation of MR and CT contrast enhancement with stereotactic biopsy. Radiology. 1988;166:823–7.
8. Janus TJ, Kim EE, Tilbury R, Bruner JM, Yung W-K-A. Use of {18F} fluorodeoxyglucose positron emission tomography in patients with primary malignant brain tumors. Ann Neurol. 1993;33:540–8.
9. Glantz M, Hoffman JM, Coleman RE, Friedman AH, Hanson MW, Burger PC, et al. Jr. identification of early recurrence of primary central nervous system tumors by {18F} fluorodeoxyglucose positron emission tomography. Ann. Neuro. 1991;29:347–55.
10. G DC. Positron emission tomography using F-18-fluorodeoxyglucose in brain tumors. A powerful diagnostic and prognostic tool. Investig Radiol. 1986;22:360–71.
11. Pardo FS, Aronen HJ, Kennedy D, Moulton G, Paiva K, Okunieff P, et al. Functional cerebral imaging in the evaluation and radiotherapeutic treatment planning of patients with malignant gliomas. Int J Rad Oncol Biol Phys. 1994;30:663–9.
12. Wenz F, Rempp K, Brix G, Hess T, Weisser G, Debus J, et al. Radiation induced rCBV changes of low grade astrocytomas and normal brain tissue: International Society of Magnetic Resonance in Medicine 2nd annual meeting; 1994. p. 667.
13. Housni A, Boujraf S. Magnetic resonance spectroscopy in the diagnosis and follow-up of brain tumors. J Biomed Sci Eng. 2012;5:853–61.
14. Brandão LA, Castillo M. Adult brain tumors. Clinical applications of magnetic resonance spectroscopy. Magn Reson Imaging Clin N Am. 2016;24:781–809.
15. Soares DP, Law M. Magnetic resonance spectroscopy of the brain: review of metabolites and clinical applications. Clin Radiol. 2009;64:12–21.
16. Buonocore MH, Maddock R-J. Magnetic resonance spectroscopy of the brain: a review of physical principles and technical methods. Rev Neurosci. 2015;26:609–32.

17. Bottomley P-A. Spatial localization in NMR spectroscopy in vivo. Ann N Y Acad Sci. 1987;508:333–48.
18. Frahm J. Localized proton spectroscopy using stimulated echoes. J Magn Reson. 1987;72:502–8.
19. Horská A, Barker P-B. Imaging of brain tumors: MR spectroscopy and metabolic imaging. Neuroimaging Clin N Am. 2010;20:293–310.
20. Hourani R, Horská A, Albayram S, Brant LJ, Melhem E, Cohen KJ, et al. Proton magnetic resonance spectroscopic imaging to differentiate between nonneoplastic lesions and brain tumors in children. J Magn Reson Imaging. 2006;23:99–107.
21. Barker P-B. N-acetyl aspartate--a neuronal marker? Ann Neurol. 2001;49:423–4.
22. Howe FA, Barton SJ, Cudlip SA, Stubbs M, Saunders DE, Murphy M, et al. Metabolic profiles of human brain tumors using quantitative in vivo 1H magnetic resonance spectroscopy. Magn Reson Med. 2003;49:223–32.
23. Lai PH, Ho JT, Chen WL, Hsu SS, Wang JS, Pan HB, et al. Brain abscess and necrotic brain tumor: discrimination with proton MR spectroscopy and diffusion-weighted imaging. AJNR Am J Neuroradiol. 2002;23:1369–77.
24. Graves EE, Nelson SJ, Vigneron DB, Chin C, Verhey L, McDermott M, et al. A preliminary study of the prognostic value of proton magnetic resonance spectroscopic imaging in gammaknife radiosurgery of recurrent malignant gliomas. Neurosurgery. 2000;46:319–26.
25. Kimura T, Sako K, Gotoh T, Tanaka K, Tanaka T. In vivo single-voxel proton MR spectroscopy in brain lesions with ring-like enhancement. NMR Biomed. 2001;14:339–49.
26. Omer MAA, A-B-A E. Quantitative diagnosis of brain tumors using magnetic resonance spectroscopy relative to analogue images. Clin Med Imag Int J. 2018;1:27–30.
27. Ferraz-Filho JRL, Santana-Netto PV, Rocha-Filho JA, Sgnolf A, Mauad F, Sanches R-A. Application of magnetic resonance spectroscopy in the differentiation of high-grade brain neoplasm and inflammatory brain lesions. Arq Neuropsiquiatr. 2009;67:250–3.
28. Chang L, Mc Bride D, Miller BL, Cornford M, Booth RA, Buchthal SD, et al. Localized in vivo 1H magnetic resonance spectroscopy and in vitro analyses of heterogeneous brain tumors. J Neuroimaging. 1995;5:157–63.
29. Vogl TJ, Friebe CE, Balzer T, Mack MG, Steiner S, Schedel H, et al. Diagnosis of cerebral metastasis with standard dose gadobutrol versus a high dose protocol. Intraindividual evaluation of a phase II high dose study. Radiologe. 1995;35:508–16.
30. Ibrahim Hamed SA, Ayad C-E. Diagnostic value of MRI and MRS in characterization of brain tumors. IOSR J Dent Med Sci. 2017;16:72–80.
31. Oshiro S, Tsugu H, Komatsu F, Abe H, Onishi H, Ohmura T, et al. Quantitative assessment of gliomas by proton magnetic resonance spectroscopy. Anticancer Res. 2007;27:3757–63.
32. Nelson S-J. Multivoxel magnetic resonance spectroscopy of brain tumors. Mol Cancer Ther. 2003;2:497–507.
33. Sjøbakk TE, Lundgren S, Kristoffersen A, Singstad T, Svarliaunet AJ, Sonnewald U, et al. Clinical 1H magnetic resonance spectroscopy of brain metastases at 1.5T and 3T. Acta Radiol. 2006;47:501–8.
34. Al-Okaili RN, Krejza J, Woo JH, Wolf RL, O'Rourke DM, Judy KD, et al. Intraaxial brain masses: MR imaging-based diagnostic strategy–initial experience. Radiology. 2007;243:539–50.
35. Kousi E, Tsougos I, Tsolaki E, Fountas KN, Theodorou K, Fezoulidis I, et al. Spectroscopic evaluation of glioma grading at 3T: the combined role of short and long TE. Sci World J. 2012;2012:1.
36. Zou QG, Xu HB, Liu F, Guo W, Kong XC, Wu Y. In the assessment of supratentorial glioma grade: the combined role of multivoxel proton MR spectroscopy and diffusion tensor imaging. Clin Radiol. 2011;66:953–60.
37. Majós C, Julià-Sapé M, Alonso J, Serrallonga M, Aguilera C, Acebes JJ, et al. Brain tumor classification by proton MR spectroscopy: comparison of diagnostic accuracy at short and long TE. AJNR Am J Neuroradiol. 2004;25:1696–704.
38. Kim JH, Chang KH, Na DG, Song IC, Kwon BJ, Han MH, et al. 3T 1H-MR spectroscopy in grading of cerebral gliomas: comparison of short and intermediate echo time sequences. AJNR Am J Neuroradiol. 2006;27:1412–8.

39. Naser RKA, Hassan AAK, Shabana AM, Omar N-N. Role of magnetic resonance spectroscopy in grading of primary brain tumors. Egypt J Radiol Nucl Med. 2016;47:577–84.
40. Preul MC, Caramanos Z, Collins DL, Villemure JG, Leblanc R, Olivier A, et al. Accurate noninvasive diagnosis of human brain tumors by using proton magnetic resonance spectroscopy. Nat Med. 1996;2:323–5.
41. Graves EE, Pirzkall A, Nelson SJ, Verhey L, Larson D. Registration of magnetic resonance spectroscopic imaging to computed tomography for radiotherapy treatment planning. Med Phys. 2001;28:2489–96.
42. Zaccagna F, Grist JT, Deen SS, Woitek R, Lechermann LM, McLean MA, et al. Hyperpolarized carbon-13 magnetic resonance spectroscopic imaging: a clinical tool for studying tumour metabolism. Br J Radiol. 2018;91:20170688.
43. Heesters MAAM, Kamman RL, Mooyaart EL, Go K-G. Localized proton spectroscopy of in operable brain tumors. Response to radiation therapy. J Neuro-Oncol. 1993;17:27–35.
44. Usenius J-P, Vaino P, Hernesniemi J, Kauppinen R-A. Choline-containing compounds in human astrocytomas studied by 1H NMR spectroscopy in vivo and in vitro. J Neurochem. 1994;63:1538–43.
45. McBride DQ, Miller BL, Nikas DL, Buchthal S, Chang L, Chiang F, et al. Analysis of brain tumors using 1H magnetic resonance spectroscopy. Surg Neurol. 1995;44:137–44.
46. Usenius JP, Kauppinen RA, Vaino P, Hernesniemi JA, Vapalahti MP, Paljarvi LA, et al. Quantitative metabolite patterns of human brain tumors: detection by 1H NMR spectroscopy in vivo and in vitro. J Comput Assist Tomogr. 1994;18:705–13.
47. Negendank WG, Sauter R, Brown TR, Evelhoch JL, Falini A, Gotsis ED, et al. Proton magnetic resonance spectroscopy in patients with glial tumors: a multicenter trial. J Neurosurg. 1996;84:449–58.
48. Sijens PE, Kopp MV, Brunetti A, Wicklow K, Alfano B, Bachert P, et al. 1H MR spectroscopy in patients with metastatic brain tumors: a multicenter study. Magn Reson Med. 1995;33:818–26.
49. Shimizu H, Kumabe T, Tominaga T, Kayama T, Hara K, Ono Y, et al. Noninvasive evaluation of malignancy of brain tumors with proton MR spectroscopy. AJNR Am J Neuroradiol. 1996;17:737–47.
50. Somorjai RL, Dolenko B, Nikulin AK, Pizzi N, Scarth G, Zhilkin P, et al. Classification of 1H MR spectra of human brain neoplasms: the influence of preprocessing and computerized consensus diagnosis on classification accuracy. J Magn Reson Imaging. 1996;6:437–44.
51. Nelson SJ, Vigneron DB, Star-Lack J, Kurhanewicz J. High spatial resolution and speed in MRSI. NMR Biomed. 1997;10:411–22.
52. Dowling C, Bollen AW, Noworolski SM, McDermott MW, Barbaro NM, Day MR, et al. Preoperative proton MR spectroscopy in brain tumor patients with a mass lesion: correlation with resection specimen histology. AJNR. 2001;22:604–12.
53. Vigneron D, Bollen A, McDermott M, Wald L, Day M, MoyherNoworolski S, et al. Three-dimensional magnetic resonance spectroscopic imaging of histologically confirmed brain tumors. MRI. 2001;19:89–101.
54. Wald AA, Day MR, Nelson SJ, Moyher SE, Henry RG, Sneed PK, et al. Response of glioblastoma multiforme to brachytherapy detected by 3D proton magnetic resonance spectroscopic imaging. J Neurosurg. 1997;87:525–34.
55. Star-Lack J, Vigneron DB, Pauly J, Kurhanewicz J, Nelson S-J. Improved solvent suppression and increased spatial excitation bandwidths for 3-D PRESS CSI using phase-compensating spectral/spatial spin-echo pulses. J Magn Reson Imaging. 1997;7:745–57.
56. Tran T-KC, Vigneron DB, Sailasuta N, Tropp J, Le Roux P, Kurhanewicz J, et al. Very selective suppression pulses for clinical MRSI studies of brain and prostate cancer. Magn Reson Med. 2000;43:23–33.
57. Duyn JH, Gillen J, Sobering G, van Zijl PC, Moonen C-T. Multisection proton MR spectroscopic imaging of the brain. Radiology. 1993;188:277–82.
58. Posse S, Tedeschi G, Risinger R, Ogg R, Bihan DL. High speed 1H spectroscopic imaging in human brain by echo planar spatialspectral encoding. Magn Res Med. 1995;33:34–40.
59. Nelson S-J. The analysis of volume MRI and MR spectroscopic imaging data for the evaluation of patients with brain tumors. Magn Reson Med. 2001;46:228–39.

60. Posse S, DeCharli C, Bihan D-L. Three-dimensional echoplanar MR spectroscopic imaging at short echo times in the human brain. Radiology. 1994;192:733–8.
61. Provencher S-W. Estimation of metabolite concentrations from localized in vivo proton NMR spectra. Magn Reson Med. 1993;30:672–9.
62. McKnight TR, Noworolski SM, Vigneron D, Nelson S-J. An automated technique for the quantitative assessment of 3D-MRSI data from patients with glioma. J Mag Reson Imaging. 2001;13:167–77.
63. Nelson SJ, Vigneron DB, Dillon W-P. Serial evaluation of patients with brain tumors using volume MRI and 3D 1H MRSI. NMR Biomed. 1999;12:123–38.
64. Pirzkall A, McKnight TR, Graves EE, Carol MP, Sneed PK, Wara WW, et al. MR-spectroscopy guided target delineation for high-grade gliomas. Int J Radiat Oncol Biol Phys. 2001;50:915–28.

Diagnostic Imaging Techniques in Oral Diseases

3

Anurag Satpathy, Rajeev Ranjan, Subhashree Priyadarsini, Somesh Gupta, Piyush Mathur, and Monalisa Mishra

3.1 Introduction

Diagnosis is an art of chronological organization and critical evaluation of information obtained from patient's history, physical examination, and the results of radiographic and laboratory examinations so as to identify and understand the disease type and its etiology [1]. The diagnosis in the context of oral diseases essentially consists of analysis of case history and evaluation of diagnostic records complemented by the results of various investigations so as to confirm the presence of disease, identification of its type, and the cause of its initiation [2]. It should also provide an understanding of the disease process. A proper assessment and diagnosis is essential for a rational and successful treatment of any disease [3].

Diagnostic imaging also referred as medical imaging which encompasses the use of electromagnetic radiation and related techniques to obtain images of internal structures of the body for facilitating accurate diagnosis [4]. It assists prevention, early detection, diagnosis, and management of various conditions and diseases. With the advent of newer technologies, modern imaging techniques are much faster with enhanced accuracy. Its use has become inherent to almost all medical and dental specialties with increasing number of patients using it, thereby being termed as one of the fastest growing areas of medicine which has transformed current healthcare system [5].

Diagnostic oral imaging plays an integral role in the diagnosis and assessment of oral diseases and should be performed whenever there is any clinical evidence of a

A. Satpathy
Institute of Dental Sciences, Siksha 'O' Anusandhan University, Bhubaneswar, Odisha, India

R. Ranjan
Community Health Centre, Government of Jharkhand, Bero-Ranchi, Jharkhand, India

S. Priyadarsini · S. Gupta · P. Mathur · M. Mishra (✉)
Neural Developmental Biology Lab, Department of Life Science, NIT Rourkela, Rourkela, Rourkela, Odisha, India
e-mail: mishramo@nitrkl.ac.in

A. K. Shukla (ed.), *Medical Imaging Methods*,
https://doi.org/10.1007/978-981-13-9121-7_3

disease or its suspicion based on patients signs and symptoms. They provide significant information about the status of the oral tissues in health and disease in addition to a permanent record throughout the course of a condition and during its follow-up [6].

With the discovery of X-rays by Wilhelm Conrad Roentgen, in the year 1895, its earliest application in dentistry was made as the first dental radiograph in 1896 by Friedrich Otto Walkhoff [7]. Current advancement in the field of oral imaging has broadened its domain from simple radiographs to advanced imaging techniques. Some of the techniques include tomography (both computed tomography (CT) and cone beam computed tomography (CBCT)), ultrasonography (USG), and magnetic resonance imaging (MRI) [8, 9]. These recent advanced techniques have provided a considerable benefit in determining of extent of invasion, diagnosis, and prognosis of various oral diseases.

3.2 Diagnostic Imaging Techniques

Broadly, diagnostic imaging techniques used for maxillofacial region can be categorized under several types as: (1) Intraoral and Extraoral; (2) Analogue and Digital; (3) Ionizing and Nonionizing (4) Two-dimensional (2-D) and Three-dimensional (3-D) (5) Conventional and Digital

1. Intraoral
   (a) Periapical
   (b) Bitewing
   (c) Occlusal
      - True
      - Topographic
2. Extraoral
   (a) Panoramic
   (b) Lateral Oblique (Ramus, Body)
   (c) True Lateral (Cephalometric)
   (d) Postero-Anterior (PA)
   (e) Occipito-Mental (Water's view)
   (f) Submento vertex (SMV)

3.3 Conventional Film Imaging

3.3.1 Intraoral Radiographic Technique

3.3.1.1 Periapical Radiography

Commonly known as Intra Oral Peri Apical (IOPA) radiography uses two projection techniques [10]:

(a) Bisecting angle technique
(b) Paralleling technique

Bisecting angle technique: This technique uses the principle of geometric theorem, namely, Cieszynski's Rule Of Isometry [11]. According to this rule, "two triangles are equal if they have one common side and two equal angles." Dental radiographs apply this theorem for the following purposes: (1) to position the film/sensor as approximately as possible to the palatal/lingual aspect of teeth. In this position, the film's plane and the teeth's long axis make an angle with its top junction where both the film and the teeth get in touch with each other. When an imaginary plane intersects this angle, it forms two congruent angles with common side. A line mimicking the imaginary central X-ray completes the third side of the two triangles when it is directed through the apices of teeth at an angle at right angles to the intersecting plane. As a consequence both the triangles are precise triangles, consistent with parallel equal sides (Fig. 3.1).

Paralleling technique: The paralleling technique was first introduced by Edmund C Keller in 1896 and then later in 1920, used by Franklin W. McCormack in practical dental radiography. F.Gordon Fitzgerald, "the father of modern dental radiography" revived the interest in paralleling technique with the introduction of long cone paralleling technique in 1947. It is also known as right angle or else long cone technique. The basic principle is as follows: X-ray film can be placed parallely with the teeth's longest axis. In this orientation of the film, there is minimal geometric distortion. Distortion can further be reduced if the X-ray source is located at some distance from the teeth. In addition, due to a greater object distance from the source reduces the apparent focal spot. Resultant images are less magnified and with superior definition (Fig. 3.2).

IOPA reveals comprehensive information regarding the teeth as well as the surrounding periodontium. It is mainly used to assess the root and morphology of the root canal. It further checks the status of supporting alveolar bone health in diseases, dental caries, periapical infections, etc. IOPA is an integral part of evaluation of pre and post endodontic treatment to know the extent of dental caries, periapical pathologies, determination of working length, and obturation of root canal (Fig. 3.3).

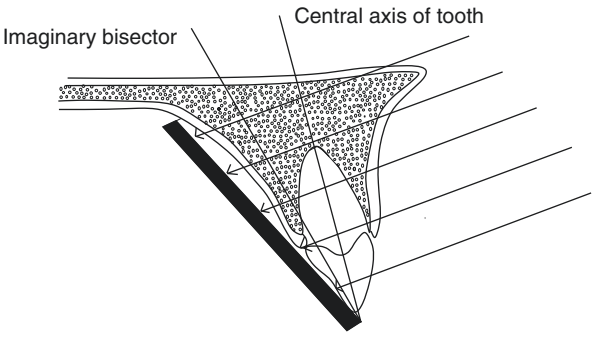

Fig. 3.1 Bisecting angle technique

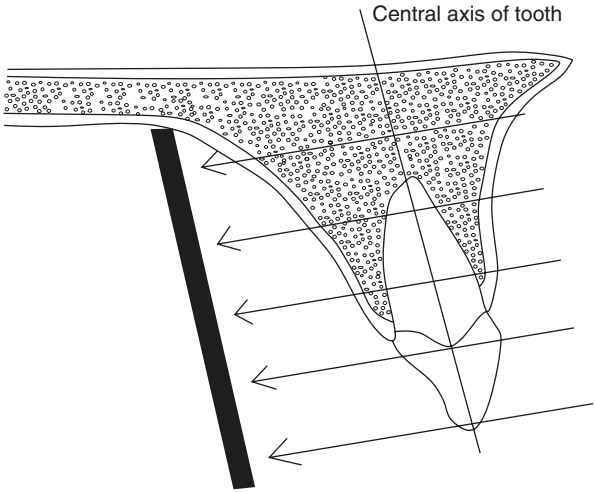

Fig. 3.2 Paralleling technique

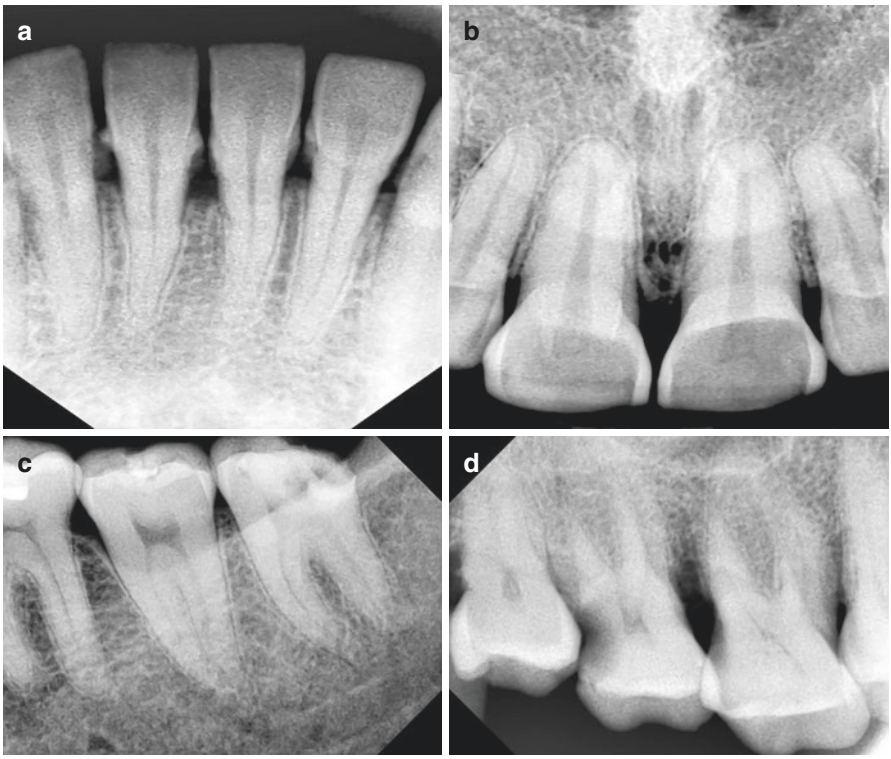

Fig. 3.3 (**a**) IOPA radiograph of Mandibular anterior teeth. (**b**) IOPA radiograph of Maxillary anterior teeth. (**c**) IOPA radiograph of Mandibular posterior teeth. (**d**) IOPA radiograph of Maxillary posterior teeth

Ideal requirements for IOPA radiographs:

1. It should represent the area of requirement.
2. The edges of the incisal and the surfaces of the occlusal upper and the lower teeth should not be more than 1–2 mm from the border of the film.
3. The apices of the teeth should be seen clearly with at least 2–3 mm of bone surrounding it.
4. The interproximal spaces between the teeth should be seen clearly without overlap.
5. The radiograph should have reasonable density and contrast.

Criteria for adequate angulation:

1. Tips of molar teeth cusps with minimal occlusal surfaces seen.
2. Enamel caps and pulp chambers seen distinctly.
3. Interproximal spaces must be open.
4. No overlap of proximal contact points unless teeth are out of line anatomically.

3.3.1.2 Bitewing Radiography [12, 13]

These are also known as interproximal radiographs. These include both the upper and lower teeth crowns and alveolar crest on the same radiographic image (Fig. 3.4). It gets its name from the tab ("wing") that the patient has to bite in order to grip the film/sensor in place. Bitewing radiographs are important for identifying interproximal caries at the primary stages of development. They also reveal secondary caries underneath restorations that may escape recognition in periapical radiographs. They provide a good perspective of alveolar bone through comparison with adjacent teeth. Because the angle of projection is directly through interproximal spaces, bitewing radiographs are also useful for detecting calculus deposits in interproximal

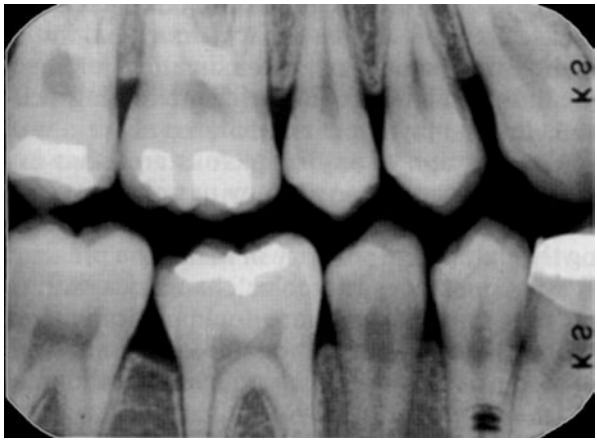

Fig. 3.4 Bitewing radiograph

areas. There are two types of bitewing projections—the horizontal bitewings and the vertical bitewings.

Horizontal Bitewing

For routine bitewing radiograph image, the long axis of the film/sensor is kept horizontal (side-to-side).

Vertical Bitewing

In patients with advanced periodontal involvement, the bone loss may be so extensive that it does not show up on the normal bitewing. For these patients, sometimes it is preferred to have the bitewing film/sensor positioned with the long axis placed vertically (up-and-down). This is called a vertical bitewing.

Ideal requirements of diagnostically useful bitewing radiographs:

1. Interproximal contact point from distal of cupid to mesial of third molar should be seen without overlap.
2. Intercrestal bone from distal of cuspid to mesial of third molar should be clearly seen.
3. Occlusal plane should be placed horizontal on the film and should be placed halfway on radiograph.
4. Radiograph should be of reasonable density and contrast.

3.3.1.3 Occlusal Radiography

It is used to image large areas of maxillary and mandibular jaws, the palate and floor of the mouth. It is also used as a supplementary radiograph along with other projections for localization (Fig. 3.5).

It is indicated for:

1. Salivary stones in submandibular gland duct.
2. Extent of lesions (cysts, tumors, malignancies).
3. Anatomical confines of maxillary sinus.

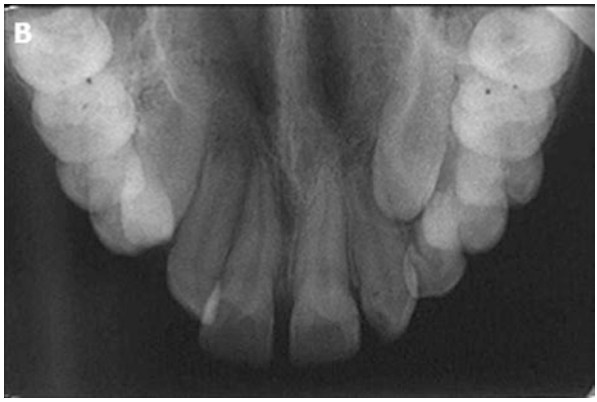

Fig. 3.5 Occlusal radiograph

4. Fractures of maxilla and mandible (nature, extent, location, and displacement).
5. Foreign objects in maxilla or mandible.
6. Cleft palate.
7. Residual or retained roots of extracted teeth.
8. Supernumerary, unerupted, or impacted teeth.

3.3.1.4 Types of Occlusal Projections

1. Maxillary:
   - *Cross sectional*
     The central ray projects with a vertical angle of +65° and a horizontal angle of 0°. The central ray is directed at the nose bridge just below the nasion. It is indicated for imaging hard palate, zygomatic process of maxilla, nasal septum, second molar to second molar teeth and nasolacrimal canals.
   - *Topographic (anterior)*
     Projection of the central ray through the tip of the nose with a vertical angulation of +45° and horizontal angulation of 0°. From maxillary right canine to maxillary left canine to canine, frontal flooring of the nasal fossa and anterior maxilla.
   - *Topographic (lateral)*
     Projection of the central ray to a point 2 cm below the lateral canthus of the eye with a vertical angulation of +60° and horizontal angulation of 0°. It is applied for the imaging of lateral incisor to contralateral third molar teeth, one fourth of the alveolar ridge of the maxilla with special reference to inferolateral aspect of antrum and maxillary tubercle. In this projection, the maxilla's zygomatic process and roots of molar superimpose with each other.
2. Mandibular:
   - *Cross sectional*
     Projection of principal ray is at the central through the floor of the mouth, approximately 3 cm below the chin, at 90° to the receptor. It is indicated for imaging the mandible's buccal cortical plate, lingual cortical plate of the mandible, teeth from mandibular second molar to second molar.
   - *Topographic (anterior)*
     The central ray is projected through the point of chin through a vertical angle of 10°, giving −45° angle to the receptor. It is indicated for imaging frontal part of the mandible, inferior cortical border of the mandible, and dentition from canine to canine.
   - *Topographic (lateral)*
     Projection of the central ray is at right angles to the center of radiographic plate, beneath the chin, approximately 3 cm posterior to chin, and 3 cm lateral to midline. It is indicated for imaging the buccal cortical plate of half of mandible, lingual cortical plate of half of mandible, lateral incisors to contralateral third molar.

3.3.2 Extraoral Radiographic Technique

Although intraoral techniques provided excellent imaging opportunities of the teeth, there was a need for unhindered view of the upper and lower jaws. The extraoral technique used most commonly in dentistry is the panoramic radiography. In 1933, Hisatugu Numata from Japan first exposed a panoramic radiograph; however, the film was placed lingually to tooth [14]. Yrjo Paatero of Finland is considered to be the "father of Panoramic Radiography" [15]. The commercial equipment for panoremic radiography was developed by Palomea under the supervision of Timo nieminen in 1960 and called it as "Orthopantomograp" [14], with its abbreviation OPG almost became synonym for panoramic radiographs. Demonstration of various anatomic structures with various extraoral radiographic projections is summarized in Table 3.1. Various types of extraoral projections are classified as follows:

(a) Panoramic
(b) Cephalometric
(c) Posteroanterior skull projection
(d) Water's view
(e) Submento vertex view or jug handle view

3.3.2.1 Panoramic Radiography

This technique allows us to produce a single tomograph of the maxillofacial structures including upper and lower arches along with their associated structures. This technique is a curvilinear modified version of conventional tomography. It follows the principle of the mutual movement of radiation source and an image receptor nearby a reference central point or plane, which is named as the image layer, and

Table 3.1 Demonstration of various anatomic structures with various extraoral radiographic projections (✓ indicates the relative usefulness of the image)

	Extraoral Projections			
Area of interest	Panoramic	Lateral Cephalometric	PA	Water's
Mandibular body	✓✓		✓	
Ramus	✓✓		✓	
Coronoid process	✓		✓	✓✓
Condylar neck			✓	✓
Posterior maxilla	✓✓			
Orbit			✓✓	✓✓
Zygoma	✓			✓✓
Nasal bone		✓✓		✓
Nasal cavity			✓✓	✓
Maxillary sinus	✓	✓		✓✓
Frontal sinus		✓✓	✓✓	✓
Sphenoid sinus	✓✓			

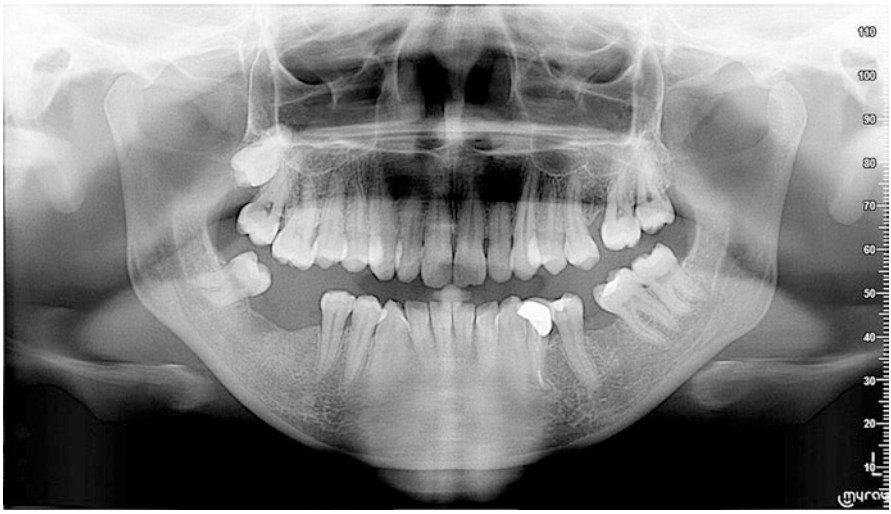

Fig. 3.6 Panoramic radiograph

it serves as the location for the object of interest. Due to the movement of reciprocating parts relative to the center of rotation, objects that are in front of the image layer or those behind it are not clearly captured (Fig. 3.6).

The advantages of panoramic images include [16]:
1. Wide-ranging analysis of maxillofacial osseous structures and teeth
2. Little radiation dosage to the patient
3. Convenience
4. Useful even in patients with restricted or no oral opening

Panoramic radiographs are very helpful in diagnostic problems requiring wider coverage of jaws. It is helpful in detecting extensive trauma, extensive diseases, suspected large lesions, and developmental anomalies [17].

The main disadvantage of panoramic radiography is its inability to demonstrate fine detail as in comparison to IOPA radiographs. Therefore, panoramic radiography has its limitations in identification of small carious lesions, integrity of marginal periodontium or periapical disease. Often there is an overlap of premolars. Also, unequal magnification and geometric distortion of images is a major limitation of panoramic radiography.

3.3.2.2 Cephalometric Radiography

Lateral cephalometric projections are frequently used in dentistry to assess the relationship among the skeletal and dental arrangements (Fig. 3.7). All cephalometric radiographs are made with a cephalostat which is meant to maintain constant relationship among the cranium, X-ray film, and the X-ray beam [18]. Lateral

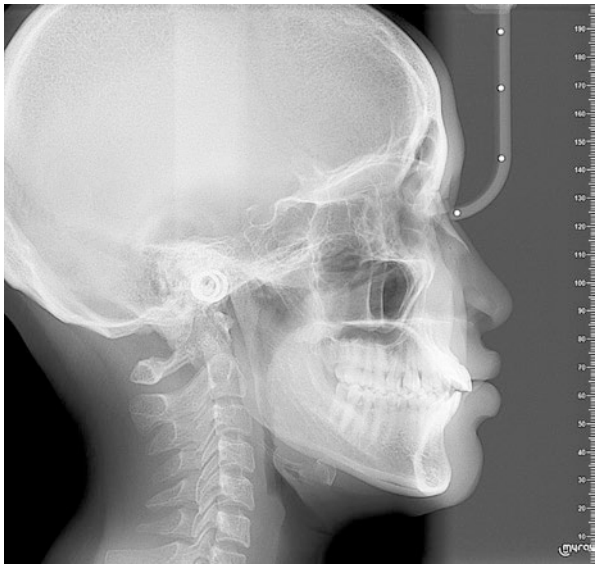

Fig. 3.7 Lateral cephalograph

cephalometric radiographs are of great value for comparison and monitoring of variations in progression and development of skeletal and dental arrangements prior, through, and post treatment [19].

3.3.2.3 Posteroanterior Skull Projection (PA Skull Projection)

PA skull projection is useful in detecting the oral diseases or trauma involving orbit, nasal cavity, and frontal sinus (Fig. 3.8). For making of this PA view, the receptor of the image is placed analogous to the coronal plane and at 90 degree angle to the mid-sagittal plane and cantho-meatal line in front of the patient [20]. The principal ray (central ray) is at right angles to the receptor of the image, intended from posterior to anterior, and parallely to patient's mid-sagittal plane, keeping the bridge of the nose at the center [21].

3.3.2.4 Occipito-mental View or Water's View

Occipito-mental view is most favorable to know the maxillary sinus diseases (Fig. 3.9). Change in radio-opacities in maxillary sinus determines extent and severity of maxillary sinus pathology [22]. It is moreover useful to know the extent and severity of pathology and trauma involving orbit, coronoid process, and zygoma. For Water's projection, image receptor is kept perpendicular to the mid-sagittal plane and in front of patient [23]. Cantho-meatal line makes 37 degree angulation with image receptor.

3.3.2.5 Submento Vertex View or Jug Handle View

Submento vertex view is also known as the base projection (Fig. 3.10) as the X-ray beam makes an entry on the head below the chin (in proximity to the mental tubercle) and comes out at the vertex of the skull. In this projection, X-ray beam is

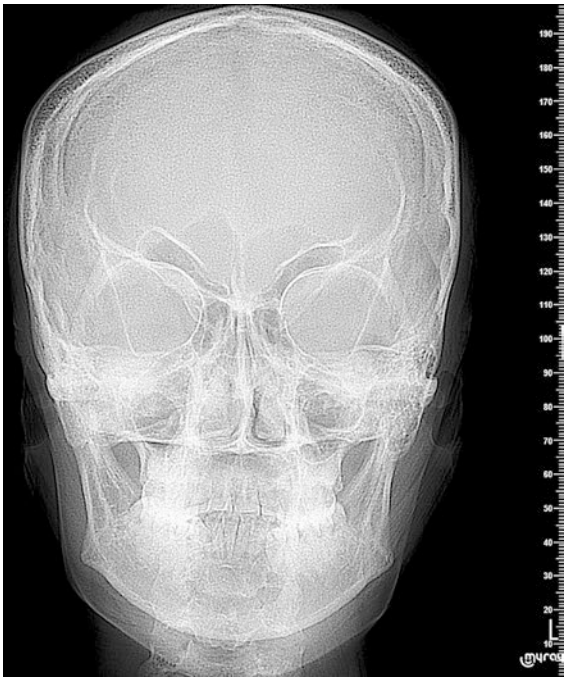

Fig. 3.8 PA Skeletal projection

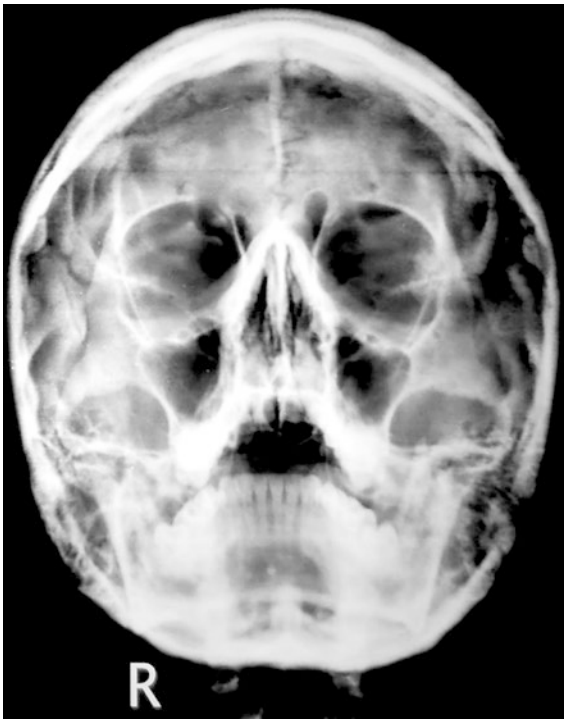

Fig. 3.9 Occipito-mental projection (Water's view)

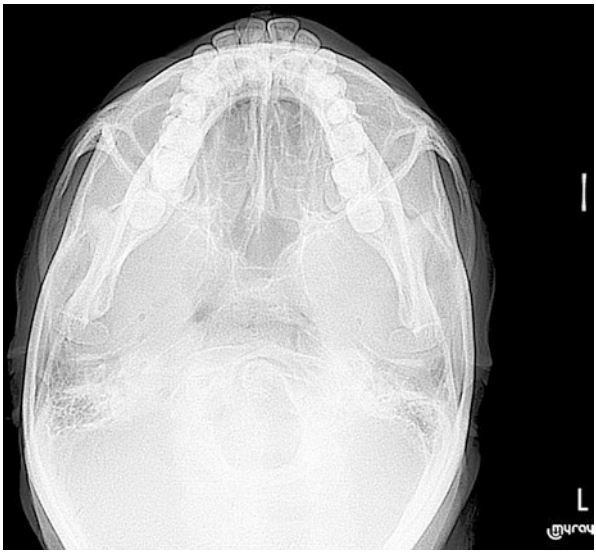

Fig. 3.10 Submento vertex view (jug handle View)

directed at right angles to the cantho-meatal line. When applied in combination with other projections, it makes it possible to directly visualize the base of the skull. Since in this view, the zygomatic arches appear like that of the handles of a jug, it is also known commonly as jug handle view [24].

3.3.3 Subtraction Radiography

Subtraction radiography requires comparison of standardized radiographs. A standardized radiographic image is procured prior to an occurrence of a structural alteration, like bone defect such as bone loss and is subsequently deducted from regular radiograph made later. The unchanged structures will get subtracted out and look as if as neutral gray, whereas bone damage appears dark gray and areas of bone gain appear light gray [25]. Deduction image once stored may be the contrast enhanced electronically to show the final image which is advantageous for disease detection. Often selective colors may be added, to different grey shaded areas for easy detection purpose [26].

A great improvement in this technique has been achieved with the amalgamation of the video, digital subtraction radiography and software technology. The light intensity transmitted through the radiograph is measured by a video camera and converted into gray level values. This digitized image is then demonstrated on the monitor as a positive image [27]. The ensuing radiographs appear on the screen as a negative image and are calibrated with the baseline image. Thus the discrepancy between the density of baseline image and consequent radiographs is revealed either darker (density loss) or brighter (density gain) [28].

Advantages of subtraction radiography [29]

- A high degree of correlation between changes in alveolar bone determined by subtraction radiography and attachment level changes in periodontal patients after therapy.
- Increased ability to detect small bony lesions in comparison to conventional radiographs from which the subtraction images are produced. Five percent of change in mineral density can be identified.
- Subtraction radiography has remarkable diagnostic potential in clinical practice due to the development of software for digitizing and image processing.

3.4 Digital Imaging

The introduction of digital imaging has brought about a revolution in the field of oral imaging. This has been possible due to innovation in the field of image acquirement technology and the improvement of advanced software for image management and analysis. Digital imaging has completely eliminated the messy chemical processing of precedent years. Notably, it has put an end to hazards from lead foil [30, 31]. Images can be now being electronically captured, stored, and transferred without any loss of detail in the image. In addition, there is a severe decline towards exposure of radiation, thus the absorbed dose is lowered. However, current digital image processors also have a number of limitations in comparison to the conventional film based technology. The cost of setup of a digital image acquisition system is comparatively more.

The word "digital" in the field of digital imaging concerns the format of the acquired image and its clarity. Digital images are expressed in numeric values and can be distinguished in two different ways: (1) Spatial distribution of various elements in the picture (pixels). (2) Different shading of gray of each pixel. Instead of silver halide grains, a large number of light sensitive elements are used to record the image data from X-ray shadow. Direct digital images are acquired using a chip like charge couple device (CCD) or complementary metal–oxide–semiconductor (CMOS). The CMOS sensors use an active pixel technology which diminishes the needed system power by a factor of 100 and eliminates the need for charge transfer [32, 33].

The phosphor plate system has a polyester base which is coated with a compound made up of europium-activated barium fluorohalide. The compound is in crystalline emulsion form [31]. A latent image is created by the incident X-ray photons [34]. Subsequently, a scanner reads the latent image information with a laser beam which is near-red wavelengths and produces a digital image as an output.

Fundamental difference between conventional and digital radiography is the fact in conventional radiographic image, the silver halide grains are randomly dispersed in emulsion, whereas electronic elements of a digital sensor are arranged in regular grid of rows and columns. The quantitative characteristics of the light sensitive element of the electronic sensor result in gray shades having a discrete value.

3.4.1 Charge Couple Device

The CCD was the first to be introduced in the field of dentistry in 1987. CCD employs a thin silicon wafer for the recording of image. Silicon crystals are produced as a picture element (pixel) matrix [33]. These systems use an intraoral sensor connected directly by cable to the computer.

Radiovisiography [35, 36] (RVG) is a widely used system in dentistry that utilizes CCD. RVG system possesses various components which includes a microcomputer, a sensor and a monitor. The sensor which receives the incident X-ray photons has a perceptive area which measures 275 × 182 mm. A digital panoramic image is displayed in Fig. 3.11.

Advantages
- Low radiation
- Instant image
- Image manipulation facilities

Disadvantages
- Small receptor size of most systems making it useful for single tooth imaging (useful in endodontics)
- Bulky sensor with cable
- Storage problem because of need for special archiving equipment

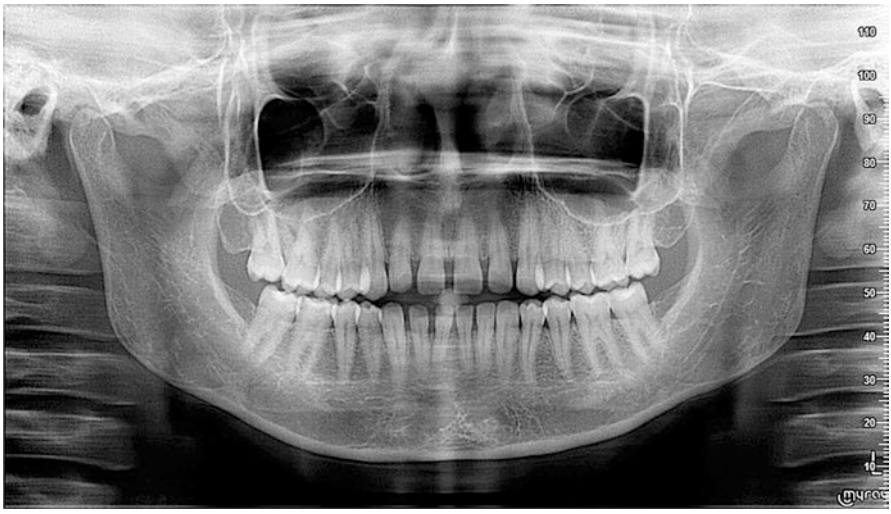

Fig. 3.11 Digital panoramic radiograph

3.4.2 Advanced Diagnostic Imaging

3.4.2.1 Computed Tomography (CT)

An innovative imaging technique was introduced by Godfrey Hounsfield in 1972, which he referred as computerized axial transverse scanning [37]. He claimed this technique is at least hundred times more sensitive than the conventional radiographic system. A CT image is actually a reconstructed digital image by a computer which accumulates and mathematically manipulates the transmission data obtained from multiple projections [38].

CT does provide good 3-D views; however, it is unable to show the fine structural details of sample thicker than 1–2 mm. Thus the slices of image are taken from various orientations. Later, the generated images of various orientations are reconstructed using a process known as multi-planar reformatting (MPR). The 3-D reconstruction allows clinicians to visualize the bony architecture, nerves, joints, sinuses, and other deeper anatomical structures completely and accurately in comparison to traditional flat radiographs.

CT generates axial images which are perpendicular to the elongated axis of patient by revolving an X-ray source. The source produces a fan-shaped beam of 360° around the patient which is captured by sensors and processed by computers. CT imaging is unique as it produces images of soft tissues, bone, and blood vessels all together in their anatomical orientation (Fig. 3.12) [39].

Computed tomography is highly favorable in determining extent and involvement of trauma of maxillofacial region and for assessing the extent of several types of infections, osteomyelitis, cysts, benign and malignant tumors. CT has a very high

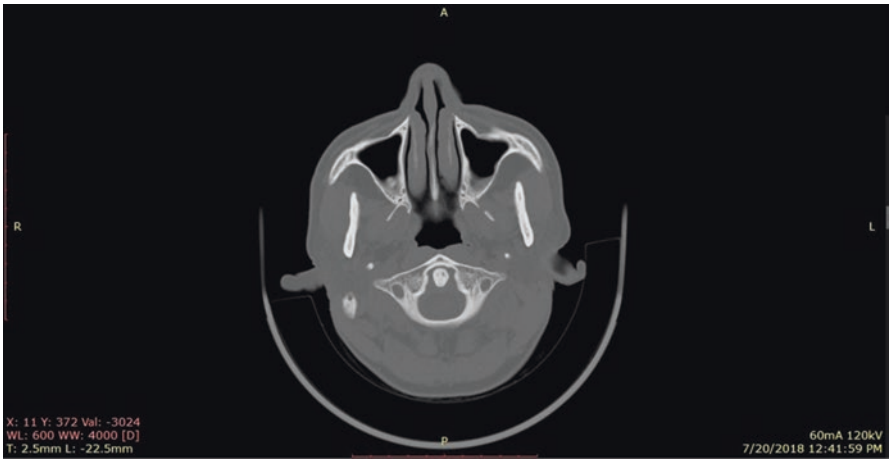

Fig. 3.12 Computed Tomography (CT) image

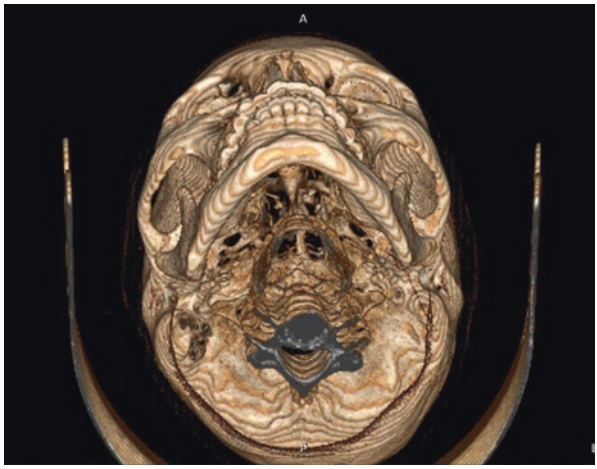

Fig. 3.13 3-D reconstruction from CT scan

ability to demonstrate any bony change. Because of this, CT is ideal modality in diagnosis of any bony pathology. CT has also been used in craniofacial and maxillofacial reconstructive surgery and in diagnosis and treatment of congenital and acquired craniofacial deformities. Also, there is minimal image distortion in the anterior and the posterior regions of the jaw. The 3-D construction of a CT scan is demonstrated in Fig. 3.13.

CBCT employs an X-ray beam which is cone shaped and it is centered on a detector (2-D). The machine rotates around the object and completes one rotation and takes one radiograph. Thus with several rotation it completes multiple 2-D images. These 2-D images are used to reconstruct 3-D images by using an algorithm [40]. One of the major advantages of CBCT is considerable reduction (3%–20%) in effective radiation dose exposure. The radiation dose also depends upon the make and design of CBCT and the area needed to be scanned [41].

A CBCT technology is efficient as it significantly enhances the utilization of X-ray and consumes very lesser amount of electrical energy as compared to fan-beam technology. Furthermore, the X-ray tubes used of CBCT are cheaper than conventional CT. The generated images have homogenous pixels size around 0.125 mm. CBCT also provides a more accurate spatial resolution of maxillofacial structures which helps in better understanding and localization.

CBCT has found multiple and wide application in dentistry. Enhanced resolution of CBCT helps to detect several maxillofacial pathologies such as infections, traumatic injuries, cysts, tumors and the developmental anomalies [42]. Another very important area where it has been extensively used is the detection of TMJ pathology and treatment planning for dental implants [43].

The quality and accuracy of CBCT is compromised due to scattered radiation. Often the beam creates hardening artifacts which are caused due to increased dense structures like enamel and radio-opaque materials [44]. Due to scattering of radiation, the contrast is reduced and decreases the quality of soft tissues images [45].

Thus, CBCT is primarily employed for imaging of hard tissues. In CBCT images, the Hounsfield Units get distorted. Thus these images are unsuitable for estimation of bone density [46]. Because of distortion of Hounsfield Units, the scan times for CBCT are usually lengthy and the patient stays completely still during the process of imaging (Fig. 3.14).

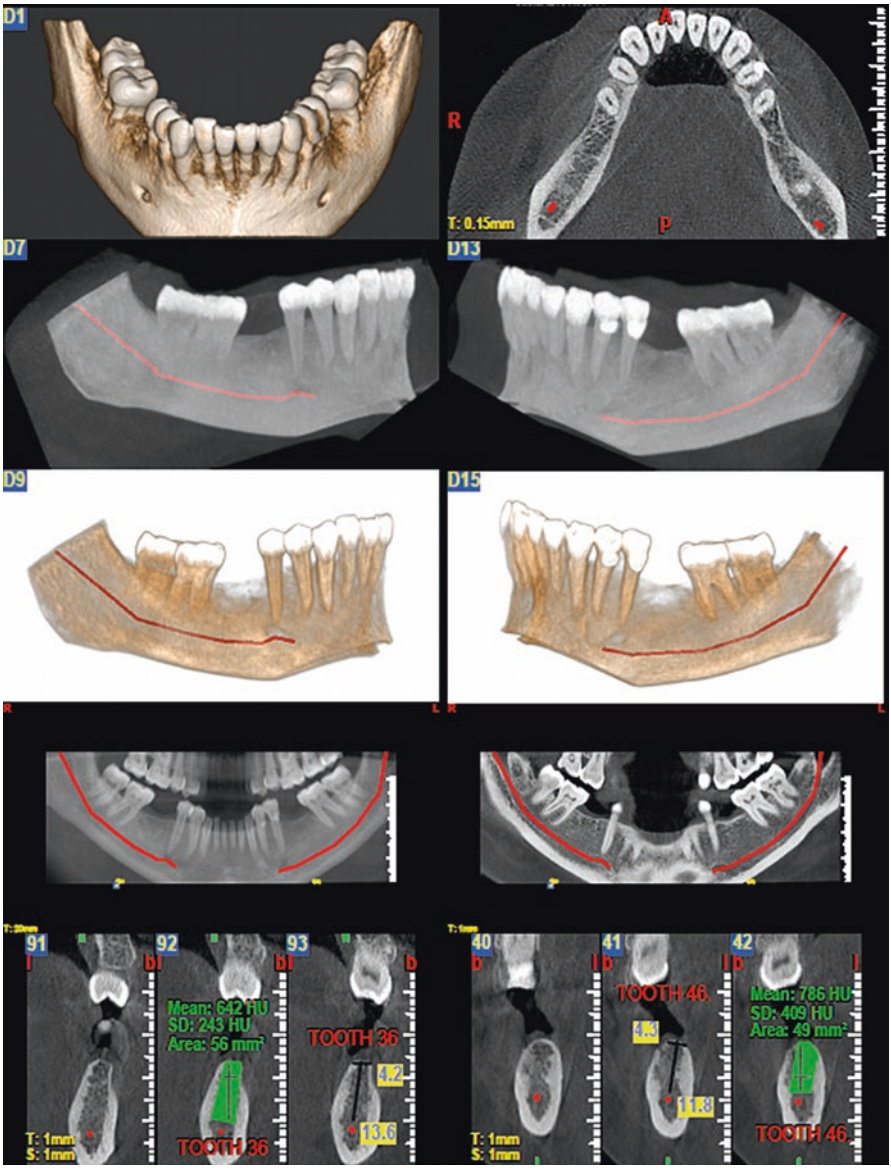

Fig. 3.14 Cone Beam Computed Tomography (CBCT) image with 3-D reconstruction

3.4.2.2 Magnetic Resonance Imaging (MRI)

Peter Mansfield devised mathematical algorithm for the MRI signals for image reconstruction [47]. MRI was introduced for medical use around 1980. In 2003, the Nobel Prize in Physiology or Medicine was awarded to Lauterbur and Mansfield.

It is noninvasive in nature. It detects the deeper anatomical structures and differentiates between soft and hard tissues of the body.

MRI uses a nonionizing radio-frequency electromagnetic radiation in the propinquity of regulated magnetic fields. MRI is used to obtain high resolution cross-sectional images of the body [48]. To make a MRI image, patient is housed in a large magnet. On application of the magnetic field, the nuclei present within the atoms of the body, particularly hydrogen atom get aligned with the magnetic field. A radio-frequency (RF) pulse is then directed into the patient's body, which leads to absorption of energy (resonance) by some hydrogen nuclei. On stoppage of RF pulse, there is a release of stored energy and this is detected as a signal by the scanner. Signals obtained are utilized to construct the magnetic resonance image. Thus, a MRI image is basically an atlas of the localization of hydrogen atom within the body.

MRI is relatively safer as it is noninvasive and uses nonionizing radiation. It generates high-quality soft tissue images with good resolution in any imaging plane. However, MRI equipment is highly expensive and requires long scan times. Presence of metals in the imaging field should be avoided, considering the fact that, metals in the imaging field are a source of distortion of the image and they may move in the strong magnetic field leading to serious injury to the patient [49].

One of the primary applications of MRI in dentistry is investigation of pathologies in salivary glands, temporomandibular joints, and staging of tumors. Because of its ability to provide excellent soft tissue contrast, it proves to be ideal to detect the internal derangement of temporomandibular joints (TMJ) [50, 51]. Further, it is helpful in detection of joint effusions, inflammation of synovial membrane (synovitis), bone marrow erosions, and edema. MRI can detect tumors and odontogenic cysts better than CT scan. Soft tissue diseases in tongue, salivary gland, cheek, neoplasia, and defect in lymph nodes can be detected by this method (Fig. 3.15).

MRI can precisely identify between solid and cystic lesions. It is also a reliable modality in imaging sialodochitis and sialectasia [52, 53]. Accurate tooth surface digitization and precision has been reported with MRI while imaging dental restorations, root resorption, and alveolar bone loss in cases undergoing orthodontic treatment [54, 55]. Inflammation and wound healing of periodontal tissues can be detected from MRI images [56–58].

Besides its advantages MRI is unsafe for patients with pacemaker implantation, ferrous foreign bodies in the eye, artificial valves within the heart, cerebral aneurysm clips, and implantable defibrillator. The presence of a strong magnetic field may cause the movement of metals which attracted towards the magnetic field since the imaging technique uses a strong magnet [59].

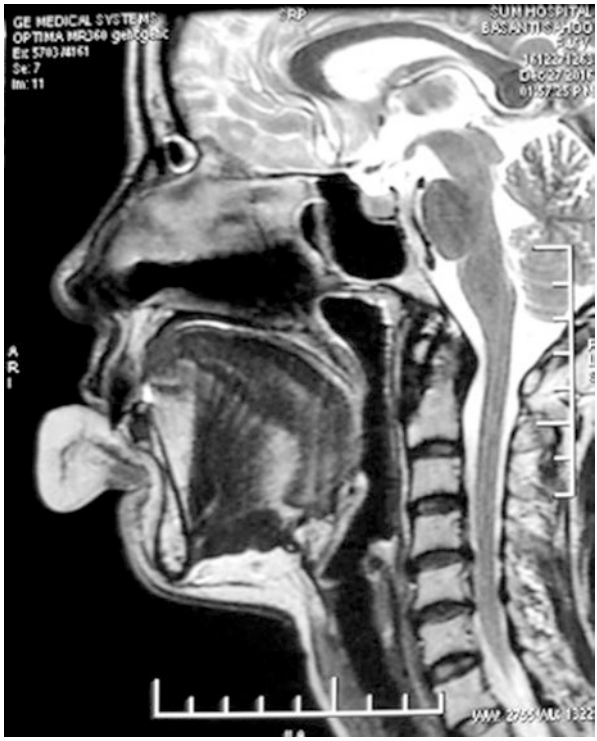

Fig. 3.15 MRI image of maxillofacial region

3.4.2.3 Ultrasonography

Ultrasonography (USG) as an imaging modality uses noninvasive and nonionizing radiation. It is cheaper, safer, and a painless imaging method in comparison to X-rays. USG can be utilized for investigation of hard and soft tissues. Baum et al. [60] in 1963 was the first to provide USG images for diagnostic relevance in the field of dentistry. He used a transducer of 15 MHz to image the internal structures of the teeth. However, the resultant radio-frequency signal was not favorable and thus produced poor quality images.

USG worked on the principle of echoes of sound waves. It utilizes a frequency beyond the range of human hearing (1–20 kHz). Thus it is applied to the interface of human tissues having dissimilar auditory properties. Due to its safety, it proves to be an essential diagnostic modality for patients with metallic prostheses where MRI does not give good result, cardiac pacemaker, and claustrophobia [61]. Further, advantage of USG is that it is safe if used repeatedly as it is nonionizing. Maxillofacial fractures involving the anterior wall of the frontal sinus, zygomatic arch and orbital margin and be identified using USG [62]. A lesion in the parotid gland (both solid and cystic) can be identified using USG (Fig. 3.16). It is commonly used to identify sialoliths in parotid, submandibular, and sublingual salivary glands [63, 64]. Determination of pathological nature of periapical lesions (granuloma vs cysts) is also assessed using USG. USG has been a boon in

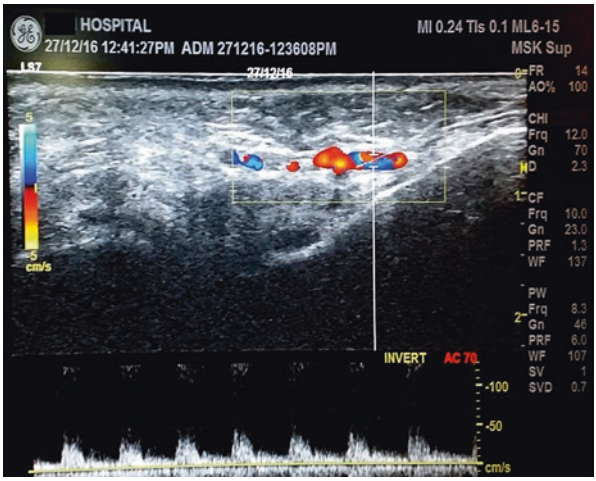

Fig. 3.16 Doppler ultrasound. Transverse view of buccal mucosa

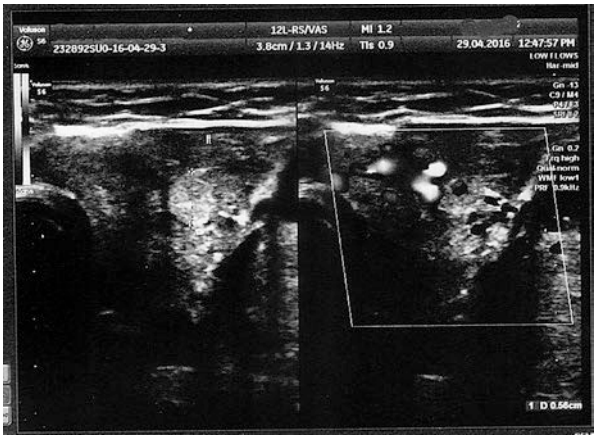

Fig. 3.17 Ultrasound: Thyroid gland

specialized investigations like diagnosis of cervical lymph nodes metastasis, guided fine-needle aspiration, and measurement of thickness in carcinoma of the tongue (Fig. 3.17) [65, 66].

Ability of USG to measure soft tissue thickness is of great help to clinicians in surgical and implant related orthodontics. Also, it is helpful in placement of dental implants in a flapless procedure which requires precise measurement of soft tissue thickness. Sometimes, when the thick connective tissue is grown over the implants, then such implants are difficult to image. USG can precisely locate such submerged implants either for surgery or prosthodontic rehabilitation [67].

3.4.2.4 Nuclear Medicine Imaging

Nuclear medicine technique is based on essential use of radiopharmaceuticals, comprising of administration of a minute dose of a chemical labeled with a very minute amount of a radioactive isotope (radionuclide) [68]. These chemicals are

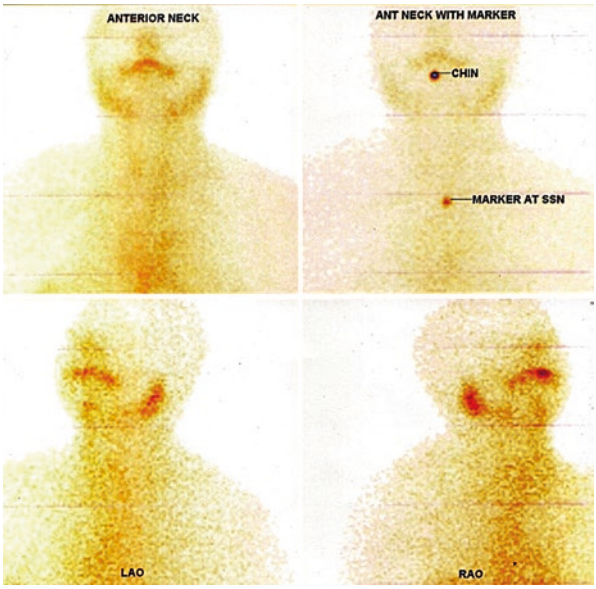

Fig. 3.18 Nuclear medicine scan: Thyroid

specifically selected based on their capacity to exhibit a normal or altered function of an organ, tissue, or organ system for which they are specifically chosen.

A radiographer performs the nuclear medicine scans. This branch of nuclear medicine is also referred to as endoradiology. It is in contrast to that of X-ray procedure as the radiation emitted from within the body is captured rather than being directed from outside. Capturing of the emitted radiation by radionuclide as it moves through the body is done through external detectors and is then processed used to generate an image (Figs. 3.18 and 3.19) [68]. Diagnosis of the condition is based on the gathered information on the way the body is known to respond to radionuclides in health and diseased state.

The fundamental difference between radionuclide scans and other imaging modalities is that these imaging techniques reveal physiology of the tissues or organ system being investigated, while conventional radiological imaging systems such as CT and MRI only show the anatomy or structure [69].

Discovered in 1937 by Carlo Perrier and Emilio Segrè, Technetium-99 metastable (^{99m} Tc) is the widely used radionuclide in scintigraphy (radionuclide imaging). Further, in 1971, Subramanian and McAfee labeled technetium to methylene diphosphonate (MDP), which is currently the most common method for the imaging of bone in nuclear medicine [70, 71]. Thyroid was one of the first organs to be investigated by radionuclide studies. Earlier, Iodine-131 was used (I-131) to diagnose and then treat thyroid disease.

3.4.2.5 Nuclear Imaging Methods [72]

(a) Static
(b) Whole body
(c) Dynamic

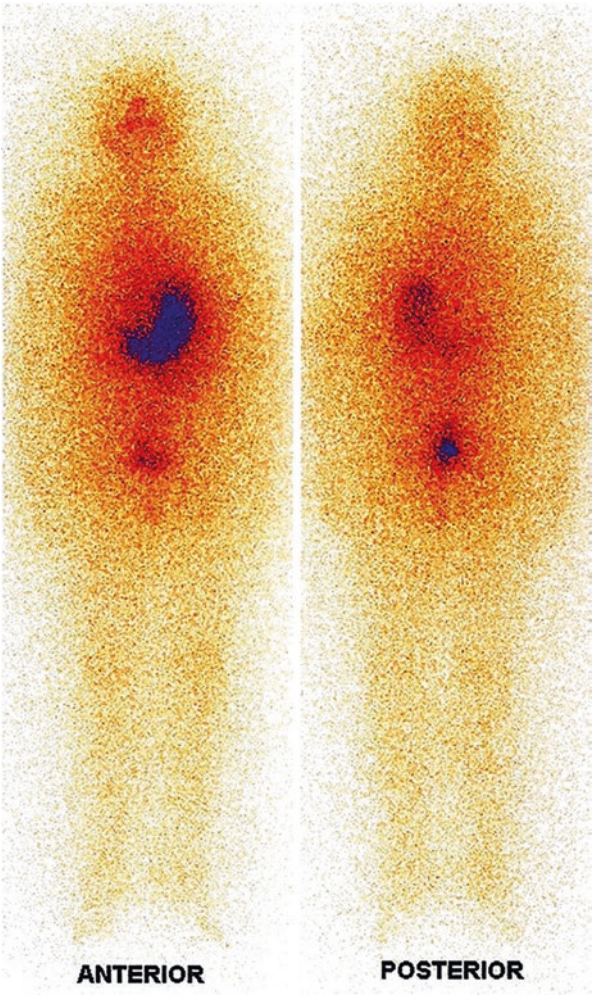

Fig. 3.19 Radionuclide scan: Whole-body scan

(d) Single photon emission computed tomography (SPECT)
(e) Positron emission tomography (PET)

- *Static:* It is a "snapshot" of the circulation of radionuclide within the body. It is commonly used for scanning thyroid, lungs, and spot bone.
- *Whole-Body Imaging:* A moving detector system is used to capture the radiation and produce an image of a large body section. The gamma camera collects the signal when it passes over the body. It is used for whole-body bone scans, tumor, or abscess imaging.
- *Dynamic Imaging:* It demonstrates the circulation of a particular radionuclide during a precise period. Also termed as "Flow" study of specific structure. It is commonly used to calculate the blood flow to tissues. It is used for time-lapse images of parotid gland studies [73].

- *Single photon emission computed tomography (SPECT*): It produces an image similar to CT and MRI in that a software program creates thin slices through a specific organ or tissue. It is used for brain, cardiac perfusion, hepato-biliary, and osseous studies.
- *Positron emission tomography (PET):* Positron of specific radionuclides is used to produce practical images of the body [74]. PET is unique in that its images are of perfusion and/or metabolic activities at the level of cell in comparison to conventional imaging by radiography, MRI, or even SPECT [75].

3.4.2.6 Patient Preparation and Safety

Preparation for nuclear imaging procedures is minimal. Most scans do not require any special prep. However, for a few procedures the patient will require to be *nil* per os (NPO) which means nothing through the mouth. Patients are usually in their own apparel. They are asked to remove all ornaments and metal objects as metal can mimic pathologic conditions [76].

After receiving the radiopharmaceutical patients are required to report back for re-scanning in a few hours. The waiting period between radionuclide dose administration and scanning differs with each study. Some radionuclides require the patients to remain in isolation after administration, or may require special disposal of urine products.

Among several advantages, there are some disadvantages of nuclear medicine imaging [77]

1. Accumulation of radiotracers in the lesion results in its high contrast against the surrounding tissues. However, spatial resolution is poor compared to radiography or MRI.
2. The scans are expensive since its cost depends on the cost of radiopharmaceuticals used and the capacity of the scanner.
3. Patients and people in vicinity are exposed to ionizing radiation administered to the bodies.
4. The radiation exposures in nuclear medicine scans differ from radiography. Radiography involves radiation from source located outside the patient's body resulting in a limited radiation exposure to the body. However, a radionuclide is administered into the patient's body and it causes whole body exposure in a non-uniform manner. This is determined by the bio-distribution and clearance kinetics of that radionuclide.
5. Additional special precautions are required for patient and staff safety.

The scope of utilization of nuclear medicine imaging in dentistry is vast but poorly understood. Use of the diagnostic isotopes may be to study the maxillofacial and neck tumors and salivary gland diseases. Even before the morphological changes are seen in the tissues, the abnormalities can be precisely detected by nuclear medicine scans [68].

3.4.3 Photoacoustic Imaging

Photoacoustic imaging is also referred to optoacoustic imaging, first discovered by Alexander Graham Bell. He observed that absorption of electromagnetic wave, like radio-frequency (RF) or optical waves causes local heating and resulted in thermoelastic expansion. The thermoelastic expansion produces ultrasonic waves (at the level of megahertz) in materials and generates transient acoustic signals through a medium [78].

Biological tissues differ by their absorption coefficient, therefore measurement of acoustic signals with ultrasonic transducers and the distribution of optical energy deposition in tissues can be rebuilt to ultimately obtain images of the biological tissues [79, 80].

Unlike ionizing radiation, which is used in radiography, computed tomography (CT) and radionuclide scans, only low energy photon and ultrasound waves are used in photoacoustic imaging. Photoacoustic imaging thereby makes this modality a safe imaging approach which is essentially useful for cases requiring frequent examination or preventive examination [80]. It is categorized into two types [80]:

1. Photoacoustic tomography (PAT) or optoacoustic tomography or thermoacoustic tomography
2. Photoacoustic microscopy (PAM) [81]

PAT can be used to identify dental caries at early stages [82]. While the B-mode contrast is associated with optical absorption, it provides sharp images of the tooth morphology. S-mode detects the microstructural and mechanical characteristics of the hard dental tissues. By looking at the tissue structure premature tooth lesions can be detected easily [83]. Also, with photoacoustic waves hemoglobin in dental pulp can be identified which may be helpful in identifying inflammatory status of the pulp and tooth vitality [84].

3.5 Oral Imaging for Dental Conditions

3.5.1 Dental caries

The decay of tooth is otherwise called as dental caries/cavity.

Symptoms: Tooth sensitivity, pain and difficulty while eating. Inflamed tissues around the tooth, tooth loss, and infection or abscess formation.

Cause: Due to the dissolution of hard tissue by acid forming bacteria. When bacteria break down carbohydrate on the surface of the teeth, they produce harmful acid. The source of energy for these bacteria is sugar, hence consumption of food rich in carbohydrate may lead to caries [85, 86].

Imaging techniques used to diagnose caries: Bitewing projection is preferred as it reduces the overlapping of contact point on image.

Interpretation: A carious lesion appears radiolucent because hypomineralized areas do not absorb as many X-ray photons.

3.5.1.1 Radiographic Techniques for Caries Detection

Bitewing: Aids in detecting proximal caries in the distal ends of premolar and molar, caries at cement-enamel junction (CEJ).

Intra Oral Peri Apical (IOPA): Gross carious lesion, changes in apical and interradicular bone.

Panoramic view: Multiple carious teeth, Rampant caries.

At proximal surfaces: Shape of lesion is triangular with a broader base at surface of the tooth spreading along enamel rods, commonly found in the region between contact point and marginal gingiva.

False Interpretation: Failure to recognize caries of proximal surface because of false-positive outcome, cervical burnout, enamel hypoplasia, and tooth wear. When demineralization is not radiographically visible.

3.5.2 Periodontal Diseases

"Peri" means around, and "odontal" means to teeth. An inflammatory host response of the periodontal tissues results in either localized or generalized alterations in supporting structures of the teeth manifesting as alveolar bone loss and ultimately loss of teeth [87, 88].

Signs and Symptoms: Include bleeding and swollen gums. Teeth become fragile and loose as structures supporting the teeth are destroyed.

Cause: Local deposits, dental plaque, and calculus.

Normal Anatomy: The crest of the alveolar bone 2 mm of the cement-enamel junction (CEJ). The periodontal ligament space is not uniform along the root length. It is narrower in the midroot, whereas wider at the apex and alveolar crest, and thus gives a typical hour-glass shape to teeth [89].

Progressive periodontal disease leads to alveolar bone loss producing horizontal and vertical bone defects appearing as radiolucency [90, 91]. Furcation involvement in the mandibular molar teeth appears as radiolucent areas on the radiograph while that on maxillary molars is obscured by palatal roots. Various radiographs used to detect the periodontal disease are summarized in Table 3.2.

Periodontal Abscess: It is a localized purulent infection associated with a periodontal pocket and commonly occurs due to the occlusion of periodontal pocket, hampering the drainage of exudate [92]. It is associated with localized swelling, pain, and discomfort [93].

Interpretation: Radiographs may show a normal appearance, or some radiolucency, ranging from a widening of the periodontal space to a remarkable radiographic bone loss.

Aggressive Periodontitis: This refers to a type of periodontal disease occurring in patients younger than 30 years, which is typically aggressive in nature as manifested by rapid destruction of periodontium [94–96].

Table 3.2 Diagnostic radiography in periodontal disease

PERIODONTAL DISEASE	Radiographs required for establishing diagnosis
Gingival disease	NO
Chronic periodontitis	NO
Aggressive periodontitis (localized and generalized)	YES (mirroring arch shaped radiolucency around first molars)
Periodontitis resulting manifestation of periodontal diseases	NO
Periodontal disease due to necrotizing factors	NO
Periodontium abscesses	YES (radiolucency along the root)
Endodontic lesions of periodontitis	YES (Periapical and/or periradicular radiolucency)
Developmental or acquired defect and conditions	YES (associated radiolucency or radio-opacity)

Interpretation: The radiographic appearance of the bone loss typically consists of arch shaped vertical defects with molar and incisors involvement and bilateral mirroring of bone loss patterns. The generalized form involves multiple teeth or the entire dentition with a rapid loss of alveolar bone which could be either vertical or horizontal pattern.

3.5.3 Cysts

A pathogenic cavity with epithelial lining that gets filled with fluid and soft materials and it grows due to movement of fluid inside the cavity due to osmosis.

List of imaging techniques used to detect cysts:
- Bitewing X-rays
- Periapical X-rays
- Computed tomography (CT)
- Cone beam CT
- MRI imaging

Dentigerous Cysts: It forms in the region of the crown of an unerupted tooth.

Interpretation: The epicenter is present just above the crown of the tooth. Some are eccentric, i.e., they are present beside the crown instead of above the crown [97]. Well-defined, curved or circular corticated outline. Appears entirely radiolucent apart from the crown of the tooth involved [98].

Keratocystic Odontogenic Tumor (KOT): Based on the tumor-like characteristics of the involved lining epithelium, it could be a unicystic or a multicystic odontogenic tumor [99, 100].

Interpretation: KOT is usually located on posterior mandible. Cortical borders are present unless they have become secondarily infected. Smooth circular or oval in shape with scalloped outline. The internal structure is radiolucent and the curved internal gives the lesion a multilocular appearance.

Lateral Periodontal Cysts: Lateral periodontal cysts are noninflammatory cysts found on the lateral tooth surface of a vital tooth arising from epithelial rests in periodontium. Usually unicystic, but several small cysts may appear to form a cluster. Such a condition is named as botryoid odontogenic cysts [101].

Interpretation: It extends between lateral incisor and second premolar with a well-defined cortical boundary. It is either round or oval in shape. The botryoid variety may have a multilocular appearance.

Nasopalatine Duct Cysts: Cysts formed in the nasopalatine canal [102].

Interpretation: Found in the nasopalatine foramen or canal. This cyst may not always be positioned symmetrically. It has a well-defined cortical boundary, is circular, oval, or heart shaped. Nasopalatine duct cysts are totally radiolucent.

Cysts like lesions: Simple Bone Cysts (SBC) [103]: It is a cavity inside the bone with connective tissue lining.

Interpretation: Almost all the simple bone cysts are found in the mandible, rarely in the maxilla. Margin of SBCs may vary from a distinct, delicate cortex to a poorly defined margin which is difficult to distinguish from the neighboring bone.

3.5.4 Salivary Gland Diseases

Salivary gland diseases are clinically categorized as [104]: Inflammatory disorders, noninflammatory disorders, and masses occupying space. Inflammatory disorders could be severe or persistent and may be due to secondary effect of any infection or trauma. Noninflammatory disorders are associated with abnormal metabolic activity, abnormal endocrine gland, malnutrition and often with neurologic disorders [105]. Masses which possess space are either cystic or neoplastic (benign or malignant).

Signs and Symptoms: Parotid and submandibular gland swelling, pain, and altered salivary flow.

Imaging technology used to detect salivary gland diseases:

- Intraoral radiography
- Extraoral radiography
- Conventional sialography
- Computed tomography
- Magnetic resonance imaging
- Scintigraphy (Nuclear medicine, PET)
- Ultrasonography

Sialolithiasis: Formation of a calcified obstruction within the salivary duct [106].

Interpretation: On radiographs, sialoliths may appear either radiopaque or radiolucent. They may vary in their shape presenting a homogeneous radiopaque internal structure.

Bacterial Sialadenitis: Bacterial infection of the terminal acini or salivary gland parenchyma [107].

Interpretation: On CT, abscess cavities seen as walled-off areas within the enlarged gland. Areas of diffuse inflammation appear as light image while areas of suppuration appear as darker image.

Sialodochitis: Inflammation in the ducts and ductal systems of the salivary glands [108].

Interpretation: Sausage-string appearance of the main salivary duct or branches with alternate strictures and dilations.

Sialadenosis: It is a non-neoplastic, noninflammatory enlargement of primarily the parotid salivary glands [109].

Interpretation: Sialography may reveal either a normal appearance or gland enlargement with splayed ducts although CT and MRI provide only a nonspecific anatomic depiction of the glands.

Warthin's tumor: A benign tumor associated with proliferating salivary ducts which get trapped in lymph nodes during embryonic development of salivary glands [110, 111].

Interpretation: CT and MRI appearance is nonspecific. On CT, it could appear either as soft tissue or as a cystic lesion. On MRI, appears heterogeneous and sometimes with hemorrhagic foci. It appears as an intensely hot lesion on 99 m Tc pertechnetate scans.

Mucoepidermoid carcinoma: A kind of malignant tumor with a mixture of epidermoid and mucous cells originating from salivary gland's ductal epithelium [112].

Interpretation: On contrast-enhanced CT or MRI, it appears as a lobulated or an irregularly and sharply circumscribed cystic area.

3.5.5 Systemic Diseases of the Jaws

The constant remodeling of bone due to disorders in endocrine system that results as change in the form and structure of bone and teeth leading to the diseases of jaws is called systemic diseases (Table 3.3).

Hyperparathyroidism: A secretion of parathyroid hormone (PTH) that induces bone remodeling that leads to osteoclastic resorption of the bone, which drives calcium from the skeleton.

Interpretation: Demineralization of the skeleton gives radiolucent appearance. Peripheral or central tumors of bone appear radiolucent. Loss of lamina dura gives the roots a tapered appearance because of loss of image contrast. Change in the normal trabecular pattern gives a ground-glass appearance to randomly oriented trabeculae [113].

Hypoparathyroidism: Low secretion of PTH can lead to a defect in the response of the tissue target cells to normal levels of PTH [115].

Interpretation: The basal ganglia get calcified. The appearance of flocculent and paired calcification (posteroanterior view) inside the cerebral hemispheres.

Hyperpituitarism: Hyperactivation of the anterior lobe of the pituitary gland leading to enhanced production of growth hormone [137].

Table 3.3 Various systemic diseases and its effect on teeth and associated structures

Systemic disease	Hypocalcification	Hypoplasia	Loss of lamina dura	Loss of teeth	Large pulp chamber	Eruption
Hyperparathyroidism [113, 114]	×	×	✓	×	×	✓
Hypoparathyroidism [115, 116]	×	✓	×	×	×	✓
Hyperpituitarism [117]	×	×	×	×	×	✓
Hypopituitarism [118, 119]	×	×	×	×	×	✓
Hypothyroidism [120, 121]	×	×	×	×	×	✓
Hyperthyroidism [121, 122]	×	×	×	×	×	✓
Cushing's syndrome [123]	×	×	×	×	×	✓
Osteoporosis [124, 125]	×	×	×	×	×	×
Rickets [126, 127]	✓	✓	✓	×	×	✓
Osteomalacia [127, 128]	×	×	×	×	×	×
Hypophosphatasia [129, 130]	✓	✓	✓	✓	✓	×
Renal osteodystrophy [131, 132]	✓	✓	✓	✓	×	×
Hypophosphatemia [133, 134]	✓	✓	✓	✓	✓	×
Osteopetrosis [135, 136]	×	×	×	×	×	✓

Interpretation: The jaws get enlarge, mostly the mandible. There is increased spacing of the teeth due to elongation of dental arches. Outbreak of the posterior teeth occurs as an attempt to reimburse the mandibular growth.

Cushing's Syndrome: Excess secretion of glucocorticoids by the adrenal glands [123].

Interpretation: Diffuse thinning accompanied by a mottled appearance.

Osteoporosis: Generalized decrease in bone mass with normal histologic appearance [138].

Interpretation: The lamina dura gets thinner than normal. The number of trabeculae gets reduced at some regions of the mandible. Density of teeth gets reduced. Cortical boundaries become thin.

Rickets: It results from an insufficiency of serum and extracellular levels of calcium and phosphate, which in turn results from vitamin D inadequacy, required for absorption of calcium in the intestine [139].

Interpretation: Jaw cortical structures appear thinner and appear intensely radiolucent, making the teeth appear to be without any support.

Hypophosphatasia: It is an inherited disorder that occurs due to reduced or low production or a not-proper functioning of alkaline phosphatase [140].

Interpretation: Mandible and maxilla appear radiolucent. Due to poor calcification of alveolar bone, the cortical bone and the lamina dura become thin. Primary and permanent teeth's enamel becomes thin and the pulp chambers become large.

Renal Osteodystrophy: Bone changes result from chronic renal failure [141].

Interpretation: Granular is the pattern of appearance of trabecular bone. Internal trabeculae number may decrease or increase. Thinner or less apparent cortical boundaries.

Osteopetrosis: Results from deficiency of osteoclasts. Primary skeleton gets abnormally formed and there is increase in the bone mass [135, 142].

Interpretation: There is an increased radiodensity of the jaws which result in a radiographic image that fails to reveal any internal structure. Even the roots may not be apparent.

Thalassemia: A hereditary disorder that results in defective synthesis of the hemoglobin. Erythrocytes are thinner, have diminished hemoglobin content and have a decreased life span [143].

Interpretation: Hyperplasia of the bone marrow restricts paranasal sinus pneumatization especially with maxillary sinus causing an expansion of the maxilla that leads to malocclusion. The jaws appear radiolucent with thinning of the cortical borders.

3.5.6 Missing Teeth, Edentulous Arches, and Maxillofacial Implants

Panoramic radiographs often are the first method used to screen patients with multiple missing teeth, partial or complete edentulous arches before complete denture therapy rehabilitation is planned [144]. Panoramic radiographs provide a view of the entire maxillo-mandibular region with minimal patient inconvenience; thereby it helps to detect the pathologic changes in otherwise healthy jaws that were missed out during routine clinical examination [145].

The surgical component that gets intact to jaw bone and acts as anchor to bones to support dental prosthesis such as crown, bridge, denture, and facial prosthesis is called as dental implant [146]. Dental implant being a metallic object appears radiopaque in all radiographs. Although a panoramic radiograph may be helpful in screening and provisional diagnosis, a CBCT is preferred for diagnosis and planning for rehabilitation with maxillofacial implants [147].

3.5.7 Maxillofacial Trauma

Injury to jaws, teeth and/or periodontium and nearby soft tissues due to dental or facial fractures is termed as trauma [148].

Interpretation: Fractures irrespective of their three-dimensional nature are referred to as "lines" in images. Fractures are seen as cleavage of plane which is extended deep into the tissue. Therefore, it is important to align the beam of X-ray in the direction of fracture or else it may not be visible on the radiograph.

Luxation: Dislocation/displacement of the tooth from its alveolar socket [149].

Interpretation: Luxation**/s**ubluxation/intrusion may appear as elevation of the tooth from its socket often apparent on a radiograph demonstrated by varying broadening of the periodontal ligament space.

Avulsion: The complete dislodgement/displacement of a tooth from its alveolar socket [150].

Interpretation: The displaced tooth may be lodged into the adjacent soft tissue with a projection of its image on the radiograph superimposing the alveolar process which may give a false impression of it being in the bone.

3.5.7.1 Fractures of teeth

Dental Crown Fracture: Fractures of the crown of deciduous or permanent teeth.

Interpretation: Fracture location, extent, and its relationship to the plane of pulp chamber may require more than one projection. In addition, the stage of development of root of the involved tooth can also be assessed.

Dental Root Fracture: Fractures of root portion of the tooth secondary to traumatic injuries to permanent teeth or deciduous teeth [151].

Interpretation: Root fractures can best be visualized on the radiographs with appropriate orientation of the angulation of the incident X-ray beam and the degree of distraction/displacement of root fragments. When aligned with the fracture plane, incident beam produces sharp radiolucent lines. When the incident beam meets the fracture plane in an oblique manner, it may appear as poorly defined single line or two converging lines.

Vertical Root Fracture: Fracture planes that run length-wise of a tooth (crown-apex) involved either partially or complete [152].

Interpretation: Fracture appears as a radiolucent line on the radiograph when the incident X-ray beam aligns with the fracture plane. It is most often missed due to overlap of dental and osseous structures. Therefore, CBCT is beneficial in diagnosis of vertical root fracture, identifying its location, extent, and the configuration of associated osseous lesion.

Acknowledgements SP is thankful to the MHRD or the financial support she received for the study. We wish to thank Dr. Diplina Barman, Dr. Vishakh Kumar Jha, Dr. Punit Bhargav, Dr. Tusar Kanti Nayak, Dr. Shayari Niyogi, and Dr. Pinali Das for contributing some of the images.

References

1. Walker HK. The origins of the history and physical examination. 1990.
2. Kornman KS. Diagnostic and prognostic tests for oral diseases: practical applications. J Dent Educ. 2005;69(5):498–508.
3. Gopalakrishnan S, Udayshankar P, Rama R. Standard treatment guidelines in primary healthcare practice. J Family Med Prim Care. 2014;3(4):424.

4. Smith-Bindman R, Miglioretti DL, Larson EB. Rising use of diagnostic medical imaging in a large integrated health system. Health Aff (Millwood). 2008;27(6):1491–502.
5. Looking back on the millennium in medicine. N Engl J Med, 2000. 342(1): p. 42–9.
6. Benson BW, et al. Advances in diagnostic imaging for pathologic conditions of the jaws. Head Neck Pathol. 2014;8(4):383–91.
7. Rezai RF. Otto Walkhoff--renaissance man of dentistry. Bull Hist Dent. 1986;34(2):115–21.
8. Shah N, Bansal N, Logani A. Recent advances in imaging technologies in dentistry. World J Radiol. 2014;6(10):794–807.
9. Suomalainen A, Pakbaznejad Esmaeili E, Robinson S. Dentomaxillofacial imaging with panoramic views and cone beam CT. Insights Imaging. 2015;6(1):1–16.
10. Forsberg J. A comparison of the paralleling and bisecting-angle radiographic techniques in endodontics. Int Endod J. 1987;20(4):177–82.
11. Maciejewska I, Chomik E. Antoni Cieszynski: a pioneering dentist. J Hist Dent. 2012;60(1):18–22.
12. Callaghan D, Crocker C. The role of bitewing radiographs--a review of current guidelines. J Ir Dent Assoc. 2007;53(2):92–5.
13. Pitts NB. The use of bitewing radiographs in the management of dental caries: scientific and practical considerations. Dentomaxillofac Radiol. 1996;25(1):5–16.
14. Hallikainen D. History of panoramic radiography. Acta Radiol. 1996;37(3 Pt 2):441–5.
15. Paatero YV. Pantomography of spherical layers. Acta Radiol. 1957;48(3):181–7.
16. Kaffe I, Fishel D, Gorsky M. Panoramic radiography in dentistry. Refuat Hapeh Vehashinayim. 1977;26(2):25–30.. 19-22
17. Reddy MS, et al. A comparison of the diagnostic advantages of panoramic radiography and computed tomography scanning for placement of root form dental implants. Clin Oral Implants Res. 1994;5(4):229–38.
18. Forsyth DB, Shaw WC, Richmond S. Digital imaging of cephalometric radiography, part 1: advantages and limitations of digital imaging. Angle Orthod. 1996;66(1):37–42.
19. Gilbert DB, et al. Analysis of condylar position changes: a test of validity of posteroanterior cephalometric and 20-degree lateral cephalometric techniques enhanced by digital subtraction. Int J Adult Orthodon Orthognath Surg. 1994;9(4):311–21.
20. Shokri A, et al. Effect of changing the head position on accuracy of transverse measurements of the maxillofacial region made on cone beam computed tomography and conventional posterior-anterior cephalograms. Dentomaxillofac Radiol. 2017;46(5):20160180.
21. Lenza MA, et al. Radiographic evaluation of orthodontic treatment by means of four different cephalometric superimposition methods. Dental Press J Orthod. 2015;20(3):29–36.
22. Konen E, et al. The value of the occipitomental (Waters') view in diagnosis of sinusitis: a comparative study with computed tomography. Clin Radiol. 2000;55(11):856–60.
23. Williams JW Jr, et al. Diagnosing sinusitis by X-ray: is a single waters view adequate? J Gen Intern Med. 1992;7(5):481–5.
24. Maglione M, Costantinides F. Localization of basicranium midline by submentovertex projection for the evaluation of condylar asymmetry. Int J Dent. 2012;2012:285693.
25. Reddy MS, Jeffcoat MK. Digital subtraction radiography. Dent Clin N Am. 1993;37(4):553–65.
26. Ort MG, Gregg EC, Kaufman B. Subtraction radiography: techniques and limitations. Radiology. 1977;124(1):65–72.
27. Mehra A, et al. Digital subtraction radiography—a technique revisited. J Indian Acad Oral Med Radiol. 2007;19(4):517–22.
28. Gröndahl H-G, Gröndahl K, Webber RL. A digital subtraction technique for dental radiography. Oral Surg Oral Med Oral Pathol Oral Radiol. 1983;55(1):96–102.
29. Hausmann E, et al. Usefulness of subtraction radiography in the evaluation of periodontal therapy. J Periodontol. 1985;56(11 Suppl):4–7.
30. van der Stelt PF. Filmless imaging: the uses of digital radiography in dental practice. J Am Dent Assoc. 2005;136(10):1379–87.
31. Jayachandran S. Digital imaging in dentistry: a review. Contemp Clin Dent. 2017;8(2):193–4.

32. Anas A, Asaad J, Tarboush K. A comparison of intra-oral digital imaging modalities: charged couple device versus storage phosphor plate. Int J Health Sci (Qassim). 2010;4(2):156–67.
33. Takeshita WM, et al. Comparison of the diagnostic accuracy of direct digital radiography system, filtered images, and subtraction radiography. Contemp Clin Dent. 2013;4(3):338–42.
34. Caliskan A, Sumer AP. Definition, classification and retrospective analysis of photostimulable phosphor image artefacts and errors in intraoral dental radiography. Dentomaxillofac Radiol. 2017;46(3):20160188.
35. Ilic DV, Stojanovic LS. Application of radiovisiography (digital radiology) in dental clinical practice. Vojnosanit Pregl. 2012;69(1):81–4.
36. Brennan J. An introduction to digital radiography in dentistry. J Orthod. 2002;29(1):66–9.
37. Bhattacharyya KB. Godfrey Newbold Hounsfield (1919-2004): the man who revolutionized neuroimaging. Ann Indian Acad Neurol. 2016;19(4):448–50.
38. Surapaneni H, et al. Role of computed tomography imaging in dental implantology: an overview. J Oral Maxillofac Radiol. 2013;1(2):43–7.
39. Worthington P, Rubenstein J, Hatcher DC. The role of cone-beam computed tomography in the planning and placement of implants. J Am Dent Assoc. 2010;141(Suppl 3):19S–24S.
40. Aboudara C, et al. Comparison of airway space with conventional lateral headfilms and 3-dimensional reconstruction from cone-beam computed tomography. Am J Orthod Dentofac Orthop. 2009;135(4):468–79.
41. Venkatesh E, Elluru SV. Cone beam computed tomography: basics and applications in dentistry. J Istanb Univ Fac Dent. 2017;51(3 Suppl 1):S102–21.
42. Ghoneima A, Kula K. Accuracy and reliability of cone-beam computed tomography for airway volume analysis. Eur J Orthod. 2013;35(2):256–61.
43. Gupta J, Ali SP. Cone beam computed tomography in oral implants. Natl J Maxillofac Surg. 2013;4(1):2–6.
44. Nagarajappa AK, Dwivedi N, Tiwari R. Artifacts: the downturn of CBCT image. J Int Soc Prev Community Dent. 2015;5(6):440–5.
45. Patcas R, et al. Accuracy of linear intraoral measurements using cone beam CT and multidetector CT: a tale of two CTs. Dentomaxillofac Radiol. 2012;41(8):637–44.
46. Patrick S, et al. Comparison of gray values of cone-beam computed tomography with hounsfield units of multislice computed tomography: an in vitro study. Indian J Dent Res. 2017;28(1):66–70.
47. Niraj LK, et al. MRI in dentistry- a future towards radiation free imaging - systematic review. J Clin Diagn Res. 2016;10(10):ZE14–9.
48. Schoppe, C., et al., Comparison of computed tomography and high-field (3.0 T) magnetic resonance imaging of age-related variances in selected equine maxillary cheek teeth and adjacent tissues. BMC Veterin Res 2017. 13(1): 280.
49. Sustercic D, Sersa I. Human tooth pulp anatomy visualization by 3D magnetic resonance microscopy. Radiol Oncol. 2012;46(1):1–7.
50. Bag AK, et al. Imaging of the temporomandibular joint: an update. World J Radiol. 2014;6(8):567–82.
51. Larheim TA. Role of magnetic resonance imaging in the clinical diagnosis of the temporomandibular joint. Cells Tissues Organs. 2005;180(1):6–21.
52. Singh A, et al. Role of MRI in evaluation of malignant lesions of tongue and Oral cavity. Pol J Radiol. 2017;82:92–9.
53. Law CP, et al. Imaging the oral cavity: key concepts for the radiologist. Br J Radiol. 2011;84(1006):944–57.
54. Agarwal SS, et al. A radiographic study of external apical root resorption in patients treated with single-phase fixed orthodontic therapy. Med J Armed Forces India. 2016;72(Suppl 1):S8–S16.
55. Ariji Y, et al. Imaging features contributing to the diagnosis of ameloblastomas and keratocystic odontogenic tumours: logistic regression analysis. Dentomaxillofac Radiol. 2011;40(3):133–40.

56. Gaudino C, et al. MR-imaging of teeth and periodontal apparatus: an experimental study comparing high-resolution MRI with MDCT and CBCT. Eur Radiol. 2011;21(12):2575–83.
57. Idiyatullin D, et al. Dental magnetic resonance imaging: making the invisible visible. J Endod. 2011;37(6):745–52.
58. Newbould RD, et al. T2 relaxation mapping MRI of healthy and inflamed gingival tissue. Dentomaxillofac Radiol. 2017;46(2):20160295.
59. Nordbeck P, Ertl G, Ritter O. Magnetic resonance imaging safety in pacemaker and implantable cardioverter defibrillator patients: how far have we come? Eur Heart J. 2015;36(24):1505–11.
60. Baum G, et al. Observation of internal structures of teeth by ultrasonography. Science. 1963;139(3554):495.
61. Rockett MS, et al. Use of ultrasonography versus magnetic resonance imaging for tendon abnormalities around the ankle. Foot Ankle Int. 1998;19(9):604–12.
62. Hayashi T. Application of ultrasonography in dentistry. Jpn Dent Sci Rev. 2012;48(1):5–13.
63. Bialek EJ, Jakubowski W. Mistakes in ultrasound examination of salivary glands. J Ultrason. 2016;16(65):191–203.
64. Orlandi MA, Pistorio V, Guerra PA. Ultrasound in sialadenitis. J Ultrasound. 2013;16(1):3–9.
65. Kim DW. Ultrasound-guided fine-needle aspiration for retrojugular lymph nodes in the neck. World J Surg Oncol. 2013;11:121.
66. Aribas BK, et al. Fine-needle aspiration biopsy of cervical lymph nodes: factors in predicting malignant diagnosis. Neoplasma. 2011;58(1):51–7.
67. Culjat MO, et al. Ultrasound detection of submerged dental implants through soft tissue in a porcine model. J Prosthet Dent. 2008;99(3):218–24.
68. Baur DA, Heston TF, Helman JI. Nuclear medicine in oral and maxillofacial diagnosis: a review for the practicing dental professional. J Contemp Dent Pract. 2004;5(1):94–104.
69. Gupta SK, et al. Radionuclide bone scan SPECT-CT: lowering the dose of CT significantly reduces radiation dose without impacting CT image quality. Am J Nucl Med Mol Imaging. 2017;7(2):63–73.
70. Gupta V. Bone scintigraphy in the evaluation of cancer. Kathmandu Univ Med J (KUMJ). 2005;3(3):243–8.
71. Shintawati R, et al. Evaluation of bone scan index change over time on automated calculation in bone scintigraphy. Ann Nucl Med. 2015;29(10):911–20.
72. Noordzij W, Glaudemans AWJM. Nuclear medicine imaging techniques. In: Glaudemans AWJM, editor. Nuclear medicine and radiologic imaging in sports injuries. Berlin: Springer; 2015. p. 25–48.
73. Loutfi I, Nair MK, Ebrahim AK. Salivary gland scintigraphy: the use of semiquantitative analysis for uptake and clearance. J Nucl Med Technol. 2003;31(2):81–5.
74. Purohit BS, et al. FDG-PET/CT pitfalls in oncological head and neck imaging. Insights Imaging. 2014;5(5):585–602.
75. Basu S, Houseni M, Alavi A. Significance of incidental fluorodeoxyglucose uptake in the parotid glands and its impact on patient management. Nucl Med Commun. 2008;29(4):367–73.
76. Cho SG, Kim J, Song HC. Radiation safety in nuclear medicine procedures. Nucl Med Mol Imaging. 2017;51(1):11–6.
77. Agency IAE. A guide to clinical PET in oncology: improving clinical Management of Cancer Patients, IAEA TECDOC series. Vienna: International Atomic Energy Agency; 2008.
78. Bell AG. Upon the production and reproduction of sound by light. Journal of the Society of Telegraph Engineers. 1880;9(34):404–26.
79. Xi L, et al. Photoacoustic imaging based on MEMS mirror scanning. Biomed Opt Express. 2010;1(5):1278–83.
80. Zhang Y, Hong H, Cai W. Photoacoustic imaging. Cold Spring Harb Protoc. 2011;2011:9.
81. Yao J, Wang LV. Photoacoustic microscopy. Laser Photon Rev. 2013;7:5.
82. Cheng R, et al. Noninvasive assessment of early dental lesion using a dual-contrast photoacoustic tomography. Sci Rep. 2016;6:21798.
83. Liu W, et al. Quad-mode functional and molecular photoacoustic microscopy. Sci Rep. 2018;8(1):11123.

84. Yamada A, Kakino S, Matsuura Y. Detection of Photoacoustic signals from blood in dental pulp. Optic Photon. 2016;06:229–36.
85. Keenan JR, Keenan AV. Accuracy of dental radiographs for caries detection. Evid Based Dent. 2016;17(2):43.
86. Analoui M, Stookey GK. Direct digital radiography for caries detection and analysis. Monogr Oral Sci. 2000;17:1–19.
87. Corbet EF, Ho DK, Lai SM. Radiographs in periodontal disease diagnosis and management. Aust Dent J. 2009;54(Suppl 1):S27–43.
88. Pattnaik N, et al. Interdisciplinary Management of Gingivitis Artefacta Major: a case series. Case Rep Dent. 2015;2015:678504.
89. Mortazavi H, Baharvand M. Review of common conditions associated with periodontal ligament widening. Imaging Sci Dent. 2016;46(4):229–37.
90. Satpathy A, et al. Serum interleukin-1β in subjects with abdominal obesity and periodontitis. Obes Res Clin Pract. 2015;9(5):513–21.
91. Baishya B, et al. Oral hygiene status, oral hygiene practices and periodontal health of brick kiln workers of Odisha. J Indian Soc Periodontol. 2019;23(2):163–7.
92. Pattnaik S, et al. Clinical and antimicrobial efficacy of a controlled-release device containing chlorhexidine in the treatment of chronic periodontitis. Eur J Clin Microbiol Infect Dis. 2015;34(10):2103–10.
93. Mohanty G, Mohanty R, Satpathy A. Simultaneous occurrence of pyogenic granuloma at multiple sites associated with bone loss: report of a rare case. J Indian Soc Periodontol. 2018;22(2):174–7.
94. Cho CM, You HK, Jeong SN. The clinical assessment of aggressive periodontitis patients. J Periodontal Implant Sci. 2011;41(3):143–8.
95. Heikkinen AM, et al. Periodontal initial radiological findings of genetically predisposed Finnish adolescents. J Clin Diagn Res. 2017;11(7):ZC25–8.
96. Satpathy A, et al. Effect of alcohol consumption status and alcohol concentration on oral pain induced by alcohol-containing mouthwash. J Oral Sci. 2013;55(2):99–105.
97. Shamim R, et al. Kidney bean shaped peripheral Giant cell granuloma of gingiva: a case report. Adv Sci Lett. 2016;22(2):311–3.
98. Sridevi K, et al. Dentigerous cysts of maxillofacial region- clinical, radiographic and biochemical analysis. Kathmandu Univ Med J (KUMJ). 2015;13(49):8–11.
99. Zhu L, Yang J, Zheng JW. Radiological and clinical features of peripheral keratocystic odontogenic tumor. Int J Clin Exp Med. 2014;7(1):300–6.
100. Grasmuck EA, Nelson BL. Keratocystic odontogenic tumor. Head Neck Pathol. 2010;4(1):94–6.
101. de Carvalho LF, et al. Lateral periodontal cyst: a case report and literature review. J Oral Maxillofac Res. 2011;1(4):e5.
102. Nelson BL, Linfesty RL. Nasopalatine duct cyst. Head Neck Pathol. 2010;4(2):121–2.
103. Suei Y, et al. Radiographic findings and prognosis of simple bone cysts of the jaws. Dentomaxillofac Radiol. 2010;39(2):65–71.
104. Seifert G, Donath K. Classification of the pathohistology of diseases of the salivary glands - review of 2,600 cases in the salivary gland register. Beitr Pathol. 1976;159(1):1–32.
105. Mahapatra A, et al. Role of salivary pH and flow rate in tooth Wear: a Clinico-physicochemical study. Adv Sci Lett. 2016;22(2):494–6.
106. Rzymska-Grala I, et al. Salivary gland calculi - contemporary methods of imaging. Pol J Radiol. 2010;75(3):25–37.
107. Abdel Razek AAK. And S. Mukherji, imaging of sialadenitis. Neuroradiol J. 2017;30(3):205–15.
108. Flores RBJ, et al. Sialodochitis fibrinosa (kussmaul disease) report of 3 cases and literature review. Medicine (Baltimore). 2016;95(42):e5132.
109. Gadodia A, et al. Bilateral parotid swelling: a radiological review. Dentomaxillofac Radiol. 2011;40(7):403–14.
110. Lommer D. Evidence of reversibility of 3 beta-hydroxysteroiddehydrogenase-5-4-isomerase reactions in rat adrenal glands. Acta Endocrinol Suppl (Copenh). 1971;152:96.

111. Tartaglione T, et al. Differential diagnosis of parotid gland tumours: which magnetic resonance findings should be taken in account? Acta Otorhinolaryngol Ital. 2015;35(5):314–20.
112. Kashiwagi N, et al. MRI findings of mucoepidermoid carcinoma of the parotid gland: correlation with pathological features. Br J Radiol. 2012;85(1014):709–13.
113. Kakade SP, et al. Oral manifestations of secondary hyperparathyroidism: a case report. Contemp Clin Dent. 2015;6(4):552–8.
114. Khalekar Y, et al. Hyperparathyroidism in dentistry: issues and challenges!! Indian J Endocrinol Metab. 2016;20(4):581–2.
115. John DR, Suthar PP. Radiological features of long-standing Hypoparathyroidism. Pol J Radiol. 2016;81:42–5.
116. Srirangarajan S, et al. Dental manifestation of primary idiopathic hypoparathyroidism. J Indian Soc Periodontol. 2014;18(4):524–6.
117. Atreja G, et al. Oral manifestations in growth hormone disorders. Indian J Endocrinol Metab. 2012;16(3):381–3.
118. Sarnat H, et al. Comparison of dental findings in patients with isolated growth hormone deficiency treated with human growth hormone (hGH) and in untreated patients with Laron-type dwarfism. Oral Surg Oral Med Oral Pathol. 1988;66(5):581–6.
119. Kosowicz J, Rzymski K. Abnormalities of tooth development in pituitary dwarfism. Oral Surg Oral Med Oral Pathol. 1977;44(6):853–63.
120. Gupta R, et al. Oral manifestations of hypothyroidism: a case report. J Clin Diagn Res. 2014;8(5):ZD20–2.
121. Chandna S, Bathla M. Oral manifestations of thyroid disorders and its management. Indian J Endocrinol Metab. 2011;15(Suppl 2):S113–6.
122. Poumpros E, Loberg E, Engstrom C. Thyroid function and root resorption. Angle Orthod. 1994;64(5):389–93.. discussion 394
123. Sahdev A, et al. Imaging in Cushing's syndrome. Arq Bras Endocrinol Metabol. 2007;51(8):1319–28.
124. Dervis E. Oral implications of osteoporosis. Oral Surg Oral Med Oral Pathol Oral Radiol Endod. 2005;100(3):349–56.
125. Cakur B, et al. Dental panoramic radiography in the diagnosis of osteoporosis. J Int Med Res. 2008;36(4):792–9.
126. Ngangom A, Jain M, Verma S. Need of early dental intervention in vitamin D deficiency rickets. Indian J Dent Sci. 2018;10(4):229–32.
127. Souza AP, et al. Dental manifestations of patient with vitamin D-resistant rickets. J Appl Oral Sci. 2013;21(6):601–6.
128. Chang CY, et al. Imaging findings of metabolic bone disease. Radiographics. 2016;36(6):1871–87.
129. Bloch-Zupan A, Vaysse F. Hypophosphatasia: oral cavity and dental disorders. Arch Pediatr. 2017;24(5S2):5S80–4.
130. Schmidt T, et al. Clinical, radiographic and biochemical characteristics of adult hypophosphatasia. Osteoporos Int. 2017;28(9):2653–62.
131. Chang JI, Som PM, Lawson W. Unique imaging findings in the facial bones of renal Osteodystrophy. Am J Neuroradiol. 2007;28(4):608.
132. Ganibegovic M. Dental radiographic changes in chronic renal disease. Med Arh. 2000;54(2):115–8.
133. Rabbani A, et al. Dental problems in hypophosphatemic rickets, a cross sectional study. Iran J Pediatr. 2012;22(4):531–4.
134. Souza MA, et al. Dental abnormalities and oral health in patients with Hypophosphatemic rickets. Clinics (Sao Paulo). 2010;65(10):1023–6.
135. Sharma SS, et al. Osteopetrosis of the mandible masquerading as tubercular osteomyelitis. BMJ Case Rep. 2013;2013
136. Celakil T, et al. Oral rehabilitation of an Osteopetrosis patient with osteomyelitis. Case Rep Dent. 2016;2016:6930567.

137. Root AW, Martinez CR. Magnetic resonance imaging in patients with hypopituitarism. Trends Endocrinol Metab. 1992;3(8):283–7.
138. White SC. Oral radiographic predictors of osteoporosis. Dentomaxillofac Radiol. 2002;31(2):84–92.
139. Jayachandran S, Kumar MS. A paradoxical presentation of rickets and secondary osteomyelitis of the jaw in type II autosomal dominant osteopetrosis: rare case reports. Indian J Dent Res. 2016;27(6):667–71.
140. Millan JL, Plotkin H. Hypophosphatasia - pathophysiology and treatment. Actual osteol. 2012;8(3):164–82.
141. Parthiban J, Aarthi Nisha V, Asokan GS, Prakash CA, Varadharaja MM. Oral manifestations in a renal osteodystrophy patient - a case report with review of literature. J Clin Diagn Res. 2014;8(8):ZD28–30.
142. Tohidi E, Bagherpour A. Clinicoradiological findings of benign osteopetrosis: report of two new cases. J Dent Res Dent Clin Dent Prospects. 2012;6(4):152–7.
143. Helmi N, et al. Thalassemia review: features, dental considerations and management. Electron Physician. 2017;9(3):4003–8.
144. Porwal A, Satpathy A. Graphic imaging tools for precise identification of shift of neutral zone in edentulous mandibular arch. Adv Sci Lett. 2016;22(2):378–80.
145. Masood F, et al. Findings from panoramic radiographs of the edentulous population and review of the literature. Quintessence Int. 2007;38(6):e298–305.
146. Gupta S, et al. Oral implant imaging: a review. Malays J Med Sci. 2015;22(3):7–17.
147. Shelley AM, et al. The impact of CBCT imaging when placing dental implants in the anterior edentulous mandible: a before-after study. Dentomaxillofac Radiol. 2015;44(4):20140316.
148. Naeem A, Gemal H, Reed D. Imaging in traumatic mandibular fractures. Quant Imaging Med Surg. 2017;7(4):469–79.
149. Gupta M. Intrusive luxation in primary teeth - review of literature and report of a case. Saudi Dent J. 2011;23(4):167–76.
150. Tezel H, Atalayin C, Kayrak G. Replantation after traumatic avulsion. Eur J Dent. 2013;7(2):229–32.
151. Wang P, et al. Detection of dental root fractures by using cone-beam computed tomography. Dentomaxillofac Radiol. 2011;40(5):290–8.
152. Khasnis SA, et al. Vertical root fractures and their management. J Conserv Dent. 2014;17(2):103–10.

Automatic Kidney Cysts Segmentation in Digital Ultrasound Images

4

Prema T. Akkasaligar and Sunanda Biradar

4.1 Introduction

Kidney encloses nephrons and is a bean-shaped structure. Any abnormality such as cyst in such a tiny organ leads to a problem. Kidney failure is found in many people suffering from the common diseases such as hypertension, diabetes mellitus, and glomerulonephritis. It is observed in a survey that there is proportionally a big number of deaths happening almost every year because of kidney abnormal functioning only. Improper functioning of kidney can lead to a lifetime risk as well. If kidney cysts are not diagnosed and treated in time, they could seriously damage kidney or cause death also.

Kidney organ can have more than one cysts developed in it. This leads to an abnormal condition called polycystic kidney disease (PCKD). For any type of kidney cyst treatment, information about exact position and size of a cyst is a key issue. These details are very important information to decide about the type of treatment including surgery. Such type of kidney cysts can be picturized using various kinds of medical imaging techniques. Among the various imaging modalities, ultrasonography (USG) is most common and primarily used diagnostic tool by medical experts such as doctors or radiologists. Among all the available medical imaging modalities, ultrasound imaging has many advantages like less time for acquisition, comparatively low cost and makes use of harmless, non-ionizing radiation. Pathology of the soft tissue organs like heart, kidney, liver, etc. can be used for clinical diagnosis [1, 2] effectively. Analysis of USG images by human experts is tedious task, non-reproducible, time-consuming and highly depends on the knowledge/experience of the medical expert. If such a task of analysis can be automated with computer systems, then it identifies the cysts and delineates its features from the image. Thus, the

P. T. Akkasaligar · S. Biradar (✉)
Department of Computer Science and Engineering, BLDEA's V. P. Dr. P.G. Halakatti College of Engineering and Technology, Vijayapur, Karnataka, India

A. K. Shukla (ed.), *Medical Imaging Methods*,
https://doi.org/10.1007/978-981-13-9121-7_4

system assists the medical experts in making their analysis job more simple and easy. However, accurate and exact extraction of required region of interest from USG images is a difficult task due to the presence of speckle noise in USG images. Proposed method focuses on effective and automatic extraction of cysts in medical USG images of kidney.

Main goals of our proposed method are as follows:

- ***Accurate and automatic segmentation:*** By generating automatic initial contour, segmentation can be fully automated. We have proposed level set method for accurate segmentation of kidney cysts.
- ***Efficient segmentation method:*** Elapsed time is reduced along with accurate segmentation of cysts in kidney USG images.

This chapter is organized into five major sections. Second section is a discussion on related literature survey of the work. In third section, methodology is explained in detail. Fourth section shows the results of experiments. Lastly, section five concludes the chapter followed by acknowledgment.

4.2 Related Work

While looking to develop an algorithm, we came across lots of object detection methods. We focused on automatic segmentation method in our research and also carried out a survey about pre-existing methods. We briefly summarize the state of art on segmentation algorithms available in the literature. Despeckling of medical ultrasound kidney images is necessary to remove noise while distinguishing the different tissue boundaries present nearer to each other. In [3], author has used genetic algorithms for segmentation of images of USG type. In [4], USG kidney images of different orientations are considered. Rotation of the kidney region part is performed followed by texture feature analysis. Texture model constructed is used for estimating the inner and outer area of segmentation curve. In [5], authors have proposed an evaluation method for principal curvature of multi-scale differential. Different categories of kidneys are determined using the measure of feature values and the extent of separation among these features. In [6], authors have used co-variance matrix based active shape model. Genetic algorithm is used to optimize the pose and variations in shape for the kidney shape model.

Discussion on spline of a higher order interpolation is done in [7]. Various methods for speckle removal, namely, Gaussian filter, median filter, and Wiener filter, are used before classification. Run length texture features and gray level co-occurrence matrix features are used. For classification of non-cystic and kidneys with cysts in USG medical images, the k-nearest neighbor classifier is used in [8]. Reviews of different segmentation techniques for USG images are discussed in [9]. Authors have explained generally highlighting the various techniques developed for B-mode USG medical images. Authors have carried out a survey of the methods that have been already investigated and validated the appropriateness of these different methods in

Table 4.1 Summary of existing methods

Authors and Year	Method	Remarks
Huang et al., 2013 [11]	Ellipse shape is used as a global shape and the Fisher-Trippets are applied to find the gray level nature of images.	A fixed elliptical shape is assumed for segmentation of kidney.
Spiegel et al., 2009 [12]	Active contour is used for computerized tomography images.	Every kidney image need to be pre-registered. Does not work for new images.
Hafizah and Supriyanto, 2012 [13]	Texture analysis based classification is carried out.	Does not work for all views of kidney images where the kidney may not lie in the central part of image.
Jeyakumar and Hasmi, 2013 [14]	Different segmentation methods like region-based, edge-based, watershed method and cluster-based are discussed.	No completely automated segmentation methods are found for ultrasound kidney images.

different clinical domains [9]. In [10], authors have highlighted segmentation of organs/tissues in B-mode ultrasound images. Challenges in segmentation of kidney in ultrasound images such as variable shape and size of the organ are discussed. Segmentation methods for both 2D and 3D ultrasound kidney images are explained. Summary of some more existing methods is highlighted in Table 4.1.

Most of these segmentation methods [11–14] are not fully automated. They need initial contour or seed point to be specified by the user. Thus, literature review motivated us to propose an algorithm for automatic generation of initial contour.

The key contributions of the proposed work are as follows:

Automation of segmentation
Automatic initial contour detection of kidney cysts and automation of the segmentation algorithm without user intervention or without user input.
Reducing computational time and increasing accuracy
Design of the efficient segmentation algorithm using reduced elapsed time to get more accurate segmented images of kidney cysts.
Performance of segmentation algorithms
Performance evaluation of the developed method using the parameters such as Dice coefficient, Jaccard coefficient, specificity, sensitivity, and accuracy.
Analysis of segmented kidney cyst images
Computation of number of cysts and their size are essential parameters to assist the medical experts for preparation of proper treatment plan.

4.3 Methodology

Automation of segmenting the kidney cysts in USG digital image is proposed. Figure 4.1 shows the methodology of the proposed algorithm. Image database considered for the study contains medical ultrasound images of kidney in various views, namely, transverse view and longitudinal views.

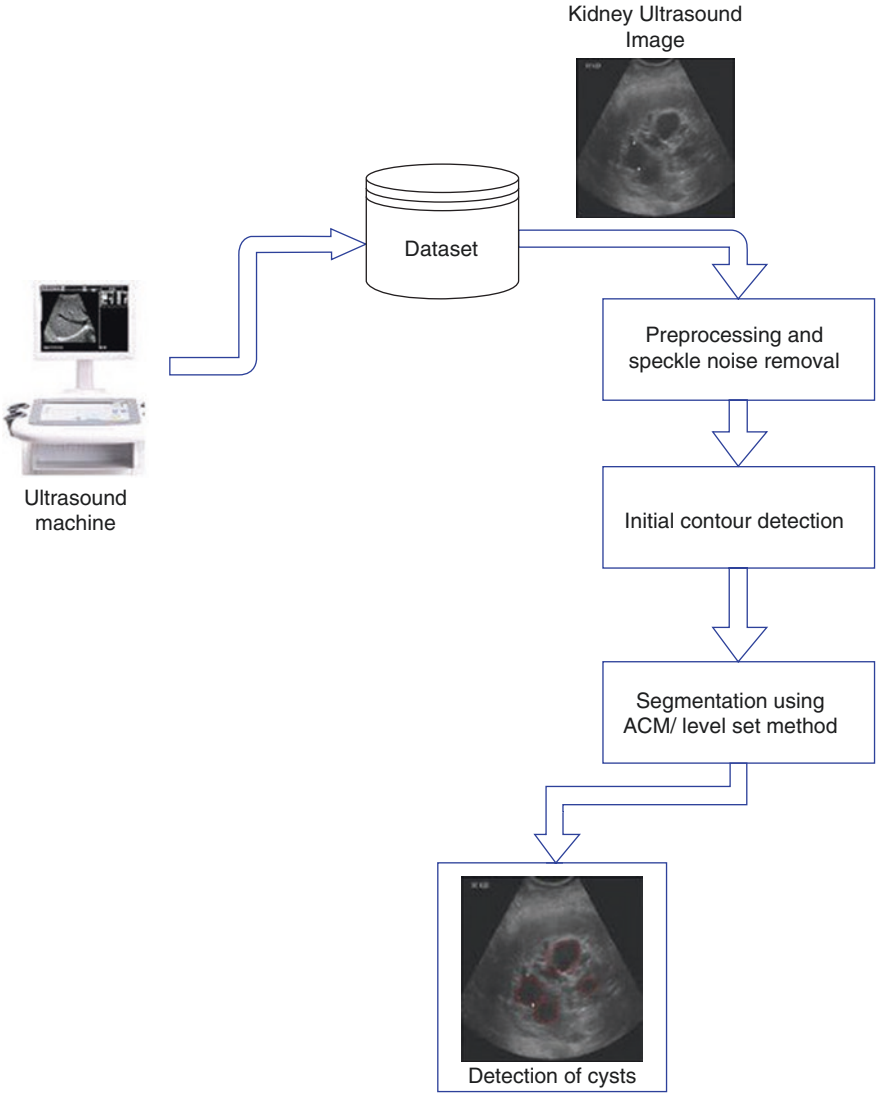

Fig. 4.1 Proposed methodology of segmentation of cysts in kidney digital ultrasound images

4.3.1 Preprocessing and Speckle Noise Removal

Ultrasound images usually contain an inherent signal noise termed as speckle noise. It is introduced by the interaction of the reflected waves from various independent scatterers within a resolution in an ultrasound system. In USG digital images of kidney, the constituent structural components along with noise are very tiny to be caught and detected by larger wavelength of ultrasound signals [15]. Speckle noise can have adverse effect in detecting the lesion. It leads to decreased image quality

of USG images to a greater extent in contrast to other modalities of medical images. Speckle contains relatively higher gray level intensities [16]. Speckle noise reduces image contrast and image resolution affecting the analytical property of USG digital images. Thus despeckling is one of the major steps required prior to the segmentation.

Contourlet transforms are more useful in smoothening of the ultrasound image contours [16]. The contourlet transform is performed in two steps. Laplacian pyramid (LP) decomposition is used in first step to capture the discontinuous points. In step two, the directional filters bank is used for connecting the points of discontinuities to frame undeviating arrangement of points. Inverse contourlet transform is used to generate despeckled image. Various steps involved in the despeckling of ultrasound image are explained in Algorithm 4.1.

Algorithm 4.1 Speckle Noise Removal of Medical Ultrasound Image of Kidney

Input: Digital ultrasound kidney image
Output: Despeckled image
Start

1. Read a digital USG image of kidney.
2. Perform log transformation of the image.
3. Perform contourlet-based transform for n_1 levels of LP decomposition and n_2 directional decomposition for individual levels.
4. Carry out thresholding.
5. Apply the inverse transform of contourlet to obtain the despeckled image.

Stop.

The values of n_1 and n_2 indicate number of levels for LP decomposition and directional decompositions for individual levels, respectively. These values depend on the image size.

In order to create more clear and distinct despeckled image, contrast enhancement is performed using histogram equalization [17]. The contrast-enhanced image (X) is brighter having more clear edges with the improved image quality.

4.3.2 Proposed Initial Contour Detection Algorithm

The aim of initial contour detection is to devise a computationally efficient method for automatic segmentation. Despeckled and enhanced image is converted into binary image. An empirically determined threshold value is used for binarization of a gray converted image. Threshold value for binarization is determined using Otsu's method. The value is selected such that the intraclass difference in black and white pixels is minimal. The morphological operators are more useful for binary image analysis such as edge detection, noise removal, and image segmentation. A series of

operations are applied on binary image to determine the region of interest (ROI) of individual cyst in an image. The various morphological operations, namely, erosion, dilation, opening, and closing, specified in Eqs. (4.1)–(4.4) are used to find individual ROI in the image.

Erosion operator deletes or erodes the boundaries of regions containing foreground pixels. Consider S, a space of Euclidean. Let I be a binary image. Erosion of an image I with structuring element S is expressed in Eq. (4.1). The details smaller than S are filtered out from I [18].

$$I \ominus S = \left\{ z \epsilon S | Sz \subseteq I \right\} \tag{4.1}$$

Sz indicates the translation operation on S by z. Dilation is used to increase the boundaries containing regions of foreground pixels. Thus it leads to enlarging the areas of foreground pixels along with filling holes within those regions [18]. Binary image I is dilated by structuring element S, which is expressed mathematically as in Eq. (4.2).

$$I \oplus S = U_{b \in S} I_b \tag{4.2}$$

I_b represents the translation of I by b. Opening and closing are making use of erosion and dilation operators and are expressed mathematically as specified in Eqs. (4.3) and (4.4). The overall effect of opening is to retain the foreground regions that are having similar shape as that of structuring element or the regions containing the complete structuring element. Closing works similar to dilation. It enlarges the foreground region boundaries in an image and shrinks or removes the holes having background color in such regions.

$$I \circ S = \left(I \ominus S \right) \oplus S \tag{4.3}$$

$$I \circ S = \left(I \ominus S \right) \oplus S \tag{4.4}$$

Further, connected components are obtained from the morphologically operated image. These components are selected as initial contour for level set segmentation method. The level set method requires initial contour to be specified by the user manually. Explicit specification of initial contour is automated in the proposed method and is automatically determined by using morphological operations. The process of detection of initial contour is explained in Algorithm 4.2.

Algorithm 4.2 Detection of Initial Contour

Input: Contrast-enhanced image (X)
Output: Initial contour generated (A)
Start

1. Read contrast-enhanced image X.
2. Convert X to a binary image I.
3. Eliminate the structures which are thinner compared to their neighboring pixels and are connected with the image boundary using erosion specified in Eq. (4.1).
4. Find out the contour matrix of image obtained.

5. Open morphological operation is carried out with structuring element (SE) of disk shape having the size of R_1 to eliminate the weaker edges using Eq. (4.3).
6. Create another SE of disk shaped having a size of R_2 pixels.
7. Apply erosion using structuring element created in step 6 on the image obtained from step 5 to eliminate spurious regions created due to noise.
8. Find the number of connected components from the image obtained from previous step and determine the bounding box region property to generate initial contour of individual regions in the image (A).

Stop.

The final output image obtained at the end of Algorithm 4.2 does not contain the regions which are having lesser area than the constants R_1 and R_2. Values of these constants are empirically identified as $R_1 = 20$ pixels and $R_2 = 10$ pixels. For this study, the ROI is automatically generated and further segmentation will be conducted using that ROI.

4.3.3 Segmentation of Cysts Using Active Contour Model (ACM)

Active contour models are also called as snakes. ACM helps in designing a framework for an object contour detection effectively for images [19] and is also suitable for noisy images such as ultrasound image. A snake is a deformable spline. Deformation model of snake is controlled by external and internal forces [20]. An external force helps in dragging the deformable spline towards object boundaries and internal force prevents the deformation. Snakes use a common method for expansion of a deformation by using an energy minimizing function. We have made use of a region-based ACM as it has some significant characteristics compared to edge-based ACM. Region-based method uses statistical information about the contour to control the deformation of the curve. We have used Chan-Vase (C-V) model [20]. The C-V model has a global virtue. It can segment any number of regions present in an image simultaneously. For an image P in domain Ω, the C-V model is expressed by the energy minimizing function as specified in Eq. (4.5).

$$\begin{aligned} E^{cv} = \lambda_1 \int \text{interior}(A) \left| P(u) - A_1 \right| du \\ + \lambda_2 \int \text{exterior}(N) \left| P(u) - A_2 \right| du \left| , u \epsilon \Omega \right. \end{aligned} \tag{4.5}$$

The constants A_1 and A_2 are the average intensities in interior and exterior of the contours. It is assumed as in Eq. (4.6), Eq. (4.7), and Eq. (4.8) respectively.

$$A = \left\{ u \epsilon \Omega : \Phi(u) = 0 \right\} \tag{4.6}$$

$$\text{Interior}(A) = \left\{ u \epsilon \Omega : \Phi(u) > 0 \right\} \tag{4.7}$$

$$\text{Exterior}(A) = \left\{ u \epsilon \Omega : \Phi(u) < 0 \right\} \tag{4.8}$$

The constants A_1 and A_2 are expressed as in Eq. (4.9) and Eq. (4.10). Working of active contour model is illustrated in Algorithm 4.3.

$$A_1(\Phi) = \frac{\int_\Omega P(x,y) H(\Phi(x,y)) dxdy}{\int_\Omega H(\Phi(x,y)) dxdy} \tag{4.9}$$

$$A_2(\Phi) = \frac{\int_\Omega P(x,y) H(1-(\Phi(x,y))) dxdy}{\int_\Omega H(1-(\Phi(x,y))) dxdy} \tag{4.10}$$

Algorithm 4.3 Active Contour Model for Segmentation of Cysts in Medical USG Images of Kidney

Input: USG kidney image with initial contour defined (A)
Output: Cysts segmented image (O)
Start

1. Read the image (A).
2. Set the function ∅(u) to zero and assign to initial contour A which is to be deformed further using Eq. (4.6).
3. Calculate interior and exterior of energy functions of initial contours of A using Eqs.(4.7–4.10).
4. Compute energy minimizing function using interior and exterior energy function values using Eq. (4.5).
5. If no change found in deformation of the zero crossing points or exceeded the number of iterations, then stop.

Otherwise, go to Step 3.
Stop.

Observations made on active contour model depicted in Algorithm 4.3 can be listed as follows:

- Proper and accurate segmentation of single cyst in kidney USG medical images.
- Unable to segment the cysts as separate regions rather it segments the group of all cysts as a single component.

4.3.4 Segmentation of Cysts Using Level Set Method

The level set method has several advantages over other segmentation methods such as parameterized ACM. Level set can better represent the complex topological contours. Also, it can efficiently manage contour merging and splitting unlike ACM as discussed in [21]. It does not require the points on a contour rather calculation is based on Cartesian grid.

Level set evolution works on choosing a surface rather than a front. The front is defined by every pixel where the surface height is zero. Apart from widely used applications, traditional level set method suffers from a drawback. The irregularities of the level set function (LSF) during its deformation lead to erroneous results. As a solution to this problem, reinitialization [22, 23] was proposed. Reinitialization helps in maintaining LSF regularity. In the proposed method, LSF used indicates a distance function with sign to abort and/or continue the evolution of contour with reinitialization. We have used an evolution of level set based on distance regularization [22]. A region-based level set method for segmentation of cysts in ultrasound image specified is represented using Algorithm 4.4. In this work, the regularity of the LSF level controls the evolution by means of a forward and backward diffusion obtained from distance regularization. Initially the image smoothening is performed using Gaussian kernel function with standard deviation of σ. Let us consider input image A, an edge indicator function f can be expressed as in Eq. (4.11). This performs image smoothening.

$$f \cong \frac{1}{1+\nabla G_a * A^2} \tag{4.11}$$

G_σ is a Gaussian kernel function with standard deviation of σ. An energy function E(∅) used for a LSF is as in Eq. (4.12).

$$\mathrm{E}(\varnothing) = \mu R_p(\varnothing) + \mathrm{Eext}(\varnothing) \tag{4.12}$$

E(∅) is energy function and R_p(∅) is level set regularization term and is defined as in Eq. (4.14). Eext (∅) is external energy which depends on the data under consideration. External energy is defined as in Eq. (4.13). μ is a constant and its value is always greater than zero.

$$\mathrm{Eext}(\varnothing) = \lambda L(\varnothing) + \alpha A(\varnothing) \tag{4.13}$$

$$R_p(\varnothing) = \int P(\|\nabla\varnothing\|)\Omega \mathrm{du} \tag{4.14}$$

Value of λ is greater than 0. α is energy coefficients for functions L(∅) and A(∅). They can be defined as in Eqs. (4.15) and (4.16).

$$\mathrm{L}(\varnothing) \cong \int_\Omega \mathrm{g} \cdot \mathrm{del}(\varnothing) \nabla\varnothing \mathrm{du} \tag{4.15}$$

$$\mathrm{A}(\varnothing) \cong \int_\Omega \mathrm{g} \cdot \mathrm{H}(-\varnothing) \mathrm{du} \tag{4.16}$$

where del is Dirac delta function and H indicates Heaviside function. L(∅) calculates the energy of the line integral of g along the initial zero level contour. A(∅) determines weighted area of the region. It increases the speed of contour deformation in the level set. Also, it is essential if the zero level contour is specified away from the actual contour [24].

Algorithm 4.4 Level Set Segmentation of Cysts in Medical USG Images of Kidney

Input: USG kidney image with initial contour defined (A)
Output: Segmented cystic kidney image (O)
Start

1. Perform smoothening on image (A) using Gaussian kernel using Eq. (4.11).
2. Obtain partial differentiation of edge indicator function of the image obtained in previous step.
3. Compute distance regularization using Eq. (4.14).
4. Compute Dirac delta function and Heaviside function.
5. Compute energy function using Eq. (4.12) and the parameters obtained in step 3 and step 4.
6. If no change in deformation of the zero crossing points or reached predefined maximum number of iterations, then stop and return output image O. Otherwise, go to Step 2.

4.3.5 Analysis of Segmented Images

It is equally essential to carry out the analysis of the segmented results. In this reasoning step, the number of cysts and area of cysts are calculated by applying the binarization method. The segmented image is converted into binary form, represented with pixel values either 0 or 1. The number of connected components in the binary image gives us a count of number of cysts. By measuring the number of black pixels covering the cyst portion, area of cyst can be obtained, applying Eq. (4.17) as specified in [23].

$$\text{Area} = \sqrt{\text{N}}\text{X}0.264 \tag{4.17}$$

N represents the area of connected component representing the cystic region in pixels. Area obtained is multiplied by the square root of N with the constant 0.264, because, "1mm is equal to 0.264 pixels."

4.3.6 Performance Evaluation Parameters

Analysis of quantitative performance of the implemented algorithm is carried out by using Dice coefficient and Jaccard coefficient [23, 25]. These are used to measure the accuracy of segmentation algorithms. Dice is expressed as in Eq. (4.18) and Jaccard coefficient is expressed with Eq. (4.19).

$$\text{D}\left(\text{R}_1,\text{R}_2\right) = \frac{2\left|\text{R}_1 1 \cap \text{R}_2\right|}{\left|\text{R}_1\right| + \left|\text{R}_2\right|} \tag{4.18}$$

$$JC = \frac{|R_1 \cap R_2|}{|R_1 \cup R_2|} \tag{4.19}$$

where R_1 is the reference region obtained from ground truth and R_2 is a region segmented by proposed method. The value of Dice coefficient ranges between 0 and 1. For complete and exact overlap of two regions, the Dice value is 1; if there is no overlap between the two regions, then its value will be 0.

The Jaccard coefficient (JC) is another metric used to find the region-based similarity between two images considered for the study. JC is defined by taking the ratio of size of intersection of images and the size of union of the sample images. The value of JC lies between 0 and 1. For exact match of the images, JC value is 1 and results into 0 for no match between the images.

Efficiency of segmentation algorithms applied on medical images is also calculated by means of finding specificity, sensitivity, and accuracy [25]. These parameters are calculated by finding true positives, true negatives, false positives, and false negatives. True positive is obtained by finding the intersection between segmented region and region in the ground truth. False positive is the unmatched segmented region not overlapping with the region in the ground truth. False negative is the missed part of the ground truth. True negative is obtained by finding part of image beyond the union output image and ground truth.

4.4 Results and Discussions

Implementation and results obtained for the proposed algorithms are discussed in this section.

4.4.1 Experimental Setup

The experimentation is carried out on a system of Intel core i5 processor with 10 GB RAM and 2.50 GHz processor. MATLAB R2016b software is used for implementation of algorithms. Medical USG digital kidney images of varying sizes and varying orientations are used to carry out the experimentation. The image database is categorized as D1 and D2. D1 contains dataset of USG kidney images prepared in consultation with the medical experts, namely, radiologist and nephrologists of BLDEDU's Shri. B. M. Patil Medical College Hospital and Research Centre, Vijayapur for the present study. Some of the images (D1) are captured from Philips HD11XE ultrasonography machine with curvilinear transducer of 5–7 MHz frequency. Some of the images (D2) are obtained from publicly available websites [https://openi.nlm.nih.gov, https://www.sonoworld.com, and https://www.ultrasoundimages.com]. The experimentation and testing are performed on entire dataset.

4.4.2 Preprocessing and Speckle Noise Removal

For despeckling, contourlet transform with two filter banks is used. In Laplacian pyramidal decomposition, biorthogonal filters are taken. For the stage of directional decomposition, Phoong-Kim-Vaidyanathan-Ansari (PKVA) filters are used. Hard thresholding is performed further. We have used two levels of LP decomposition with six directional band pass sub-bands and hard thresholding further, to get better results as specified in Hiremath et al. [16]. Despeckled image is contrast enhanced using histogram equalization. The contrast-enhanced image is brighter having more clear edges with improved image quality.

4.4.3 Initial Contour Detection

Kidney organ can have more than one cysts developed in it. This leads to an abnormal condition called polycystic kidney disease (PCKD). We have carried out segmentation of multiple cysts in kidney USG digital images. Figure 4.2 is used to demonstrate the robustness of the proposed approach of automatic initial contour detection. After despeckling, image is converted to binary form. We have applied morphological operators as specified in Algorithm 4.2 to get initial contour. Despeckled and contrast-enhanced image of the sample image using histogram equalization is depicted in Fig. 4.2a. Binarized image of contrast-enhanced image is

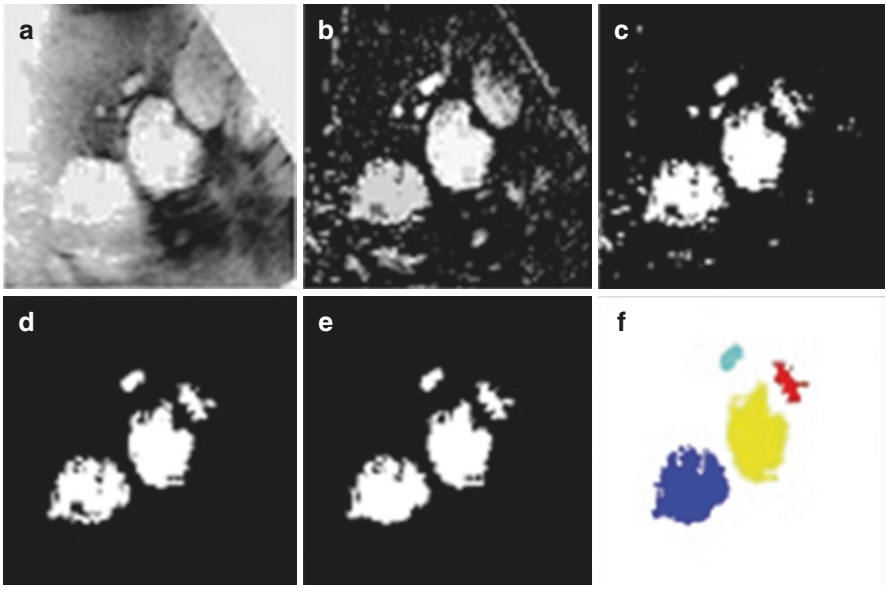

Fig. 4.2 Various stages of finding initial contour: (**a**) Contrast-enhanced image (**b**) Image after eliminating lighter components near border in gray form (**c**) Binary converted image (**d**) Morphologically opened image (**e**) Filled image (**f**) Morphologically segmented regions

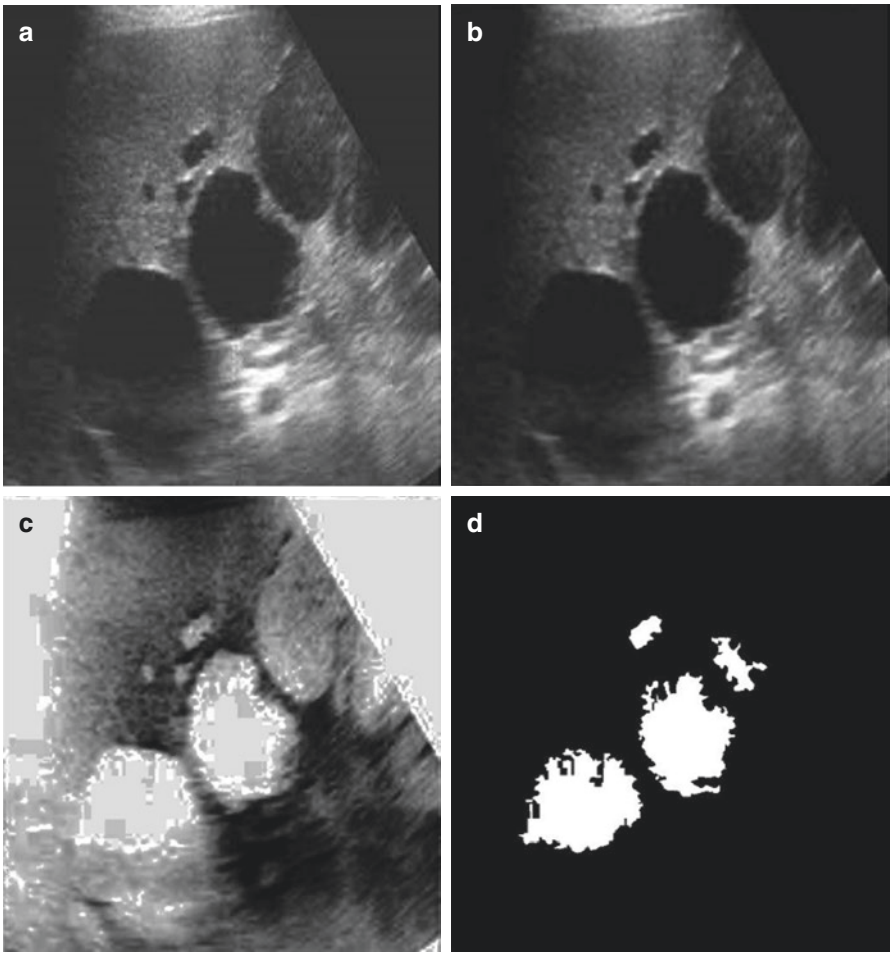

Fig. 4.3 (**a**) Original polycystic USG image (**b**) Despeckled image (**c**) Contrast-enhanced image (**d**) Morphologically operated image

shown in Fig. 4.2b. Elimination of lighter components near the border is carried out resulting into Fig. 4.2c. Morphological open operation and process of filling holes are carried out sequentially as revealed in Fig. 4.2d, e, respectively. Figure 4.2f demonstrates clear distinctions of various regions represented in color form. These regions can be used to determine the initial contour for segmentation of polycystic regions.

Figure 4.3 shows the generation of initial contour for polycystic kidney ultrasound image using the proposed Algorithm 4.2. Figure 4.3a–d shows the images of polycystic kidney USG image, despeckled image, contrast-enhanced image, and morphologically operated image to obtain the initial contour for segmentation algorithms. Thus, the stage of initial contour detection obtains the approximate boundary for required ROI successfully.

4.4.4 Segmentation of Cyst in Single-Cystic Kidney USG Images

Kidney cyst is a fluid-filled sac, inhibiting the functionality of kidney organ. We have proposed two algorithms for segmentation of cysts in kidney USG images. Initial contour required for segmentation is identified by using Algorithm 4.2. Despeckled image of Fig. 4.4a is shown in Fig. 4.4b. This is further contrast enhanced using histogram equalization as depicted in Fig. 4.4c. Further, the image is converted to binary form. We have applied morphological operators as specified in Algorithm 4.2 to get initial contour as depicted in Fig. 4.4d.

The boundaries of a single component obtained in Fig. 4.4d are used as initial contour by ACM and level set segmentation methods. Thus, explicit specification of manual input for generation of initial contour needed by segmentation algorithms is completely eliminated. Figure 4.5 shows various stages involved in ACM segmentation model. Initial contour (Fig. 4.5a) is calculated on the basis of image in Fig. 4.4d. Intermediate deformation is shown in Fig. 4.5b and final

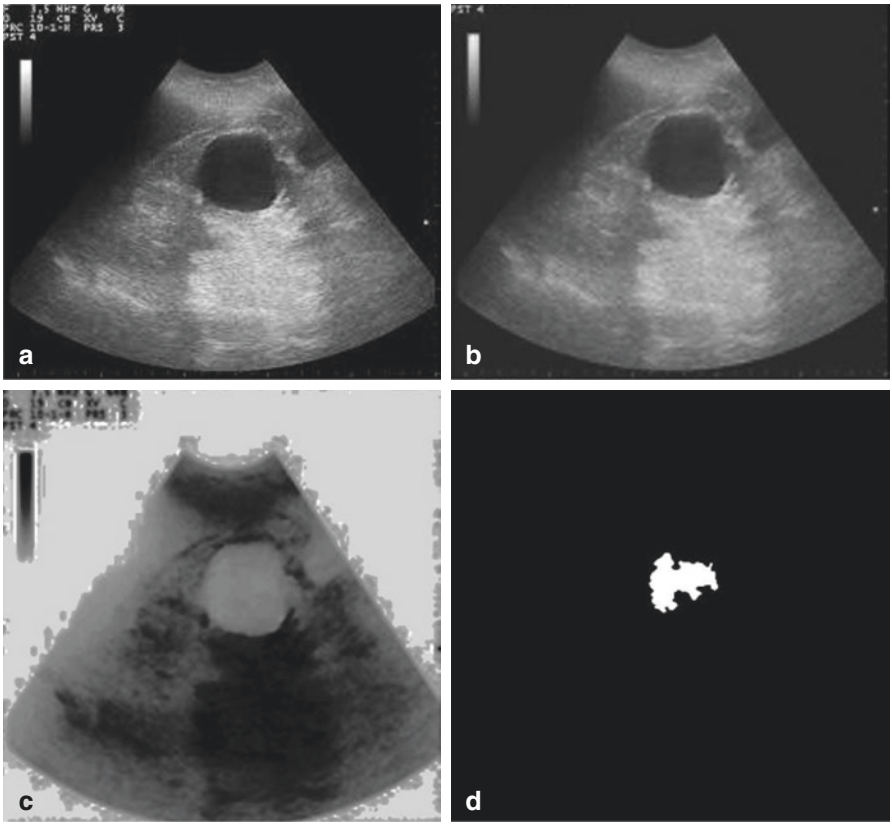

Fig. 4.4 (**a**) Original single-cystic USG image (**b**) Despeckled image (**c**) Contrast-enhanced image (**d**) Morphologically operated image

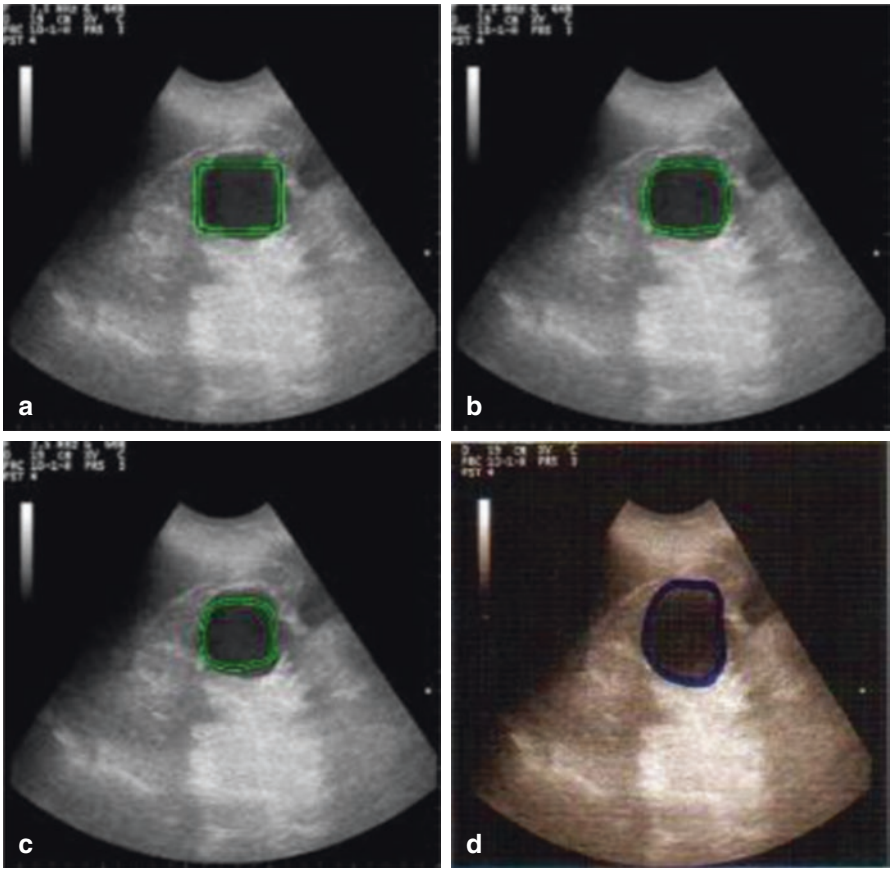

Fig. 4.5 ACM segmentation stages: (**a**) Initial contour (**b**) Intermediate deformation (**c**) Final segmented region boundary (**d**) Ground truth

segmented region is as in Fig. 4.5c. Accuracy of segmentation is confirmed by taking a ground truth by medical expert as shown in Fig. 4.5d. A good agreement is found between experimentally segmented image and manual segmentation by nephrologist.

We have also performed level set segmentation method on images after morphological operations as in Fig. 4.6. Initial contour in Fig. 4.6a is calculated on the basis of image in Fig. 4.4d. Figure 4.6(a, c) show the LSF at initial level and after complete evolution, respectively. For this example, complete evolution is completed in 305 iterations. Figure 4.6(b, d) show the behavior of LSF using a graph at initial level and after complete evolution, respectively. Thus the algorithm perfectly segments cysts in the image automatically. Further, the size of the segmented cyst is calculated by applying the formula specified in Eq. (4.17). The size for the cyst for the image shown in Fig. 4.6c is 27.6 mm^2. ACM segmentation algorithm can perfectly segment the single cysts in kidney ultrasound images.

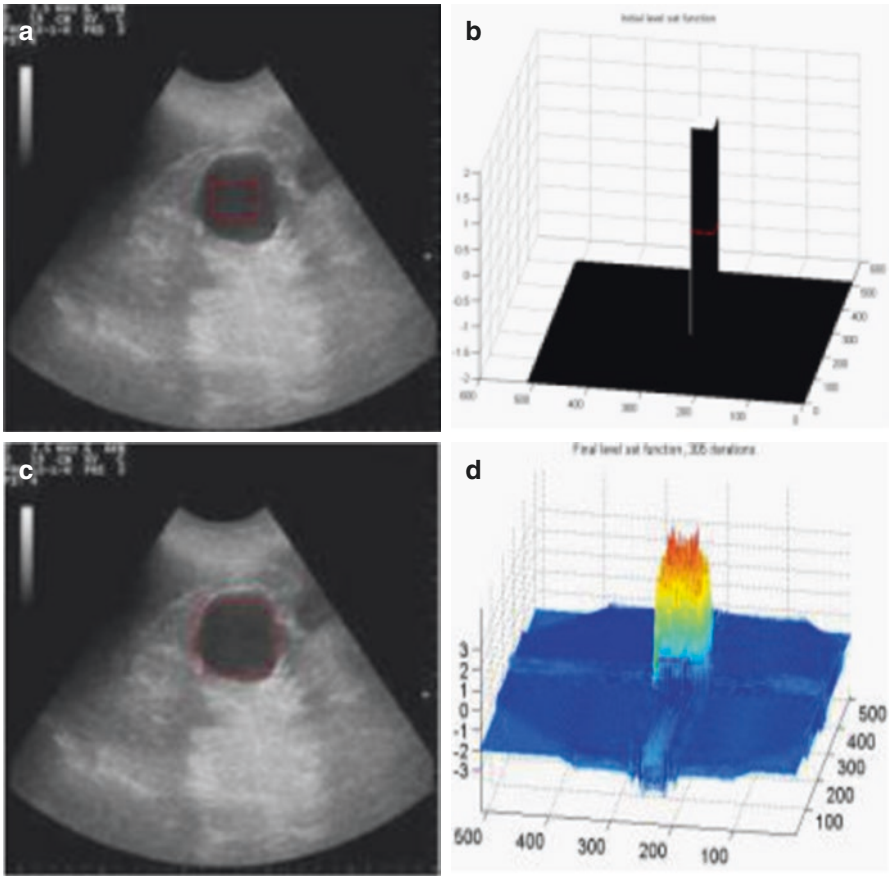

Fig. 4.6 Level set segmentation stages for single-cystic kidney image: (**a**) Initial contour (**b**) Behavior of LSF at initial stage (**c**) Final segmented region boundary of cyst (**d**) Behavior of LSF at final stage

4.4.5 Segmentation of Multiple Cysts in Kidney USG Images

Active contour model (ACM) also called as snake model is also suitable for noisy images such as ultrasound image. We have implemented region-based C-V (Chan–Vese) model for segmentation of polycystic kidney ultrasound images. Figure 4.7 shows various stages involved in segmentation of kidney USG images of polycystic kidney using ACM. Figure 4.7a shows original image, Fig. 4.7b segmentation by ACM, Fig. 4.7c shows ground truth by medical experts. Figure 4.7b shows that the ACM method is unable to segment individual cysts separately in case of polycystic kidney images. It is also not possible to analyze the individual cyst size.

We have also performed level set segmentation method on polycystic kidney medical USG images using automatically generated initial contour, as depicted in Fig. 4.8. Figure 4.8a shows initial contour calculated for the sample image

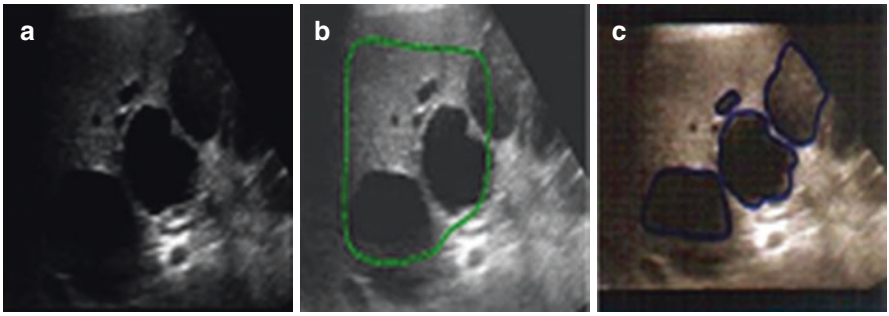

Fig. 4.7 ACM segmentation for polycystic kidney image: (**a**) Original image (**b**) Segmentation by ACM (**c**) Manual segmentation by expert

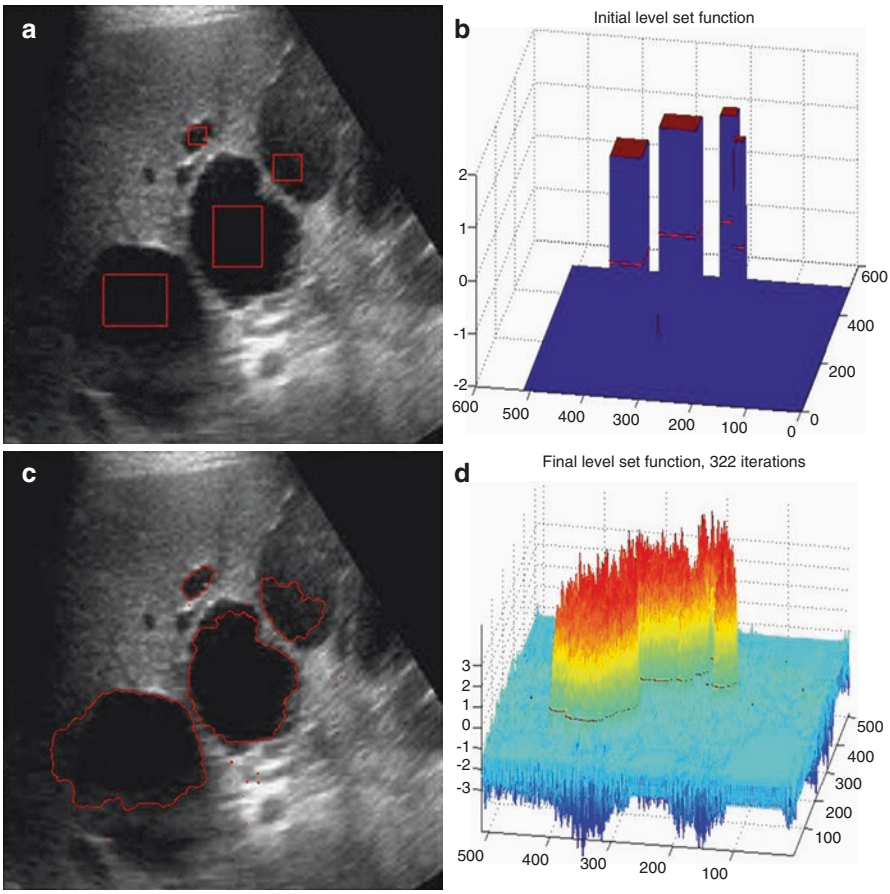

Fig. 4.8 Level set segmentation stages for polycystic kidney image: (**a**) Initial contour (**b**) Behavior of LSF at initial stage (**c**) Final segmented region boundary (**d**) Behavior of LSF at final stage

calculated using proposed Algorithm 4.2. Final segmented region is as in Fig. 4.8c. Figure 4.8(a, c) show the LSF at initial level and after complete evolution, respectively. After 322 iterations, the zero level contour converges to a desired object boundary as shown in column 2 of Fig. 4.8. Figure 4.8(b, d) show the behavior of LSF using a graph at initial level and after complete evolution, respectively. Level set clearly segments individual cysts as in Fig. 4.8c. Thus, level set segmentation method works perfectly on polycystic kidney ultrasound images. The segmented image is converted into binary form. From the binary image, we calculated the total number of pixels in each cyst and applied Eq. (4.17) to find the area of individual cysts. For the sample image shown in Fig. 4.8c, the area of four cysts is determined as 26.8 mm^2, 7.56 mm^2, 26.95 mm^2, and 10.24 mm^2. Thus, automatic segmentation and analysis has a greater impact in the field of medicine. It relaxes the medical experts from manual marking and evaluation of the size of cystic region in kidney ultrasound images.

4.4.6 Performance of Segmentation Methods

Performance of the implemented algorithm is analyzed by using Dice coefficient, Jaccard coefficient, and statistical parameters such as sensitivity, specificity, and accuracy. Figure 4.9a, b depict the values of these parameters for single-cystic and polycystic images, respectively. Average, minimum, and maximum values are calculated by taking into account of all the images in D1 (clinical) and D2 (web) dataset. Obtained values demonstrate the accuracy of the segmentation method. Level set method results into more accurate segmentation. Segmentation using ACM method is also carried out and comparison of level set method with ACM is shown in the plots of Fig. 4.9. It contains the results obtained for both D1 and D2 datasets separately. Results obtained demonstrate the efficiency of level set method over ACM method. From Fig. 4.9, it is clear that level set segmentation is found to be better segmentation algorithm for cystic kidney USG images.

Figure 4.10 shows the average elapsed time in seconds for the complete segmentation of the cysts in renal medical ultrasound images. It demonstrates the average elapsed time for single and polycystic images considering individual datasets (D1 and D2) separately. Plots obtained for both ACM and level set segmentation methods are shown in Fig. 4.10. Average elapsed time varies from 6.3 to 9.5 s on a standalone machine of i5 processor. Developed automatic segmentation method improves the accuracy of segmentation of kidney cysts in ultrasound images with reduced elapsed time.

Comparison of the proposed method is made with the method proposed in [13]. They have generated an initial contour by the assumption that kidney organ always lies in the center of USG image. A larger central part of the kidney ultrasound image of the same size is used as initial contour always. A larger initial contour increases the number of iterations in segmentation algorithms. This problem is resolved in our proposed method using morphological operations for automatic initial contour generation. Promising and more accurate results of segmentation in our proposed

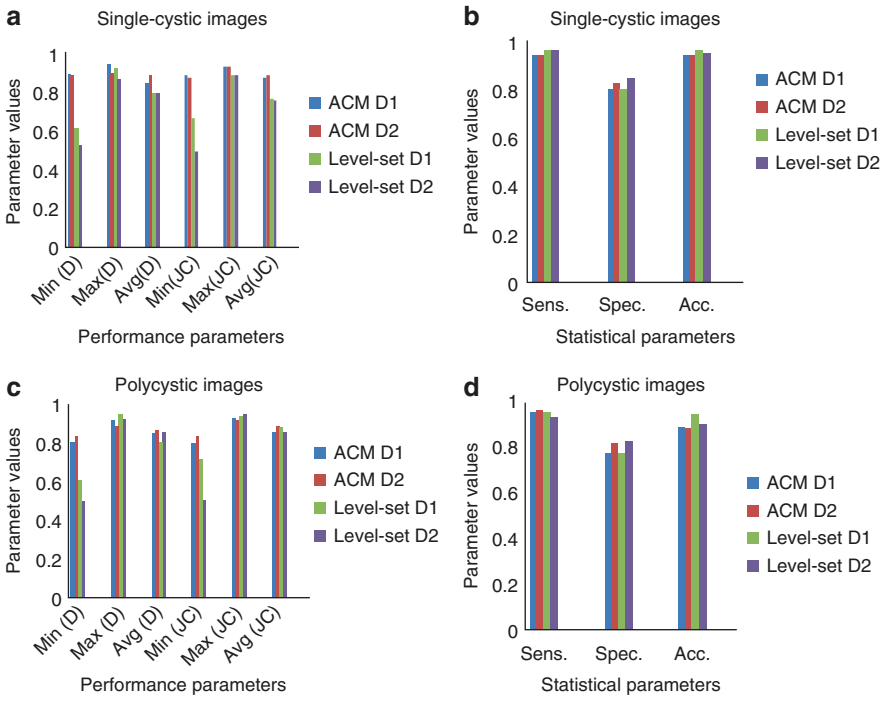

Fig. 4.9 Performance analysis of segmentation: (**a**) Statistical parameters for single-cystic images (**b**) Analytical parameters for single-cystic images (**c**) Statistical parameters for polycystic images (**d**) Analytical parameters for polycystic images

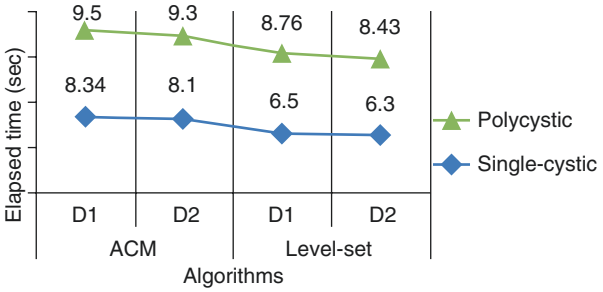

Fig. 4.10 Elapsed time for segmentation of cystic images

method are compared with the method specified in [26]. Gradient vector snakes method specified by the authors segments a single region for the entire group of cysts in polycystic kidney ultrasound images. Hence, information like number of cysts and their individual sizes cannot be revealed. Also, performance and statistical parameters used for verification of segmentation results are proposed.

4.5 Conclusion

In this chapter, segmentation algorithms, namely, active contour model and level set method, are proposed for segmenting the cysts in digital ultrasound images of kidney. Initially, denoising of USG images is performed effectively using contourlet transform and contrast enhancement using histogram equalization. Both of these segmentation algorithms require initial contour as input. In the proposed work, we have generated initial contour automatically using morphological operators. Thus, cysts segmentation algorithm using ACM and level set are automated. The performance of the segmentation is measured using Dice coefficient, Jaccard coefficient, sensitivity, specificity and accuracy. Maximum of 0.977 for Dice coefficient and 0.956 for Jaccard coefficient is obtained. Average values of sensitivity, specificity, and accuracy obtained are up to 0.995, 0.847, and 0.972, respectively. Elapsed time for segmentation varies from 6.3 to 9.5 s. Thus automatic identification of initial contour shows improvement in speed and accuracy of further segmentation process using level set segmentation method. This model also shows the analysis of the cystic kidney disease by determining the number of cysts and their sizes. The proposed method can be effectively utilized for medical applications.

Acknowledgements The authors are thankful to Dr. Bhushita B. Lakhkar, Radiologist, BLDEDU's Shri. B. M. Patil Medical College Hospital and Research Centre, Vijayapur for providing USG image set of kidney. Authors are also thankful to Dr. Vinay Kundaragi, Nephrologist, BLDEDU's Shri. B. M. Patil Medical College Hospital and Research Centre, Vijayapur for rendering manual segmentation of images. This work is financially supported by Vision Group of Science and Technology (VGST), Government of Karnataka under RGS/F scheme.

References

1. Hagen-Ansert S. Urinary system. Diagnostic ultrasonography-diagnostic ultrasound. St. Louis: Mosby; 1995.
2. Pollack HM, McClennan BL. Clinical urography. 2nd ed. Reading: W.B. Saunders; 2000. p. 1817–23.
3. Maulik U. Medical image segmentation using genetic algorithms. IEEE Trans Inform Tecnol Biomed. 2009;13(2):166–73.
4. Xie J, Jiang Y, Tsui H. Segmentation of kidney from ultrasound images based on texture and shape. Prioris IEEE Trans Med Imag. 2005;24(1):45–57.
5. Raja KB, Madheswaran M, Thyagarajah K. Quantitative and qualitative evaluation of US kidney images for disorder classification using multi-scale differential features. ICGST-BIME J. 2000;7:1):1–8.
6. Mendoza CS, Kang X, Safdar N, Myers E, Peters CA, Linguraru MG. Kidney segmentation in ultrasound via genetic initialization and active shape models with rotation correction. Proc IEEE Symp Biomed Imag (ISBI'13) 2013; 69–72.
7. Raja KB, Madheswaran M, Thyagarajah K. A general segmentation scheme for contouring kidney region in ultrasound kidney images using improved higher order spline interpolation. Int J Biological and Life Sci. 2007;2(2):81–8.
8. Akkasaligar Prema T, Biradar S. Classification of medical ultrasound images of kidney. Int J Comput Appl 2014. (ISSN:0975–8887). Special Issue on ICICT. 2014:32–6.

9. Noble JA, Boukerroui D. Ultrasound image segmentation: a survey. IEEE Trans Med Imag. 2006;25(8):987–1010.
10. Meiburger KM, Acharya UR, Molinari F. Automated localization and segmentation techniques for B-mode ultrasound images: a review. Comput Biol Med. 2018;92:210–35.
11. Huang J, Yang H, Chen Y, Tang L. Ultrasound kidney segmentation with a global prior shape. J Vis Commun Image Rep. 2013;24:937–43.
12. Spiegel M, Dieter AH, Volker D, Jakob W, Joachi H. Segmentation of kidney using a new active shape model generation technique based on non-rigid image registration. J Comput Med Imag Graph. 2009;33:29–39.
13. Hafizah WM, Supriyanto E. Automatic generation of region of interest for kidney ultrasound images using texture analysis. Int J Biol Biomed Eng. 2012;6(1):1289–305.
14. Jeyakumar V, Hasmi MK. Quantitative analysis of segmentation methods on ultrasound kidney image. Int J Adv Res Comput Commun Eng. 2013;2(5):2319–5940.
15. Burckhardt C. Speckle in ultrasound B- mode scans. IEEE Trans Sonics Ultrason. 1978;25:1–6.
16. Hiremath PS, Akkasaligar Prema T, Badiger S. Speckle reducing Contourlet transform for medical ultrasound images. World Acad Sci Eng Technol Special J Issue. 2011;80:1217–24.
17. Agarwal T, et al. Modified histogram based contrast Enhancementusing Homomorphic filtering for medical images. Paper presented at International Advance Computing Conference (IACC) 2014 Gurgaon, New Delhi, India,21st-22nd Feb 2014, p 964–968.
18. Sonka Milan VH, Roger B. Image processing, analysis and machine vision, 3rd ed. Cengage Learning, Boston. 2013:630–5.
19. Cohen LD, Cohen I. A finite element method applied to new active contour models and 3D reconstruction from cross sections. Paper presented at the 3rd international conference on computer vision, Osaka, Japan, 1990; p 587–591.
20. Chan T, Vese L. Active contours without edges. IEEE Trans Image Proc. 2001;10(2):266–77.
21. Sussman M, Smereka P, Osher S. A level set approach for computing solutions to incompressible two-phase flow. J Comput Phys. 1994;114(1):146–59.
22. Osher S, Fedkiw R. Level set methods and dynamic implicit surfaces. New York: Springer; 2002.
23. Udupa JK, LeBlanc VR. Methodology for evaluating image segmentation algorithms SPIE medical imaging; 2002.
24. Li C, Xu C, Gui C, Fox MD. Level set evolution without re-initialization: A new variational formulation. IEEE Trans Image Process. 2010;19(12):3243–54.
25. Cerrolaza J, et al. Quantification of kidneys from 3D ultrasound in pediatric hydronephrosis. IEEE International Symp. 2015:157–60.
26. Akkasaligar Prema T, Biradar S. Analysis of polycystic kidney disease in medical ultrasound images. Int J Med Eng Inform. 2018;10(1):49–64.

5 Noninvasive Imaging Techniques of Metal Nanoparticles and Their Future Diagnostic Applications

Sourav Das, Rajesh Kotcherlakota, and Chitta Ranjan Patra

Abbreviations

ABC	Accelerated blood clearance
AgNPs	Silver nanoparticles
AuNPs	Gold nanoparticles
CARS	Coherent anti-Stokes Raman scattering
CeO2	Cerium dioxide
CNS	Central nervous system
CT	Computed tomography
ESIONs	Extremely small iron oxide nanoparticles
FDA	Food and drug administration
FITC	Fluorescein isothiocyanate
FRET	Fluorescence resonance energy transfer
GBNs	Gadolinium based-nanoparticles
GSH	Glutathione
IgG	Immunoglobulin G
IGT	Image guided therapy
LLC	Lewis lung carcinoma
MAP	Maximum intensity projections
MCS	Merocyanines
MPR	Magnetic resonance-photoacoustic-Raman

S. Das · R. Kotcherlakota (✉) · C. R. Patra (✉)
Department of Applied Biology, CSIR-Indian Institute of Chemical Technology, Hyderabad, Telangana, India

Academy of Scientific and Innovative Research (AcSIR), Ghaziabad, UP, India
e-mail: crpatra@iict.res.in

A. K. Shukla (ed.), *Medical Imaging Methods*,
https://doi.org/10.1007/978-981-13-9121-7_5

MRgFUS	Magnetic resonance-guided focused ultrasound
MRI	Magnetic resonance imaging
MRS	Magnetic relaxation switch
MSOT	Multispectral optoacoustic tomography
NIH	NIH-3T3- Mouse embryonic fibroblast cell line
OCT	Optical coherence tomography
PAA	Polyacrylic acid
PAI	Photoacoustic imaging
PEG	Polyethylene glycol
PLGA	Poly(lactic-co-glycolic acid)
PSMA	Prostate-specific membrane antigen
QDs	Quantum dots
SCC	Squamous cell carcinoma
SERS	Surface-enhanced Raman spectroscopy
SiNPs	Silica nanoparticles
SKOV3	Human breast cancer cell line
SLN	Sentinel lymph node
SPIONs	Superparamagnetic iron oxide nanoparticles
SP-PCL	Spiropyran-terminated poly(ε-caprolactone)
$Ti(SP)_4$	Tetra spiropyran titanate
TiO2	Titanium oxide
UCL	Upconversion luminescence
UCNPs	Upconversion nanoparticles
ZnO	Zinc oxide

5.1 Background of Bio-imaging

Bio-imaging aids in diagnosis of diseases using less invasive methods and specific image guided treatments [1]. The fields of biology and medicine require bio-imaging to visualize the anatomical structures and their function for diagnosis of the disease and treatment. Medical imaging is an interdisciplinary field that employs the basis of physics, statistics, mathematics, computer science, radiology, biology, nuclear medicine, etc. [2]. Several technological advancements occurred over the last several decades and emerged with new applications [2]. Significant development has been shown in the field of bio-imaging over the last 50 years. The discovery of X-ray in 1895 by Wilhelm Conrad Roentgen has revolutionized the area of bio-imaging which further strengthened by contrast agents used to visualize bones and blood vessels [3]. Further, nuclear biomedical imaging method has emerged as potent technique with the use of gamma cameras. By 1906–1912, the application of pharmaceutical contrast agents advanced the field of medical radiography for imaging blood vessels and organs in the body. From 1971 to present, many other imaging techniques are implemented in medical imaging in order to improve the image quality and explore various advancements. Different bio-imaging techniques that are

being used are X-ray-based imaging, magnetic resonance imaging (MRI), fluorescence-based imaging, computed tomography (CT), Raman based imaging, luminescence upconversion imaging, etc.[4].The following section describes the applications of various bio-imaging methods.

5.1.1 Types of Bio-imaging

The techniques of various bio-imaging methods used for the diagnosis of the different diseases are described below:

- **Computed tomography (CT):** From the introduction in 1970s, CT has modernized the disease diagnosis [5]. CT has many applications than other imaging methods because of its lesser time to perform and mostly available to doctors for conforming the diseases [6].
- **X-ray microscopy:** This is an important tool for cellular imaging. X-rays generally obviate the need of sectioning of the specimens as they can penetrate easily into the thick biological samples [7].
- **Magnetic resonance imaging (MRI):** MRI employs a magnetic field and radio waves for imaging organs and tissues of the body. This imaging technique has changed the field of diagnosis by avoiding the exposure to harmful ionizing radiation [8].

Other techniques are demonstrated in the latter sections of this review article.

5.2 Nanotechnology and Its Role in Bio-imaging

Nanotechnology plays crucial role in bio-imaging. The following sections will discuss the various roles of nanoparticles in bio-imaging use in different techniques.

5.2.1 Metal-Based Nanoparticles for Bio-imaging

Over the past decades, the field of nanotechnology has been grown in a wide range for various fields. Multifunctional metal-based nanoparticles are introduced by various scientists all over the world to treat various diseases such as cancer, diabetes, cardiovascular diseases, etc. [9–11]. The diagnosis and the therapy as well as monitoring the therapeutic efficacy of various diseases became fruitful after the usage of various imaging techniques. The high surface to volume ratio, size, and solubility of nanoparticles help in moderating the pharmacodynamics and pharmacokinetics profiles of various agents (therapeutic, imaging) in enhancing their therapeutic efficacy [12]. Researchers are still probing new nanomaterials for better efficacy in therapeutic as well as diagnostic purpose. Figure 5.1 shows the usage of inorganic nanoparticles for therapy and imaging of tumor [12]. It has been observed that due to the tunable size, easy fabrication, generation of ROS (reactive oxygen species),

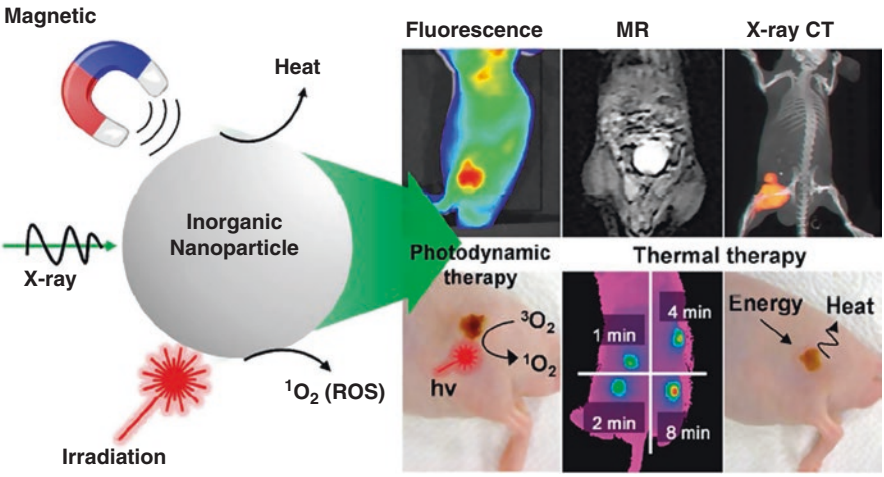

Fig. 5.1 Inorganic nanoparticles for tumor imaging and therapy. Reprinted with permission from [12]. Copyright © 2016 American Chemical Society

energy transfer, X-ray absorption, and properties, inorganic nanoparticles are favorable choice for image guided therapy (IGT) as well as in bio-imaging.

5.2.1.1 Fluorescence-Based Imaging

Since long time, the fluorescence-based nanoparticles have been using for imaging of various cells, tissues, organs, etc. for the biomedical applications which advanced the current labeling technology. Dyes such as indocyanine green and fluorescein are conventionally used. Fluorescence detection method generally depends on either emission from externally administered markers (fluorescent) or the autofluorescence of the tissues coming from different concentrations of the fluorophores (endogenous) or fluorescent materials induced [13, 14]. For example, Lai et al. prepared FRET (fluorescence resonance energy transfer) based monitoring system (real) which consisted four components, a) mesoporous silica nanoparticles for drug carrier which was further labeled with coumarin (donor); b) FITC (acceptor) attached beta cyclodextrin in order to trap the drugs inside the nanoparticles; c) to release the drug molecule in a redox-responsive manner through disulfide linkage; d) coumarin and FITC as FRET donor-acceptor pair for observing the drug release [15]. The authors observed that under non-reducing conditions the disulfide bond was intact that assisted the FRET between coumarin (donor) and FITC (acceptor). The close proximity of both the donor and acceptor helped the process. The group showed that in presence of glutathione (GSH), no FRET was observed between donor and acceptor because of the breakage of disulfide bond. This process helped in the drug release from the nanoparticles. The group mentioned that the donor-acceptor pair could operate the drug release process by changing the FRET signal in real time. On the other hand, Nakamura et al. prepared fluorescent organosilica nanoparticles coated with PEG by one-step process for bio-imaging [16]. The group

evaluated the stealth function of the nanoparticles by observing the kinetics, patterns, and uptake of these nanoparticles using flow cytometry analysis and single cells time-lapse microscopic imaging. Additionally, they observed that stealth function was not observed in case of PEG-insensitive macrophages, whereas it mostly observed in PEG-sensitive macrophages. Finally, the interaction of the nanoparticles with the immune cells helped in understanding the accelerated blood clearance (ABC) phenomenon. Not only the silica-based nanoparticles, but also the carbon dots are used as fluorescent-based imaging probes. For example, Bhunia et al. chemically synthesized the carbon dot nanoparticles (size within 1–10 nm) for cell imaging that exerted tunable emission in the visible region (blue to red) in a size dependent manner [17]. They further modified these nanoparticles by surface functionalization for cell imaging probes. Altogether, the authors concluded that these non-toxic carbon dot nanoparticles could be used as an alternative to toxic nanoparticles (cadmium based) useful for biomedical applications. In another example, Li et al. used the next generation optical imaging method for noninvasive imaging of tumor metastasis and vessel by near infrared emission (beyond 1500 nm) that showed high sensitivity and resolution (spatial) [18]. The group prepared polyacrylic acid (PAA)-modified $NaLnF_4$:40Gd/20Yb/2Er nanorods (Ln = Y, Yb, Lu, PAA-Ln-NRs) having downshifted NIR-IIb emission. To validate its applicability, the PAA-Lu-NRs were used in cancer therapy for small tumor detection in Lewis lung carcinoma (LLC) tumor-bearing mouse model. The schematic representation of the small tumor diagnosis in vivo model was carried out using PAA-Lu-NRs as shown in Fig. 5.2a. The PAA-Lu-NRs were intravenously injected inside the tumor-bearing mouse and images were captured at various time points (1–60 h) as shown in Fig. 5.2b. At 1 h time point, the signals were mainly observed in spleen and liver. After 24 h the signals were found in the tumor site and significantly increased upto 48 h, indicating the feasible application of the PAA-Lu-NRs as shown in Fig. 5.2b. The bright NIR-IIb emission was observed in the spleen, liver, lung, and tumor site of the mouse which corroborated the distribution trend in living mouse as shown in Fig. 5.2c-d. Finally, the group concluded that the low toxicity, high quantum yield, size uniformity, and narrow band emission capability made the nanoparticles useful candidate for multimodal imaging.

5.2.1.2 Photoacoustic Imaging

Among different optical imaging techniques, the photoacoustic imaging has got immense attention. It is generally based on the thermoelastic expansion of the tissue after illuminating with the pulsed laser light, resulting in absorption of energy as well as generation of heat. Actually, PAI (photoacoustic imaging) binds both the properties of ultrasound imaging (the high penetration depth, sensitivity) along with the pulsed laser light illumination (multispectral possibilities) [19, 20]. PAI is used in various areas in biomedical applications such as vascularization, for detection and monitoring of tumors, lymph nodes (sentinel), etc. [21–23]. Recently, several nanoparticles are employed such as gold [24], polymeric nanoparticles [25], carbon nanotubes [26], etc. for PAI [19]. For example, Wu et al. applied green synthetic approach for the synthesis of carbon nanoparticles from honey for photoacoustic

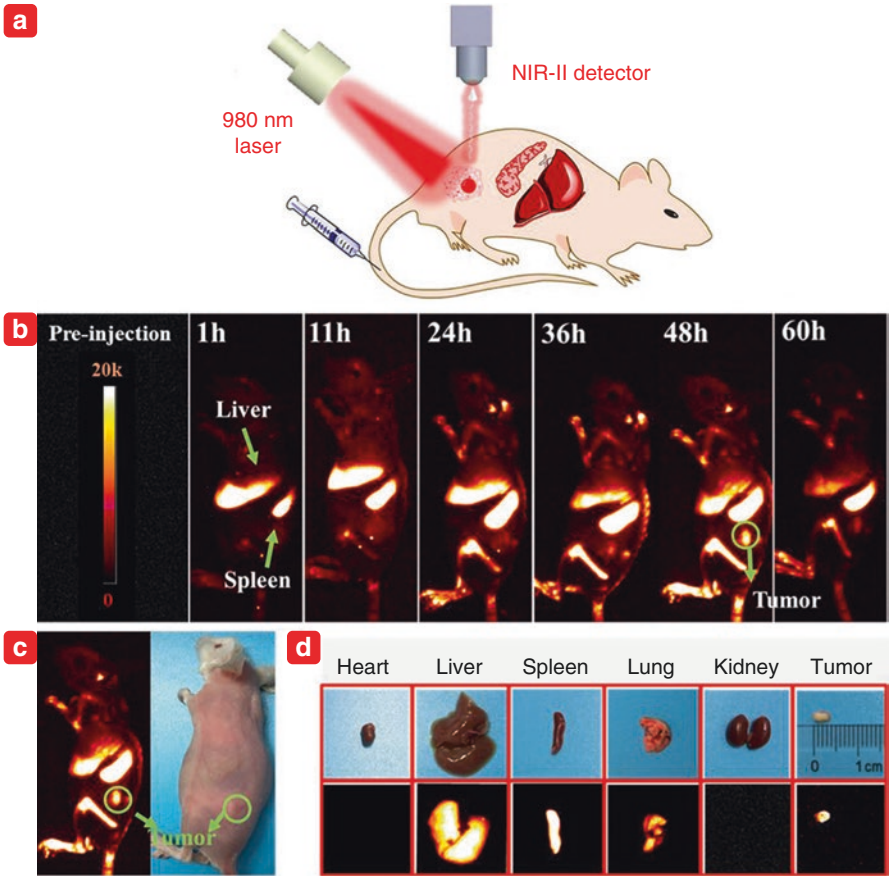

Fig. 5.2 (**a**) Schematic illustration of in vivo small tumor diagnosis by using PAA-Lu-NRs. (**b**) NIR-IIb bio-imaging of LLC tumor-bearing mouse after intravenously injecting PAA-Lu-NRs at different time periods. (**c**) Digital photograph of tumor-bearing mouse and in vivo NIR-IIb fluorescent imaging of the tumor-bearing mouse (the green circle indicated the tumor site). (**d**) Digital photographs of the isolated organs/tumor and the corresponding ex-vivo NIR-IIb imaging, respectively. Reprinted with permission from [18]. Copyright © 2019 American Chemical Society

imaging (real time). Researchers used the solvent-free condition for surface modification of those carbon nanoparticles with organic macromolecules [27]. Figure 5.3 shows the PA (photoacoustic) imaging of SLN (sentinel lymph node) in nude mice at 650 nm laser. At different time point, images were captured: (1) before OCN (luminescent carbon nanoparticles) injection, (2) after 2 min, (3) 210 min of postinjection. Blood vessels, SLN, and lymph vessel were clearly visible after 2 min of injection. The PA control images before OCN injection referred as maximum intensity projections (MAP). The enhancement of PA was observed 51 times in case of SLN after 2 min of injection. The group revealed that after 210 min postinjection, the contrast of the PA images decreased owing to rapid clearance of the particles

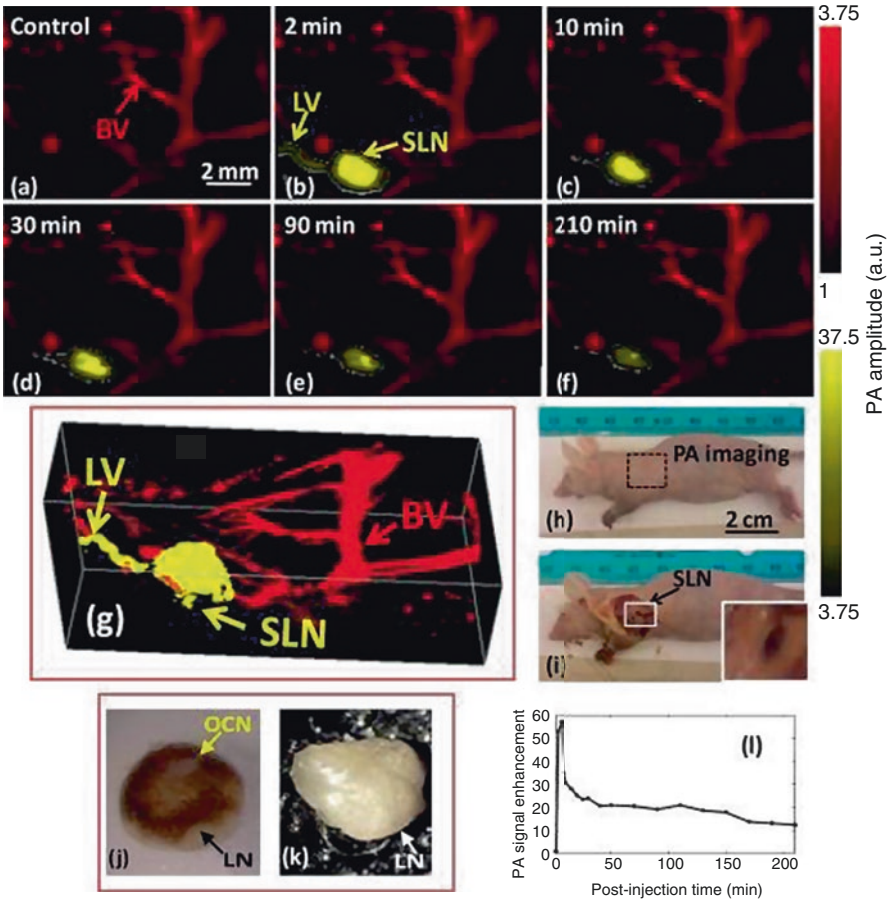

Fig. 5.3 Noninvasive real-time in vivo PA imaging of SLN in nude mouse: For all PA images, the laser was tuned to 650 nm wavelength. (**a**) Control PA image acquired before OCN injection. Red parts represent optical absorption from blood vessels (BV); (**b**) PA image acquired immediately (2 min) after the OCN injection; blood vessel (BV), lymph vessel (LV), and sentinel lymph node are marked with arrows, and the SLN is visible in (**b**–**e**); however, the contrast is much weaker after 210 min postinjection in (**f**). (**g**) 3D depiction of the SLN and BVs immediately after OCN particles injection, (**h**) Photograph of the nude mouse before taking the PA images. The scanning region is marked with a black dotted square. (**i**) Photograph of the mouse with the skin removed after PA imaging, accumulation of dark-colored OCN particles is visible in lymph node; (**j**) excised and isolated lymph node from mouse injected with OCN after 0.5 h and (**k**) injected with saline; (**l**) PA signal enhancement in the SLN after the injection of OCN nanoparticle as a function of postinjection time. For (**a**–**d**): FOV = 12 mm × 10 mm, step size along the X direction = 40 μm, step size along the Y direction = 100 μm, raster scanning for a 3D image = ~1 min, B-scan frame rate = ~1.5 Hz, total scan time = ~210 min. No signal averaging was used. Reprinted with permission from [27]. Copyright © 2019 Elsevier B.V

from lymph node. The nude mice were photographed before and after PA images. No dark color was found in case of saline-treated nude mice, whereas OCN-treated nude mice demonstrated dark color accumulation of the nanoparticles. The group revealed that there was a huge increment in the PA signal after injection which went away in a time dependent manner. On another example, Kricher et al. designed nanoparticles consisting of gold core useful for PAI, outer layer for SERS (surface-enhanced Raman spectroscopy) along with a gadolinium-based layer for MRI [28]. Researchers employed this kind of MPR (magnetic resonance-photoacoustic-Raman) nanoparticles to identify the tumors using MRI. Additionally, the deep-seated tumor was localized using PAI and the fine margin re-sectioning was carried out using SERS. Finally, the authors shed lights on the future applicability of this PAI as noninvasive techniques by making it more clinically effective tools for imaging. Apart from that, advanced PAI setups were enabled for the differentiation of the background signals from the probe-specific signals. In this context, multispectral optoacoustic tomography (MSOT) is used for the quantitative assessment of the exogenous (porphyrin, methylene blue, etc.) and endogenous (hemoglobin, melanin, etc.) contrasting agents [29] [30]. Meanwhile, in order to visualize the gastrointestinal cancer, PEGylated gold nanoparticles were successfully employed in MOST as signal amplifiers. Similarly, to specifically target the integrin $\alpha_v\beta_3$ (overexpressed in tumor neovasculature), RGD peptide conjugated gold nanoparticles were prepared for PAI useful for sensitive angiography [31].

5.2.1.3 Raman Based Imaging

Raman based imaging is a powerful, noninvasive, label-free imaging technique used for the study in different chemical processes in biology [32].The in-elastic scattering of the light (photon) from a particular object gives rise to Raman effect. It can be performed in robust conditions and useful in providing the molecular details, fingerprints of tissues, cells, etc. For example, Lu et al. developed gold nanopopcorn functionalized with RNA aptamers and incubated in cancerous as well as non-cancerous cells for imaging [33]. The authors showed that the central AuNP (gold nanoparticle denoted as "popcorn") acted as electron reservoir, whereas the surrounding AuNPs focused the Raman field at the apexes. The group demonstrated that in the cancer cells, the aggregated nanoparticles formed "hot spots" and promoted surface-enhanced Raman scattering (SERS) imaging. Additionally, they observed that Raman signal enhancement property differentiated the cancer cells and normal cells. Finally, the authors concluded that this system could be used for early diagnosis of cancer cells using Raman spectroscopy. Generally, Raman spectroscopy does not depend on the endogenous fluorophores and local environment. Over the years, variants of Raman spectroscopy are explored to increase the sensitivity and to address the problems of continuous Raman scattering. This new type of imaging technique [Coherent anti-Stokes Raman scattering (CARS)] can improve vibrational signals and has high speed video rate imaging capacity. Monger et al. used this noninvasive technique in order to locate the metal oxide nanoparticles [cerium dioxide (CeO2), zinc oxide (ZnO-NP), and titanium oxide (TiO2-NP)] in gills of *Oncorhynchus mykiss* (rainbow trout) [34]. The authors observed the

structures of the lamella in the gills after H and E staining using CARS techniques. In addition, the group explained that the carbon- and hydrogen-rich structures depicted the high strain uptake areas as observed by the CARS images. Also, they detected the various sizes nanoparticles in the agarose gel and found aggregated nanoparticles applying the Forward CARS. Small size nanoparticles were not observed because of the reduction of the Forward CARS signal. Researchers showed that small aggregated nanoparticles of TiO_2 generally located in the periphery of the lamella for short time exposure, whereas under long exposure period the large aggregated particles were found inside the secondary lamella [35]. In another example, the uptake of PLGA [poly (lactic-co glycolic acid)] nanoparticles loaded with C6-ceramide-d_{11} drug for targeting the epidermal growth factor receptor in SKOV3 cell was observed [36]. The uptake of the growth factor targeted nanoparticles in the SKOV3 cells was observed after 2 h as shown in Fig. 5.4a. The non-targeted nanoparticles did not enter the cells upto 6 h. The authors mentioned that the cell body, nucleus (blue), endocytic vesicle (yellow), membrane organelles (green), and the red colored nanoparticles were visible by applying the vertex component analysis. The group demonstrated that overlaid of these components showed the nanoparticles distribution in the cell. In another study, inside the PLGA nanoparticles beta-carotene was encapsulated and the nanoparticles were incubated in NIH-3T3

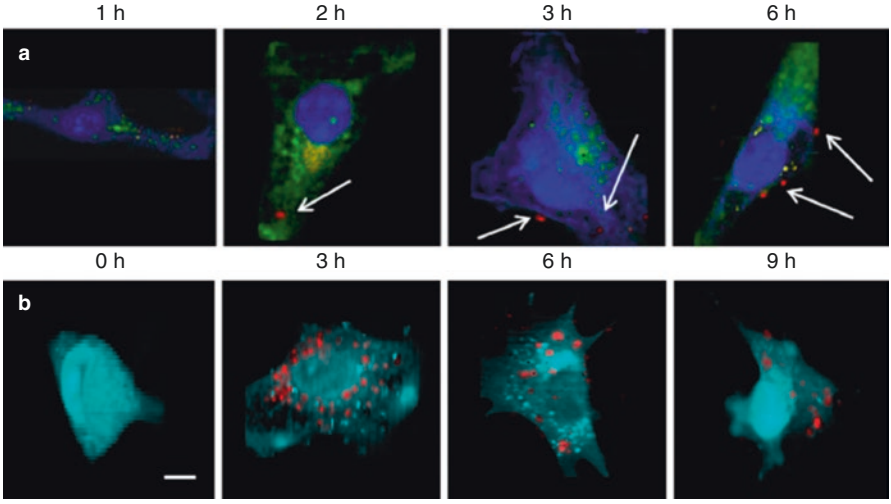

Fig. 5.4 The uptake of polymeric nanocarriers. (**a**) The uptake of epidermal growth factor receptor targeted nanoparticles to SKOV-3 cells over time shows that particles enter after 2 h. Images are overlays of the cell body and nucleus (blue), membranous organelles (green), early endocytic vesicles (yellow), and nanoparticles (red). White arrows show regions of nanoparticle aggregation. Reproduced with permission from [82], published by Springer Nature (2013). (**b**) The uptake of β-carotene-loaded poly lactic-co-glycolic acid (PLGA) nanoparticles into murine NIH-3T3 cells showing the cell body (cyan) and nanoparticles (red). Scale bar = 10 μm. Reproduced with permission from [83], Copyright John Wiley. Reprinted with permission from [36]. Copyright © 1996–2019 MDPI (Basel, Switzerland)

cells (mouse fibroblast) [36]. The presence of the double bonds (conjugated) and the extended vibrational structure indicated the possibility of resonance Raman spectroscopy at a discrete wavenumber. Researchers observed that there were discrete strong bands which are unique to the beta-carotene. The uptake of the nanoparticles at different time points were shown in Fig. 5.4b, in which the cell body was observed in cyan and the nanoparticles were in red.

5.2.1.4 MRI-Assisted Imaging

MRI imaging is based on nuclear magnetic resonance principle in which the hydrogen nuclei absorb radiofrequency pulses of the resonant and get excited in presence of strong magnetic field [37]. The excited nuclei then returned back to the ground state after emission of the absorbed radiofrequency. The different relaxation characteristics of the hydrogen atom in presence of magnetic fields give contrast to the MRI. It has been observed that paramagnetic materials increase the longitudinal relaxation (T1 relaxation) resulting to brighter signals, whereas ferromagnetic as well as superparamagnetic materials give rise to transverse relaxation (T2 relaxation) producing hypointense signal. Based on the concept, the gadolinium (Gd^{3+})-based and superparamagnetic iron oxide materials are used as contrasting agents [38]. Earlier, T2 contrast imaging agent Feridex and Resovist (first generation) and Combidex (second generation) were used to detect liver lesions, but they became obsolete from the market owing to more usefulness of T1 contrast images [39]. There are various side effects of gadolinium-based agents like nephrogenic systemic fibrosis, whereas the iron oxide nanoparticles are typically degraded in liver and spleen and entered into the iron metabolism when injected intravenously [40, 41]. According to reports, the iron oxide nanoparticles are useful in MRI of gastrointestinal tract when administered orally. Additionally, the controlled size, tunable magnetic property, crystalline nanoparticles can be obtained by synthesizing the nanoparticles based on their thermal decomposition. This alteration in the synthesis process results as an alternative to T1 contrast agents such as Gd (III) based along with the T2 contrast agents which are highly sensitive. For example, ESIONs (extremely small iron oxide nanoparticles) with size around 3 nm exerted high T1 contrast effect [42]. In another example, good T2 contrast effects were observed from the 30 nm sized iron oxide nanoparticles owing to the facile cellular uptake of the nanoparticles [43]. Also, it has been observed that 22 nm iron oxide nanoparticles gave rise to stronger contrast effects attributed from the balanced magnetization as well as diffusion rate predicted by the outer-sphere relaxation theory [44]. Furthermore, the surface modification of the nanoparticles, attachment of targeting ligands (aptamer, folic acids, etc.), and functional molecules (fluorescent dyes) potentiate the nanoparticles-based MRI contrast agents. Meanwhile, in order to overcome the intrinsic drawbacks of MRI itself such as artifact signals, hypointensity, or hyperintensity owing to the endogenous factors like fat, bleeding, metal deposition, etc., the dual mode contrasting agents (T1–T2) came into action [45]. This system contained superparamagnetic nanoparticles along with paramagnetic metal ions to provide better contrast. Apart from that, clustering of the nanoparticles also creates problem by changing the T2 relaxation rate known as magnetic

relaxation switch (MRS). Ling et al. reported an iron oxide nanoparticle which can activate the MR signals in acidic environment because of the presence of the pH responsive polymer surrounding it [46]. The authors observed that appearance of strong T2 contrast effects retards the T1 contrasting effects in aggregated form. Additionally, disassemble of the nanoparticles augmented T1 weighed MRI signal in acidic condition. Other than the iron-based nanoparticles, lanthanide-based nanoparticles hold superior position as MRI contrast agents. For example, $NaGdF_4$ nanoparticles are used for T1 weighed MRI. Holmium-based, dysprosium-based nanoparticles also got much attention due to their large magnetic moment along with short relaxation time beneficial for high field MRI [47, 48].

5.2.1.5 CT Imaging

CT (computed tomography) imaging is a kind of whole-body imaging system which has been widely used because of its high resolution as well as rapid acquisition power [49]. It is based on the principle of the X-ray interaction with the contrasting agents or body. The intensity of the X-ray generally measures from different angles using computer, which captures the crosssectional images (tomographic) produced due to the rotation of the detector and the X-ray tube. It is used to visualize organs like brain, lung, gastrointestinal tract, abdominal portion as well as cardiovascular system, etc. As the X-ray depletion property increases with increasing the atomic number, high Z value is preferable option as CT contrast agents. In the clinical situations, iodine-based and barium-based contrasting agents are in use till date [50, 51]. Since high dose is required for CT scan, toxicity of the materials is major concern. Barium sulfate suspension which has been used for long time for gastrointestinal imaging showed renal and cardiovascular toxicity when administered in intra-vascular route. On the other hand, iodine-based molecules such as iodixanol and iopamidol were FDA approved for intravenous CT contrast agents. The induction of allergic reactions, lower blood circulation time as well as renal toxicity is major drawbacks [50, 52]. Last but not least, the gold-based CT contrasting agents are a great alternative than that of iodinated agents because of its easy synthesis along its biocompatible nature. For example, Reuveni et al. injected the gold nanoparticles conjugated with anti-epidermal growth factor receptor into the nude mice which were implanted with human squamous cell carcinoma (SCC) head and neck cancer [53]. Figure 5.5 shows the volume-rendered images of mouse under X-ray computed tomography before injection with gold nanoparticles, postinjection after 6 h with IgG-coated gold nanoparticles and the anti-epidermal growth factor receptor targeted gold nanoparticles. The group observed that CT number of the tumor targeted by the anti-epidermal growth factor receptor conjugated gold nanoparticles was much higher than that of only gold nanoparticles injection, which clearly showed that the attachment of the nanoparticles with the SCC head and neck tumor resulted in high contrast effects. Finally, the authors shed lights on the future applicability of this imaging technique for the detection of smallest tumors possible. According to reports, almost 50 gm gold is required for each whole-body scanning which makes it difficult to use in terms of cost. So, lanthanide metal such as Ytterbium (Yb) can be a good alternative. But, the large-scale production of

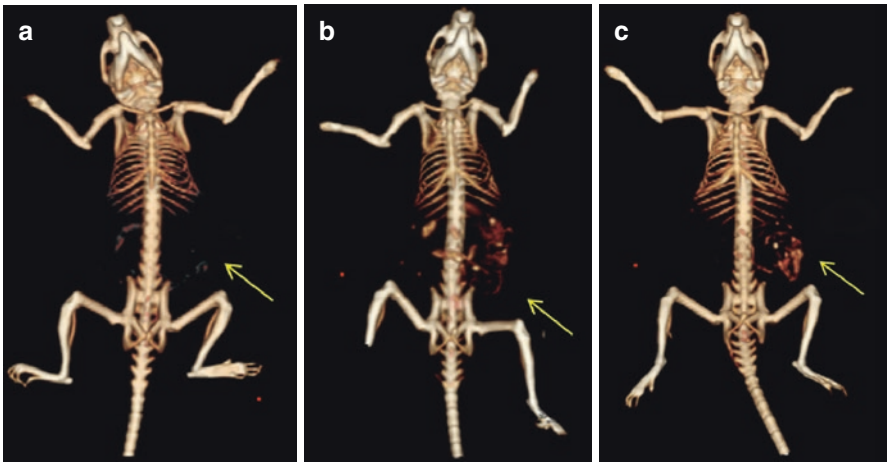

Fig. 5.5 In vivo X-ray computed tomography (CT) volume-rendered images of (**a**) mouse before injection of gold nanoparticles (GNPs), (**b**) mouse 6 hours postinjection of nonspecific immunoglobulin G GNPs as a passive targeting experiment, and (**c**) mouse 6 hours postinjection of anti-epidermal growth factor receptor (EGFR)-coated GNPs that specifically targeted the squamous cell carcinoma head and neck tumor. The anti-EGFR-targeted GNPs show clear contrast enhancement of the tumor (**c**, yellow arrow), which was undetectable without the GNPs contrast agents (**a**, yellow arrow). CT numbers represent the average Hounsfield units (HU) of the whole tumor area. All scans were performed using a clinical CT at 80 kVp, 500 mAs, collimation 0.625 × 64 mm, and 0.521 pitch size (64 detector CT scanner, LightSpeed VCT; GE Healthcare, Little Chalfont, UK). Reprinted with permission from [53]. Copyright © 2019, Dove Press Ltd.

lanthanide is a problem in order to utilize it as CT contrast agents. Even though the radiation dose is high in case of CT, the vast availability and fast scanning speed make it the most useful imaging tools [54–56]. Meanwhile the usage of the contrasting agents arises conspicuity of the images, necessary action can be taken on the administered dosage to reduce the radiation exposure resulting in safer imaging. Also, the toxicity evaluation of the nanoparticles is urgently needed, for successful translocation of the nanoparticles into clinical trials.

5.2.1.6 Multiphoton Microscopy Imaging

Now-a-days, the multiphoton imaging system has got paramount importance because of their several advantages over whole-body imaging techniques like MRI and CT scan [57, 58]. The multiphoton imaging system is a kind of anti-strokes emission that creates shorter emission wavelength compared to wavelength of excitation [59]. It is well known that it reduces the photobleaching of fluorophores as well as decreases the damages of sample after photoinduction. Additionally, in combination with infrared, this multiphoton fluorescence imaging system can minimize the background autofluorescence and improve penetration depth [60]. But, most of the multiphoton imaging dyes consist of small molecule; they are in general less photostable which prohibit them for prolonged imaging and frequent excitation.

Hence, metal nanoparticles-based multiphoton imaging probes are in good demand owing to their ease surface modification, fictionalization and reduced photobleaching capability. Among various nanoparticles, quantum dots (QDs) are well studied in this area because of their tunable emission and broad multiphoton cross sections [61]. In this context, quantum dots containing cadmium such as CdSe/CdS/ZnS nanoparticles (two-photon imaging system) were studied which showed potential toxicity. To address this toxicity issue, manganese doped ZnS nanoparticles (ZnS:Mn) (three-photon imaging probes) have been used owing to their larger absorption cross sections [62]. Despite their low toxicity value, they can penetrate deep as well as enable more light to escape from the tissue. Simultaneously, this system decreases the background fluorescence, the out of focus excitation and automatically escalates the spatial resolutions. Other than the ZnS:Mn quantum dots, there are other QDs which are well known for their non-toxic nature such as $CuInS_2$/ZnS, etc. [63]. Meanwhile, the light scattering from biological tissue creates additional problem during fluorescence imaging by using three-photon system that uses NIR laser. To overcome the pitfalls, and to decrease the light scattering, it has been taken into account that the three-photon system can be excited at second NIR-II range (1000–1700 nm) to get better efficacy [64]. It has been observed that in the ZnS:Mn system, the excitation of the manganese dopant at 1050–1310 nm light source is more beneficial than excitation of the ZnS host at 600 nm laser because of the vast two-photon cross sections of manganese ions which improves penetration depth. Apart from that, there are several issues that need to take care to get a high-resolution image in quick acquisition time using multiphoton imaging system.

5.2.1.7 Super Resolution Methods in Optical Microscopy

Super resolution methods for optical imaging have got immense attention after the breakthrough invention of "Super resolved fluorescence microscopy" by Eric Betzig, Stefan W. Hell, and William E. Moerner, those who got the noble prize in 2014 in chemistry [65, 66]. Since then, it has become a very captivating field in the science. In 2014, Zhu et al. prepared biodegradable SP-PCL [spiropyran-terminated poly(ε-caprolactone)] nanoparticles using Tetra spiropyran titanate [$Ti(SP)_4$] as precursor [67]. The authors explained that upon UV irradiation the SP-PCL exhibited photochromism owing to the transformation of SPs into merocyanines (MCs). The group observed that upon excitation at 420 nm, the SP-PCL and MC-PCL exerted emission at green (530 nm) and red region (650 nm), respectively. The group found out that owing to interconversion of both the forms (SP- and MC-), SP-PCL nanoparticles showcased both the green and red fluorescence. The authors declared that this biodegradable SP-PCL nanoparticle acted as potential candidate as fluorophores (photoswitchable) in super resolution microscopy (localization based) in order to visualize sub-cellular nanostructures which is higher than normal fluorescence microscopy. On the other hand, Lin et al. observed that in order to detect the surface-enhanced fluorescence (SEF) on metal nanostructures, photoactivation localization microscopy (PALM) have been studied well [68].

5.2.1.8 Luminescence Upconversion Imaging

Recently, the upconversion imaging probes have got huge attention in the field of imaging owing to the longer luminescence lifetime and newly developed luminescent probes. Upconversion generally follows a kind of anti-stokes mechanism, where the photon absorption process occurs through intermediate electronic states (real) [69]. Compared to multiphoton absorption, this imaging system provides much higher emission frequency [70]. It has been observed that for the lanthanide doped upconversion nanoparticles (UCNPs), it is possible to tune the emission color by simply changing the composition of the elements due to dependency on the energy levels of each elements other than its quantum confinement [71, 72]. Other advantages observed in case of lanthanides that the lifetime (luminescence) can also be adjustable several folds (microseconds) useful for multiplex imaging by using different types as well as the changing dopant percentages [70]. These UCNPs are also useful for time-gated fluorescence imaging due to segregation of light scattering from the nanoparticles emission which give rise to better contrast [73]. According to reports, the lanthanide doped UCNPs exceeded the popularity of organic-based materials owing to the triplet-triplet annihilated upconversion along with enhanced photon collection efficacy arising from functionalization with antenna materials (NIR dyes, QDs, etc.). Besides, they have extreme photostability and chemical stability [74, 75]. Apart from that, there are several limitations associated with these luminescence upconversion nanoparticles. First of all, owing to the ladder like energy levels, multiple emission peaks appear in case of lanthanide doped NPs. Thallium generates peaks at NIR, UV, blue region; erbium gives both red and green emission [76]. Secondly, the heating effect of the laser (980 nm NIR) is used in case of UCNPs, which can increase the temperature of the water molecules rendering problems to the imaging techniques. It can cause the damage to the tissue during in vivo imaging. To overcome this problem, Xie et al. introduced the Nd^{3+}(ions) in the system that used laser (800 nm) with moderate heating [77]. The used laser can be absorbed minimally by water which ultimately solved the heating issue. The group mentioned that Nd^{3+} ions acted as sensitized dopant in this system. They illustrated the idea of the core–shell strategy that precisely described the control over the ions (acted as dopant) in forming the core and shell layers of nanoparticles in Fig. 5.6a. The authors demonstrated that the less amount of Nd^{3+} doping as a core led to less concentration quenching, whereas high amount of doping in the shell layer carried out for effective harvesting of light (~800 nm). Researchers observed that the absorption intensity was much higher in case of Nd^{3+} doping (shell layer) compared to control (no Nd^{3+} doping in the shell layer) at 794 nm as shown in Fig. 5.6a. They also found that there was significant difference in the absorption intensity of the Nd^{3+} doped (shell layer) and the Yb^{3+} doped (core) at 794 nm and 976 nm, respectively. The Nd^{3+} doped (shell layer) demonstrated remarkable increase in intensity compared to Yb^{3+} doped (core) nanoparticles. The absorption spectra of the system were normalized at 976 nm as shown in Fig. 5.6b. Meanwhile, there are various applications of these UCNPs observed in in vivo system. Park et al. used Tm^{3+}-doped UCNPs for optical imaging and trafficking of nanoparticles in lymphatic system

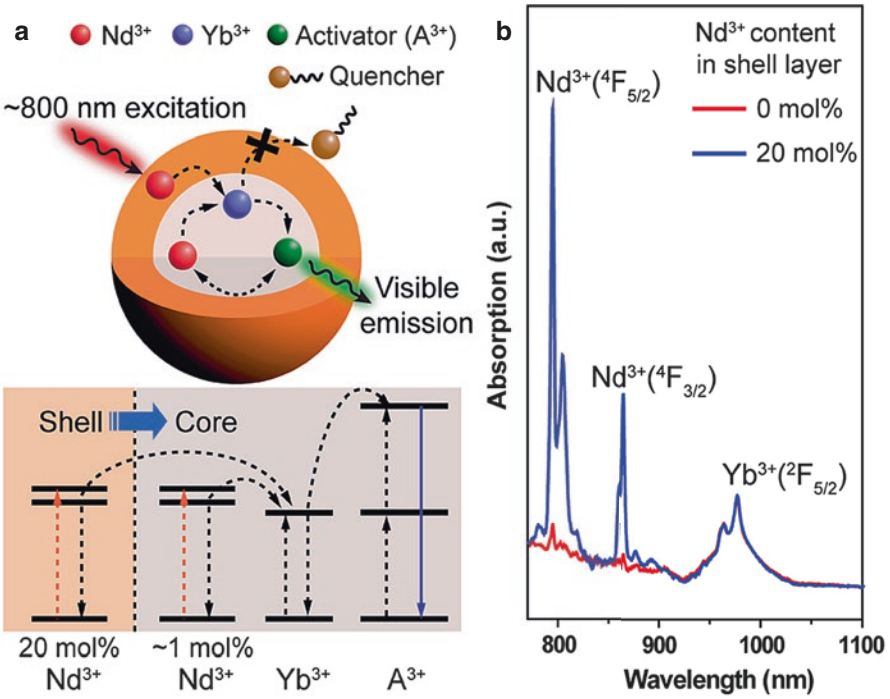

Fig. 5.6 (**a**) Schematic design (top) and simplified energy level diagram (bottom) of a core–shell nanoparticle for photon upconversion under 800 nm excitation. Nd3+ ions doped in the core and shell layers serve as sensitizers to absorb the excitation energy and subsequently transfer it to Yb3+ ions. After energy migration from the Yb^{3+} ions to activator ions, activator emission is achieved via the Nd3 + −sensitization process. (**b**) Near-IR absorption spectra of NaYF4:Yb/Nd(30/1%) nanoparticles coated with an inert NaYF4 shell or an active NaYF4:Nd(20%) shell. The absorption spectra were normalized at 976 nm for comparison. Reprinted with permission from [77]. Copyright © 2013 American Chemical Society

of mice [78]. Researchers mentioned that this high advanced NIR-NIR upconversion luminescence (UCL) provided the luminescence profiles in SLN (sentinel lymph node) tissues, organs, etc. even in feaces of mice for over one month studying time. Additionally, the group observed the clearance of the injected NPs through hepatobiliary site evincing from the flowing of the NPs rapidly via lymph node to the main blood stream. Finally, the authors shaded lights on the future applicability of the UCNPs in immunology along with biopsy analysis in SLN. Another study laid by Jayakumar and co-workers, where they used this UCNPs (silica-coated nanocrystals) in order to study the gene expression in zebrafish model proved to be a game changer in this field [79]. The silica-coated Ytterbium, Yttrium, and Thulium (lanthanide elements) exerted UV light when activated by the NIR light resulting in the photoactivation in deep tissue. The authors described that the knockdown of the notochord creator and mesoderm modulating gene (−ntl) was light guided. In the adult zebrafish model, the

knockdown was guided through GFP transplanted tumor cells using NIR light. Additionally, the embryos as well as the adult zebrafish were imaged which gave future direction of potential use of this system in development of biologics.

5.2.2 Image Guided Disease Therapy Using Nanoparticles

The major challenges of cancer including early detection, limitations of chemotherapeutic agents, and continuous monitoring of metastatic cancer cells require a strategy in order to visualize as well as fight against them. Therefore, nanotechnology-based approaches are emerging as vital platforms for disease diagnosis and therapy. Image guided disease therapy means simultaneous imaging and therapy of the disease which is a combined approach to understand the localization of therapeutic molecules in real time. This strategy also enables in estimating the therapeutic effect of the nanoconjugates in the body by imaging the tumor volume [80]. Nanotechnology offers conjugation of imaging molecules (fluorescent agents, MRI contrast agents, etc.) and therapeutic molecules together in order to visualize the tumor and also for treatment [81]. Various research groups have practicing in the development of such kind approaches using different types of nanomaterials. Among all, iron nanoparticles are widely employed for the image guided therapy. For example, Yu et al. developed nanotheranostic approach for prostate cancer therapy [82]. The authors designed thermally cross-linked superparamagnetic iron oxide nanoparticles (TCL-SPIONs) conjugated with aptamer which is specific ligand for prostate-specific membrane antigen (PSMA) and loaded with doxorubicin as anticancer agent. The Apt-hybr-TCL-SPION nanoconjugate exhibited the tumor-specific uptake in LNCaP xenograft mouse model. The study explained dual role of iron oxide nanoparticles for imaging and therapy of prostate cancer. Similarly, Tomitaka et al. synthesized magnetic core/gold shell (MNP@Au) magneto-plasmonic nanoparticles for MRI imaging of brain diseases [83]. The as-synthesized nanoparticles displayed superparamagnetic properties and MRI contrast applications. Further, magneto-plasmonic nanoparticles could be able to cross the BBB (blood–brain barrier) as confirmed by transmigration study *in vitro*. Considering these observations, the authors claimed that magneto-plasmonic nanoparticles help in treatment of neurological disease. On the other hand, Satpathy et al. developed amphiphilic polymer iron oxide nanoparticles conjugated with HER2 affibody labeled with NIR dye as targeted agent and cisplatin as chemotherapeutic agent [84]. The study demonstrated that iron oxide nanoparticles significantly suppressed the primary and metastatic ovarian tumor growth observed in xenograft mice model. Duc et al. developed Gadolinium based-nanoparticles (GBNs) for image guided radiation therapy for brain tumors [85]. The group stated that the GBNs were able to induce MRI contrast and radiosensitizing effect. The GBNs were activated by X-ray microbeams to kill the brain cancer cells resulted in increased lifespan of rats bearing the brain tumors.

Gold nanoparticles (AuNPs) are also widely employed for the image guided therapy. Due to their unique photonic properties, AuNPs are employed as optical contrast agents [86]. Optical coherence tomography (OCT) and photoacoustic (PA)

imaging are the two important imaging modalities which employs the light scattering or absorption properties of AuNPs [87]. For example, Etame et al. demonstrated the magnetic resonance-guided focused ultrasound (MRgFUS) using AuNPs to deliver therapeutic agents for central nervous system (CNS) [88]. The authors found that AuNPs were able to deliver the therapeutic agents into CNS in presence of focused ultrasound. Similarly, Gao et al. nicely described the image guided therapy using AuNPs with graphene oxide (GO) [86].The AuNPs were seeded on to GO to form GO/Au complex which was conjugated with Cy5.5 labeled-matrix metalloproteinase-14 (MMP-14) substrate (CP) [CPGA: final conjugate]. The CPGA exhibited the high fluorescent and PA signals in the mice bearing the SCC7 tumor and able to inhibit the tumor growth upon irradiation using laser.

5.2.3 Biosynthesized Nanoparticles for Bio-imaging

In recent times, biosynthesized nanoparticles are also employed for bio-imaging applications. For instance, our group for the first time demonstrated the bio-imaging applications of biosynthesized nanoparticles silver:b-AgNPs prepared by *Olax scandens* leaf extract [89]. We observed that the *Olax scandens* plant contains different phytochemicals attached to the nanoparticles during the synthesis (in situ) which could be used for fluorescence-based bio-imaging. The b-AgNPs displayed the red color fluorescence upon administration in A549 cells [89, 90]. UT or control cells did not show any fluorescence (Fig. 5.7a). The only leaf extract showed less fluorescence due to lesser uptake by the cells as shown in Fig. 5.7b. Similarly, the b-AgNPs exhibited the red color fluorescence in B16F10 cells, whereas the chemically synthesized silver nanoparticles (c-AgNPs) did not show any fluorescence inside the cells as shown in Fig. 5.7c-d, respectively. The phase contrast images of various treatment groups and control cells are shown in Fig. 5.7a'-d'. Interestingly, the normal cells did not show the fluorescence color. However, this cancer cell specific property of these biosynthesized silver nanoparticles is yet to understand. The bio-imaging properties of biosynthesized nanoparticles show the future directions to develop the plant-based fluorescence molecules towards biomedical applications.

5.3 Clinical Status of Nanoparticles-Based Bio-imaging

Presently, various nanoparticle-based imaging agents are approved for clinical uses which by FDA or some in clinical trials. For example, definity is an FDA approved perflutren lipid microspheres used as ultrasound contrast agents [91].These microspheres are the lipid microspheres filled with gas which reflect the sound waves to provide the better contrast picture. Generally, these microspheres are administered through intravenous injection for the diagnosis of heart diseases. Similarly, Optison (GE Healthcare) is also another contrast agent approved by FDA which is a human serum albumin stabilized perflutren microspheres [91]. Further, ferumoxytol is

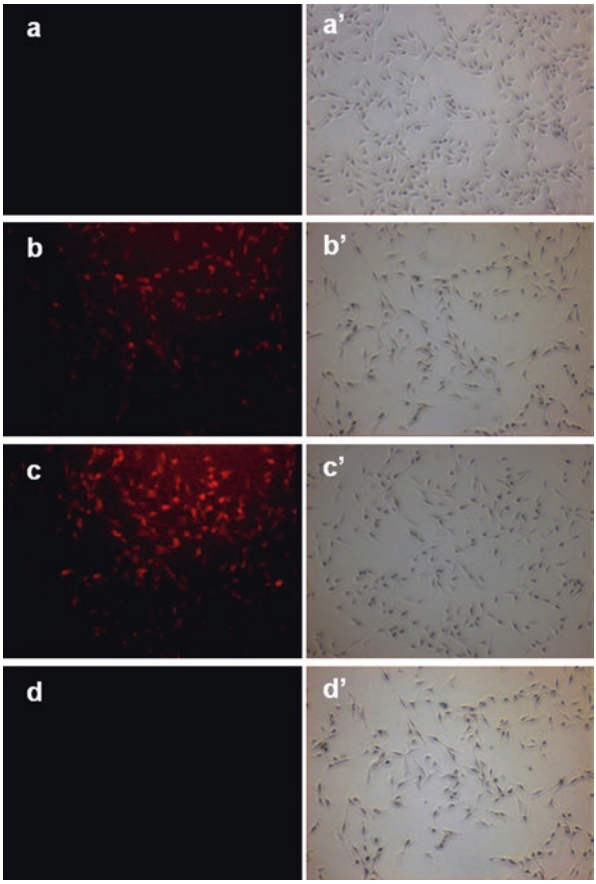

Fig. 5.7 Fluorescence and the corresponding phase images of untreated B16 cells and cells treated with Olax, b-AgNPs, and c-AgNPs, observed by an Olympus Fluorescence Microscope. Fluorescence images of B16 cells treated with (**a**) untreated or control, (**b**) Olax (100 µg/ml) leaf extract, (**c**) b-AgNPs (at 30 µM), and (**d**) c-AgNPs (at 30 µM). Images of a', b', c', and d' correspond to phase images. All the treated B16 cells were extensively washed with DPBS (6 times) before taking the fluorescence images. It is to be noted that there is no significant cell killing observed at 30 µM. Reprinted with permission from [89]. Copyright ©2019 Ivyspring International Publisher

another FDA-approved imaging agent for off-label as MRI angiography agent as well as for iron deficiency anemia [92]. AuNPs-based formulations are also approved by FDA for diagnosis applications. For instance, Verigene® is a gold nanoparticle-based formulation approved by FDA for diagnosis of Gram positive bacterial infections in blood stream [93]. This technology employs advanced automation for rapid detection of nucleic acids and proteins at the molecular level.

5.4 Challenges and Future Perspectives

Whether the nanoparticles for bio-imaging or therapy, the challenges are remaining same for clinical translation. Currently, nanoparticles are mostly used for healthcare applications because of their unique physicochemical properties. Especially, many researchers focused on development of various metal nanoparticle (AuNPs, AgNPs, SiNPs, iron NPs, etc.) based formulations for disease diagnosis and therapy. However, according to the experts, the toxicity concern of nanoparticles is not

completely addressed [94]. Further, investigation of nanoparticle interaction with the biomolecules (proteins, nucleic acids, lipids, and sugars) is very important to understand the toxicity profiles. Also, pharmacokinetics and pharmacodynamics are the crucial factors for evaluation of nanoparticle toxicity [95]. On the other hand, sometimes the in vitro toxicity responses of nanoparticles cannot be correlated with the in vivo systems without proper investigation. Therefore, toxicological investigation needs to be performed very carefully before translating them into human use. Additionally, bioavailability and clearance of nanoparticles is a major concern which should be undertaken for conducting the toxicity evaluation. Therefore, the functionalized nanoparticles should first pass through above stated criteria in order to keep them for the clinical use.

5.5 Conclusion

Several nanoparticles are emerged as probes for in vivo bio-imaging. Nanoparticles as imaging contrast agents are shown to be alternative for conventional small molecules for better imaging. Additionally, their less toxic effects and long circulation time enable them as the suitable candidates for bio-imaging. Moreover, multiphoton or upconversion based imaging methods make use of NIR light to acquire the images from deeper tissues. Despite of advantages, nanoparticle-based bio-imaging cannot completely replace the conventional imaging dyes or contrast agents due to some other issues like bio-degradability, immunogenicity, bio-availabilities, and clearance. Therefore, further research on nanotechnology is required for improving the effectiveness of the imaging techniques to diagnose the disease with more accuracy.

Acknowledgments The Authors are thankful to the Director, CSIR-IICT for his support and encouragement and for his keen interest in this work. IICT communication number IICT/Pubs./2019/113 dated March 25th 2019 for this manuscript is duly acknowledged.

References

1. Tempany CM, McNeil BJ. Advances in biomedical imaging. JAMA. 2001;285:562–7.
2. Sun Z, Ng KH, Ramli N. Biomedical imaging research: a fast-emerging area for interdisciplinary collaboration. Biomed Imag Interv J. 2011;7:e21.
3. Babic RR, Stankovic Babic G, et al. 120 years since the discovery of x-rays. Med Pregled. 2016;69:323–30.
4. Ding H, Wu F. Image guided biodistribution and pharmacokinetic studies of theranostics. Theranostics. 2012;2:1040–53.
5. Mettler FA Jr, Thomadsen BR, Bhargavan M, et al. Medical radiation exposure in the U.S. in 2006: preliminary results. Health Phys. 2008;95:502–7.
6. Power SP, Moloney F, Twomey M, et al. Computed tomography and patient risk: facts, perceptions and uncertainties. World J Radiol. 2016;8:902–15.
7. Larabell CA, Nugent KA. Imaging cellular architecture with X-rays. Curr Opin Struct Biol. 2010;20:623–31.

8. Grover VPB, Tognarelli JM, Crossey MME, et al. Magnetic resonance imaging: principles and techniques: lessons for clinicians. J Clin Exp Hepatol. 2015;5:246–55.
9. DiSanto RM, Subramanian V, Gu Z. Recent advances in nanotechnology for diabetes treatment. Wiley Interdiscip Rev Nanomed Nanobiotechnol. 2015;7:548–64.
10. Godin B, Sakamoto JH, Serda RE, et al. Emerging applications of nanomedicine for the diagnosis and treatment of cardiovascular diseases. Trends Pharmacol Sci. 2010;31:199–205.
11. Wang X, Yang L, Chen Z, Shin DM. Application of nanotechnology in cancer therapy and imaging. CA Cancer J Clin. 2008;58:97–110.
12. Yoon HY, Jeon S, You DG, et al. Inorganic nanoparticles for image-guided therapy. Bioconjug Chem. 2017;28:124–34.
13. Bigio IJ, Mourant JR. Ultraviolet and visible spectroscopies for tissue diagnostics: fluorescence spectroscopy and elastic-scattering spectroscopy. Phys Med Biol. 1997;42:803–14.
14. Kollias N, Zonios G, Stamatas GN. Fluorescence spectroscopy of skin. Vib Spectrosc. 2002;28:17–23.
15. Lai JP, Shah BP, Garfunkel E, Lee KB. Versatile fluorescence resonance energy transfer-based mesoporous silica nanoparticles for real-time monitoring of drug release. ACS Nano. 2013;7:2741–50.
16. Nakamura M, Hayashi K, Nakano M, et al. Identification of polyethylene glycol-resistant macrophages on stealth imaging in vitro using fluorescent organosilica nanoparticles. ACS Nano. 2015;9:1058–71.
17. Bhunia SK, Saha A, Maity AR, et al. Carbon nanoparticle-based fluorescent bioimaging probes. Sci Rep. 2013;3:1473.
18. Li Y, Zeng S, Hao J. Non-invasive optical guided tumor metastasis/vessel imaging by using lanthanide nanoprobe with enhanced down-shifting emission beyond 1500 nm. ACS Nano. 2019;13:248–59.
19. Kunjachan S, Ehling J, Storm G, et al. Noninvasive imaging of nanomedicines and nanotheranostics: principles, progress, and prospects. Chem Rev. 2015;115:10907–37.
20. Ntziachristos V. Going deeper than microscopy: the optical imaging frontier in biology. Nat Methods. 2010;7:603–14.
21. Hu S, Wang LV. Photoacoustic imaging and characterization of the microvasculature. J Biomed Opt. 2010;15:011101.
22. Kim C, Cho EC, Chen JY, et al. In vivo molecular photoacoustic tomography of melanomas targeted by bioconjugated gold nanocages. ACS Nano. 2010;4:4559–64.
23. Song KH, Kim CH, Cobley CM, et al. Near-infrared gold nanocages as a new class of tracers for photoacoustic sentinel lymph node mapping on a rat model. Nano Lett. 2009;9:183–8.
24. Chen YS, Frey W, Kim S, et al. Silica-coated gold nanorods as photoacoustic signal nanoamplifiers. Nano Lett. 2011;11:348–54.
25. Repenko T, Fokong S, De Laporte L, et al. Water-soluble dopamine-based polymers for photoacoustic imaging. Chem Commun. 2015;51:6084–7.
26. De La Zerda A, Zavaleta C, Keren S, et al. Carbon nanotubes as photoacoustic molecular imaging agents in living mice. Nat Nanotechnol. 2008;3:557–62.
27. Wu L, Cai X, Nelson K, et al. A green synthesis of carbon nanoparticles from honey and their use in real-time photoacoustic imaging. Nano Res. 2013;6:312–25.
28. Kircher MF, de la Zerda A, Jokerst JV, et al. A brain tumor molecular imaging strategy using a new triple-modality MRI-photoacoustic-Raman nanoparticle. Nat Med. 2012;18:829–34.
29. Beziere N, Lozano N, Nunes A, et al. Dynamic imaging of PEGylated indocyanine green (ICG) liposomes within the tumor microenvironment using multi-spectral optoacoustic tomography (MSOT). Biomaterials. 2015;37:415–24.
30. Ho CJH, Balasundaram G, Driessen W, et al. Multifunctional photosensitizer-based contrast agents for photoacoustic imaging. Sci Rep. 2014;4:5342.
31. Nie LM, Wang SJ, Wang XY, et al. In vivo volumetric photoacoustic molecular angiography and therapeutic monitoring with targeted plasmonic nanostars. Small. 2014;10:1585–93.
32. Kundu PP, Narayana C. Raman based imaging in biological application-a perspective. J Med Allied Sci. 2012;2:41.

33. Lu W, Singh AK, Khan SA, et al. Gold nano-popcorn-based targeted diagnosis, nanotherapy treatment, and in situ monitoring of photothermal therapy response of prostate cancer cells using surface-enhanced Raman spectroscopy. J Am Chem Soc. 2010;132:18103–14.
34. Moger J, Johnston BD, Tyler CR. Imaging metal oxide nanoparticles in biological structures with CARS microscopy. Opt Express. 2008;16:3408–19.
35. Lin L, Nufer K, Tomihara S, Prow T. Non-invasive nanoparticle imaging technologies for cosmetic and skin care products. Cosmetics. 2015;2:196–210.
36. Vanden-Hehir S, Tipping WJ, Lee M, et al. Raman imaging of nanocarriers for drug delivery. Nanomaterials (Basel). 2019;9:341.
37. Brown MA, Semelka RC, Dale BM. MRI: basic principles and applications. New York: Wiley; 2015.
38. Bulte JWM, Modo MMJ. Molecular and cellular MR imaging. Hoboken: CRC Press; 2007.
39. Bulte JWM, Kraitchman DL. Iron oxide MR contrast agents for molecular and cellular imaging. NMR Biomed. 2004;17:484–99.
40. Giovagnoni A, Fabbri A, Maccioni F. Oral contrast agents in MRI of the gastrointestinal tract. Abdom Imaging. 2002;27:367–75.
41. Penfield JG, Reilly RF. What nephrologists need to know about gadolinium. Nat Clin Pract Nephrol. 2007;3:654–68.
42. Kim BH, Lee N, Kim H, et al. Large-scale synthesis of uniform and extremely small-sized iron oxide nanoparticles for high-resolution T1 magnetic resonance imaging contrast agents. J Am Chem Soc. 2011;133:12624–31.
43. Lee N, Kim H, Choi SH, et al. Magnetosome-like ferrimagnetic iron oxide nanocubes for highly sensitive MRI of single cells and transplanted pancreatic islets. Proc Nat Acad Sci U S A. 2011;108:2662–7.
44. Lee N, Choi Y, Lee Y, et al. Water-dispersible ferrimagnetic iron oxide nanocubes with extremely high r2 relaxivity for highly sensitive in vivo mri of tumors. Nano Lett. 2012;12:3127–31.
45. Shin TH, Choi JS, Yun S, et al. T1 and T2 dual-mode MRI contrast agent for enhancing accuracy by engineered nanomaterials. ACS Nano. 2014;8:3393–401.
46. Ling D, Park W, Park SJ, et al. Multifunctional tumor pH-sensitive self-assembled nanoparticles for bimodal imaging and treatment of resistant heterogeneous tumors. J Am Chem Soc. 2014;136:5647–55.
47. Ma D, et al. NaGdF4:Yb3+/Er3+@NaGdF4:Nd3+@sodium-gluconate: multifunctional and biocompatible ultrasmall core–shell nanohybrids for UCL/MR/CT multimodal imaging. ACS Appl Mater Interfaces. 2015;7:16257–65.
48. Zhang XH, Blasiak B, Marenco AJ, et al. Design and regulation of NaHoF4 and NaDyF4 nanoparticles for high-field magnetic resonance imaging. Chem Mater. 2016;28:3060–72.
49. Lee N, Choi SH, Hyeon T. Nano-sized CT contrast agents. Adv Mater. 2013;25:2641–60.
50. Choudhury H, Cary R. Barium and barium compounds. Geneva: World Health Organization; 2001.. http://www.who.int/iris/handle/10665/42398
51. Galper MW, Saung MT, Fuster V, et al. Effect of computed tomography scanning parameters on gold nanoparticle and iodine contrast. Investig Radiol. 2012;47:475–81.
52. Stacul F, van der Molen AJ, Reimer P, et al. Contrast induced nephropathy: updated ESUR contrast media safety committee guidelines. Eur Radiol. 2011;21:2527–41.
53. Reuveni T, Motiei M, Romman Z, et al. Targeted gold nanoparticles enable molecular CT imaging of cancer: an in vivo study. Int J Nanomedicine. 2011;6:2859–64.
54. Bernstein AL, Dhanantwari A, Jurcova M, et al. Improved sensitivity of computed tomography towards iodine and gold nanoparticle contrast agents via iterative reconstruction methods. Sci Rep. 2016;6:26177.
55. Kim D, Park SJ, Lee JH, et al. Antibiofouling polymer-coated gold nanoparticles as a contrast agent for in vivo X-ray computed tomography imaging. J Am Chem Soc. 2007;129:7661–5.
56. Manohar N, Reynoso FJ, Diagaradjane P, et al. Quantitative imaging of gold nanoparticle distribution in a tumor-bearing mouse using benchtop x-ray fluorescence computed tomography. Sci Rep. 2016;6:22079.
57. Giepmans BNG, Adams SR, Ellisman MH, et al. Review - the fluorescent toolbox for assessing protein location and function. Science. 2006;312:217–24.

58. Kobayashi H, Ogawa M, Alford R, et al. New strategies for fluorescent probe design in medical diagnostic imaging. Chem Rev. 2010;110:2620–40.
59. Gamelin DR, Gudel HU. Design of luminescent inorganic materials: new photophysical processes studied by optical spectroscopy. Acc Chem Res. 2000;33:235–42.
60. Weissleder R. A clearer vision for in vivo imaging. Nat Biotechnol. 2001;19:316–7.
61. Larson DR, Zipfel WR, Williams RM, et al. Water-soluble quantum dots for multiphoton fluorescence imaging in vivo. Science. 2003;300:1434–6.
62. Yu JH, Kwon SH, Petrasek Z, et al. High-resolution three-photon biomedical imaging using doped ZnS nanocrystals. Nat Mater. 2013;12:359–66.
63. Cichy B, Wawrzynczyk D, Bednarkiewicz A, et al. Optical nonlinearities and two-photon excited time-resolved luminescence in colloidal quantum-confined CuInS2/ZnS heterostructures. RSC Adv. 2014;4:34065–72.
64. Subha R, Nalla V, Yu JH, et al. Efficient photoluminescence of Mn2+−doped ZnS quantum dots excited by two-photon absorption in near-infrared window II. J Phys Chem C. 2013;117:20905–11.
65. Betzig E, Patterson GH, Sougrat R, et al. Imaging intracellular fluorescent proteins at nanometer resolution. Science. 2006;313:1642–5.
66. Sochacki KA, Shtengel G, van Engelenburg SB, et al. Correlative super-resolution fluorescence and metal-replica transmission electron microscopy. Nat Methods. 2014;11:305–U278.
67. Zhu MQ, Zhang GF, Hu Z, et al. Reversible fluorescence switching of spiropyran-conjugated biodegradable nanoparticles for super-resolution fluorescence imaging. Macromolecules. 2014;47:1543–52.
68. Lin H, Choi Y, Lee Y, et al. Mapping of surface-enhanced fluorescence on metal nanoparticles using super-resolution photoactivation localization microscopy. Chem Phys Chem. 2012;13:973–81.
69. Auzel F. Upconversion and anti-stokes processes with f and d ions in solids. Chem Rev. 2004;104:139–73.
70. Lu YQ, Zhao JB, Zhang R, et al. Tunable lifetime multiplexing using luminescent nanocrystals. Nat Photonics. 2014;8:33–7.
71. Bunzli JCG, Piguet C. Taking advantage of luminescent lanthanide ions. Chem Soc Rev. 2005;34:1048–77.
72. Zhang F, Shi QH, Zhang YC, et al. Fluorescence upconversion microbarcodes for multiplexed biological detection: nucleic acid encoding. Adv Mater. 2011;23:3775–9.
73. Zheng XL, Zhu XJ, Lu YQ, et al. High-contrast visualization of upconversion luminescence in mice using time-gating approach. Anal Chem. 2016;88:3449–54.
74. Lee J, Yoo B, Lee H, et al. Ultra-wideband multi-dye-sensitized upconverting nanoparticles for information security application. Adv Mater. 2017;29:1603169.
75. Wu X, Zhang YW, Takle K, et al. Dye-sensitized core/active shell upconversion nanoparticles for optogenetics and bioimaging applications. ACS Nano. 2016;10:1060–6.
76. Wang F, Liu XG. Upconversion multicolor fine-tuning: visible to near-infrared emission from lanthanide-doped NaYF4 nanoparticles. J Am Chem Soc. 2008;130:5642.
77. Xie XJ, Gao NY, Deng RR, et al. Mechanistic investigation of photon upconversion in nd3+−sensitized core-shell nanoparticles. J Am Chem Soc. 2013;135:12608–11.
78. Park HS, Nam SH, Kim J, et al. Clear-cut observation of clearance of sustainable upconverting nanoparticles from lymphatic system of small living mice. Sci Rep. 2016;6:27407.
79. Jayakumar MKG, Bansal A, Li BN, et al. Mesoporous silica-coated upconversion nanocrystals for near infrared light-triggered control of gene expression in zebrafish. Nanomedicine. 2015;10:1051–61.
80. Yong-Dong K, Park TE, Singh B, et al. Image-guided nanoparticle-based siRNA delivery for cancer therapy. Curr Pharm Des. 2015;21:4637–56.
81. Iyer AK, He J, Amiji MM. Image-guided nanosystems for targeted delivery in cancer therapy. Curr Med Chem. 2012;19:3230–40.
82. Yu MK, Kim D, Lee IH, et al. Image-guided prostate cancer therapy using aptamer-functionalized thermally cross-linked superparamagnetic iron oxide nanoparticles. Small. 2011;7:2241–9.

83. Tomitaka A, Arami H, Raymond A, et al. Development of magneto-plasmonic nanoparticles for multimodal image-guided therapy to the brain. Nanoscale. 2017;9:764–73.
84. Satpathy M, Wang L, Zielinski RJ, et al. Targeted drug delivery and image-guided therapy of heterogeneous ovarian cancer using her2-targeted theranostic nanoparticles. Theranostics. 2019;9:778–95.
85. Le Duc G, Miladi I, Alric C, et al. Toward an image-guided microbeam radiation therapy using gadolinium-based nanoparticles. ACS Nano. 2011;5:9566–74.
86. Gao S, et al. Hybrid graphene/au activatable theranostic agent for multimodalities imaging guided enhanced photothermal therapy. Biomaterials. 2016;79:36–45.
87. Riley RS, Day ES. Gold nanoparticle-mediated photothermal therapy: applications and opportunities for multimodal cancer treatment. Wiley Interdiscip Rev Nanomed Nanobiotechnol. 2017;9:e1449.
88. Etame AB, Diaz RJ, O'Reilly MA, Smith CA, Mainprize TG, Hynynen K, Rutka JT. Enhanced delivery of gold nanoparticles with therapeutic potential into the brain using MRI-guided focused ultrasound. Nanomedicine. 2012;8:1133–42.
89. Mukherjee S, Chowdhury D, Kotcherlakota R, et al. Potential theranostics application of biosynthesized silver nanoparticles (4-in-1 system). Theranostics. 2014;4:316–35.
90. Patra CR, Mukherjee S, Kotcherlakota R. Biosynthesized silver nanoparticles: a step forward for cancer theranostics. Nanomedicine (Lond). 2014;9:1445–8.
91. Anselmo AC, Mitragotri S. Nanoparticles in the clinic. Bioeng Transl Med. 2016;1:10–29.
92. Thakor AS, Jokerst JV, Ghanouni P, et al. Clinically approved nanoparticle imaging agents. J Nucl Med. 2016;57:1833–7.
93. Scott LJ. Verigene® gram-positive blood culture nucleic acid test. Mol Diagn Ther. 2013;17:117–22.
94. Elsaesser A, Howard CV. Toxicology of nanoparticles. Adv Drug Deliv Rev. 2012;64:129–37.
95. Yildirimer L, Thanh NTK, Loizidou M, et al. Toxicology and clinical potential of nanoparticles. Nano Today. 2011;6:585–607.